



---

# Transverse momentum distributions of primary charged particles in pp, p–Pb and Pb–Pb collisions measured with ALICE at the LHC

---

**Messung der Transversalimpulsspektren von primären geladenen Teilchen in  
hochenergetischen Kern-Kern-Kollisionen mit ALICE**

Zur Erlangung des Grades eines Doktors der Naturwissenschaften (Dr. rer. nat.)  
genehmigte Dissertation von Dipl.-Phys. Michael Linus Knichel, geboren in Mainz  
Tag der Einreichung: 23. September 2014, Tag der Prüfung: 1. Dezember 2014  
D 17 — Darmstadt, 2015

---

1. Gutachten: Prof. Dr. Peter Braun-Munzinger
2. Gutachten: Prof. Dr. Jochen Wambach

---



Fachbereich Physik  
Institut für Kernphysik

Transverse momentum distributions of primary charged particles in pp, p-Pb and Pb-Pb collisions measured with ALICE at the LHC

Messung der Transversalimpulsspektren von primären geladenen Teilchen in hochenergetischen Kern-Kern-Kollisionen mit ALICE

Genehmigte Dissertation von Dipl.-Phys. Michael Linus Knichel, geboren in Mainz

1. Gutachten: Prof. Dr. Peter Braun-Munzinger
2. Gutachten: Prof. Dr. Jochen Wambach

Tag der Einreichung: 23. September 2014

Tag der Prüfung: 1. Dezember 2014

D 17 — Darmstadt, 2015



---

für meine Eltern Annemarie und Wolfgang, meinen Bruder Peter  
und für Taraneh

---



# Abstract

According to the standard model of Big Bang cosmology the earliest universe contained an extremely hot and dense medium that subsequently expanded and cooled. The evolution of the early universe happened through a phase with of deconfined quarks and gluons: the quark-gluon plasma (QGP). This phase ended about ten microseconds after the Big Bang when the temperature dropped below the critical temperature  $T_c$  and quarks and gluons became confined into hadrons. The existence of a QGP phase at high temperature is also predicted by Quantum Chromodynamics (QCD), the fundamental field theory describing the strong interaction of quarks and gluons.

In high-energy collisions of heavy nuclei a QGP can be created and studied experimentally. The energy loss of high energy partons in the hot QCD medium results in a suppression of particle production at large transverse momenta. Measurements of the parton energy loss can be used to characterize the QGP properties.

The Large Hadron Collider (LHC) at CERN provides hadron-hadron (pp), nucleus-nucleus (Pb–Pb) and proton-nucleus (p–Pb) collisions at the highest energies reached in an accelerator so far. The ALICE experiment at the LHC is dedicated to the investigation of the QGP in heavy-ion collisions and complemented by the study of pp and p–Pb collisions. In p–Pb collisions the QGP is not expected to be formed and the nuclear initial state and cold nuclear matter effects can be studied. Measurements in pp collisions serve as a reference for p–Pb and Pb–Pb collisions. They also allow to tune phenomenological models and are a test of theoretical predictions from perturbative QCD.

The data analyzed for this thesis were collected in pp, p–Pb and Pb–Pb collisions by ALICE in 2010-2013 with different minimum bias triggers using the two VZERO scintillators and the Silicon Pixel Detector (SPD). Charged tracks are reconstructed using combined information from the Inner Tracking System (ITS) and the Time Projection Chamber (TPC), the main tracking detectors of ALICE. Events used for the analysis are required to have a reconstructed primary vertex. The selection of tracks is optimized to provide high purity of primary particles and optimal  $p_T$  resolution. Measured  $p_T$  distributions are corrected for tracking efficiency and acceptance effects as well as contamination from secondary particles originating from particle decays or particle production in the detector material. Both corrections are evaluated from full detector simulations using GEANT3 for particle transport through the detector with events generated from the Monte Carlo event generators PYTHIA (pp), DPMJET (p–Pb) and HIJING (Pb–Pb). Corrections for the finite momentum resolution of the detector are derived from the measured  $p_T$  resolution and the  $p_T$  spectra in an unfolding procedure. Spectra are normalized to inelastic yields and cross sections (pp), respectively non-single-diffractive yields (p–Pb), taking into account the efficiencies of the trigger and the vertex reconstruction. Possible sources of systematic uncertainties are identified and their contribution is estimated.

Transverse momentum ( $p_T$ ) distributions of primary charged particles have been measured at mid rapidity  $|\eta| < 0.8$  in inelastic pp collisions at center-of-mass energies of  $\sqrt{s} = 0.9$  TeV (for  $0.15 < p_T < 20$  GeV/c),  $\sqrt{s} = 2.76$  TeV (for  $0.15 < p_T < 32$  GeV/c) and  $\sqrt{s} = 7$  TeV

(for  $0.15 < p_T < 50$  GeV/c). In non-single-diffractive p–Pb collisions at the nucleon-nucleon center-of-mass energy  $\sqrt{s_{NN}} = 5.02$  TeV  $p_T$  distributions have been obtained for three different pseudorapidity intervals ( $|\eta_{\text{cms}}| < 0.3$ ,  $0.3 < \eta_{\text{cms}} < 0.8$  and  $0.8 < \eta_{\text{cms}} < 1.3$ ). The analysis of the first p–Pb collisions at the LHC in 2012 covered  $0.5 < p_T < 20$  GeV/c, the kinematic range was extended to  $0.15 < p_T < 50$  GeV/c with the data collected during the long p–Pb run in 2013. Pb–Pb collisions were analyzed in nine intervals of centrality covering 80% of the total hadronic cross section. Transverse momentum spectra were measured at mid rapidity  $|\eta| < 0.8$  and cover  $0.15 < p_T < 50$  GeV/c for all centrality classes.

The nuclear modification factor  $R_{\text{AA}}$  ( $R_{\text{pPb}}$ ) is calculated as the  $p_T$  differential yield measured in Pb–Pb (p–Pb) collisions divided by the cross section in pp collisions, scaled by the nuclear overlap function calculated in a Monte Carlo Glauber approach. Cold and hot nuclear matter effects can be quantified with the nuclear modification factors as the deviation from binary collision scaling.

To obtain the nuclear modification factor  $R_{\text{pPb}}$  a pp reference is required at  $\sqrt{s} = 5.02$  TeV, where no measurement is available. At large  $p_T$ , the pp reference is constructed from measured spectra at  $\sqrt{s} = 7$  TeV multiplied by scaling factors from NLO pQCD calculations. At low  $p_T$ , where perturbative calculations are not reliable, the pp reference is interpolated between the measurements at  $\sqrt{s} = 2.76$  TeV and  $\sqrt{s} = 7$  TeV, assuming a power law behavior of the cross section as function of  $\sqrt{s}$ . As pp reference for  $R_{\text{AA}}$  the measurement at  $\sqrt{s} = 2.76$  TeV is used, with a parameterization of the data for  $5 < p_T < 32$  GeV/c and an extrapolation to  $32 < p_T < 50$  GeV/c.

Fully corrected transverse momentum spectra are also obtained as a function of the measured particle multiplicity. The average transverse momentum  $\langle p_T \rangle$  as a function of the true multiplicity is constructed using a reweighting procedure with effective corrections obtained from Monte Carlo simulations which account for limited acceptance, tracking efficiency and contamination. The multiplicity dependence of the average transverse momentum is compared to predictions from Monte Carlo event generators and (in p–Pb and Pb–Pb collisions) to expectations from binary collision scaling.

In pp collisions the expected power-law behavior at large transverse momentum is observed, but the measured cross section does not agree with next-to-leading order (NLO) perturbative QCD calculations. At small transverse momenta the shape of the spectrum is approximately exponential. The data are compared to the MC event generators PHOJET and PYTHIA; none of them agrees with the data over the full  $p_T$  range.

In p–Pb collisions  $p_T$  spectra are softer at forward pseudorapidity (in the Pb fragmentation region). The nuclear modification factor  $R_{\text{pPb}}$  reveals that at low  $p_T$  approximate participant scaling is in place. In the intermediate  $p_T$  region, a hint of Cronin enhancement is visible, but at the edge of the experimental uncertainties. At high  $p_T$  no deviation from binary collision scaling is observed and  $R_{\text{pPb}}$  is consistent with unity. Theoretical predictions from a Color Glass Condensate initial state model are in agreement with the measured  $R_{\text{pPb}}$ , as well as as calculations based on NLO pQCD with EPS09s nuclear parton distribution functions.

In Pb–Pb collisions particle production is suppressed compared to the expectation from binary collision scaling. The suppression is largest for central collisions but remains substantial also for peripheral collisions. For central (0–5%) collisions the nuclear modification factor is about

0.4 at the largest measured momenta. The observations are in quantitative agreement only with part of theoretical models that incorporate medium-induced parton energy loss.

In the future, improvements in the simulations and analysis procedure are expected to reduce the systematic uncertainties to about half the current values. With the inclusion of Pb–Pb data recorded in 2011 and the use of other triggers than minimum bias the  $p_{\mathrm{T}}$  reach could be extended up to 100 GeV/c.



# Zusammenfassung

Die Quantenchromodynamik (QCD) als fundamentale Theorie der stark wechselwirkenden Teilchen sagt die Existenz einer Phase mit freien Quarks und Gluonen voraus, die als Quark-Gluon-Plasma (QGP) bezeichnet wird. Gemäß dem kosmologischen Standardmodell befand sich das frühe Universum in einem extrem heißen und dichten Zustand und enthielt bis wenige Mikrosekunden nach dem Urknall ein QGP. In relativistischen Kern-Kern-Kollisionen kann ein QGP kurzzeitig hergestellt und untersucht werden. Das so erzeugte QGP existiert nur etwa 10 fm/c (Größenordnung  $10^{-23}$  Sekunden), dann sinkt durch die Expansion des Mediums die Temperatur unter die Phasenübergangstemperatur und Quarks und Gluonen werden wieder in farbneutralen Hadronen gebunden. Dieser hadronische Endzustand wird in Detektoren gemessen und erlaubt Rückschlüsse auf die Eigenschaften des QGP. Ein charakteristischer Effekt ist der Energieverlust von hochenergetischen Partonen (Quarks und Gluonen) bei der Durchquerung des umgebenden Mediums. Dieser Energieverlust wird in Messungen als Unterdrückung von hochenergetischen Hadronen sichtbar. Eine Einführung in die Grundlagen von relativistischen Schwerionenkollisionen findet sich in Kapitel 1.

Der Large Hadron Collider (LHC) des CERN in Genf erreicht die größten Kollisionsenergien aller bisherigen Teilchenbeschleuniger und liefert seit seiner Inbetriebnahme Proton-Proton- (pp), Blei-Blei- (Pb-Pb) und Proton-Blei- (p-Pb) Kollisionen für die Experimente. Das ALICE-Experiment ist primär auf die Untersuchung des QGP in Pb-Pb-Kollisionen konzentriert, misst aber auch pp- und p-Pb- Kollisionen. Die pp-Kollisionen dienen dabei als wichtige Referenzmessung, um nukleare Effekte in p-Pb- und Pb-Pb-Kollisionen zu untersuchen. Darüber hinaus lassen sich Vorhersagen von störungstheoretischer QCD und Monte-Carlo-Modellen überprüfen. Messungen in Pb-Pb-Kollisionen ermöglichen es, die Mechanismen des Energieverlusts zu untersuchen und das QGP zu charakterisieren. In p-Pb-Kollisionen wird kein QGP erzeugt und es lassen sich Effekte des nuklearen Anfangszustands untersuchen.

Im Rahmen dieser Arbeit wurden Daten von allen drei Kollisionssystemen analysiert, die in den Jahren 2010-2013 vom ALICE-Detektor aufgezeichnet wurden und daraus die Verteilung des Transversalimpulses  $p_T$  von inklusiven primären geladenen Teilchen bestimmt. Für die Analyse wurden Teilchenkollisionen mit einem Trigger mit minimalem Bias ausgewählt. Als Triggerdetektoren dienen der Silizium-Pixel-Detektor (SPD) sowie in Vorwärtsrichtung zwei Szintillationsdetektoren (V0-A und V0-C) beiderseits des Kollisionspunktes. Die Rekonstruktion der Spuren von geladenen Teilchen erfolgt mithilfe der Spurendriftkammer TPC (Time Projection Chamber) und des Silizium-Detektors ITS (Inner Tracking System). In Kapitel 2 dieser Arbeit wird der ALICE-Detektor vorgestellt. Nur Spuren, die bestimmte Qualitätskriterien erfüllen, werden in der Analyse berücksichtigt. Die Auswahl von langen Spuren mit zahlreichen Rekonstruktionspunkten ermöglicht eine optimale Transversalimpulsauflösung. Außerdem wurden nur Spuren berücksichtigt, die mit dem primären Vertex verträglich sind. Damit wird der Anteil an Sekundärteilchen, die aus Zerfällen von kurzlebigen Teilchen und aus der Wechselwirkung mit dem Detektormaterial stammen, unterdrückt. Für beide Kriterien ist es notwendig, dass die Spuren auch im ITS gemessen wurden. Die aus den Daten rekonstruierten  $p_T$ -Spektren werden um die Unzulänglichkeiten der Akzeptanz des Detektors

und der Effizienz der Spurenrekonstruktion sowie für den Anteil sekundärer Teilchen korrigiert. Die Korrekturfaktoren werden aus simulierten Teilchenkollisionen gewonnen, auch das Verhalten des gesamten Detektors wird dabei simuliert. Die Transversalimpulsauflösung wurde aus den Fits der gemessenen Spuren bestimmt und die Spektren damit für Effekte der begrenzten Auflösung korrigiert. In p–Pb-Kollisionen erfolgt eine zusätzliche Akzeptanzkorrektur, um Ergebnisse im Schwerpunktssystem des Nukleon-Nukleon-Systems zu erhalten. Die Normierung der korrigierten Spektren berücksichtigt die Triggereffizienz, die Rekonstruktionseffizienz des primären Vertex und die Selektion der Ereignisse. Dabei sind besonders die Ereignisse relevant, in denen keine Spuren rekonstruiert wurden, die aber dennoch zur Normierung beitragen. Die Ergebnisse werden als differentieller Wirkungsquerschnitt (pp) und als differentieller Yield (pp, p–Pb, Pb–Pb) präsentiert. Die Analyse von Pb–Pb-Kollisionen erfolgt als Funktion der Zentralität, in p–Pb-Kollisionen wurden verschiedene Bereiche der Pseudorapidität getrennt untersucht. Folgende Faktoren wurden in Bezug auf Ihren Einfluss auf das Messergebnis untersucht und zur Bestimmung der systematischen Unsicherheiten verwendet: die Variation der Auswahlkriterien für Ereignisse und Spuren, die Bestimmung der Zentralität in Pb–Pb-Kollisionen, der Einfluss der Triggerbedingung sowie die Rekonstruktion des primären Vertex, die Effizienz der Spurenrekonstruktion, die Transversalimpulsauflösung, die Variation der Materialmenge im Detektor, die Variation der relativen Verhältnisse der primären Teilchenspezies (vor allem Pionen, Kaonen und Protonen), die Abhängigkeit von dem zur Simulation benutzen Monte-Carlo-Modell und der Anteil an sekundären Teilchen. Die Details der Datenanalyse samt Korrekturen und systematischen Unsicherheiten sind in Kapitel 3 ausführlich dargestellt.

Die Ergebnisse werden in Kapitel 4 präsentiert. Es wurden  $p_T$ -Spektren für primäre geladene Teilchen im zentralen Rapiditätsbereich gemessen, die einen  $p_T$ -Bereich von minimal 150 MeV/c bis maximal 50 GeV/c abdecken. Die Begrenzung auf  $p_T > 150$  MeV/c ist durch die bei kleineren Impulsen rapide sinkende Effizienz bedingt, zu höheren  $p_T$  hin sind die  $p_T$ -Auflösung und die statistischen Unsicherheiten die begrenzenden Faktoren.

In pp-Kollisionen wurden Transversalimpulsverteilungen für die Pseudorapidität  $|\eta| < 0.8$  bei den Schwerpunktenergien  $\sqrt{s} = 0.9$  TeV (für  $p_T < 20$  GeV/c),  $\sqrt{s} = 2.76$  TeV (für  $p_T < 32$  GeV/c) und  $\sqrt{s} = 7$  TeV (für  $p_T < 50$  GeV/c) gemessen. Im Bereich niedriger  $p_T$  fällt der Wirkungsquerschnitt dabei annähernd exponentiell mit  $p_T$  ab, bei hohen  $p_T$  wird das von QCD vorhergesagte Potenzspektrum beobachtet. Im Vergleich zu den gemessenen Spektren ist ein mit Störungstheoretischer QCD berechneter Wirkungsquerschnitt um etwa einen Faktor 2 zu groß. Auch keines der getesteten Monte-Carlo-Modelle kann das Spektrum über den gesamten Bereich beschreiben.

Nukleare Effekte in Pb–Pb- (p–Pb-) Kollisionen werden durch das Verhältnis  $R_{AA}$  ( $R_{pPb}$ ) quantifiziert. Dabei wird die Teilchenproduktion im QCD-Medium (p–Pb, Pb–Pb) mit der im QCD-Vakuum (pp) verglichen.  $R_{AA}$  ( $R_{pPb}$ ) ist das Spektrum in Pb–Pb- (p–Pb-) Kollisionen dividiert durch das mit der mittleren Anzahl der Nukleon-Nukleon-Kollisionen multiplizierte Spektrum in pp-Kollisionen der gleichen Energie. Abweichungen von der Skalierung mit Nukleon-Nukleon-Kollisionen sind als von Eins verschiedenes Verhältnis erkennbar. Die Verhältnisse  $R_{AA}$  und  $R_{pPb}$  erleichtern einen Vergleich mit theoretischen Modellrechnungen, da sich Unterschiede in der zugrunde liegenden Produktion von Teilchen im QCD-Vakuum teilweise aufheben.

In p–Pb-Kollisionen beträgt die Schwerpunktsenergie im Nukleon-Nukleon-System  $\sqrt{s_{\text{NN}}} = 5.02 \text{ TeV}$ . Da für diese Energie keine entsprechende Referenzmessung von pp-Kollisionen existiert, muss das Referenzspektrum aus den bei  $\sqrt{s} = 2.76 \text{ TeV}$  und  $\sqrt{s} = 7 \text{ TeV}$  gemessenen Daten abgeleitet werden. Für  $p_T > 5 \text{ GeV}/c$  wurden hierzu die bei  $\sqrt{s} = 7 \text{ TeV}$  gemessenen Spektren auf  $\sqrt{s} = 5.02 \text{ TeV}$  skaliert. Die Skalierungsfaktoren stammen aus dem Verhältnis der mithilfe störungstheoretischer QCD berechneten Spektren. Im Bereich von niedrigen  $p_T$  sind störungstheoretische Berechnungen nicht verlässlich, daher wurde für  $p_T < 5 \text{ GeV}/c$  zwischen den gemessenen Daten bei  $\sqrt{s} = 2.76 \text{ TeV}$  und  $\sqrt{s} = 7 \text{ TeV}$  interpoliert. Dabei wurde die Energieabhängigkeit des differentiellen Wirkungsquerschnitts durch ein Potenzgesetz beschrieben.

In einem kurzen Testlauf mit p–Pb-Kollisionen 2012 wurden  $p_T$ -Spektren und  $R_{\text{pPb}}$  im Bereich  $0.5 < p_T < 20 \text{ GeV}/c$  gemessen. Nachdem 2013 weitere p–Pb-Kollisionen mit einer um fast zwei Größenordnungen höheren Statistik aufgenommen wurden, konnte die Messung auf  $0.15 < p_T < 50 \text{ GeV}/c$  ausgedehnt werden. Für beide Datensätze wurden neben einem Bereich zentraler Pseudorapidität ( $|\eta_{\text{cms}}| < 0.3$ ) auch zwei Intervalle in Richtung des fragmentierenden Bleikerns ( $0.3 < \eta_{\text{cms}} < 0.8$  und  $0.8 < \eta_{\text{cms}} < 1.3$ ) untersucht. Die Teilchenproduktion in p–Pb-Kollisionen zeigt bei großen  $p_T > 5 \text{ GeV}/c$  eine Skalierung mit der Anzahl der binären Nukleon-Nukleon-Kollisionen. Bei niedrigen  $p_T$  zeigen sich, wie erwartet, Abweichungen von dieser Skalierung, wobei bei sehr niedrigen  $p_T < 500 \text{ MeV}/c$  die Teilchenproduktion etwa mit der Anzahl der an der Kollision beteiligten Nukleonen skaliert.

In Pb–Pb-Kollisionen wurden  $p_T$ -Spektren und  $R_{\text{AA}}$  für neun verschiedene Zentralitätsintervalle im Bereich von 0% (zentralste Kollisionen) bis 80% (peripherie Kollisionen) gemessen, die  $0.15 < p_T < 50 \text{ GeV}/c$  abdecken. In zentralen Kollisionen zeigt sich eine starke Unterdrückung der Teilchenproduktion, auch bei großem  $p_T$ . Für die 0-5% zentralsten Kollisionen ist  $R_{\text{AA}} \approx 0.13$  um  $p_T = 7 \text{ GeV}/c$  und  $R_{\text{AA}} \approx 0.4$  bei  $p_T = 50 \text{ GeV}/c$ . Mit abnehmender Zentralität ist die Unterdrückung schwächer ausgeprägt. Die Ergebnisse bei großem  $p_T$  in peripheren Kollisionen sind mit der Annahme einer inkohärenten Überlagerung von Nukleon-Nukleon-Kollisionen verträglich. Bei sehr niedrigen ( $p_T < 0.5 \text{ GeV}/c$ ) und mittleren ( $4 < p_T < 8 \text{ GeV}/c$ ) Transversalimpulsen skaliert die Teilchenproduktion näherungsweise mit der Anzahl der beteiligten Nukleonen.

Die Analyse der  $p_T$ -Spektren in pp- und p–Pb-Kollisionen wurde ergänzend auch als Funktion der Anzahl von rekonstruierten geladenen Teilchen  $N_{\text{acc}}$  durchgeführt. Damit lässt sich die Korrelation von mittlerem Transversalimpuls  $\langle p_T \rangle$  mit der Multiplizität untersuchen. Durch eine entsprechende Gewichtung wird dabei  $\langle p_T \rangle$  auch als Funktion der wahren Multiplizität  $N_{\text{ch}}$  abgeleitet. Die Ergebnisse werden mit theoretischen Modellrechnungen verglichen. Kapitel 5 beschreibt die Methode und Ergebnisse der Analyse von  $\langle p_T \rangle$  als Funktion von  $N_{\text{ch}}$ .

Die Ergebnisse sind in Kapitel 6 zusammengefasst. Die Transversalimpulsverteilung von geladenen Teilchen in pp-Kollisionen wird durch theoretische und phänomenologische Modelle nur unzureichend beschrieben und Messungen stellen eine unverzichtbare Referenz für die Interpretation der Ergebnisse in p–Pb- und Pb–Pb-Kollisionen dar. Das Verhältnis  $R_{\text{pPb}}$  deutet darauf hin, dass nukleare Effekte die Teilchenproduktion in p–Pb-Kollisionen bei hohem  $p_T$  nur wenig beeinflussen. In Pb–Pb-Kollisionen ist die Teilchenproduktion bei hohen  $p_T$  deutlich unterdrückt, im Einklang mit theoretischen Vorhersagen, die den Energieverlust von Partonen im QGP modellieren. Schlussfolgerungen über den nuklearen Anfangszustand, den Mechanismus

---

---

des Energieverlusts und die Eigenschaften des QGP erfordern den Vergleich von theoretischen Modellen auch mit Messungen anderer Observablen.

Ein Ausblick auf zukünftige Möglichkeiten der Analyse wird in Kapitel 7 gegeben. Es wird eine verbesserte Genauigkeit der bisherigen Ergebnisse sowie Erweiterung der Messungen zu höheren  $p_T$  angestrebt. Dazu sind kleine Unsicherheiten und eine größere Datenmenge notwendig. Vor allem durch Optimierung von Detektorkalibrierung, Spurrekonstruktion, Spurauswahl und Simulationen könnten die systematischen Unsicherheiten deutlich verringert werden. Bis-her wurden nicht alle vorhandenen Daten analysiert, insbesondere die 2011 aufgezeichneten Pb–Pb-Kollisionen sowie die mit besonderen Triggern aufgenommen pp- und p–Pb-Kollisionen ermöglichen höhere Statistik. Nach dem Ende der Betriebspause des LHC Anfang 2015 werden Kollisionen mit nochmals deutlich höherer Schwerpunktsenergie folgen. Zunächst sind pp-, später auch Pb–Pb- und p–Pb-Kollisionen vorgesehen. Die Messungen von  $p_T$ -Spektren bei diesen Energien erlauben eine zusätzliche Eingrenzung von theoretischen Modellen.

# Contents

<b>1. Introduction</b>	17
1.1. The standard model of particle physics . . . . .	18
1.2. Quantum chromodynamics . . . . .	20
1.2.1. Perturbative QCD . . . . .	23
1.2.2. Chiral symmetry . . . . .	26
1.3. The phase diagram of nuclear matter and the QGP . . . . .	28
1.4. Evolution of heavy-ion collisions . . . . .	30
1.5. Experimental observables of the QGP . . . . .	32
1.6. Parton energy loss and jet quenching in the QGP . . . . .	33
1.7. Glauber model . . . . .	35
1.8. Event types in pp collisions . . . . .	37
<b>2. The ALICE experiment at the LHC</b>	41
2.1. The Large Hadron Collider . . . . .	41
2.1.1. Experiments at the LHC . . . . .	42
2.2. The ALICE experimental setup . . . . .	43
2.2.1. ALICE Coordinate system . . . . .	44
2.3. Central Barrel Detectors . . . . .	45
2.3.1. Inner Tracking System . . . . .	46
2.3.2. Time Projection Chamber . . . . .	47
2.3.3. Transition Radiation Detector . . . . .	48
2.3.4. Time-Of-Flight detector . . . . .	49
2.3.5. Electromagnetic Calorimeter . . . . .	49
2.3.6. Photon Spectrometer . . . . .	49
2.3.7. High Momentum Particle Identification Detector . . . . .	50
2.4. Forward and trigger detectors . . . . .	50
2.4.1. V0 detectors . . . . .	50
2.4.2. T0 detectors . . . . .	50
2.4.3. Forward Multiplicity Detector . . . . .	50
2.4.4. Photon Multiplicity Detector . . . . .	51
2.4.5. Zero Degree Calorimeter . . . . .	51
2.5. Muon spectrometer . . . . .	51
2.6. Track reconstruction . . . . .	52
2.7. Centrality determination in ALICE . . . . .	53
<b>3. Measurement of transverse momentum spectra</b>	57
3.1. Introduction . . . . .	57
3.1.1. Kinematic range . . . . .	57
3.1.2. Primary charged particles . . . . .	58
3.2. Analysis strategy . . . . .	61

3.3.	Data and MC samples . . . . .	61
3.4.	Trigger and event selection . . . . .	62
3.4.1.	Trigger . . . . .	62
3.4.2.	Selection of collision candidates . . . . .	63
3.4.3.	z-Vertex selection . . . . .	64
3.4.4.	Centrality selection in Pb–Pb . . . . .	69
3.4.5.	Summary of event statistics . . . . .	69
3.5.	Track selection . . . . .	70
3.5.1.	TPC cuts . . . . .	71
3.5.2.	ITS cuts . . . . .	71
3.5.3.	Primary selection . . . . .	75
3.5.4.	TPC-ITS $\chi^2$ cut . . . . .	75
3.5.5.	Track cut performance . . . . .	76
3.6.	Corrections . . . . .	77
3.7.	Track-level corrections . . . . .	78
3.7.1.	Tracking Efficiency . . . . .	78
3.7.2.	Contamination . . . . .	82
3.7.3.	Fake tracks . . . . .	86
3.7.4.	Transverse momentum resolution . . . . .	86
3.7.5.	Acceptance Corrections in p–Pb . . . . .	91
3.8.	Event Level corrections . . . . .	94
3.8.1.	Trigger efficiency . . . . .	97
3.9.	Application of track and event corrections . . . . .	99
3.10.	Systematic uncertainties . . . . .	101
3.10.1.	Overview . . . . .	101
3.10.2.	Procedure . . . . .	101
3.10.3.	Event Selection . . . . .	104
3.10.4.	Centrality selection in Pb–Pb . . . . .	104
3.10.5.	Trigger and Vertex . . . . .	105
3.10.6.	Tracking efficiency . . . . .	106
3.10.7.	$p_T$ resolution . . . . .	107
3.10.8.	Material Budget . . . . .	111
3.10.9.	Particle composition . . . . .	112
3.10.10.	MC generator . . . . .	113
3.10.11.	Secondary particles . . . . .	114
3.10.12.	$p_T$ dependence of the systematic uncertainties . . . . .	114
3.10.13.	Ratios of spectra at different pseudorapidities in p–Pb . . . . .	114
<b>4.</b>	<b>Results</b> . . . . .	119
4.1.	pp collisions . . . . .	119
4.2.	Construction of pp references . . . . .	128
4.2.1.	pp reference for $\sqrt{s} = 2.76$ TeV . . . . .	128
4.2.2.	pp reference for $\sqrt{s} = 5.02$ TeV . . . . .	131
4.3.	p–Pb collisions . . . . .	134
4.3.1.	2012 pilot run . . . . .	134
4.3.2.	2013 run with extended $p_T$ range . . . . .	138

---

---

4.4. Pb–Pb collisions . . . . .	141
<b>5. Multiplicity dependence of the average transverse momentum</b>	151
5.1. Analysis . . . . .	151
5.2. Glauber Model for average transverse momentum . . . . .	155
5.3. Results . . . . .	159
<b>6. Summary and Conclusions</b>	165
<b>7. Outlook</b>	169
7.1. pp collisions and pp reference . . . . .	169
7.2. p–Pb collisions and $R_{pPb}$ . . . . .	171
7.3. Pb–Pb collisions and $R_{AA}$ . . . . .	172
7.4. Possibilities for smaller systematic uncertainties . . . . .	172
7.5. Possibilities for larger statistics data . . . . .	175
7.6. Future running . . . . .	175
<b>A. List of runs used in the analysis</b>	177
<b>B. Comparison of Pb–Pb results to the ALICE identified charged particle measurement</b>	180
<b>C. Comparison of HIJING particle composition to the ALICE measurement</b>	182
<b>D. Distributions of cut variables</b>	184
<b>E. Cut Performance</b>	203
<b>References</b>	207



# 1 Introduction

All matter surrounding us consists of atoms build from electrons and nuclei which are composed of protons and neutrons (nucleons). Protons and neutrons are bound states of quarks and gluons. The fundamental theory describing the dynamics of quarks and gluons is called Quantum Chromodynamics (QCD). Quarks and gluons do not occur as free particles, but only in bound states called hadrons.

If condensed matter is heated it will undergo phase transition(s) to the gas phase, and, if heated further, will become an electric plasma with free electrons and ions. Similarly, nuclear matter will undergo a phase transition to a medium of deconfined quarks and gluons if it is heated or compressed. The deconfined medium is called the Quark-Gluon Plasma (QGP).

As we know from the red-shift of distance galaxies the universe<sup>1</sup> is expanding at a rate described by the Hubble constant  $H_0 \approx 70 \text{ km s}^{-1} \text{ Mpc}^{-1}$  [2]. Assuming a constant expansion rate the age of the universe is given by the inverse of the Hubble constant  $1/H_0 \approx 13$  billion years.<sup>2</sup> If this expansion is extrapolated backwards in time it means the universe was once much smaller, but much denser and hotter, with a temperature scale related to the time scale via  $T(\text{MeV}) \sim 1/\sqrt{t(\text{s})}$  [5]. After the Planck era, the GUT era, the inflation and the electroweak era, at times around  $10^{-12} \text{ s}$  after the Big Bang the temperature dropped below the electroweak symmetry breaking scale of about 200 GeV leading to the separation of the strong and electromagnetic force and the universe consisted of a QGP until the temperature dropped below the critical temperature  $T_c \approx 160 \text{ MeV}$ . This happened a few microseconds after the Big Bang.

The conditions that have existed during the early phase of the universe can be created in ultrarelativistic heavy-ion collisions. Heavy nuclei, like lead or gold, are accelerated to relativistic energies and form a very dense medium with high temperature. The Large Hadron Collider (LHC) at CERN provides the highest energy achieved so far in particle accelerators. In high energy collisions of heavy nuclei a medium with initial temperatures of several times  $T_c$  is formed. This estimate of the initial temperatures is based on measurements of thermal photons and hydrodynamic simulations [6, 7].

The QGP created in an accelerator lives only for a short time ( $\approx 10 \text{ fm}/c$  [8]) before the temperature drops below  $T_c$  and quarks and gluon form hadrons again that are observed in the experiments. The properties of the QGP can be studied only via these final state hadrons. One characteristic feature of the QGP is the fact that fast quarks or gluons that travel inside the medium loose energy, similar to the electromagnetic energy loss of particles in matter, while for particles that do not interact strongly (like electrons or photons) the QGP is transparent.

The high-energy partons that are used to probe the medium are created in the same collisions where the QGP is formed. However, due to their high energy they are created at early times ( $\tau \sim 1/Q$ ), according to the uncertainty relation between time and energy. High-energy partons fragment into jets of high energy hadrons, the energy loss of partons is therefore

<sup>1</sup> See [1] for an introduction to the early universe.

<sup>2</sup> Taking into account the accelerated expansion the universe is estimated to be 13.8 billion years old [3, 4].

also known as jet quenching. It can be used as a tool to study the medium, known as jet tomography.

Experimentally, jet quenching has been prominently observed at the Relativistic Heavy-Ion Collider (RHIC) in the suppression of hadron production by all four experiments: PHENIX [9, 10], STAR [11, 12], BRAHMS [13] and PHOBOS [14].

At the even higher LHC energies, more high-energy partons are produced making the LHC ideally suited for the study of jet quenching and parton energy loss.

Many theoretical models aim to describe jet quenching from parton energy loss using different approaches. This requires not only understanding the interaction of a parton with the medium in an energy loss model but needs also a model of the medium evolution.

For experimental observables it is useful to study also smaller collision systems, in particular proton-proton or proton-nucleus collisions, where no QGP is formed, as a reference for measurements in heavy ion collisions.

---

## 1.1 The standard model of particle physics

---

In the present theoretical understanding of physics there are known four fundamental interactions with the relative strength given by the coupling constant:

- strong interaction (relative strength  $\sim 1$ )
- electromagnetic interaction (relative strength  $\sim 10^{-2}$ )
- weak interaction (relative strength  $\sim 10^{-13}$ )
- gravity (relative strength  $\sim 10^{-38}$ )

The strong interaction is responsible for binding quarks inside the nucleons and the nucleons inside the nucleus. Also most of the mass of hadrons is generated by the strong interaction. Theoretically it is an interaction between color charges and described by Quantum Chromodynamics (QCD) which is further explained in the following sections. It is the strongest of the four interactions but its range is limited to a couple fm, corresponding to the size of a nucleus.

All our everyday life experiences are based on the electromagnetic interaction which is the fundamental interaction responsible not only for macroscopic electric and magnetic phenomena but also for chemistry and friction. Theoretically the electromagnetic interaction is described by Quantum electrodynamics (QED).

The weak interaction is responsible for the decay of many unstable particles, including the nuclear  $\beta$  decay. An example is the decay of the free neutron:  $n \longrightarrow p + e^- + \bar{\nu}_e$ .

The fact that the weak interaction has a small strength compared to the electromagnetic interaction is a result of the high mass of the force carriers, the  $W$  and  $Z$  bosons. At energies larger than the mass of these bosons, the electromagnetic and weak interaction are equally strong. Weak and electromagnetic interactions are described by the unified theory of electroweak interactions. The theory of electroweak interactions also includes the Higgs field that give masses to all fundamental particles. Gauge bosons acquire mass via spontaneous symmetry breaking and fermion masses are the result of Yukawa interactions.

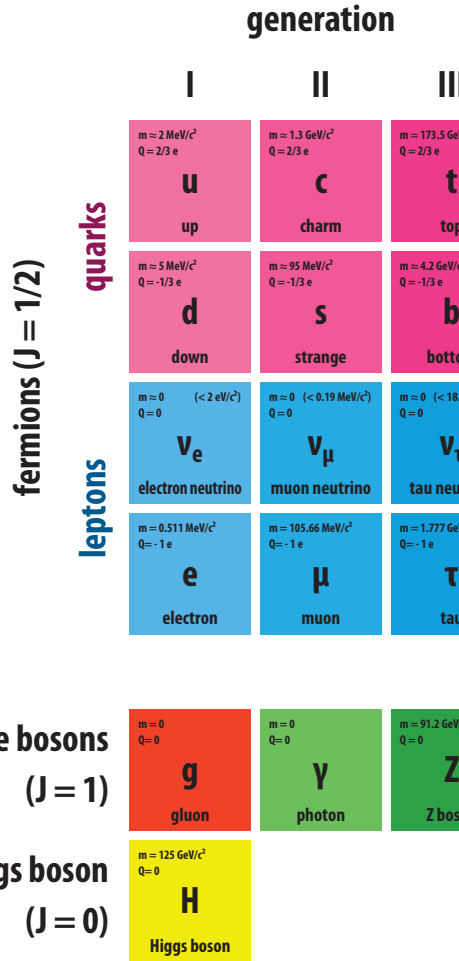


Figure 1.1.: Standard model particles (masses from [17]). For quarks  $\overline{MS}$  masses are quoted, pole mass for the top. Neutrinos are massless in the standard model. The upper limits are direct measurements, constraints from cosmology [18] imply  $m_\nu < 0.23$  eV. Corresponding antiparticles exist for all listed particles, except for H, g,  $\gamma$  and  $Z^0$  (which are their own antiparticles).

Gravity is the weakest force but has an infinite range. Theoretically it is described by Einsteins general theory of relativity. Strong and weak force are short-ranged, while electromagnetic interactions are screened because atoms are neutral thus gravity is dominating our universe on large scales.

An overview over the fundamental particles is shown in Figure 1.1 along with their properties. With the recent discovery of the Higgs boson at the LHC [15, 16] all the standard model particles have been experimentally observed.

Fundamental Particles can be divided into two groups: fermions with half-integer spin and bosons with integer spin. The fermions (quarks and leptons) interact via the exchange of gauge bosons. Electromagnetic interactions are mediated by the photon  $\gamma$ , the weak interaction by the  $W^\pm$  and  $Z^0$  bosons. The gluon is the gauge boson of the strong interaction. Gravity is not part of the standard model of particle physics and a generally accepted quantum theory of

gravity does not exist (see Refs. [19, 20]) for a historical summary). In theoretical attempts to quantum gravity the gauge boson is a massless spin-2 particle called graviton.

In the lepton and quark sector three generations of particles with increasing mass can be identified. Measurements of the  $Z$  boson decay width indicate that there are only these three generations [21].

## 1.2 Quantum chromodynamics

The theory to describe the strong interactions between quarks and gluons is called Quantum chromodynamics (QCD). Its dynamics are governed by the Lagrangian density:

$$\mathcal{L}_{\text{QCD}} = \bar{q} (i\gamma^\mu \partial_\mu - m) q + g \bar{q} \gamma^\mu T_a A_\mu^a q - \frac{1}{4} F_{\mu\nu}^a F_a^{\mu\nu} \quad (1.1)$$

Here  $q, \bar{q}$  are the quarks fields (3-vectors in color space, each one a 4-component spinor) with mass  $m$ .  $A_\mu^a$  are the eight gluon potentials and  $T_a$  are the eight generators of  $\text{SU}(3)$ , which are commonly represented by the Gell-Mann matrices  $T_a = \lambda_a/2$ .  $g$  is the dimensionless coupling constant.

The first term encodes the Dirac equation and describes a free (non-interacting) quark with mass  $m$ , it is exactly the same as in QED. Interactions between quarks and gluons are described by the second term, which is a vertex with two quarks and one gluon. As such it describes the gluon emission and absorption of quarks, as well as gluon splitting, a process in which a gluon produces a quark-antiquark pair. The interaction with a gluon changes the color state of a quark. Note that there are no direct interaction between quarks, so quarks (must) couple via gluon exchange.

The third term is the squared field strength tensor describing the dynamics of the gauge field:

$$F_{\mu\nu}^a = \partial_\mu A_\nu^a - \partial_\nu A_\mu^a + g f^{abc} A_\mu^b A_\nu^c \quad (1.2)$$

Here  $f^{abc}$  are the structure constants of  $\text{SU}(3)$ .

In the field strength tensor the first part is the kinetic term of a massless vector field, again very similar to QED. The interesting part is the additional component, required by gauge invariance. The appearance of the commutator of gluon potentials in equation 1.2 leads to three and four gluon vertices when squared in the Lagrangian (equation 1.1) with the universal coupling  $g$  ( $g^2$  in the case of the 4-gluon vertex). This is fundamentally different to QED, where there are no direct interactions between the gauge bosons (photons). The gluon-gluon vertices are the reason why the strong interaction is short-ranged, even though the force carriers are massless. Interesting phenomena in QCD like asymptotic freedom and color confinement emerge from the self interaction between gluons.

Only the parts for the free fields and the basic interaction of the QCD Lagrangian are shown in Equation 1.1. In the quantization and renormalization of QCD additional terms, counterterms and ghosts, arise in the Lagrangian.

The QCD Lagrangian (Equation 1.1) conserves color, because this is the gauge principle it is based on. In addition, it is diagonal in flavor space, i.e. for each quark flavor the net flavor (difference between quark and anti-quarks) is conserved.

$$n_i - n_{\bar{i}} = \text{const} \quad i = u, d, s, c, b, t$$

This flavor number conservation implies also conservation of electric charge and the baryon number

$$B = \frac{1}{3}(n_q - n_{\bar{q}}).$$

In the renormalization of QCD a scale dependence on the renormalization scale  $\mu_R$  is introduced. All quantities, including masses and coupling constants, become a function of  $\mu_R$ . In perturbative calculations the renormalization scale is usually taken to be the 4-momentum transfer of a reaction  $\mu_R^2 = Q^2$ .

The change of the strong coupling constant  $\alpha_s = \frac{g^2}{4\pi}$  with the scale  $\mu_R$  is described by the  $\beta$  function in the renormalization group equation:

$$\frac{\partial \alpha_s(\mu_R^2)}{\partial \ln \mu_R^2} = \beta(\alpha_s) = -\frac{\alpha_s^2}{4\pi} \beta_0 + \mathcal{O}(\alpha_s^3) \quad (1.3)$$

Assuming that the coupling constant is small, the  $\beta$  function can be expanded in powers of  $\alpha_s$ , corresponding to the number of vertices in the diagrams. A one-loop diagram has two additional vertices, so the lowest power is  $\propto \alpha_s^2$ . The parameter  $\beta_0$  has to be calculated from the corresponding diagrams.

Taking only the this first order, corresponding to one loop, into account the solution to equation 1.3 is the scale dependence of  $\alpha_s$  (running coupling):

$$\alpha_s(\mu_R^2) = \frac{4\pi}{\beta_0 \ln(\mu_R^2 / \Lambda_{\text{QCD}}^2)} \quad (1.4)$$

The integration introduces an additional constant  $\Lambda_{\text{QCD}}$ , the QCD scale. Its value can not be calculated in perturbative QCD (pQCD) and has to be determined from experiments or lattice QCD calculations and is  $\Lambda_{\text{QCD}} \approx 200 \text{ MeV}$ .

From pQCD the  $\beta$  coefficients have been calculated up to four loops [22], the lowest order one is:

$$\beta_0 = \frac{11}{3}C_A - \frac{4}{3}T_f n_f = 11 - \frac{2}{3}n_f \quad (1.5)$$

In this expression  $C_A = N_c = 3$  is the color factor for three-gluon vertex, identical to the number of colors,  $T_f = 1/2$  is the color factor for gluon splitting to a quark-antiquark pair. The number of active flavors  $n_f \leq 6$  depends on the scale.

In equation 1.5 two contributions can be identified, the second parts which has negative sign corresponds to the quark-antiquark loop, and is similar to the QED vacuum polarization. It

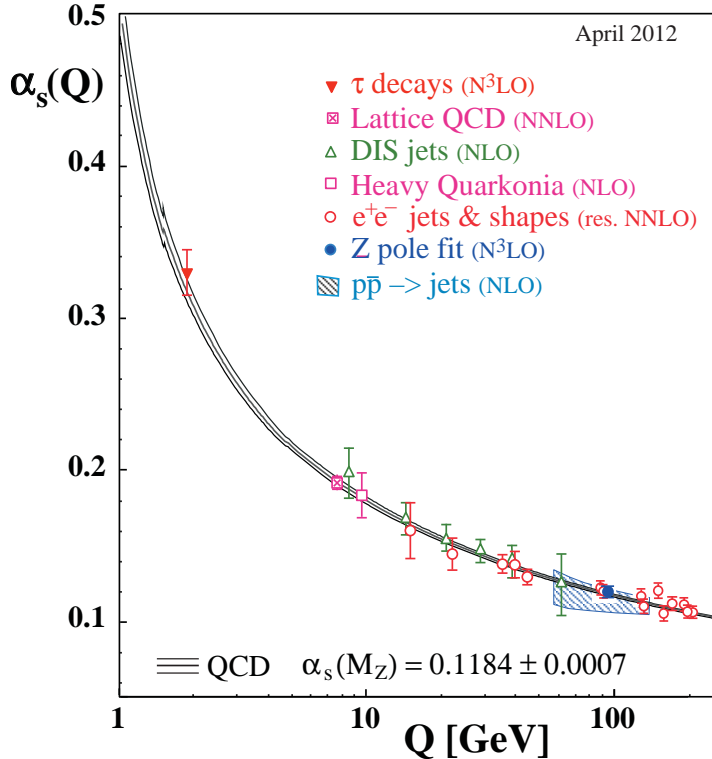


Figure 1.2.: Dependence of the QCD coupling constant on the energy scale  $Q$ . The QCD prediction uses the world average of  $\alpha_s$ , measured at the  $Z$  boson mass.  
Figure taken from [24].

would lead to a coupling that gets stronger with increasing momentum scale. The first part is the contribution from the gluon loop, it is always larger than the second part and responsible for the decrease of  $\alpha_s$  at large scales.

The running coupling has also been measured, Figure 1.2 shows the dependence of  $\alpha_s$  on the energy scale  $Q$  obtained from various measurements together with the QCD prediction.

The scale dependence of  $\alpha_s$  tells us that the effective coupling becomes small at momentum scales that are large compared to  $\Lambda_{\text{QCD}}$  (or, equivalently, at small distances). This is known as asymptotic freedom [25, 26] and perturbative QCD calculations are applicable in this regime.

If the momentum scale is small (or, equivalently, at large distances) the coupling constant of QCD becomes large. In this regime, perturbation theory can not be applied. The most successful theoretical approach to this soft regime of QCD is lattice QCD. It is based on the Feynman path integral formulation and numerically evaluates the path integrals on a discrete space-time grid.

Another important feature of QCD known as color confinement (or simply confinement) is that no free quarks or gluons have ever been observed, they are always bound into colorless hadrons. These states are also called color-singlets. While the running QCD coupling hints towards confinement at low-energy, it is not known how this emerges from the Lagrangian. One way to see confinement comes from lattice QCD, Figure 1.3 shows the potential between two quarks as a function of their distance from quenched lattice calculation. Quenched means

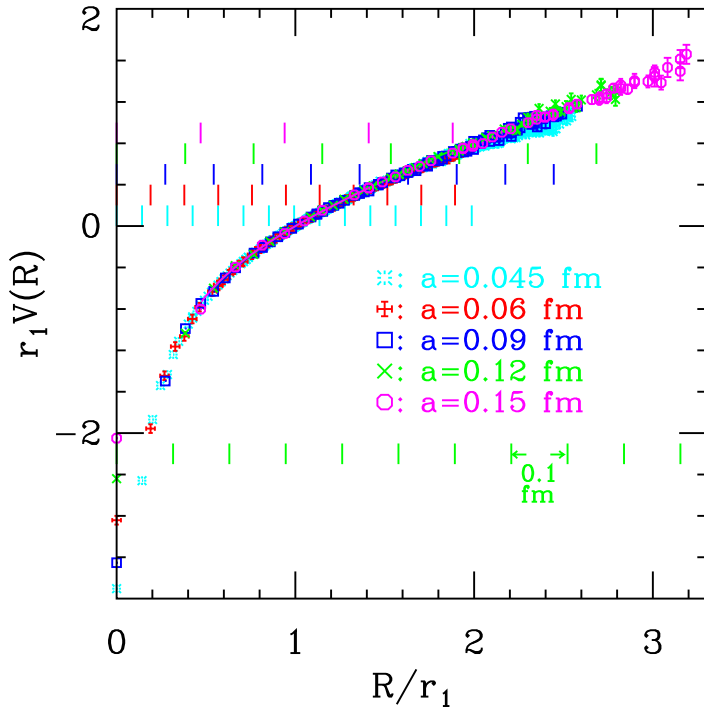


Figure 1.3.: Potential between two quarks from lattice QCD calculations.

Figure taken from [28].

that there are no new quarks produced. Practically this is done by putting two infinitely heavy quarks at a distance  $r$  and evaluating the energy of the gluon field between them. It is seen that above some  $r_0$  the potential energy of the two quarks depends linearly on the distance between them. From lattice QCD also the spatial distribution of the gluons can be calculated. As illustrated in Figure 1.4 the gluons form a flux-tube between the quarks, this string has an almost constant energy density (string tension) of  $\kappa \approx 1$  GeV/fm [27].

If two quarks are pulled apart, more and more energy is put in this string until the stored energy is large enough to produce new quark-antiquark pairs. The Lund string-fragmentation-model [31] is based on these breaking strings and part of the PYTHIA event generator [32].

---

### 1.2.1 Perturbative QCD

---

QCD cross sections can be calculated in perturbation theory, i.e. an asymptotic expansion in powers of the coupling constant  $\alpha_s$ . This approach is valid only if the coupling is small  $\alpha_s \ll 1$ , in QCD this is the case for processes with  $Q^2 \gg \Lambda_{\text{QCD}}^2$ . However, even in this case the cross sections involve only reactions of partons while in reality the initial and final states of a reaction consists of hadrons, that inevitable involve dynamics at the soft QCD scale.

The factorization theorem [33] allows to separate the two scales (soft and hard) and relate partonic cross sections to hadronic reactions. The partonic cross section is calculated from perturbative QCD and related to hadrons using parton distribution functions (PDF) and fragmentation functions (FF) that are extracted from measurements of deeply inelastic scattering and jet fragmentation, respectively.

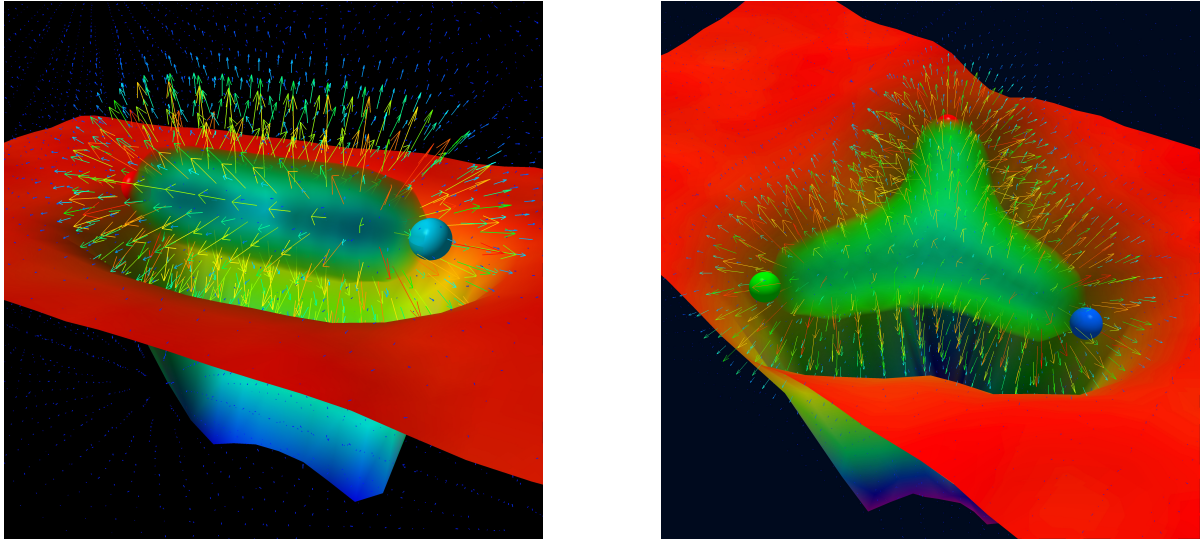


Figure 1.4.: Visualization of gluon flux tubes between two quarks (left) and three quarks (right) calculated with lattice QCD [29].

Figure [30] courtesy of Derek Leinweber.

As an example the cross section for high  $p_T$  particle production in hadronic collisions can be evaluated as [34]

$$E \frac{d^3\sigma}{dp^3} = \sum_{abc} \int dx_a dx_b \frac{dz}{z} \quad f_a(x_a, \mu_f^2) \otimes f_b(x_b, \mu_f^2) \quad (1.6)$$

$$\otimes |\vec{k}| \frac{d\hat{\sigma}_{A+B \rightarrow C+X}}{dk^3} (k = p/z, \mu_r^2) \quad (1.7)$$

$$\otimes D_c^h(z, \mu_{f'}^2) \quad (1.8)$$

using pQCD factorization.  $f_a(x_a, \mu_f^2)$  and  $f_b(x_b, \mu_f^2)$  are the PDFs of the initial state protons evaluated at the factorization scale  $\mu_f$ .  $d\hat{\sigma}_{A+B \rightarrow C+X}$  is the partonic cross section for the reaction, calculated with the renormalization scale  $\mu_r$ . Here, the fragmentation functions  $D_c(z, \mu_{f'}^2)$  represent the probability that a parton  $c$  fragments into a hadron  $h$  which carries a fraction  $z$  of the parton's momentum, evaluated at the fragmentation scale  $\mu_{f'}$ . The sum is over all partonic processes (involving quarks and/or gluons) that contribute to the reaction  $A + B \rightarrow C + X$ .

---

### Parton distribution functions

---

The parton distribution function  $f(x, Q^2)$  is the number density to find a parton (quark, antiquark or gluon) to carry the momentum fraction  $x$  of the nucleon at a resolution scale  $Q^2$ . In total there are 13 PDFs (six quarks, six antiquarks and the gluon). Even though the PDFs include also non-perturbative phenomena (i.e. the soft scale) their evolution can be described perturbatively. The evolution of PDFs as a function of the scale  $Q^2$  can be calculated by the Dokshitzer-Gribov-Lipatov-Altarelli-Parisi (DGLAP) [35–37] evolution equations, which are related to the renormalization group equation. The Balitsky-Fadin-Kuraev-Lipatov (BFKL) equations [38–40] are used to evaluate the evolution with  $x$ . DGLAP evolution resummes

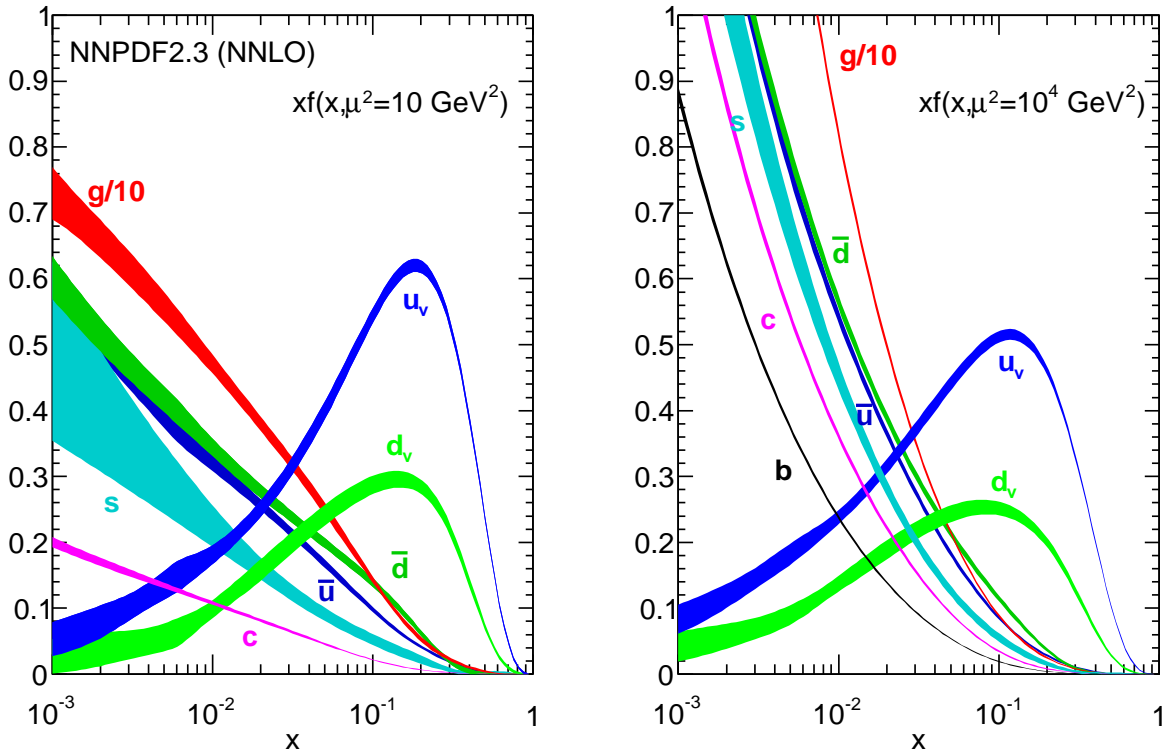


Figure 1.5.: Example of proton PDFs  $xf(x, \mu^2)$  at two different scales  $\mu^2 = 10 \text{ GeV}^2$  (left) and  $\mu^2 = 10^4 \text{ GeV}^2$  (right) from the NNLO NNPDF2.3 analysis [42]. PDFs for  $u_v$  and  $d_v$  show the contribution from the valence quarks. The  $\bar{u}$ ,  $\bar{d}$ ,  $s$ ,  $c$ ,  $b$  quarks are sea quarks. Gluon PDFs are scaled down by a factor ten.

Figure taken from [46].

terms to all powers of  $\alpha_s \ln(Q^2/\Lambda_{\text{QCD}}^2)$  which fails at small  $x$  since terms can be enhanced by  $1/x$ , while BFKL resummes powers of  $\alpha_s \ln(1/x)$  [41].

Figure 1.5 shows an example of the proton PDFs for different  $Q^2$  from the NNPDF2.3 PDF set [42]. The valence quarks  $u$  and  $d$  dominate at large  $x$  while at smaller  $x$  the parton density steeply rises and the gluon and sea quarks dominate. If the proton is probed at a larger scale  $Q^2$ , equivalent to a smaller distance, the parton density dramatically rises at small  $x$ . At very small  $x$ , the interactions between the partons become important, limiting the parton density [43, 44], an effect known as saturation. The growth of the parton density is especially prominent for gluons (scaled down by a factor 10 in the graph), leading to gluon saturation at small  $x$ . This is the basis of the Color glass condensate (CGC) framework [47].

PDFs of nucleons inside a nucleus are different from proton PDFs. The nuclear modification can be described by the ratio of PDFs:

$$R_i^A(x, Q^2) = \frac{f_i^A(x, Q^2)}{f_i^P(x, Q^2)} \quad (1.9)$$

Figure 1.6 shows an illustration of different nuclear effects [48]. Shadowing is a depletion of the parton densities at small  $x$  ( $< 0.03$ ) and anti-shadowing is an enhancement at interme-

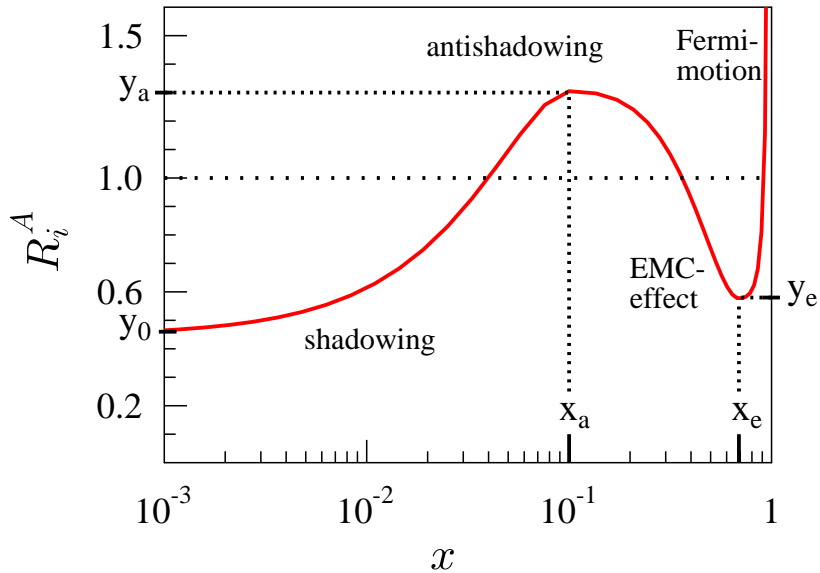


Figure 1.6.: Illustration of the nuclear modification of parton distribution functions.

Figure taken from [48].

diate  $x$  (0.3-0.9). The EMC effect [49] results in  $R_i^A$  below unity at  $0.3 < x < 0.9$ . At the largest  $x$  ( $\approx 1$ ) the Fermi motion leads to  $R_i^A > 1$ . The spatial dependence of the nuclear PDFs is included in impact parameter dependent nuclear PDFs [50].

---

### Fragmentation functions

---

A high virtuality (i.e. large  $Q^2$ ) parton develops into a parton shower containing many partons with smaller virtualities moving in approximately the same direction. Two processes contribute to this evolution: the splitting of a gluon into a quark-antiquark pair (gluon splitting) and the emission of a gluon by a parton (gluon emission). These processes are similar to the evolution of the PDFs and can be, as long as the  $Q^2$  is large, calculated in the framework of pQCD.

The hadronization takes places at small scales  $\mathcal{O}(\Lambda_{\text{QCD}})$  and is thus inherently a non-perturbative effect. The fragmentation functions incorporate both, perturbative and non-perturbative, effects and their scale dependence is governed by the DGLAP equation (similar to the PDFs).

Models of hadronization employ different mechanisms, like cluster fragmentation (as used by the Monte Carlo event generator HERWIG [51]) or string fragmentation (used in PYTHIA [32]).

---

#### 1.2.2 Chiral symmetry

---

The chiral symmetry means that left-handed and right-handed fields of  $N$  flavors transform independent of each other under the chiral rotations of  $U(N)_L \times U(N)_R$ . Since a mass term in the Lagrangian inevitably mixes the two chiral components chiral symmetry can only be an exact symmetry for massless particles. But it can still be an approximate symmetry. The group  $U(N)_L \times U(N)_R$  can be decomposed into several subgroups. First, into a vector part transforming the left and right-handed fields equally and an axial vector part treating them

opposite. In addition, a unitary group  $U(N)$  can be split into the product of the special unitary group and phase:  $U(N) = SU(N) \times U(1)$ . So,

$$U(N)_L \times U(N)_R = SU(N)_V \times SU(N)_A \times U(1)_V \times U(1)_A \quad (1.10)$$

Often, only the first two components ( $SU(N)_V \times SU(N)_A$ ) are referred to as chiral symmetry, sometimes even only the axial vector part.

Using the notation of the  $\tau$  matrices for the flavor space, and  $q, \bar{q}$  denoting the flavor vectors, the transformations corresponding to the four subgroups are:

$$SU(N)_V : \quad q \longrightarrow e^{-i\frac{\vec{\tau}}{2} \cdot \vec{\Theta}} q; \quad \bar{q} \longrightarrow e^{+i\frac{\vec{\tau}}{2} \cdot \vec{\Theta}} \bar{q} \quad (1.11)$$

$$SU(N)_A : \quad q \longrightarrow e^{-i\gamma^5 \frac{\vec{\tau}}{2} \cdot \vec{\Theta}} q; \quad \bar{q} \longrightarrow e^{-i\gamma^5 \frac{\vec{\tau}}{2} \cdot \vec{\Theta}} \bar{q} \quad (1.12)$$

$$U(1)_V : \quad q \longrightarrow e^{-i\theta} q; \quad \bar{q} \longrightarrow e^{+i\theta} \bar{q} \quad (1.13)$$

$$U(1)_A : \quad q \longrightarrow e^{-i\gamma^5 \theta} q; \quad \bar{q} \longrightarrow e^{-i\gamma^5 \theta} \bar{q} \quad (1.14)$$

In the limit of massless quarks the QCD Lagrangian is invariant under all of the four transformations. However, quarks are not massless and thus chiral symmetry can only be an approximation in QCD. For the two lightest quarks (u, d) which have current masses of only few  $\text{MeV}/c^2$ , i.e.  $m_{u,d} \ll \Lambda_{\text{QCD}}$  this is a very reasonable approximation. The strange quark has a sizeable current mass  $m_s \approx 100 \text{ MeV}/c^2$ , but still part of the chiral symmetry remains visible. For the heavy quarks (c, b, t) with  $m_{c,b,t} > \Lambda_{\text{QCD}}$  chiral symmetry is certainly not a valid approximation since the large mass mixes the two chiralities.

The vector part of the chiral symmetry (Equation 1.11) represents the invariance under rotations in  $N$ -dimensional flavor space and is a consequence of the flavor-blindness of the strong interaction. It still holds even if a quark mass term is included in the Lagrangian, as long as this mass is common to all flavors. In the case of two quark masses this symmetry is labeled  $SU(2)_I$  and corresponds to the observed isospin symmetry. Within QCD it is explicitly broken by the difference of the up and down quark masses. In addition, the electroweak interaction also breaks the isospin symmetry, because u and d quarks have different (electric) charge and the weak interaction depends on the chirality.

If the strange quark is also included in Equation 1.11 the approximate  $SU(3)$  flavor symmetry can explain the patterns of hadrons.

The  $SU(2)_A$  axial vector symmetry (equation 1.12) is spontaneously broken by the quark condensate  $\langle \bar{q}q \rangle$  giving masses to the hadrons, while leaving the pions as (pseudo-)Goldstone bosons (approximately) massless. The explicit breaking of this symmetry due to the quark masses leads to the non-vanishing pion masses. This model of spontaneously broken chiral

symmetry has been very successful in explaining hadron masses as well as pion decay and scattering data. It can be used to study the behavior of the quark condensate, masses, etc. in nuclear matter at different baryon densities and temperatures.

An extension of this model in terms of pion (or quark) masses leads to an effective theory that is called chiral perturbation theory and is based on the expansion of calculations in terms of the (small) quark masses. This is a possible approach to describe QCD at low energies.

The  $U(1)_V$  transformation (equation 1.13) corresponds only to a phase change of the fields. It does not couple different flavors and also is not broken by the quark masses. Thus this part is an exact symmetry of the QCD Lagrangian, it corresponds to a conserved current, or equivalently charge. This is the conservation of net quark–antiquark numbers, equivalent to baryon number conservation and the conservation of flavor quantum numbers like strangeness, charm, etc.

The axial  $U(1)_A$  (equation 1.14) symmetry, which is a symmetry of the Lagrangian in the case of massless quarks, is violated by the so-called axial anomaly <sup>3</sup>, as a consequence of quantization.

While the QCD vacuum has non-vanishing chiral condensate  $\langle \bar{q}q \rangle \approx -(250\text{MeV})^3$  [53]. Inside a hadron the magnitude of the condensate is reduced and at even higher density it is expected to vanish leading to restoration of chiral symmetry. This happens in the Quark-Gluon-Plasma described in the following section.

### 1.3 The phase diagram of nuclear matter and the QGP

The existence of a phase of deconfined quarks and gluons ("quark soup") at high temperature and/or large net baryon density has been theoretically predicted early on and assumed to exist in neutron stars and the early universe [54, 55]. Strong evidence for a deconfined phase also came from lattice gauge theory [56, 57].

In a system with many interacting particles a description on the single-particle level is neither practical nor required. The interesting quantities are macroscopic ones describing the system in terms of thermodynamic state variables.

Figure 1.7 shows the scaled<sup>4</sup> energy density  $\varepsilon/T^4$ , pressure  $3p/T^4$  and entropy density  $3s/(4T^3)$  as a function of temperature from lattice QCD calculations [58]. At the crossover region, around the critical temperature  $T_c$  the energy density increases signaling an increase in the number of degrees of freedom. This is due to the confinement-deconfinement (crossover) phase transition, where the degrees of freedom change from hadrons in the hadron gas phase to quarks in the QGP phase. The increase is not as pronounced as in earlier [59] lattice QCD calculations. The Stefan-Boltzmann limit for an ideal gas is not reached even at temperatures of several times  $T_c$ , showing that in the QGP quarks and gluons are interacting.

A similar behavior as for the energy density is observed also for the Polyakov loop. The gradual increase over a wide range around  $T_c$  indicates that the confinement-deconfinement transition at  $\mu_B = 0$  is not a first order phase transition but rather a crossover.

<sup>3</sup> see your favorite field theory textbook, or [52]

<sup>4</sup> For an ideal gas of massless particles  $\varepsilon \propto T^4$ ,  $p = \varepsilon/3$  and  $s = 4\varepsilon/(3T)$

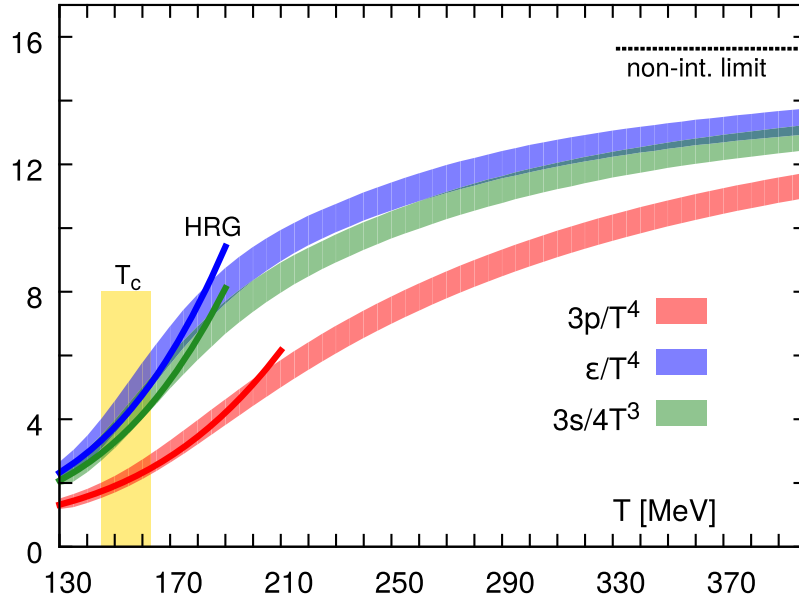


Figure 1.7.: Temperature dependence of the scaled energy density  $\varepsilon/T^4$ , pressure  $3p/T^4$  and entropy density  $3s/(4T^3)$  of QCD matter obtained from lattice QCD calculations with two light quarks and a heavier strange quark (2+1 flavor). The dark curves show predictions from the hadron resonance gas model (HRG). The Stefan-Boltzmann limit for three flavors is indicated as horizontal line on the right. The crossover region,  $T_c = (154 \pm 9)$  MeV, is indicated by the yellow band.

Figure taken from [58].

For nuclear matter in thermodynamic equilibrium the grand canonical ensemble is employed, characterizing nuclear matter in terms of the temperature  $T$ , the baryo-chemical potential  $\mu_B$  and the volume  $V$ . The baryo-chemical potential  $\mu_B$ , is the chemical potential of the (conserved) baryon number.

A schematic view of the phase diagram of nuclear matter in the  $\mu_B, T$  plane is shown in Figure 1.8. Ordinary nuclear matter has a temperature  $T \approx 0$  and a baryo-chemical potential  $\mu_0 \approx 1$  GeV. The line starting from there and ending in a critical point shows the nuclear liquid-gas phase boundary. A second phase boundary that also ends in a critical end-point starts at larger  $\mu_B$  and separates the hadron resonance gas phase from the quark-gluon plasma. The location of the critical point has also been deduced from lattice QCD [62]. At vanishing  $\mu_B$ , the transition is a cross-over with a critical temperature  $T_c \approx 170$  MeV<sup>5</sup>. At small temperature and large baryon density a deconfined color superconducting phase is expected, along with possibly other phases [65, 66].

The QGP is characterized by the deconfinement of quarks and the restoration of the spontaneously broken chiral symmetry. This means that in the QGP the quark condensate vanishes and quarks become approximately massless. The two phase transitions, chiral symmetry restoration and deconfinement, do not generally need to coincide, but in lattice calculations at small  $\mu_B$  they do.

<sup>5</sup> Recent lattice calculations yield a somewhat lower transition temperature  $T_c \approx 155$  MeV [60, 61], in good agreement with the chemical freeze-out temperature from the statistical hadronization model [64].

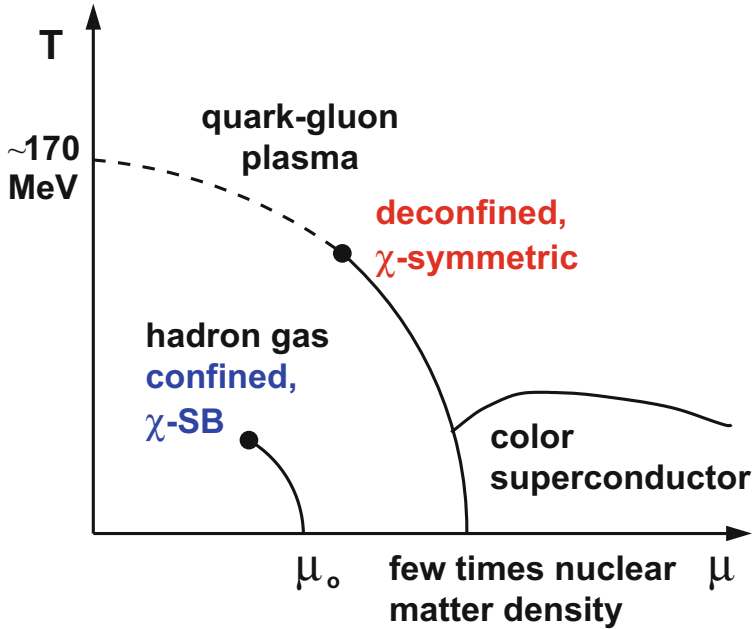


Figure 1.8.: Illustration of the phase diagram of nuclear matter.  
Figure taken from [63].

In lattice QCD the order parameter of the phase transition to deconfinement is the expectation value of the Polyakov loop  $\langle L \rangle$ , which is related to the energy of a free quark. It vanishes for a confined phase ( $\langle L \rangle = 0$ ), and is finite in the deconfined phase ( $\langle L \rangle \neq 0$ ). [67]

Experimentally, measured particle yields can be used to determine  $T$  and  $\mu_B$  in the statistical hadronization model [68, 69]. It is remarkable that for heavy-ion collisions at sufficiently large energies the temperature and chemical potential at the freeze-out agree with the values for the phase transition from lattice QCD [70].

#### 1.4 Evolution of heavy-ion collisions

In high-energy collisions of heavy ions the QCD phase diagram can be explored experimentally. The evolution of a heavy ion collision is depicted in Figure 1.9.

Prior to the collision the two nuclei are moving in opposite direction at almost the speed of light, in the laboratory frame they are flat Lorentz-contracted discs. The interaction starts at  $\tau = 0$  where the two nuclei have the first "contact". The initial state could be the CGC [47, 72].

Hard parton-parton collisions occur at very early times  $\tau \approx 1/\sqrt{Q^2}$ , with  $Q$  being the 4-momentum transfer. High  $p_T$  hadrons are produced in the fragmentation of these high momentum partons. Hard processes with  $Q^2 \gg \Lambda_{\text{QCD}}$  are theoretically calculable using pQCD.

The next phase is often called pre-equilibrium phase where the bulk of the (softer) initial parton-parton collisions occur. It is characterized by a fast increase of the energy density. The strong interaction between the partons leads to a rapid thermalization at a time  $\tau \approx 1 \text{ fm}/c$  and the formation of a medium with deconfined quarks and gluons, the Quark-Gluon-Plasma. The pre-equilibrium phase and the mechanism that leads to rapid thermalization is still not fully understood [73]. The transition from CGC initial conditions to a QGP in thermal equilib-

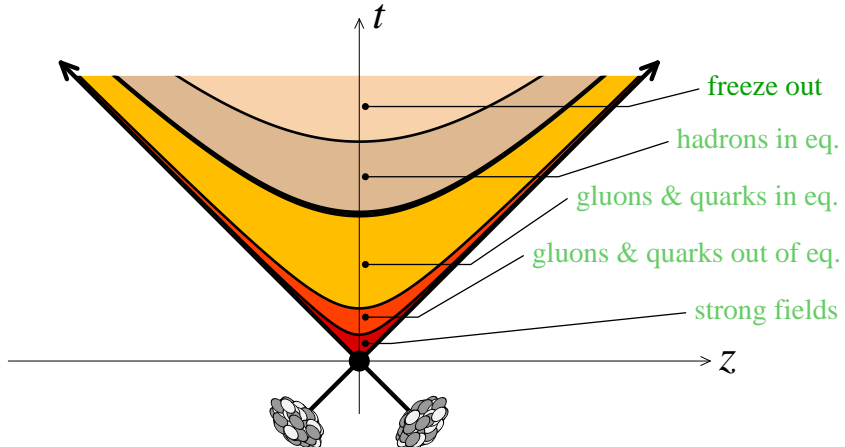


Figure 1.9.: The space-time picture of a heavy-ion collision in the  $(t, z)$  plane illustrating the evolution of the fireball. The two colliding nuclei move along the light cone, the evolution of the fireball is boost invariant. Hyperbolic lines show regions of constant proper time  $\tau = \sqrt{t^2 - z^2}$ .

Figure taken from [71].

rium could happen through instabilities in a weakly coupled, strongly interacting intermediate phase called Glasma [74].

The following expansion of the system happens at (almost) the speed of light in beam direction, and at about half the speed of light in the transverse direction. This phase can successfully be described by relativistic hydrodynamics assuming local thermodynamic equilibrium. The acceleration in radial direction is called radial flow. During this expansion also the initial spatial asymmetry transforms into a momentum anisotropy leading to a azimuthal modulation of particle production. This modulation can be decomposed into a Fourier series with respect to the reaction plane. The 2nd order asymmetry depends on the impact parameter of the collision, higher order asymmetries are caused by fluctuations.

During the expansion of the fireball the energy density (and thus also the temperature) decreases and when it falls below  $T_c$  the free partons hadronize forming a hadron gas. At this time the energy density has dropped to about  $1 \text{ GeV/fm}^3$ . Even below  $T_c$  this hadron gas is still very dense with a mean free path of the hadrons much smaller than the system size and can be described by hydrodynamics as well.

The hadron gas continues to expand and cool and eventually the rate of inelastic collisions becomes small. At this stage, the chemical freeze-out, the hadron abundances become fixed. The hadronic stage with inelastic collisions could also be very short with hadron abundances fixed already at the phase transition. From the measured yields of particles with different mass the temperature of the chemical freeze-out can be deduced.

The kinetic freeze-out occurs when also the elastic collisions stop, at this time the particle momenta are fixed. This marks the transition from a fluid description to free streaming particles. The bulk particle spectra follow a thermal (exponential) distribution in the local rest frame reflecting the freeze-out temperature. Measured identified particle spectra can be well described

---

if a blue-shift from a common radial velocity is folded into the exponential spectra leading to the so-called blast wave parameterization [75].

After the chemical freeze-out, decays of resonances and unstable particles occur. These decays continue to happen also after the kinetic freeze-out. Particles that reach the detector consist of directly produced hadrons and hadrons from decays.

---

## 1.5 Experimental observables of the QGP

---

The observation of a *new state of matter*, the QGP, has been announced by the CERN SPS Experiments in 2000 [76]. Later the RHIC experiments found that the QGP is not a gas-like plasma but strongly interacting and behaves rather like an almost perfect fluid: the strongly coupled QGP (sQGP) [77].

Early evidence of the QGP came from strangeness enhancement compared to pp collisions, which has been proposed as a signature of QGP formation [78]. But it is not a clear signature of deconfinement: instead of an enhancement in heavy ion collisions also a suppression of strangeness in pp collisions is a possible explanation. This canonical suppression is the result of an exact conservation of strangeness in pp [79].

Especially at RHIC and LHC models based on relativistic hydrodynamics have been successful to describe the fluid-like behaviors and related observables like radial expansion, elliptic flow and also higher order flow harmonics.

If the nuclear matter phase diagram has a cross-over at  $\mu_B = 0$  and a first order phase transition at high density, there must be a critical point. At a critical point the correlation length diverges leading to fluctuations of conserved charges. Measurements of this fluctuations could give experimental access to the critical point.

The potential between heavy quarks is subject to color Debye screening [80], similar to the Debye screening in an electrical plasma. For heavy quarkonia, which are bound states containing c or b quark and its antiquark, this leads to a reduction of the binding, and eventually a breakup of the  $q\bar{q}$  state, depending on the medium temperature. Different quarkonia states have different binding energies so they should melt at different temperature. This sequential melting has been proposed as a thermometer of the QGP [81].

In a phase with chiral symmetry restoration the chiral partners  $a_1$  and  $\rho$  as well as  $\pi$  and  $\sigma^6$  should become degenerate [82]. Experimentally the broadening of the  $\rho$  meson in heavy ion collision has been observed.

The QGP as a thermalized hot medium should emit thermal photons. Photons can be real photons or virtual photons that are detected as dilepton pairs. A hadronic phase would also radiate. The expected exponential spectrum has been observed for real photons and dileptons. A fit of the measured exponential photon spectrum yields an inverse slope parameter  $T$ , that can be interpreted as an effective temperature, averaged over all stages of the collision. It remains debated how much of the radiation originates from the QGP phase. An puzzling observation is the large elliptic flow  $v_2$  of the direct photons. The large temperature indicates that they come predominantly from the early QGP phase, but in this case they are expected to

---

<sup>6</sup> the chiral partners are related by the  $SU(3)_A$  axial vector transformation.

have a small  $v_2$  since the flow has not had time to build up. However, the direct photon  $v_2$  is comparable to that of pions.

Parton energy loss and jet quenching are described in the following section.

## 1.6 Parton energy loss and jet quenching in the QGP

The fragmentation of highly energetic parton results in a collimated spray of hadrons (see also section 1.2.1). These final state hadrons are called a jet. The highest energy hadron is called the leading particle. Experimentally, jets can be identified as high energy particles produced in a narrow "jet cone", i.e. moving in approximately the same direction. The reconstruction of a jet in the detector is based on the distribution of tracks or calorimeter hits in the kinematic variables  $(\eta, \varphi)$ . Jet reconstruction algorithms (see Refs. [83, 84] for reviews) can use a cone in the  $(\eta, \varphi)$  plane with fixed or variable radius (cone algorithms), for instance around the leading particle. Other approaches are successive recombinations of tracks based on a distance measure, as done in the  $k_T$  algorithm [85, 86] or the anti-anti- $k_T$  algorithm [87]. The goal of the jet reconstruction and related corrections is to recover the momentum of the parton.

Due to momentum conservation high energy partons emerging from  $2 \rightarrow 2$  parton scatterings are produced back-to-back in the center of momentum frame of the 2 partons. If the two initial partons carry different momentum fractions  $x_1, x_2$ , the partons are not back-to-back in pseudorapidity (but they are still back-to-back in the azimuth). Mostly jets are produced in pairs called dijets. However, the momentum of a hard parton can be also balanced by a photon or heavy boson leading to the production of a single jet. Events with three or more jets are possible but rare; historically three jet events provided the first direct evidence for the gluon [88].

In  $e^+e^-$  collisions jets are straightforward to identify as they are the only event activity. Proton-proton collisions at high energy are collisions of two piles of partons. While hard parton scatterings are rare events there are many soft interactions leading to a "QCD background" of produced particles called the underlying event. This background has to be taken into account and subtracted in the analysis. In heavy-ion collisions this background is a sizeable effect that represents a major challenge in the analysis, especially since fluctuations of the background have to be taken into account [89].

Energy loss of high energy partons in the QGP leading to a suppression of jets in heavy ion collisions has been proposed by Bjorken [90] as a signature of QGP formation. For an introduction to jet quenching and parton energy loss see [91–93]. The amount of energy loss depends on the parton type (i.e. quark or gluon), energy and mass as well as on the medium properties (temperature, size, coupling), the path length and the mechanism of the energy loss. Similar to the energy loss of charged particles in ordinary matter, parton energy loss in the QGP can arise due to two mechanisms: elastic scattering of the high energy parton with partons in the medium (collisional energy loss) and medium-induced gluon radiation (radiative energy loss). The initial production of high energy partons can be calculated in pQCD.

Collisional energy loss as a incoherent superposition of scattering depends linearly on the path length in the medium and logarithmically on the parton energy. The stopping power depends on the energy density:  $dE/dx \propto \sqrt{\varepsilon} \propto T^2$  [90]. For an ideal gas the temperature dependence of the energy density is  $\varepsilon \propto T^4$ . Bjorken only considered collisional energy loss, which is now

believed to be only a small component of the total energy loss [94] for gluons and light quarks, but can be important for energy loss of heavy quarks.

Radiative energy loss is the dominant mechanism of energy loss in the QGP. It is calculable in pQCD. The main difference to QED energy loss is the interaction of radiated gluon with the medium with a characteristic mean free path  $\lambda = 1/(\rho\sigma)$ . Here  $\rho$  denotes the number density of scattering centers and  $\sigma$  is the total cross section.

Two different regimes can be distinguished: The Bethe-Heitler (BH) regime deals with a thin medium ( $L \ll \lambda$ ) in which only a single scattering occurs while the Landau-Pomeranchuk-Migdal (LPM) regime assumes a thick medium ( $L \gg \lambda$ ). In the LPM regime, the interference of the emitted gluons has to be taken into account if the formation time is larger than the mean free path  $\tau > \lambda$ . In this case the the emission of soft gluons is suppressed. The total radiative energy loss in both regimes is given by [93]:

$$\Delta E_{\text{BH}} \approx \alpha_s C_R \hat{q} L^2 \ln \frac{E}{m_D^2 L} \quad (1.15)$$

$$\Delta E_{\text{LPM}} \approx \alpha_s C_R \hat{q} L^2 \quad (1.16)$$

Here  $C_R$  are the color factor,  $C_R = (N_c^2 - 1)/(2N_c) = 4/3$  for quarks and  $C_R = N_c = 3$  for gluons (the number of colors is  $N_c = 3$ ). In both cases the total radiative energy loss is approximately proportional to the path length squared, but in the case of a thick medium the energy loss is approximately independent of the parton energy.

Medium properties are commonly encoded in the transport coefficient  $\hat{q}$ , which is the average squared transverse momentum-transfer per unit path length

$$\hat{q} = \frac{\langle q_T^2 \rangle}{\lambda} = \frac{m_D^2}{\lambda} = m_D^2 \rho \sigma \quad (1.17)$$

The Debye mass  $m_D \sim g^2 T$  is the inverse color screening length of the medium.

In Ref. [95] different energy loss models are compared for the case of static QGP "brick". Since the QGP is not a static medium, a realistic medium evolution from hydrodynamics has to be included in model calculations of the energy loss. The implementation of the medium evolution differs for most energy loss calculations.

For the experimental observation of parton energy loss the hard partons are created in the same collision as the QCD medium. But since hard probes with transverse momenta (or masses) that are large compared to the QCD scale  $p_T$ ,  $m \gg \Lambda_{\text{QCD}}$  are produced early in the collision (formation time  $\tau \propto 1/Q$ ), before the thermalized medium is formed. Estimates of the thermalization time for RHIC energies yield  $\tau \lesssim 1 \text{ fm/c}$ , see [96] and references therein.

Parton energy loss is experimentally observable through different observables: jet spectra, charged particle spectra, dijet imbalance and particle correlations. Suppression of jet and leading particle spectra is the most direct measurement of energy loss. The suppression is

observed by comparing the results in nucleus-nucleus collisions (QCD medium) to those in pp collisions (QCD vacuum), expressed by the nuclear modification factor

$$R_{AA} \sim \frac{\text{QCD medium}}{\text{QCD vacuum}} \sim \frac{AA}{pp} \quad (1.18)$$

For a quantitative nuclear modification factor, the differences in the production of initial hard partons in nucleus-nucleus and pp collisions have to be taken into account. Assuming binary collision scaling the pp yield (cross section) is scaled by the average number of nucleon-nucleon collisions  $\langle N_{\text{coll}} \rangle$  (average nuclear overlap  $T_{AA}$ ) calculated from a Glauber model (see next section).

$$R_{AA}(p_T) = \frac{d^2N_{\text{ch}}^{\text{Pb-Pb}}/d\eta dp_T}{\langle N_{\text{coll}} \rangle \cdot d^2N_{\text{ch}}^{\text{pp}}/d\eta dp_T} = \frac{d^2N_{\text{ch}}^{\text{Pb-Pb}}/d\eta dp_T}{\langle T_{AA} \rangle \cdot d^2\sigma_{\text{ch}}^{\text{pp}}/d\eta dp_T} \quad (1.19)$$

In the absence of any initial or final state nuclear effects  $R_{AA}$  equals unity.  $R_{AA}$  includes not only the effects of parton energy loss in the QGP, but also initial and final state cold nuclear matter effects. Data from proton-nucleus collisions (where no QGP is created) can serve as an additional baseline for energy loss measurements in heavy-ion collisions.

---

## 1.7 Glauber model

---

The Glauber model of nuclear collisions is a classical approach with a geometrical interpretation of the collision. It allows to calculate the number of colliding or participating nucleons based on the impact parameter in an eikonal approach. For a comprehensive review see Ref. [97].

Nuclei are extended objects with the size (radius  $r$ ) of several fm. In a first approximation the collision of two nuclei at highly relativistic energies can be interpreted in a geometrical picture as the two flat discs colliding. The overlap between the two discs is given by the radial distance between the centers of the two nuclei, called impact parameter  $b$ .

In this geometrical model collisions can only occur if  $b \leq 2r$ . A collision is called (most) central, if  $b = 0$  and there is full overlap between the nuclei. If  $b = 2r$  there is minimal overlap and the collision is (most) peripheral.

For a random distribution of the two nuclei the probability distribution for the impact parameter growth linearly with  $b$  for  $b < 2r$  and is zero for  $b > 2r$ . The full impact parameter range corresponds to 100% of the nuclear cross section, the slicing is done in the impact parameter. So the smallest fraction of cross section expressed in percentage corresponds to the smallest impact parameter.

However, the nuclei do not have a uniform density and a sharp surface. A good approximation of the nuclear density  $\rho$  as a function of the distance from the nucleons center  $r$  is given by the Woods-Saxon distribution:

$$\rho(\vec{r}) = \frac{\rho_0}{1 + e^{(|\vec{r}| - r_0)/a}} \quad (1.20)$$

Here, the  $r_0$  is the nuclear radius and  $a$  is the skin thickness or surface diffusion parameter. The normalization parameter  $\rho_0$  is chosen such that  $\int d^3r \rho(\vec{r}) = A$  with  $A$  being the number of nucleons in the nucleus.  $\rho(\vec{r})/A$  can be interpreted as the probability per unit volume to find a specific nucleon at position  $\vec{r}$ .

The integrated density along a path in  $z$  direction is called nuclear thickness function  $T_A$ . It represents an area density and can be thought of a projection of the nucleus on the  $xy$ -plane.

$$T_A(\vec{s}) = \int_{-\infty}^{+\infty} dz \rho_A(\vec{s}) \quad (1.21)$$

$T_A$  gives the number of nucleons per unit area located along a path through the nucleus at a the position  $\vec{s}$  in the  $xy$ -plane.

For collisions of two nuclei  $A$  and  $B$  at an impact parameter  $\vec{b}$  the product of their respective nuclear thickness functions  $T_A(\vec{s})T_B(\vec{s} - \vec{b})d^2s$  gives the combined area density at a position  $\vec{s}$ . The integral of the product  $T_A(\vec{s})T_B(\vec{s} - \vec{b})$  over the  $xy$ -plane yields the nuclear overlap function  $T_{AB}$

$$T_{AB}(b) = \int d^2s T_A(s) T_B(s - b) \quad (1.22)$$

gives the number of nucleons that are in each other's path. The number of binary collisions is then

$$N_{\text{coll}}(b) = T_{AB} \cdot \sigma_{\text{NN}}^{\text{inel}} \quad (1.23)$$

The geometrical quantities like the average nuclear overlap  $T_{AA}$ , the average number of binary collisions  $N_{\text{coll}}$  and the average number of participants can be calculated from an optical Glauber [97]. In a Monte Carlo approach the Glauber Model implementation consists of the following steps:

1. The two nuclei are initialized using random positions for the nucleons in the transverse  $(x, y)$  plane according to the nuclear density profile.
2. The impact parameter  $b$  is randomly taken from the interval  $(0, b_{\text{max}})$ .  $b_{\text{max}}$  is chosen sufficiently large ( $> 2r$ ) to include all collisions.
3. For every pair of nucleons (one from each nucleus) the distance  $d$  is calculated. If the distance is within the geometrical cross section ( $d < \sqrt{\sigma/\pi}$ ) they are assumed to collide. In this case the number of binary collisions is increased by one and the two nucleons are marked as participants
4. The total number of participants is calculated

Performance of this calculation can be improved by letting the two nuclei collide multiple times with different impact parameter.

Note that the optical and Monte Carlo Glauber approaches give slightly different results, especially for peripheral collisions.

## 1.8 Event types in pp collisions

In pp collisions different event types can be distinguished by their final state, mostly the rapidity distribution. The different processes are illustrated in Figure 1.10 with a Feynman diagram of the underlying interaction and a sketch of the distribution of the particles in the  $(\eta, \varphi)$ -plane after the collision as it would be observed in a detector.

In elastic collisions (Figure 1.10a) both interacting protons remain intact. The momentum transfer is small and both protons emerge close to beam rapidity with a large rapidity gap.

Inelastic (INEL) are all collisions in which new particles are produced, they are commonly divided into diffractive and non-diffractive collisions.

Diffractive collisions are typically soft collisions with a small 4-momentum-transfer  $Q^2$ . A diffractive system  $X$  is characterized by an invariant mass  $M_X$ , called the diffractive mass. Characteristic for a diffractive event is a gap in the rapidity distribution of the final state particles.

In a single diffractive collision (Figure 1.10b) one proton is excited and breaks up into several hadrons clustered in phase-space. The other proton remains intact. If both protons are excited the collision is double diffractive (Figure 1.10c) with a rapidity gap between the two diffractive systems. Central diffractive collisions (Figure 1.10d) leave both protons intact, but particles around midrapidity are produced in addition.

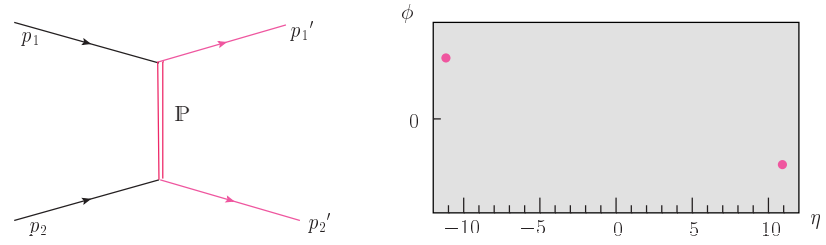
Non-diffractive collisions (Figure 1.10e) produce particles over a wide range of rapidity. ND events can have large  $Q^2$ .

The total cross section in pp collisions  $\sigma_{\text{total}}$  is the sum of all contributions:

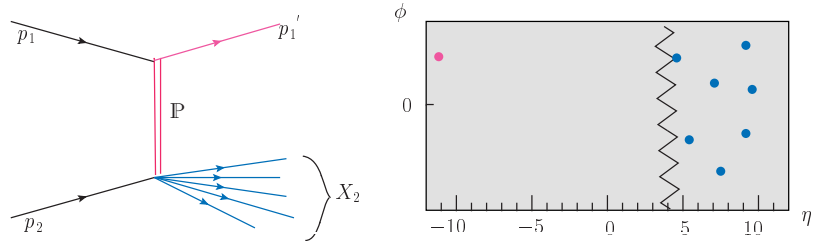
$$\sigma_{\text{total}} = \sigma_{\text{elastic}} + \overbrace{\sigma_{\text{SD}} + \underbrace{\sigma_{\text{DD}} + \sigma_{\text{CD}} + \sigma_{\text{ND}}}_{\sigma_{\text{NSD}}}}^{\sigma_{\text{INEL}}} \quad (1.24)$$

Typical detectors at hadron colliders cover only a limited range around  $\eta = 0$ , thus elastic events are usually invisible to the detectors. SD events require a single-arm trigger (on the diffractive system), DD and ND events can be studied also using a double-arm trigger. The classification of events as non-single diffractive (NSD) is motivated from these trigger requirements.

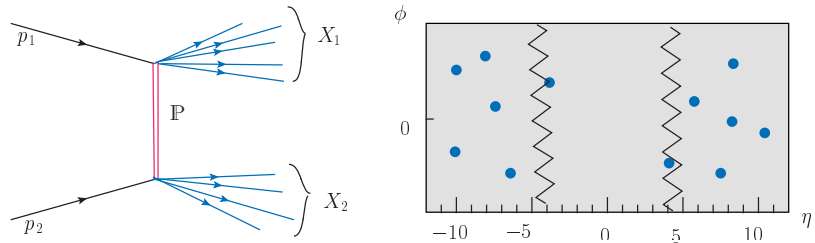
Figure 1.11 shows the characteristic rapidity distributions for single diffractive, double diffractive and non-diffractive events simulated with PYTHIA, Perugia0 tune. In SD collisions the scattered protons are clearly visible as a narrow peak at forward rapidity, the particles from the diffractive system cover a large range of  $y$ . The rapidity distribution of DD collisions is similar to the sum of the two SD distributions, without the proton peaks. The  $dN/dy$  distribution for ND collisions has an approximately Gaussian shape. As apparent from Figure 1.11, ND collisions produce much more particles and are the dominant process of particle production, especially at mid-rapidity. The transverse momenta of particles generated in diffractive collisions are much smaller compared to ND processes. Nevertheless, diffractive processes account for a large fraction of the total cross section and need to be taken into account when calculating the inelastic cross sections.



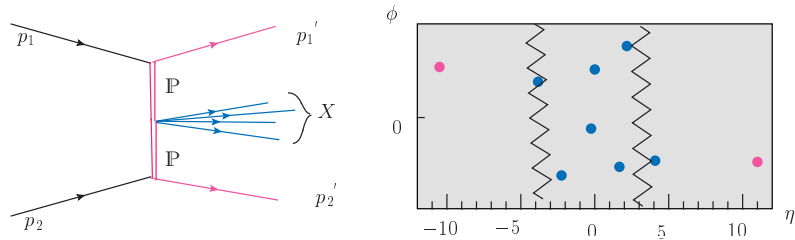
(a) Elastic



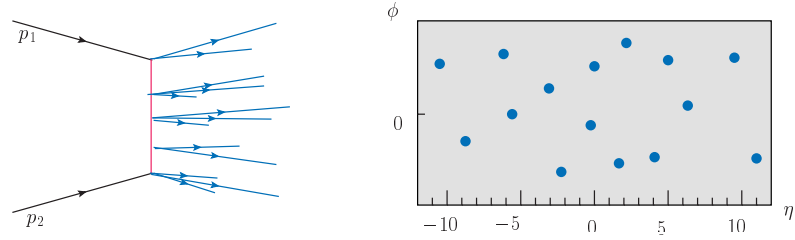
(b) Single diffractive



(c) Double diffractive



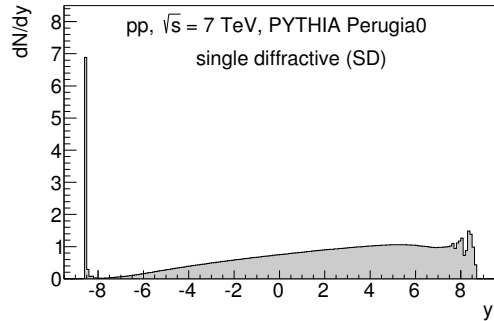
(d) Central diffractive



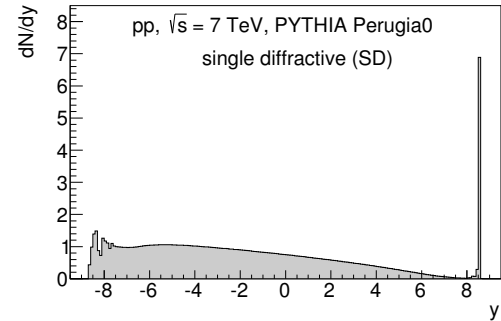
(e) Non-diffractive

Figure 1.10.: Illustration of different event types in  $pp$  collisions. The Feynman diagrams show the Pomeron ( $\mathbb{P}$ ) exchange graphs in Regge theory. The distributions of particles in the  $(\eta, \phi)$ -plane illustrates the characteristics of the event types as observed in a detector.

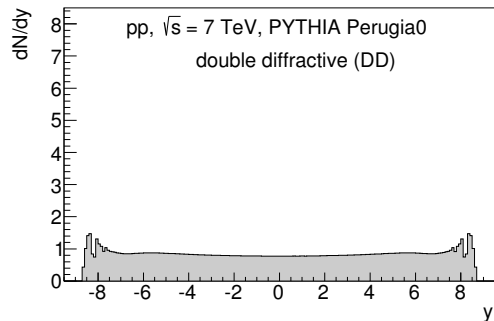
Figures Taken from [98].



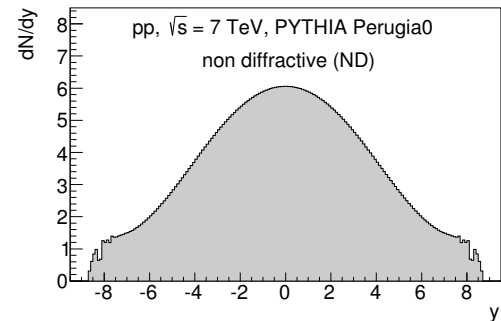
(a) Single diffractive (SD) events with the intact proton at negative  $y$ .



(b) Single diffractive (SD) events with the intact proton at positive  $y$ .



(c) Double diffractive (DD) events.



(d) Non diffractive (ND) events.

Figure 1.11.:  $dN/dy$  distributions for different event types in pp collisions at  $\sqrt{s} = 7$  TeV simulated with PYTHIA: single diffractive (a, b), double diffractive (c) and non-diffractive (d). There is no rapidity gap visible in the case of SD and DD collisions since the average over many ( $\approx 10^7$ ) events with different diffractive mass  $M_x$  and 4-momentum transfer  $Q^2$  is shown. The fluctuating bins at large  $|y|$  are numerical artefacts from the calculations of  $y$ .



## 2 The ALICE experiment at the LHC

### 2.1 The Large Hadron Collider

The *Large Hadron Collider (LHC)* [99–102] located at CERN, Geneva is a 26.7 km circumference ring accelerator (synchrotron). It is the largest<sup>1</sup> and the highest energy particle accelerator ever built. It consists of eight arcs intercepted by eight straight sections. In four of these straight sections the two beams cross inside the experiments.

Interest in the LHC came from high energy particle physics and high-energy heavy-ion physics and the LHC was designed for a physics program studying proton-proton collisions as well as collisions of lead-lead and proton-lead. The LHC can also be operated with lighter ions, Argon has been considered for instance.

With a design beam energy of 7 TeV for protons (equivalent to  $\sqrt{s} = 14$  TeV) and the design luminosity of  $\mathcal{L}_{pp} = 10^{34} \text{ cm}^{-2}\text{s}^{-1}$  the LHC features a factor 7 higher energy and a factor 60 higher luminosity compared to the p $\bar{p}$  Collider Tevatron at Fermilab. In the heavy ion (Pb–Pb) mode the LHC is designed for a luminosity of  $\mathcal{L}_{\text{Pb–Pb}} = 10^{27} \text{ cm}^{-2}\text{s}^{-1}$  and a collision energy per colliding nucleon pair of  $\sqrt{s_{\text{NN}}} = 5.52$  TeV. This energy is almost a factor 30 higher than at the heavy-ion Collider RHIC<sup>2</sup> at BNL<sup>3</sup>. In the LHC run I (2009–2013) the LHC has reached about half its design energy and luminosity.

The LHC uses superconducting dipole and quadrupole magnets with a peak field of 8.33 T (dipoles). 1232 superconducting dipole magnets to bend the particle beams to a ring and 392 lattice quadrupoles to focus the beams are installed. multipole magnets of up to 6. order serve as correction magnets. In total, the LHC main ring contains over 9000 magnets.

The high luminosity of the LHC was the reason to design it for proton-proton collisions in contrast to previous hadron colliders that used proton-antiproton like Tevatron and SppS. While particle-antiparticle colliders need only one accelerator ring, two separate rings with opposite magnetic fields are required to collide particles that have the same charge. Unlike RHIC, where two completely independent rings are used, the LHC uses one magnet with two beam pipes for the two beams. This design is much more compact but does not allow to vary the field strength separately for the two beams. For collisions of nuclei with different A/Z this results in asymmetric collisions.

Figure 2.1 shows a schematic illustration of the CERN’s accelerator complex with the four main LHC experiments (ALICE, ATLAS, CMS, LHCb) and the injector chain.

The start of the LHC accelerator-chain is the creation of ions in two ion sources (one for hydrogen ions, one for heavy ions). Electrostatic fields are used to extract the ions. The following radio-frequency quadrupoles (RFQ) splits the continuous proton/ions beams in bunches. These bunches enter the linear accelerators LINAC2 (protons) and LINAC3 (lead)

<sup>1</sup> LEP had the same size and used the same tunnel.

<sup>2</sup> Relativistic Heavy Ion Collider

<sup>3</sup> Brookhaven National Laboratory

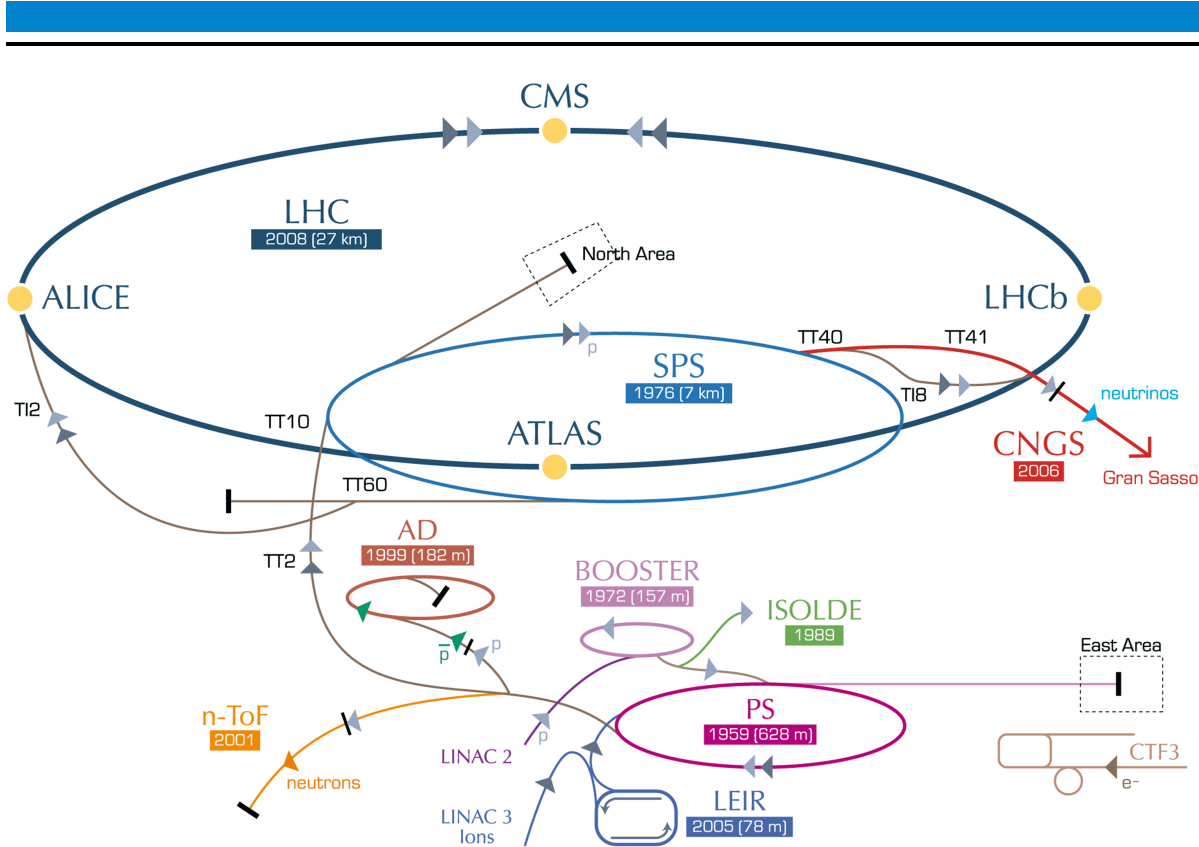


Figure 2.1.: Schematic layout of the CERN accelerator complex including the LHC with the four big experiments and the injector chain.

Figure taken from [103].

where drift tubes and AC voltage increase the energy of the particles to 50 MeV (p) and 4.2 MeV/u (Pb). After the LINACs lead ions are accelerated in the Low Energy Ion Ring (LEIR) to 72.2 MeV/u and transferred to the Proton Synchrotron Booster (PSB), where the energy is increased to 94 MeV/u. Protons are injected directly into the PSB and accelerated to 1.4 GeV. The next stage is the Proton Synchrotron (PS), accelerating the particles to 25 GeV (p), respectively 5.9 GeV/u (Pb). Also the final bunch structure is shaped in the PS splitting the bunches into 72 (p) resp. 54 (Pb) bunches with a length of 4 ns. In the super proton synchrotron (SPS) the particles are accelerated further to the LHC injection energy of 450 GeV (p) and 177 GeV/u (Pb) and injected in the two counter-rotating LHC rings.

One complete fill of the LHC requires 12 fills from the SPS, each of which needs 3 to 4 cycles of the PS. While the acceleration up to the LHC injection energy takes only few seconds, the LHC takes about 20 minutes to accelerate protons and/or lead ion to the final energy.

Two beams of protons or ions circulate in the LHC in opposite directions: *beam 1* clockwise and *beam 2* counter-clockwise (in the top view of the LHC). The bunches are brought into collision at four interaction regions (Point 1-4) with a small crossing angle.

### 2.1.1 Experiments at the LHC

Four large experiments are installed in caverns along the LHC accelerator ring: ATLAS (Point 1), ALICE (Point 2), CMS (Point 5) and LHCb (Point 8). The ALICE experiment is described in detail in the following section 2.2.

ATLAS [104] and CMS [105] are general-purpose detectors and explore a similar range of physics topics. They are designed primarily for proton-proton physics at the highest energy and luminosity. Major physics motivation for these experiments was not only the prominent search for the standard model Higgs boson but also precision tests of QCD and electroweak interaction as well as the possibility to investigate beyond-standard-model physics, like supersymmetry. While the lightest supersymmetric particle (LSSP) could be produced and directly observed (via missing transverse energy), heavy supersymmetric particles can show up as deviations of cross sections or decay rates from the standard model predictions. Both experiments also have a significant heavy-ion physics program. Especially their large pseudorapidity acceptance with full calorimetry coverage and the strong magnetic fields makes them ideally suited for high- $p_T$  observables like jets.

LHCb [106] is a forward-detector with strong focus on pp physics. It is designed to study the production and decays of beauty quarks, especially CP violation.

TOTEM (TOTal Elastic and diffractive cross section Measurement) LHCf (LHC forward) are two smaller special-purpose experiments installed in the interaction region ATLAS/IP2 (LHCf) and CMS/IP5 (TOTEM).

LHCf [107] is dedicated to study the production of neutral particles at very forward rapidities relevant for models describing hadron interactions of very high energy cosmic rays. Two zero degree calorimeters are installed at  $\pm 140$  m distance from the interaction point and particles in the very-forward pseudorapidity  $|\eta| > 8.4$ .

TOTEM [108] is dedicated to measure the elastic, diffractive and total pp cross sections. Two forward trackers embedded in the CMS detector are installed on each side of the interaction region at  $\pm 9$  m and  $\pm 13.5$  m from the interaction point covering the pseudorapidity range  $3.1 < |\eta| < 6.5$ . Two stations of Roman Pots are installed at  $\pm 150$  m and  $\pm 217$  m distance from the vertex, each consisting of two units with three pots. These detectors can be moved closed to the LHC beam to detect protons only a few millimeters away from the beam.

MoEDAL (Monopole and Exotics Detector At the LHC) [109] searches for magnetic monopoles and highly charged exotic particles. It is installed in the LHCb/IP8 region and covers  $30\text{ m}^2$  with passive detection material.

---

## 2.2 The ALICE experimental setup

---

ALICE (A Large Ion Collider Experiment) [110–113] is a general-purpose detector focused on the study of the QGP in heavy ion collisions.

The ALICE detector has been designed for very high particle multiplicities of up to 8000 charged particles per unit of pseudorapidity, and is optimized for  $dN_{\text{ch}}/d\eta = 4000$ , representing the upper end of the extrapolation from lower energy to central Pb–Pb collisions at the LHC. In fact, the measured multiplicities, although at half the LHC design energy, are significantly lower [114–116].

The focus of ALICE on the low-momentum, bulk part of particle production in pp and heavy ion collisions, required a detector with tracking and particle identification (PID) capabilities down to very low momenta. This is achieved by a moderate magnetic field and a low amount of material to suppress energy loss and multiple scattering of low-momentum particles.

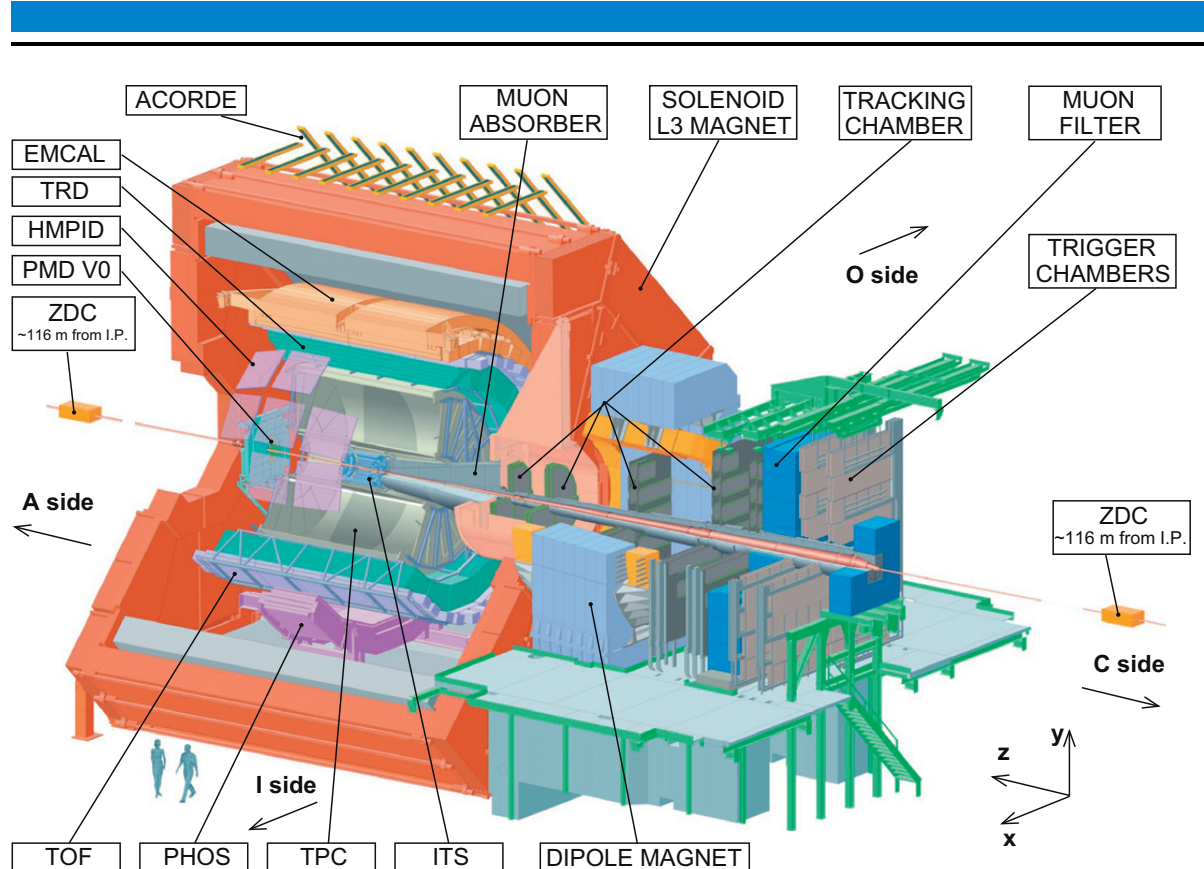


Figure 2.2.: Overall layout of the ALICE detector.

Figure taken from [117].

ALICE is complex detector setup and consists of several sub-detectors, the main component is formed by the central barrel detectors, located inside the L3 magnet. Additional forward detectors are also located in the L3 magnet, except the two zero-degree-calorimeters. Is is accompanied by a single-arm forward muon spectrometer (muon arm). In addition a cosmic ray trigger (ACORDE) is installed on top of the magnet.

The overall layout of the ALICE detector with all sub-detectors is shown in Figure 2.2. An enlarged view of the detectors surrounding the interaction region, in particular the Inner Tracking System (ITS), is shown in Figure 2.3.

The ability of the ALICE detector for particle identification over a wide momentum range and the tracking down to low momenta are unique at the LHC. Running conditions and detector performance of ALICE during the data taking from 2009 until 2013 is described in ref. [119].

### 2.2.1 ALICE Coordinate system

The ALICE global coordinate system [120, 121] is used to describe the positions of detectors and parameters of reconstructed tracks are also given in the global coordinate frame. Is a right-handed Cartesian coordinate system with the origin at the nominal interaction point (IP). The  $z$ -axis is aligned along the beam direction. Positive  $z$  points along the direction of the LHC beam 2 and towards the access shaft to the ALICE cavern. Negative  $z$  points towards the muon arm in the direction of LHC beam 1. The  $x$ -axis is horizontal, with positive  $z$  pointing towards the center of the LHC ring. The  $y$ -axis is vertical with positive  $y$  pointing up.

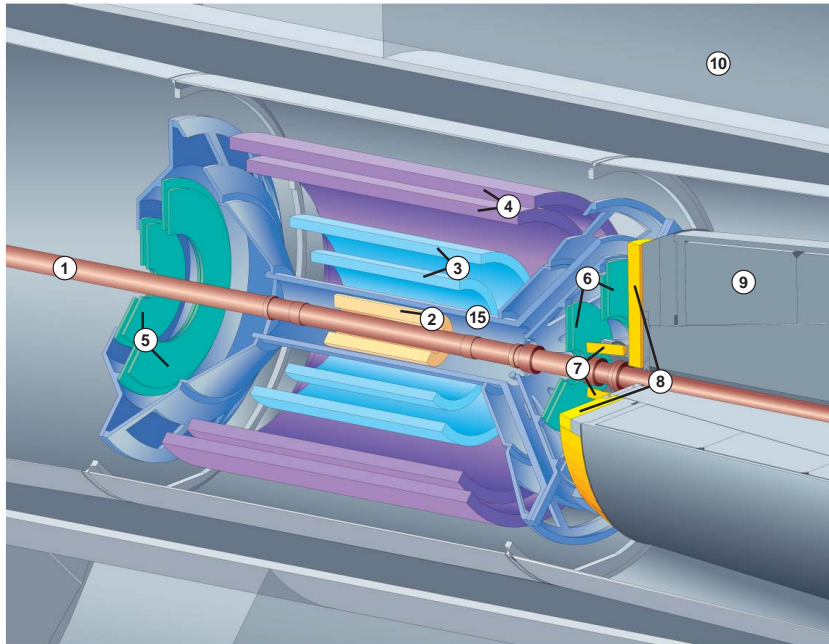


Figure 2.3.: Layout of the ALICE inner detectors surrounding the interaction region close to the beam pipe (1). the ITS consisting of SPD (2), SDD (3) and SSD (4); the FMD (5, 6), TZERO-C (7), VZERO-C (8). The inner detectors are surrounded by TPC (10). On the C side the muon absorber (9) is visible.

Figure taken from [118].

The region of positive  $z$  is called *A side*, the region of negative  $z$  *C side*. The *I side* is the region of positive  $x$ , the *O side* is the region of negative  $x$ . This naming is also indicated in Figure 2.2.

The Cartesian coordinate system  $(x, y, z)$  can be expressed in cylindrical  $(\rho, \phi, z)$  or spherical  $(r, \phi, \theta)$  coordinates as well. It is common to define the pseudorapidity in terms of the polar angle

$$\eta = -\ln\left(\tan\frac{\theta}{2}\right) \quad (2.1)$$

do describe the acceptance of detectors. Here,  $\eta = \pm\infty$  coincides with the  $z$  axis while  $\eta = 0$  is perpendicular to the beam axis.

### 2.3 Central Barrel Detectors

The central barrel of ALICE covers approximately the pseudorapidity region  $|\eta| < 1$  and contains the main tracking and particle identification detectors. The L3 magnet provides a uniform solenoidal magnetic field of 0.5 T.

For tracking of charged particles the Inner Tracking System (ITS) and the Time Projection Chamber (TPC) are used. Both detectors also provide particle identification. In addition, several detectors with more specific tasks and, partially, also smaller acceptance are located in the central barrel. Most of these detectors are used only for particle identification.

Below a brief description of the central barrel detectors is given.

---

### 2.3.1 Inner Tracking System

---

The subdetector located closest to the beam pipe and closest to the interaction region is the Inner Tracking System (ITS) [122], a silicon semiconductor detector with six cylindrical detector layers.

The six layers use different detector technology. The innermost two layers are made of hybrid pixels and form the Silicon Pixel Detector (SPD). They are followed by the two layers of the silicon drift detector (SDD). The two outermost layers compose the Silicon Strip Detector (SSD). The individual detector components are described in more detail below.

Each layer covers the full azimuthal angle while the pseudorapidity coverage slightly differs for the individual layers, ranging from  $|\eta| < 0.9$  to  $|\eta| < 2$ .

Due to its proximity to interaction region the ITS is the main detector that measures the position of the primary interaction vertex. The closest distance of a given track to that vertex and allows to separate particles originating from the primary interaction vertex to those that have a displaced vertex. This distance is called DCA (distance of closest approach) to the primary vertex and is determined by the tracking information from the ITS. Especially the SPD provides the high impact parameter resolution required to study charm and beauty decays via their decay length.

---

#### Silicon Pixel Detector

---

The Silicon Pixel Detector (SPD) constitutes the innermost two layers (layers 0,1) of the ITS. It is located at a radial distances of 3.9 cm (layer 0) and 7.6 cm (layer 1) and cover the full azimuth. The elongation along  $z$  of  $\pm 14.1$  cm translated into a pseudorapidity coverage of  $\eta = \pm 2$  (layer 0) and  $\eta = \pm 1.4$  (layer 1) with the nominal interaction point as origin. Due to the small radii the actual acceptance in terms of the particles pseudorapidity depends on the location of the particles origin.

Partial overlap of the  $\eta$  acceptance with the FMD allows the measurement of charged particle multiplicities over a wide range of pseudorapidity. Including displaced vertices the coverage can be extended to 10 units of pseudorapidity.

The SPD uses the hybrid silicon pixel technology, i. e. separate silicon chips for the detector and readout, that are bonded together with a cell (pixel) size of  $50\text{ }\mu\text{m}(r\phi) \times 425\text{ }\mu\text{m}(z)$ . In total the SPD has about 10 million channels which are read out in a binary mode (signal below/above threshold). The low amount of material, about 1% of a radiation length  $X_0$  per layer, allow to track particles with momenta down to 80 MeV/c.

With a spacial precision in  $r\phi$  of 12  $\mu\text{m}$  the determination of the radial position of the primary and secondary vertices is dominated by the SPD.

In addition the SPD is an important trigger detector and can also be used for centrality determination in Pb–Pb collisions.

Problems with the cooling system of the SPD lead to significant parts (20-30%) of the detector being inactive for the data taking in 2009-2011, increasing with time. After an intervention of the cooling system in 2012 most of the detector could be switched on again, reducing the inactive part to about 5%.

---

## Silicon Drift Detector

---

The Silicon Drift Detector (SDD) forms the two intermediate layers of the ITS. They are located at radial distances of 15 cm (layer 2) and 23.9 cm (layer 3) from the IP. They both cover  $|\eta| < 0.9$  in pseudorapidity.

With 84 and 176 detectors in the two layers and 512 channels in each detector the SDD has a total of 133120 channels, which are read out with 10b it ADCs to provide  $dE/dx$  measurements.

The position resolution is 35  $\mu\text{m}$  along in the  $r\phi$  direction (along the drift) and 25  $\mu\text{m}$  along the  $z$  direction (anode).

---

## Silicon Strip Detector

---

The Silicon Strip Detector (SSD) composes the two outer layers the ITS and covers  $|\eta| < 0.98$ . It is important for track matching to the TPC and provides two  $dE/dx$  samples for particle identification in the ITS.

The two layers are located at radii of 38 and 43 cm where the track density is below 1 particle per  $\text{cm}^2$ . It consists of 1698 double sided silicon strip sensors with a stereo angle of 35 mrad covering an area of 5  $\text{m}^2$ . Each sensor has a thickness 300  $\mu\text{m}$  an active area of 73 x 40  $\text{mm}^2$  with 768 readout strips on each side resulting in at total of 2.6 million analog readout channels. The spatial resolution of the SSD is 20  $\mu\text{m}$  ( $r\phi$ ) and 820  $\mu\text{m}$  ( $z$ ).

---

### 2.3.2 Time Projection Chamber

---

The Time Projection Chamber (TPC) [117,123] is the main tracking and particle identification detector of the central barrel. With the TPC, charged particles can be reconstructed in three spacial dimensions.

The TPC covers the full azimuth and  $|\eta| < 0.9$  for tracks crossing the full detector. For larger pseudo rapidities the track length in the TPC decreases, with 1/3 of radial track length the acceptance increases to  $|\eta| < 1.5$ .

The TPC has the shape of a hollow cylinder with an inner radius of 848 mm and an outer radius of 2466 mm for the active volume. It is filled with a Ne-CO<sub>2</sub>-N<sub>2</sub> mixture as a counting gas. The total length of 4.994 m is divided into to drift regions by the central high voltage (HV) electrode located at  $z = 0$ . The drift voltage of -100 kV at the central electrode results in a 400 V/cm drift field, pointing towards the central electrode.

A charged particle crossing the TPC ionizes the gas creating free electrons and ions. In the drift field the two charges are separated and the electrons drift towards the end-plates with a drift velocity of 2.65 cm/ $\mu\text{s}$ . The drift velocity of the ions is about a factor 1000 smaller.

Each end-plate is instrumented with 36 readout chambers. The readout chambers are organized in 18 sectors, each covering 20° in azimuth. One inner readout chamber (IROC) and one outer readout chamber (OROC) compose a sector.

All readout chambers designed as conventional wire chambers with cathode pad readout. The cathode wires separate the drift region from the amplification region. In the vicinity of the anode wires, electron are accelerated in the electric field and creating additional electrons in

an avalanche ionization. The movement of the electrons induces a signal on the pad plane that is read out. The slow drifting ions induce a much smaller signal with longer duration ("ion tail"). A set of gating wires ("gating grid") prevents backflow of ions into the drift region and allows electrons to enter the amplification region only in a time of about  $100\ \mu\text{s}$  after a trigger.

Segmentation of the pad plane into pads allows for two dimensional position reconstruction ( $x$  and  $y$ ). The pad sizes of the IROC are  $4 \times 7.5\ \text{mm}^2$  (innermost 63 padrows). OROCs have two different pad sizes,  $6 \times 10\ \text{mm}^2$  (64 padrows) and  $6 \times 15\ \text{mm}^2$  (outermost 32 padrows). The  $z$  coordinate is calculated in the reconstruction using the drift time of the electrons.

Each IROC (OROC) has 5504 (9984) pads arranged in 63 (96) padrows. All pads (557 568 in total) are read out individually with 10bit, 10 MHz ADCs after passing analog pulse shapers. The drift time of about  $100\ \mu\text{s}$  leads to 1000 samples in  $z$  direction.

The total number of padrows of 159 corresponds to the maximal number of space points and  $dE/dx$  samples that can be measured along the track. This large number of measured points is responsible for the excellent particle identification and tracking performance of the TPC. The TPC with many measured space points, long radial extension and the high space point resolution in combination with the ITS enables the excellent  $p_{\text{T}}$  resolution of the ALICE central barrel (see section 3.7.4).

The position resolution of the TPC depends on the radius and is  $1100\text{--}800\ \mu\text{m}$  in  $r\phi$  and  $1250\text{--}1100\ \mu\text{m}$  in  $z$ .

The total data volume read out from the ALICE detector and stored is dominated by the TPC with event sizes of about 70 MByte for a central Pb–Pb event.

### 2.3.3 Transition Radiation Detector

The primary purpose of Transition Radiation Detector (TRD) [124] is to identify electrons, especially in the momentum range above  $1\ \text{GeV}/c$ . Tracking information from the TRD also extends the measured track length which improves the overall transverse momentum resolution at high  $p_{\text{T}}$ . The TRD can be also used as a trigger detector for electrons and high  $p_{\text{T}}$  charged particles. By requiring several particles above some  $p_{\text{T}}$  threshold, a jet trigger has been implemented as well.

The detector measures in addition to the direct ionization also transition radiation composed of photons in the X-ray range. Transition radiation is emitted by charged particles passing the boundary between two polarizable media with different dielectric constants. Many such boundaries are required to produce a detectable amount of transition radiation. The intensity of the transition radiation depends linearly on the Lorentz factor  $\gamma \approx p/m$ , so for a fixed momentum electrons produce about  $m_{\pi}/m_e \approx 280$  times more transition radiation.

The TRD is located outside of the TPC at a radial distance of 2.9–3.68 m from the IP and covers  $|\eta| < 0.84$  in pseudorapidity and, upon completion, the full azimuth. It is segmented into 18 super modules following the azimuthal structure of the TPC. Each supermodule contains 30 chambers, arranged in five stacks along the  $z$  direction and six layers in the radial direction. Each chamber contains a radiator, made of a 4.8 cm fiber/foam sandwich structure followed by 3.7 cm drift chamber filled with a Xenon/CO<sub>2</sub> mixture as a counting gas. The drift chamber contains a 3 cm drift region and 0.7 cm amplification region with cathode pad readout. Detector electronics are mounted on each individual chamber.

Transition radiation created in the radiator creates ionization at the beginning of the drift region, while direct ionization is created all along the track in the complete drift region. The combination of the larger energy loss for electrons in combination with the transition radiation allows to identify electron on a track-by-track bases.

In total the TRD has a total of 1.18 million readout channels read out with 10 bit, 10 MHz ADCs. The TRD contributes significantly to the total data volume .

The number of installed TRD supermodules was 7 in 2009-2010 and increased to 10 for the 2011 run. During the data taking in 2012-2013 13 (out of 18) supermodules where installed.

---

#### 2.3.4 Time-Of-Flight detector

---

The Time-Of-Flight detector (TOF) [125, 126] is designed for identification of charged particles, especially in the momentum ranges where the TPC  $dE/dx$  cannot be used. In particular the TOF provides pion/kaon separation up to 4 GeV/c and proton/kaon up to 2.5 GeV/c at the  $3\sigma$  level. Also the identification of electrons and nuclei improves with the TOF information. Furthermore, the TOF also acts as a wake-up pre-trigger for the TRD and has been successfully used as a trigger on cosmic rays.

The detector measures the velocity  $\beta$  of charged particles via the time they need to travel from the collision to the detector. The required start signal is delivered by the T0 detector. The time resolution of the TOF is better than 40 ps (RMS), this also allows to separate particles produced in the interactions of different bunch crossings (pile-up).

The TOF is designed as a Multi-gap Resistive Plate Chamber (MRPC) and follows the 18-fold segmentation of the TPC and TRD. It is located at a radius of 3.78 m and covers  $|\eta| < 0.9$  in pseudorapidity and the full azimuth.

---

#### 2.3.5 Electromagnetic Calorimeter

---

The Electromagnetic Calorimeter (EMCal) [127, 128] is an electromagnetic sampling calorimeter designed to measure the energy of electrons and photons (from  $\pi^0$  and  $\eta$  decays) at high  $p_T$ . It can also provide trigger signals on photons, electrons and jets.

The EMCal is a lead/plastic-scintillator sampling calorimeter with a thickness of  $20 X_0$ . Scintillation light is detected with avalanche photo diodes.

It covers  $|\eta| < 0.7$  in pseudorapidity and  $80^\circ < \phi < 187^\circ$  in azimuth, giving partial back-to-back calorimeter coverage together with PHOS. The energy resolution of the EMCal is about 2% at 100 GeV [129].

The EMCal has been added at a late stage to the ALICE design and as a result the installation was delayed. In the years 2009-2011 only part of the EMCal was installed. Since 2012 all modules are installed and running.

---

#### 2.3.6 Photon Spectrometer

---

The Photon Spectrometer (PHOS) [130] is a homogeneous electromagnetic calorimeter designed to measure photons with spatial and energy resolution in the range  $0.1 < E_\gamma < 100$  GeV/c. It is using high-density lead-tungstate ( $\text{PbWO}_4$ ) crystals as scintillator and large area

avalanche photo diodes for readout. It covers  $|\eta| < 0.12$  in pseudorapidity and  $220^\circ < \phi < 320^\circ$  in azimuth. Compared to the EMCal, PHOS has a much smaller acceptance, but provides a better energy resolution of about 1% at  $E = 100$  GeV [131].

The PHOS has (2009-2013) only 3 (out of 5) modules installed, resulting in an azimuthal coverage lower to the number quoted above.

---

### 2.3.7 High Momentum Particle Identification Detector

---

The High Momentum Particle Identification Detector (HMPID) [132] extends the PID capabilities for hadrons towards larger  $p_T$ . It is based on the Ring Imaging Cherenkov (RICH) technology and measured velocity of charged particles via opening angle of Cherenkov radiation in a liquid perfluorohexane radiator. For particle identification this information needs to be combined with the momenta measured in ITS/TPC.

The HMPID covers about 5% of the central barrel phase space with in the pseudorapidity range  $|\eta| < 0.6$  and an azimuthal angle  $1.2^\circ < \phi < 58.8^\circ$ .

---

## 2.4 Forward and trigger detectors

---

### 2.4.1 V0 detectors

---

The VZERO (V0) [133, 134] detector is mainly used as a trigger detector. It provides several triggers: minimum bias (MB), multiplicity trigger, central and semi-central trigger (in heavy ion collisions). The multiplicity measured by the V0 detector is also used in the offline analysis as a primary measure of the centrality in heavy ion collisions. In pp collisions, the V0 also contributes to luminosity measurements. The good time resolution of about 1 ns allows to identify beam induced background<sup>4</sup>.

The V0 consists of two detectors located at forward pseudorapidities on either side of the interaction region: V0-A covering  $2.8 < \eta < 5.1$  and V0-C with  $-1.7 < \eta < -3.7$ . Both detectors use disk-shaped arrays of plastic scintillator connected to photomultiplier tubes via wavelength shifting fibers. Each detector is segmented into 4 rings in the radial direction and 8 sectors in azimuth. The segmentation also allows the measurement of anisotropic flow observables and the determination of an event plane.

### 2.4.2 T0 detectors

---

The two TZERO (T0) [133] detectors are designed to provide an accurate start signal for the TOF detector and a wake-up pretrigger for the TRD. It consists of two arrays of 12 Cherenkov counters, placed close to the beam pipe covering  $4.61 < \eta < 4.92$  (T0-A) and  $-3.28 < \eta < -2.97$  (T0-C) in pseudorapidity. The time resolution is about 50 ps (RMS).

### 2.4.3 Forward Multiplicity Detector

---

The Forward Multiplicity Detector (FMD) [133] measures charged particle at forward rapidities. The FMD covers  $-3.4 < \eta < -1.7$  and  $1.7 < \eta < 5$  in pseudorapidity, partially overlapping with the SPD to allow multiplicity measurements over a large  $\eta$  range.

<sup>4</sup> Beam-related background is colloquially referred to as *beam-gas* or *gas-gas* collisions.

The FMD consists of five rings, two on the C side and three on the A side (causing the asymmetric  $\eta$  acceptance) composed of a total of 51200 silicon strips.

---

#### 2.4.4 Photon Multiplicity Detector

---

The Photon Multiplicity Detector (PMD) [135,136] is designed to measure the multiplicity and spatial distribution of photons in the forward region on the A side, covering  $2.3 < \eta < 3.7$  and the full azimuth.

It consists of two gas proportional counters with lead converter in-between. Photons convert in the lead and are detected in the second detector layer while charged particles leave a signal in both layers. The gas counter are segmented hexagonal cells with an area of  $0.22 \text{ cm}^2$  each.

---

#### 2.4.5 Zero Degree Calorimeter

---

The Zero Degree Calorimeter (ZDC) [137] measures the energy of the spectator nucleons that do not take part in an heavy-ion collision. This allows to determine the number of spectators and thus gives an estimate of the impact parameter or centrality of the collision.

The hadronic ZDCs are located at a distance of 116 m from the interaction point in the LHC tunnel. Spectator neutrons are not deflected by the LHC bending magnets and are detected in the two neutron ZDCs (ZN), while spectator protons have a higher charge-to-mass ratio and deflected stronger than the beam. They are detected in the proton ZDCs (ZP).

Both ZDCs use an passive absorber with embedded quartz fibers as detection material. In the absorber a particle shower is created and in the fibers Cherenkov radiation is produced that is detected in photomultiplier tubes (PMT). The ZDCs can be moved out of the horizontal beam plane when they are not in use.

The ZDC can also provide Level-1 triggers to the other detectors.

In peripheral heavy ion collisions, part of the spectators are bound in nuclear fragments that escape the detection of the hadronic ZDCs, leading to a small number of detected spectators, similar to central collisions. To distinguish the two cases, two Electromagnetic ZDCs (ZEM) measure the energy of particles emitted at forward rapidity, which increases monotonically with centrality. The ZEM is located only on the A side of the detector and covers  $4.8 < \eta < 5.7$ .

---

### 2.5 Muon spectrometer

---

Muon detection and identification in ALICE is performed in the forward pseudorapidity  $-4.0 < \eta < -2.5$  by a dedicated muon spectrometer located on the C side of the detector. The main goal is to measure heavy flavor and vector mesons in their dimuon decay channel.

The muon spectrometer [138–140] consists of the front absorber (about 4 m long,  $\approx 10\lambda_{int}$ ,  $\approx 60X_0$ ) to absorb the large amount of hadrons produced in the collision. The absorber is followed by a dipole magnet with a field integral of 3 Tm. Muons are tracked through the magnetic field with five tracking stations: two before the magnet, one inside the magnet and two after the magnet. Each tracking station has two detection planes to reconstruct also the direction of the muon in addition to its position. Cathode pad chambers with Ar/C<sub>2</sub>O<sub>2</sub> are used for detection with a total of about 1 million readout channels.

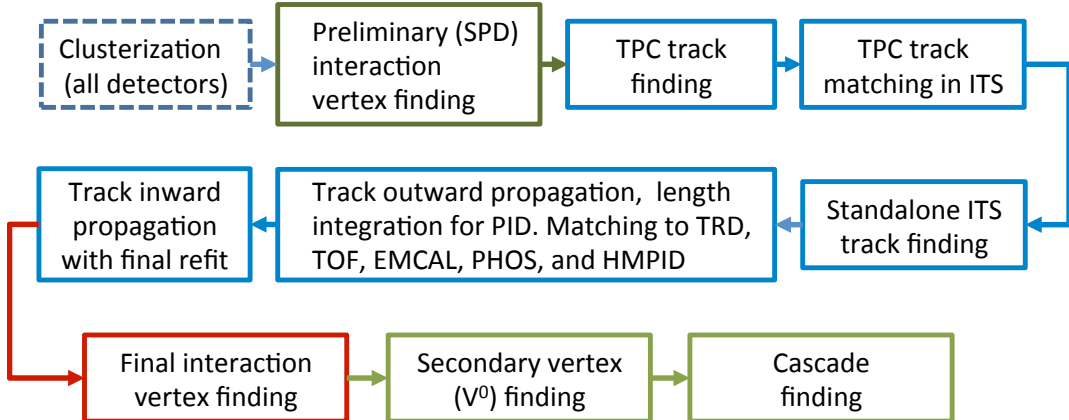


Figure 2.4.: Illustration of the tracking and reconstruction procedure in ALICE.  
Figure taken from [119].

The muon filter, a 1.2 m thick iron wall, acts as second absorber after the tracking stations and in front of the trigger stations. Only muons with a momentum  $p > 4$  GeV/c are able to reach the trigger two trigger stations, resulting in a high-purity muon trigger.

The trigger stations consist of two detector planes each equipped with Resistive Plate Chambers (RPC) operated in streamer mode. The spacial resolution of the trigger detector allows a  $p_T$ -selective muon trigger.

The muon spectrometer is able to take data at a higher rate and luminosity compared to most of the central barrel detectors.

## 2.6 Track reconstruction

The procedure of track finding and fitting procedure is schematically shown in Figure 2.4. The various steps are specified in [119] and briefly described below. A more detailed description, is given in [141] for the TPC tracking and in [142] for the combined tracking.

The first step is the clusterization, during which the raw data (signals from ADCs) are converted into clusters. This is done for all detectors separately. In the TPC the clusterization is performed in the  $r\phi$  and time direction, i.e. signals in consecutive time-bins and neighboring pads (in the same pad row) are combined into one cluster.

The TPC clusters are characterized by the total charge  $Q_{\text{tot}}$  and the maximal charge  $Q_{\text{max}}$ , and the position in three spacial dimensions. Most clusters have a signal above threshold in more than one pad, this allows to calculate the position as the weighted mean with much higher accuracy than the pad size. For clusters with a signal only on a single pad (called *single pad clusters*) the position cannot be resolved better than the pad width and these clusters are excluded from the tracking procedure. For particle identification with  $dE/dx$  they can be used.

Overlapping clusters are separated using an unfolding procedure. Clusterization in the TPC can be performed during the offline reconstruction or online in the HLT. Clusterization in the HLT can significantly reduce the data volume, since only cluster information is stored, not the complete signals. During the early runs 2009-2011 the offline clusterization was used. In the

Pb–Pb data taking 2011 the HLT clusterization was commissioned and used in the 2012-2013 data taking.

In the next step a preliminary interaction vertex is constructed using the information from the SPD. Afterwards the track finding start in the outermost padrows of the TPC by combining clusters to track seeds. These track candidates are then propagated inwards through the TPC using a Kalman filter approach. Clusters that are compatible with the estimate of the track parameters are added to the track. Likewise the seeding procedure continues inwards using the clusters that are not assigned to a track. This procedure continues until all tracks in the TPC have been found.

The clusters found in the TPC are used to determine a preliminary particle hypothesis based on the  $dE/dx$  measurements. The particle mass is used to correct for the energy loss in the further steps of track finding and fitting. The tracks are propagated inwards to the ITS and matching ITS clusters are added to the track, updating the track parameters. On all ITS clusters that are not associated to these TPC-ITS “global” tracks, a stand-alone ITS track finding is performed. The ITS stand-alone tracking allows to find tracks with transverse momenta down to 80 MeV/c.

Afterwards a second iteration of the tracking fitting is performed starting with the track parameters obtained for the smallest radii, propagation the track to larger radii. Since the estimate of the track parameters is more precise now, clusters can be removed or added during this step. From the TPC the track is further propagated to the other detectors at larger radii, i.e. TRD, TOF, EMCal, PHOS and HMPID.

With an updated PID information from the TPC a final inward track fit is performed using the previously found clusters of the TPC and ITS. This step results in the final parameters and covariance matrix of the track.

Using the combined ITS-TPC tracks a final vertex finding is performed that determines the position of the primary vertex (“track vertex”). For events with small number of tracks, the average beam interaction profile measured over many events “interaction diamond” provides additional information for the vertexer. Details of the vertex reconstruction can be found in Ref. [143].

In an additional step secondary vertices coming from decays of neutral particles or photon conversions in the material (so called  $V^0$ -candidates) are reconstructed. This is followed by a search for cascade decay topologies.

---

## 2.7 Centrality determination in ALICE

---

The centrality determination in ALICE is described in detail in ref. [144], only a short description based on this reference is given here.

Centrality is defined as the percentage of the total nuclear cross section and allows to relate measured signals in the detector to geometrical quantities that can not be directly observed. In particular the impact parameter  $b$ , the number of participating nucleon  $N_{\text{part}}$  or the number of binary collisions  $N_{\text{coll}}$  or the nuclear overlap  $T_{\text{AA}}$  can be obtained (see section 1.7 for a definition of these quantities). Various detectors with different pseudorapidity coverage are used to estimate the centrality of a Pb–Pb collision, including the ZDC, VZERO, TPC and SPD. The different centrality estimators are implemented and calibrated in a central framework

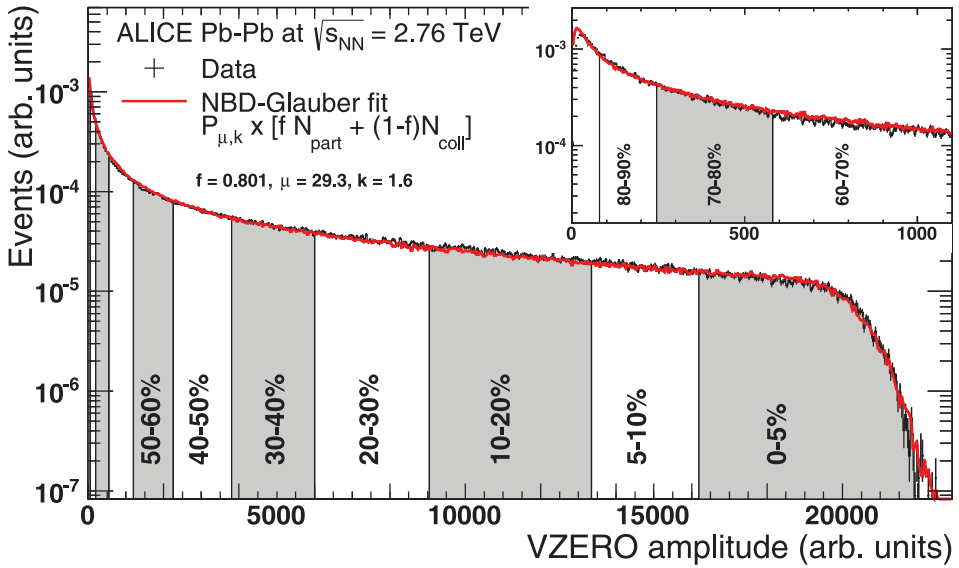


Figure 2.5.: Distribution of the VZERO amplitudes (sum of V0A and V0C) measured in Pb-Pb collisions at  $\sqrt{s_{\text{NN}}} = 2.76$  TeV together with the NBD-Glauber-Fit. The centrality intervals obtained from the VZERO amplitudes are indicated. The insert shows the most peripheral centrality intervals.

Figure taken from [144].

and can be used in the data analysis. All methods are based on a monotonic behavior of the detector signal on the collision centrality.

The best centrality resolution is achieved for the combined multiplicity (V0M) of the V0A and V0C detectors. For this analysis this V0M is used as a estimator for the collision centrality, which represents also the main method used by ALICE. Part of the machine induced background and electromagnetic dissociation is removed with cuts on the ZDC signals.

The multiplicity distribution in Pb-Pb collisions can be well described by a convolution of a Monte Carlo Glauber model with a negative binomial distribution (NBD) for particle production. The distribution of the signals in the VZERO detectors is shown in Figure 2.5 along with a NBD-Glauber-Fit. Only the range of 0-90% of the total cross section is used for the fit, as the contamination with background events from Electromagnetic (QED) processes and beam-gas collisions and trigger inefficiencies are negligible in this range. The lower end of the fit range (90%) is called the Anchor Point (AP).

Centrality percentiles as indicated in Figure 2.5 are obtained by sharp cuts on the V0M distribution, the corresponding geometrical quantities are obtained via the NBD-Glauber-Fit. A pure MC Glauber model with centrality intervals obtained from slicing in the impact parameter  $b$  and without fit to the data results in geometrical quantities that are only marginally<sup>5</sup> different from those obtained with the NBD-Glauber-Fit.

The parameters used in the MC Glauber model of ALICE are the nucleon-nucleon cross section of  $\sigma_{\text{NN}}^{\text{inel}} = (64 \pm 5)$  mb and the Woods-Saxon parameters  $r_0 = (6.62 \pm 0.06)$  fm for the nuclear radius and  $a = (0.546 \pm 0.010)$  fm for the skin thickness. In addition a minimal exclusion

<sup>5</sup> The relative difference is < 1% for 0-50% centrality and < 2% for more peripheral collisions.

---

---

distance for two nucleons of  $d_{\min} = (0.4 \pm 0.4)$  fm is required. All parameters have been varied by their quoted uncertainties to estimate the systematic uncertainties of the centrality-related geometrical quantities. Values and systematic uncertainties of  $\langle T_{AA} \rangle$ ,  $\langle N_{\text{part}} \rangle$  and  $\langle N_{\text{coll}} \rangle$  that are relevant for this thesis are listed in Table 4.2 of section 4.4, where the results in Pb–Pb collisions are presented.



# 3 Measurement of transverse momentum spectra

## 3.1 Introduction

The overall analysis strategy for the measurement of transverse momentum ( $p_T$ ) distributions of primary charged particles is common in all three collision systems (pp, p–Pb, Pb–Pb). This chapter gives a detailed description of the analysis procedure, including the differences between the collision systems. The analysis procedure is partially also described in the ALICE analysis notes on the pp reference [145],  $R_{\text{Pb}}$  [146],  $R_{\text{CP}}$  [147] and  $\langle p_T \rangle$  [148].

The analysis was performed using the ROOT [149] and AliROOT [150] software packages. ROOT consists of a set of C++ libraries for data analysis and the C++ interpreter CINT. It is complemented by the AliROOT package containing the implementation of functionality that is specific to the ALICE experiment.

Differential yields of primary charged particles were measured for centrality-selected Pb–Pb collisions (0–80% central) and for non-single-diffractive (NSD) p–Pb collisions. For inelastic (INEL) pp collisions differential yields as well as differential cross sections were obtained.

### 3.1.1 Kinematic range

The analysis is restricted to  $p_T > 0.15$  GeV/c since the track reconstruction efficiency drops close to zero for smaller  $p_T$ . This is mainly a consequence of the cut on the number of crossed rows in the TPC (see below), selecting long tracks which need a  $p_T > 0.15$  GeV/c to cross at least 120 pad rows in the TPC in a magnetic field of  $B = 0.5$  T. Taking all track selection criteria into account the efficiency drops below 0.1% for  $0.1 < p_T < 0.15$  GeV/c.

Considerations of acceptance effects (see section 3.7.5) present only in p–Pb collisions and the focus on large transverse momenta lead to the choice of  $p_T > 0.5$  GeV/c for the analysis of the first p–Pb data collected in 2012.

For the 2013 p–Pb data set, the available measurements of identified pions, kaons and protons have been taken into account, leading to a reduction of the systematic uncertainty arising from the acceptance corrections. The analyzed  $p_T$  range for 2013 p–Pb data could therefore be extended down to  $p_T > 0.15$  GeV/c, the same range as in pp and Pb–Pb. This range is required for the study of  $\langle p_T \rangle$  as a function of multiplicity (see section 5), as about half of the produced particles have a  $p_T < 0.5$  GeV/c.

The upper end of the  $p_T$  reach is a result of the analyzed statistics leading to  $p_T > 20$  GeV/c (for pp 0.9 TeV and 2012 p–Pb 5.02 TeV) and to  $p_T < 32$  GeV/c (for pp 2.76 TeV). In pp 7 TeV and Pb–Pb the upper limit of  $p_T > 50$  GeV/c is motivated from the systematic uncertainty of the  $p_T$  resolution, which becomes dominant at larger  $p_T$ . With the much larger number of events collected in the 2013 the upper edge of the  $p_T$  reach could be extended to  $p_T < 50$  GeV/c for this data set.

The polar angle of tracks accepted in the analysis is restricted in terms of the pseudorapidity to  $|\eta| < 0.8$  to remove all tracks which do not cross the TPC fully within its active area.

For the analysis of the asymmetric p–Pb collisions the selection of  $|\eta| < 0.8$  applies to  $\eta$  measured in the laboratory frame. In the nucleon-nucleon center-of-momentum (cms) frame, this corresponds to  $-0.3 < \eta_{\text{cms}} < 1.3$ . This range in  $\eta_{\text{cms}}$  has been subdivided into three intervals. Comparing pp and p–Pb in terms of the nuclear modification factor requires the same acceptance in both systems. The interval  $|\eta_{\text{cms}}| < 0.3$  corresponds to the maximal overlap with the acceptance in pp collisions which is symmetric in  $\eta_{\text{cms}}$ . The two forward ranges  $0.3 < \eta_{\text{cms}} < 0.8$  and  $0.8 < \eta_{\text{cms}} < 1.3$  make use of the remaining acceptance to study the pseudorapidity dependence of the  $p_{\text{T}}$  distributions.

In order to compare to results from p–Pb, also all pp data was re-analyzed with an acceptance even further restricted to the equivalent in p–Pb of  $|\eta| < 0.3$ .

### 3.1.2 Primary charged particles

Only charged particles create direct ionization and can leave an observable track in the detector. In addition, to be detectable they have to be long-lived enough to cross the detector. This fundamentally limits the direct detection to the following particle species (note that this list is exhaustive):  $e^-$ ,  $\mu^-$ ,  $\pi^+$ ,  $K^+$ ,  $p$ ,  $\Xi^-$ ,  $\Sigma^+$ ,  $\Sigma^-$ ,  $\Omega^-$  plus their antiparticles. The definition of primary charged particles in ALICE which has been used for the analysis (and this thesis) includes exactly these particles.

Note that the detection efficiency depends on the track selection criteria as well as on the decay length  $c\tau$ . Therefore strange baryons, which have a decay length of only few cm, have a greatly reduced probability to be detected.

The following definition of primary and primary charged particles is used within this thesis:

*Primary particles are all particles that are produced in the collision and remain after all subsequent strong, electromagnetic and weak decays, with the exception of weak decays of hadrons containing only light quarks and muons. Primary charged particles are all primary particles that are charged.*<sup>1</sup>

This definition includes all particles which have a decay length of  $c\tau > 1$  cm. For unstable particles like D mesons or neutral pions their decay products are considered primary particles. Table 3.1 gives an overview of all particles included in the definitions of primary and primary charged particles and their decay length.

The scope of this analysis is the measurement of primary charged particles. This includes directly produced charged hadrons like  $\pi^\pm$ ,  $K^\pm$ ,  $p$ ,  $\bar{p}$  but also electrons (from Dalitz decays<sup>2</sup> of non-secondary  $\pi^0$  or  $\eta$ ) as well as charged decay products of hadrons containing charm and beauty quarks.

Relative fractions of primary charged particle species are shown in Figure 3.1 for Pb–Pb and pp collisions as an example. These fractions were obtained from simulations using the event

<sup>1</sup> The definition of primary charged particles differs slightly from the ones commonly found in ALICE publications, the following being taken from [151]: *Here, primary particles are defined as prompt particles produced in the collision and all decay products, except products from weak decays of strange particles such as  $K^0$  and  $\Lambda$ .*

<sup>2</sup> Dalitz decay:  $(\pi^0, \eta) \rightarrow \gamma^* \gamma \rightarrow e^+ e^- \gamma$

	neutral	$c\tau$	charged	$c\tau$
photon	$\gamma$	stable		
leptons	$\nu \bar{\nu}$	stable	$e^+ e^-$	stable
			$\mu^+ \mu^-$	660 m
mesons	$K_S^0$	2.7 cm	$\pi^+ \pi^-$	7.8 m
	$K_L^0$	15 m	$K^+ K^-$	3.7 m
nucleons	$n \bar{n}$	$2.6 \cdot 10^8$ km	$p \bar{p}$	stable
baryons $S = \pm 1$	$\Lambda \bar{\Lambda}$	7.9 cm	$\Sigma^+ \bar{\Sigma}^-$	2.4 cm
			$\Sigma^- \bar{\Sigma}^+$	4.4 cm
baryons $S = \pm 2$	$\Xi^0 \bar{\Xi}^0$	8.7 cm	$\Xi^- \bar{\Xi}^+$	4.9 cm
baryons $S = \pm 3$			$\Omega^- \bar{\Omega}^+$	2.5 cm
nuclei			all (anti-)nuclei	

Table 3.1.: Particles included in the definition of primary and primary charged particles. For unstable particles also the decay lengths  $c\tau$  (values from [17]) are given.

generators HIJING (Pb–Pb) and PYTHIA (pp) so they can differ from the actual particle composition in measured collisions. Nevertheless they show important characteristics of particle production in high energy hadron collisions. Particle production is dominated by pions, especially at low transverse momenta. Together with kaons and protons they account for about 95% of all produced primary particles at large  $p_T$ . As low and intermediate  $p_T$  this fraction becomes even larger.

Except for protons and electrons all primary charged particles are unstable and can possibly decay (see also Table 3.1) with a proper lifetime  $\tau$ . In the lab frame the probability that a particle with momentum  $p$  and mass  $m$  survives at least a distance  $d$  is

$$P(d) = e^{-\frac{dm}{p\tau}}. \quad (3.1)$$

Figure 3.2 show this probability for all unstable primary particles as function of  $p$  with  $d = 200$  cm, corresponding approximately to the track selection criteria. Here, the distance of 200 cm is determined by the cut on the number of crossed padrows in the TPC, see section 3.5.1. The survival probabilities shown in Figure 3.2 represent also an upper limit of the efficiency.

While muons can be considered stable, pions and kaons have a significant probability to decay inside the detector resulting in a lower efficiency at low  $p_T$ . Strange and multi-strange baryons ( $\Sigma^-$ ,  $\Sigma^+$ ,  $\Xi^-$ ,  $\Omega^-$ ), except at very large momenta, all decay before they reach a sufficient track length to be detected reducing the efficiency to essentially zero.

All particles that decay potentially contribute to the contamination of the track sample with secondary particles via their charged decay products. This affects charged particles as well as neutral particles ( $K^0$ ,  $\Lambda$ ,  $\Sigma^0$ ) with a magnitude depending on the particle abundances. Even

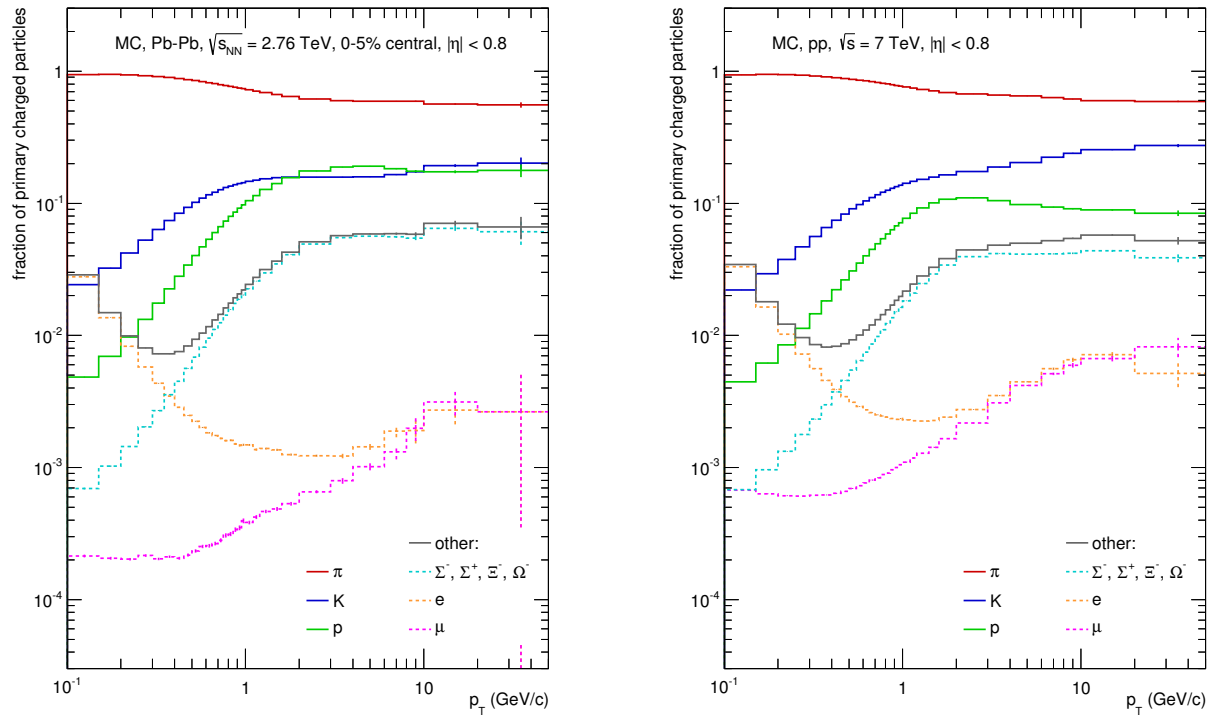


Figure 3.1.: Composition of primary charged particles in MC simulations for most central (0-5%) Pb-Pb events (left plot) and pp collisions at  $\sqrt{s} = 7$  TeV (right plot). Fractions shown were obtained with the event generators HIJING (Pb-Pb) and PYTHIA, tune Perugia0 (pp). The grey curve labeled *other* shows the sum of primary particles that are not pions, kaons or protons.

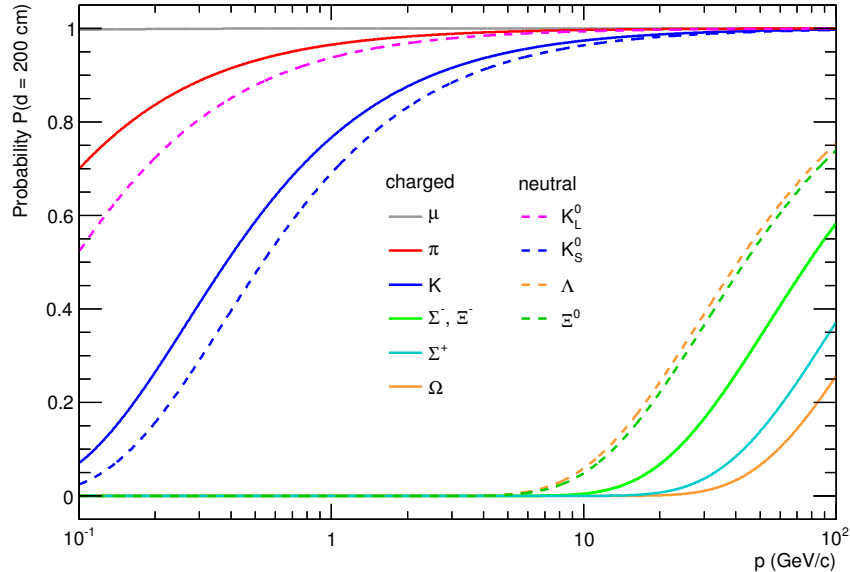


Figure 3.2.: Momentum dependence of the probability for unstable particles to survive a distance of at least 200 cm prior to the decay. This distance corresponds roughly to the selection of tracks in the analysis (see section 3.5 for details of the track selection).

with track cuts that strongly limit the effective distance in Equation (3.1) there are always particles decaying within this distance.

### 3.2 Analysis strategy

The analysis is performed on tracks that are reconstructed using the combined tracking information of the TPC and ITS. The relevant track parameters are the transverse momentum  $p_T$ , and the pseudorapidity  $\eta$ . In addition the event is characterized by several parameters, like multiplicity (centrality in the case of Pb–Pb) and z-position of the reconstructed primary vertex. The analysis aims at reconstructing the underlying (true)  $p_T$  distributions from the measured ones. Detector effects enter at various stages and have to be corrected for. These corrections are largely based on Monte Carlo simulations but also include data-driven methods. Correction procedures are described in this section. In order to limit the systematic uncertainties related to these corrections, it is desired to keep them as small as possible.

### 3.3 Data and MC samples

After the successful startup of the LHC in 2009 with first pp collisions the main pp data taking started in 2010 with collision energies of  $\sqrt{s} = 0.9$  and 7 TeV. Data used for this thesis were recorded in May 2010 (pp,  $\sqrt{s} = 900$  GeV) and June-July 2010 (pp,  $\sqrt{s} = 7$  TeV). In this early phase of the LHC the luminosity and the beam-induced background were very low making these data ideally suited for the analysis of global event properties like transverse momentum spectra.

Data taking continued with pp collisions at 7 TeV with increasing luminosity until beginning of November 2010, when the LHC switched to Pb ions and turned into a heavy-ion collider for the first time. This analysis uses the data recorded in the following running period, which continued till beginning of December 2010.

In 2011 LHC resumed pp operation, including a short period end of March when collisions at  $\sqrt{s} = 2.76$  TeV, the nucleon-nucleon center-of-mass energy matching the Pb-Pb running, were recorded. In February 2013 the LHC was providing pp collisions at  $\sqrt{s} = 2.76$  TeV for the second time, with increased luminosity. Only the data recorded in 2011 has been included in this analysis.

The first p–Pb collisions at the LHC were recorded during a short test run in September 2012. This pilot run was followed by the main p–Pb data taking period in January-February 2013, delivering larger luminosity with increased number of bunches. For the analysis of  $p_T$  spectra and  $R_{p\text{Pb}}$  the pilot run data was used, while the measurement of  $\langle p_T \rangle$  vs.  $N_{\text{ch}}$  (see section 5) is based on data from the main p–Pb period.

For the analysis only runs with stable detector conditions and verified QA information have been selected. In an additional survey all data and MC samples have been analyzed on run-by-run basis to identify possible problems and verify the stability of the results. Complete lists of the runs analyzed together with the corresponding simulations can be found in appendix A.

All data taking periods have corresponding Monte Carlo simulations which were used to determine the corrections. All simulations were performed using GEANT3 [152] for the simulation of the detector response and events generated without any event selection criteria (minimum

system	$\sqrt{s_{\text{NN}}}$	year	data sample	MC sample	generator	remarks
pp	0.9 TeV	2010	LHC10c, pass3	LHC10e13	PYTHIA6	
pp	2.76 TeV	2011	LHC11a, pass2	LHC11b10a	PYTHIA6	without SDD
pp	7 TeV	2010	LHC10d, pass2	LHC10f6a	PYTHIA6	
p–Pb	5.02 TeV	2012	LHC12g, pass2	LHC12g4	DPMJET	for $R_{\text{pPb}}$
p–Pb	5.02 TeV	2013	LHC13b, pass3	LHC13b2_efix_p1	DPMJET	only for $\langle p_{\text{T}} \rangle$
p–Pb	5.02 TeV	2013	LHC13c, pass2	LHC13b2_efix_p1	DPMJET	only for $\langle p_{\text{T}} \rangle$
Pb–Pb	2.76 TeV	2010	LHC10h, pass2	LHC11a10a	HIJING	

Table 3.2.: ALICE names of the analyzed pp data sets and the corresponding MC samples used for corrections.

bias). Various event generators were used for different collision systems: PYTHIA6 [153–155] and PHOJET [156] for pp, HIJING [157] and DPMJET [158] for p–Pb and Pb–Pb.

Table 3.2 shows the ALICE names of the data samples analyzed and the corresponding Monte Carlo simulations used to determine the corrections. Cross-checks and evaluation of systematic uncertainties included several additional Monte Carlo productions, as mentioned in the description of systematic uncertainties (section 3.10).

### 3.4 Trigger and event selection

Selection of events occurs during two different stages. During data taking only a fraction of all events is recorded, this selection is controlled by the *trigger* and determines the online selection of events. In addition, in the offline analysis of the data further selection criteria are applied to the recorded events leading to the offline selection. This includes a reevaluation of the trigger condition, selection of collision candidates, acceptance cuts and centrality selection.

#### 3.4.1 Trigger

It is not important that every collision is recorded, but any trigger favors events with certain characteristics and thus imposes a possible bias on the data. A bias-free trigger has to record every possible collision. In ALICE this is implemented in a bunch-crossing (BC) trigger on the coincidence of two bunches crossing the detector at the same time. In low-luminosity operation of the experiment most of these bunch crossings do not contain hadronic interactions, leading to very low rates of recorded collisions. While the BC trigger is not suitable to record large amounts of data, it is useful for studying the performance of interaction triggers.

Machine-induced background was studied with triggers on the passage of single bunches (beam-empty) or no bunches (empty-empty), each in time with the LHC clock signal.

For the data taking of ALICE interaction triggers from the SPD and VZERO detectors are used in coincidence with the bunch crossing. The trigger configuration which imposes the smallest bias by accepting most of all events is called *Minimum Bias (MB) trigger*. Not all trigger signals are caused by genuine collisions, background from the LHC beams can cause fake triggers. These events have to be excluded from the analysis.

trigger	logic	usage
MB <sub>OR</sub>	VOA    VOC    SPD	pp
V0 <sub>OR</sub>	VOA    VOC	p-Pb 2012
V0 <sub>AND</sub>	VOA && VOC	p-Pb 2013, Pb-Pb
2-out-of-3	(VOA && VOC)    (VOA && SPD)    (VOC && SPD)	Pb-Pb
3-out-of-3	(VOA && VOC && SPD)	Pb-Pb

Table 3.3.: Online triggers used in this analysis.

All data samples used in this analysis have been collected with various minimum bias triggers. Table 3.3 shows an overview of the applied online triggers. The triggers differ mainly in their sensitivity for Single Diffractive (SD) events and background (beam-induced, electromagnetic).

In pp collisions this trigger required either a hit in the SPD detector or in either one of the two VZERO detectors and is denoted MB<sub>OR</sub>.

In the Pb-Pb data taking different triggers were employed to reduce background from non-hadronic collisions. At the beginning of the Pb-Pb run a 2-out-of-3 trigger required a signal in two out of the three trigger detectors VZERO-A, VZERO-C and SPD. During the data taking the trigger was first changed to V0<sub>AND</sub> (signal in both VZERO detectors) and later to 3-out-of-3 (signal in all three trigger detectors). For the centrality interval considered here (0-80%) all these triggers are equivalent and fully efficient.

For p-Pb 2013 the trigger required a signal in both VZERO detectors (V0<sub>AND</sub>). During the pilot run 2012 data was recorded with the online (hardware) trigger V0<sub>OR</sub> (signal in either one of the two VZERO detectors), but during the offline analysis hits in both VZEROs are required changing the trigger effectively to a V0<sub>AND</sub> selection.

During the data taking of pp at  $\sqrt{s} = 2.76$  TeV two trigger schemes were used with different groups of detectors read out: fast cluster and slow cluster. Both included the TPC, SPD, and SSD detectors, but the SDD was only read out in the slow cluster. In the analysis both trigger/readout clusters were used, but all the data were reconstructed without the SDD to obtain a uniform data sample. The absence of the SDD lead to a slight (< 2% relative) reduction in tracking efficiency, but no deterioration in the  $p_T$  resolution.

### 3.4.2 Selection of collision candidates

Only events that are collision candidates are accepted for the analysis. An event is only accepted if the trigger condition is also fulfilled using the information from the offline reconstructed data.

In addition, background and pile-up events are rejected in the following way. If more than one primary vertex is reconstructed within an event, it is considered to be pile-up and excluded from the analysis. Events which are flagged as beam-gas from the offline reconstruction of the VZERO information are rejected likewise. This background rejection is based on the timing information from the VZERO detectors, which has to be compatible with an interaction in the

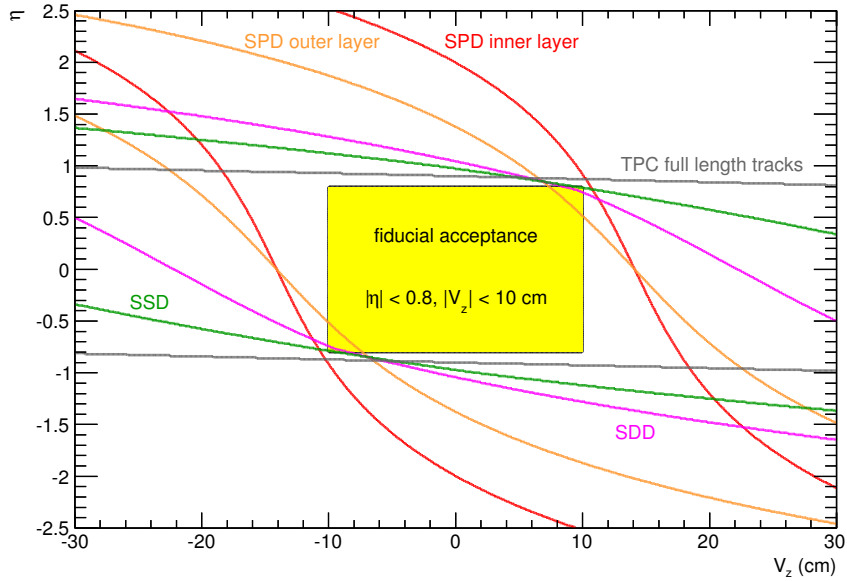


Figure 3.3.: Dependence of the detector acceptances of the SPD, SDD, SSD and TPC on the z-position of the primary vertex. For SDD and SSD the displayed acceptance is only the overlap where both individual layers are sensitive. Indicated as a yellow box is the utilized acceptance.

center of the detector. In addition the correlation between the number of clusters vs. tracklets in the SPD is used to reject background events using the fact that background events have too few tracklets for the number of clusters.

In Pb–Pb collisions the restriction of the analysis to the centrality range of 0–80% ensures that all events have a track in the acceptance and negligible contributions from beam-gas background or electromagnetic interaction.

### 3.4.3 z-Vertex selection

The  $\eta$ -acceptance of a detector depends on the z-position of the primary vertex as shown in Figure 3.3. This is simply the effect of the detector geometry, and most pronounced for the detectors at small radii (SPD), while being negligible for the TPC. An example of the distribution of reconstructed tracks in the  $(V_z, \eta)$  plane is shown in Figure 3.4.

The acceptance cut of  $\eta < 0.8$  motivates the selection of events which have a reconstructed primary vertex within  $\pm 10$  cm around the nominal interaction point (center of the detector), for full ITS acceptance. This choice of the acceptance is indicated in Figure 3.3 and contains the vast majority of reconstructed tracks as illustrated in Figure 3.4. Furthermore, the cut on z-Vertex removes unwanted collisions from satellite bunches.

For the Pb–Pb data this selection of events is also part of the centrality determination, which implies that no reliable centrality is assigned to events with vertex position outside of this window.

Distributions of the reconstructed z-vertex positions are shown in Figure 3.5 for all energies and collision systems. The fraction of events that pass the z-Vertex selection criterion is also indicated and ranges from 85–90%.

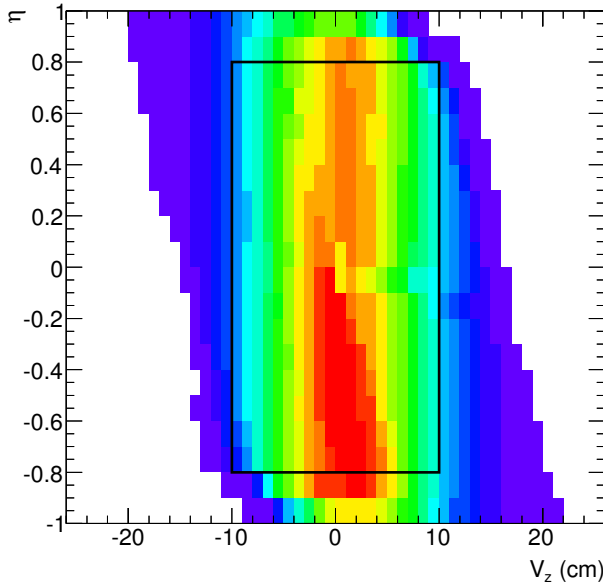


Figure 3.4.: Distribution of reconstructed tracks in the  $(V_z, \eta)$ -plane as observed in pp collisions at  $\sqrt{s} = 7$  TeV. The black rectangle shows the acceptance ( $|V_z| < 10$  cm,  $|\eta| < 0.8$ ) selected for the analysis.

The resolution of the primary vertex reconstruction was studied in Monte Carlo simulations. Figure 3.6 shows the difference observed between the generated and reconstructed primary vertex ( $\Delta V_z$ ) in pp collisions at  $\sqrt{s} = 7$  TeV for different track multiplicities  $N_{cv}$  (number of tracks contributing to the vertex reconstruction). Even for small number of tracks most vertices are reconstructed with less than 1 mm difference. The accuracy of the z-vertex reconstruction improves if a larger number of tracks contribute, and the non-Gaussian tails at large residuals are greatly reduced. The resolution of the primary vertex reconstruction  $\sigma_{V_z}$  is extracted from fits of a Gaussian function to the distribution of residuals  $\Delta V_z$  and shown in Figure 3.7 as a function of the number of contributing tracks for all pp data sets. Average values of  $N_{cv}$  and  $N_{cv}$  are also indicated in Figure 3.7. In p–Pb and Pb–Pb collisions the average multiplicities are much larger than in pp leading to an even better primary vertex resolution.

In general the efficiency of the z-Vertex reconstruction depends on the position of the primary vertex as shown in Figure 3.8 for pp collisions. Within the selected range of  $|V_z| < 10$  cm the efficiency is approximately independent of the vertex position. The dependence on the event multiplicity is shown in Figure 3.9, revealing a deficiency for low multiplicity events with 1-2 particles produced in the acceptance. This has an impact also on the  $p_T$  spectra, as discussed in section 3.10.5. For events with at least one reconstructed track in the acceptance the vertex reconstruction is fully efficient. The vertex reconstruction algorithm uses the average interaction profile measured over many events as a constraint of the primary vertex position. This allows to reconstruct the z-position of the vertex also for events that have only a single reconstructed track.

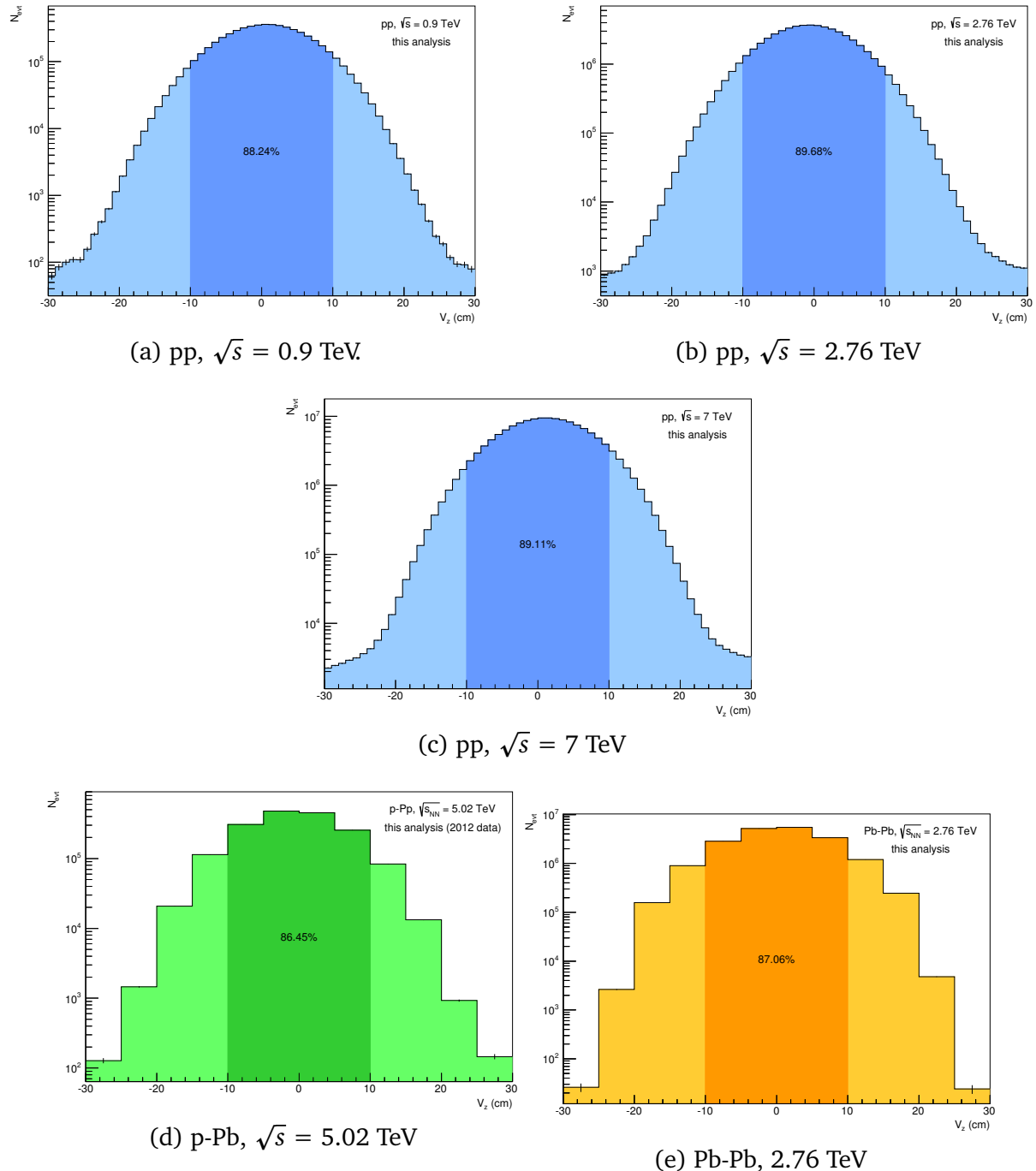


Figure 3.5.: Distribution of the z-position of the primary vertex for the data sets used in this analysis. The 10 cm range used to measure the  $p_T$  spectra is indicated as well as the fraction of events selected (out of all events that have a reconstructed vertex).

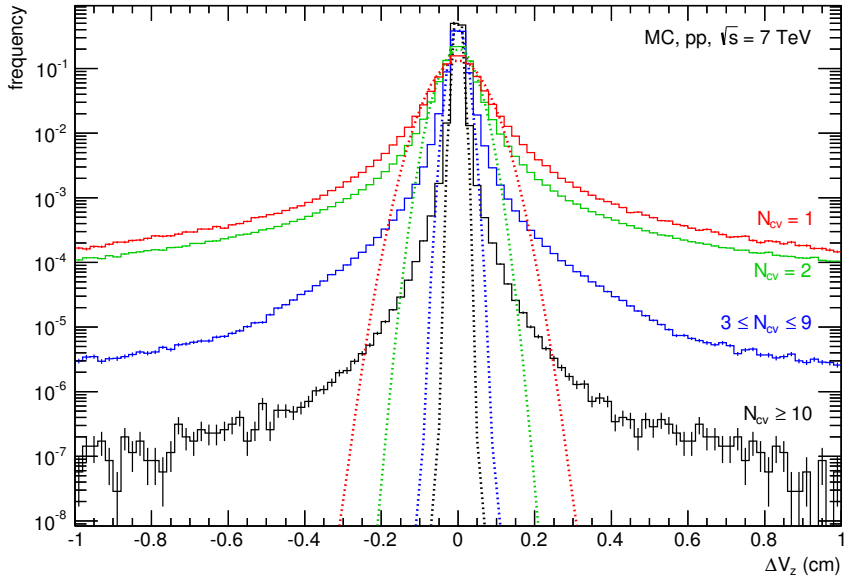


Figure 3.6.: Distribution of the difference between the generated and reconstructed vertex positions obtained for different number of tracks contributing to the reconstruction of the primary vertex obtained from Monte Carlo simulations with PYTHIA Perugia0 for pp collisions at  $\sqrt{s} = 7$  TeV together with Gaussian fits to the distribution that are used to extract  $\sigma_{Vz}$ .

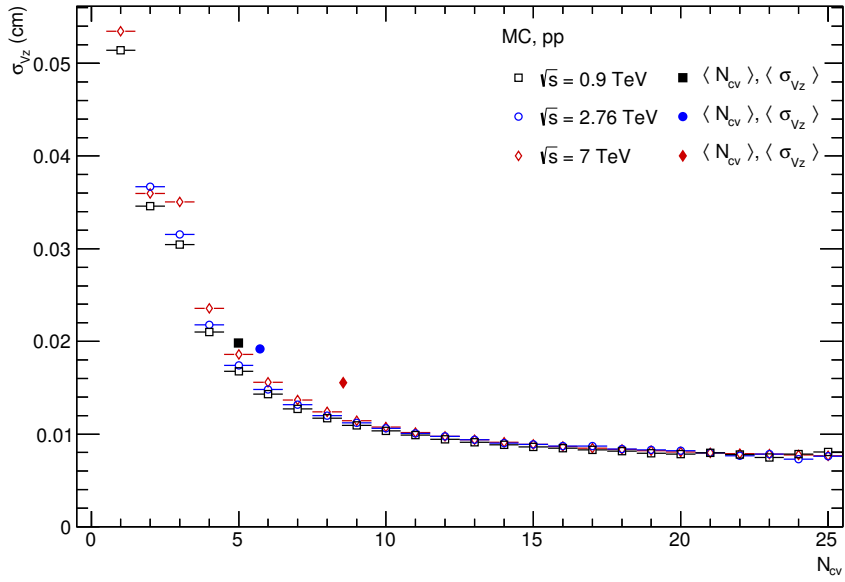


Figure 3.7.: The resolution of the z-Vertex reconstruction  $\sigma_{Vz}$  (calculated from fits of a Gaussian distribution to the residuals  $\Delta V_z$ ) for pp at all energies as a function of the number of tracks contributing to the vertex (open symbols). The average values of the number of contributers and the average resolution is also indicated (full symbols). Statistical uncertainties are smaller than the size of the symbols.

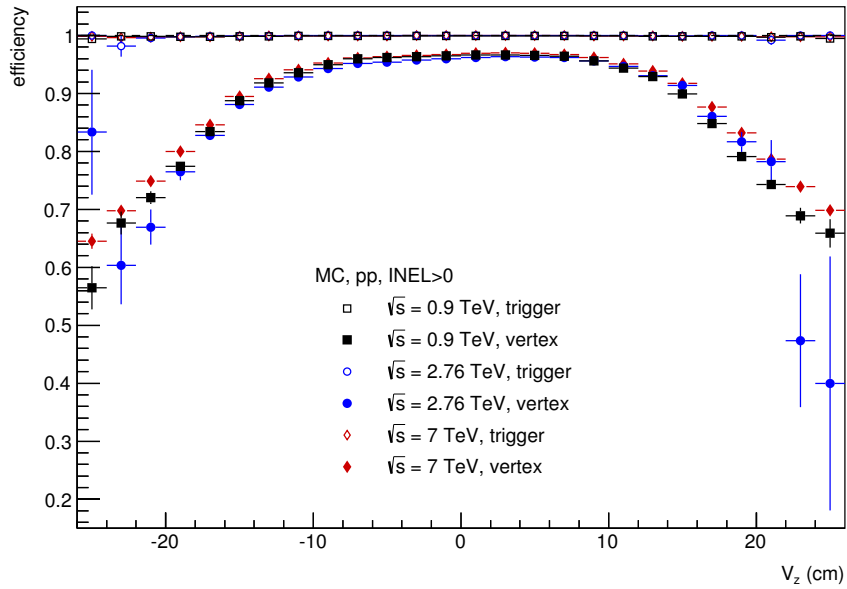


Figure 3.8.: Dependence of the trigger and primary vertex reconstruction efficiencies on the  $z$ -position of the primary vertex for events which have at least one produced charge particle in the acceptance. Values were obtained from MC simulations for pp collisions at different energies.

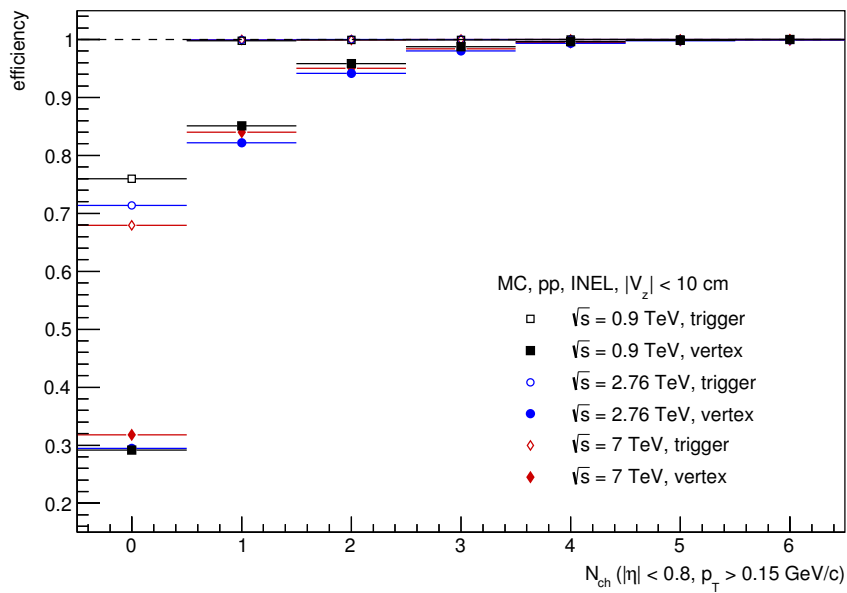


Figure 3.9.: Trigger and primary vertex reconstruction efficiencies in pp collisions as a function of the number of charged particles in the acceptance, obtained in MC simulations.

event class	event numbers after selection criteria	
	data	MC
pp, 0.9 TeV	5 051 124	4 519 879
pp, 2.76 TeV	50 068 777	2 668 398
pp, 7 TeV	117 429 412	101 238 457
p–Pb, 5.02 TeV, 2012	1 439 810	2 301 174
p–Pb 5.02 TeV, 2013	108 084 501	24 887 125
Pb–Pb, 2.76 TeV, 0-5% central	810 667	8 157
Pb–Pb, 2.76 TeV, 5-10% central	810 896	10 107
Pb–Pb, 2.76 TeV, 10-20% central	1 612 402	22 272
Pb–Pb, 2.76 TeV, 20-30% central	1 618 480	25 384
Pb–Pb, 2.76 TeV, 30-40% central	1 626 091	27 593
Pb–Pb, 2.76 TeV, 40-50% central	1 619 740	28 768
Pb–Pb, 2.76 TeV, 50-60% central	1 619 763	31 209
Pb–Pb, 2.76 TeV, 60-70% central	1 623 225	32 569
Pb–Pb, 2.76 TeV, 70-80% central	1 619 009	33 761

Table 3.4.: Event statistics in data and MC simulations used for corrections. Numbers are given for events which fulfil all event selection criteria including a reconstructed vertex.

#### 3.4.4 Centrality selection in Pb–Pb

In Pb–Pb the complete analysis was done for different centrality intervals. This includes the estimate of corrections and systematics uncertainties for each centrality. In the ALICE implementation of the centrality selection a 10 cm cut on the z-position of primary vertex is applied.

The centrality was determined from the multiplicity in the two VZERO detectors. A brief overview of the centrality determination in ALICE is included in section 2.7, a more detailed description can be found in [144].

#### 3.4.5 Summary of event statistics

Table 3.4 shows the number of events that remain after the application of all event selection criteria. These are the events which determine the statistical uncertainties of the  $p_T$  spectra. Only events with the proper trigger and a reconstructed primary vertex which are not flagged as background are included. For comparison also the number of simulated MC events used to extract the corrections is given.

For the normalization of the spectra also events without reconstructed vertex are taken into account as well as events which are not triggered.

TPC cuts		
TPC refit		required
$\chi^2$ per TPC cluster	$\chi^2_{\text{TPC}}/n_{\text{cl}}$	$\leq 4$
number of crossed rows in the TPC	$n_{\text{rows}}$	$\geq 120$ (out of 159)
ratio of crossed rows over findable clusters in the TPC	$n_{\text{rows}}/n_{\text{findable}}$	$\geq 0.8$
fraction of shared TPC clusters	$n_{\text{shared}}/n_{\text{cl}}$	$\leq 0.4$
ITS cuts		
number of hits in the ITS	$n_{\text{ITS}}$	$\geq 2$ (out of 6 or 4)
ITS refit		required
$\chi^2$ per ITS cluster	$\chi^2_{\text{ITS}}/n_{\text{ITS}}$	$\leq 36$
number of hits in the SPD	$n_{\text{SPD}}$	$\geq 1$
selection of primaries		
DCA to primary vertex in $z$	$\text{DCA}_z$	$\leq 2 \text{ cm}$
DCA to primary vertex in $x, y$	$\text{DCA}_{xy}$	$\leq 7\sigma_0$ (see text)
golden cut		
$\chi^2$ between TPC-ITS and TPC constrained track	$\chi^2_{\text{TPC-ITS}}$	$\leq 36$

Table 3.5.: Track quality cuts. The maximal number of ITS clusters is 6 (the number of ITS layers); in  $\text{pp } \sqrt{s} = 2.76 \text{ TeV}$  the data was reconstructed without SDD reducing the maximal number of ITS clusters to 4 in this data set.

### 3.5 Track selection

The tracks that are used in the analysis have to fulfill several requirements:

- best  $p_{\text{T}}$  resolution
- high tracking efficiency
- low contamination from secondaries
- few fake tracks or multiple reconstructed tracks

All these criteria aim at small corrections but are mutually exclusive. Tracks reconstructed only with the TPC have a larger efficiency compared to ITS-TPC combined tracks, but feature a worse  $p_{\text{T}}$  resolution and have a larger contamination from secondaries.

For the large transverse momenta of up to 50 GeV/c covered in this analysis the  $p_{\text{T}}$  resolution is crucial. This can only be achieved by ITS-TPC combined tracks (also called global tracks). In addition a sufficient length of the track inside the TPC is necessary. To suppress secondary particles a tight cut on the distance-of-closest approach to the primary vertex (DCA) is applied. All track cuts are listed in Table 3.5, they are identical for the analysis of pp, p–Pb and Pb–Pb collisions.

Distribution of all relevant cut variables in simulations and data are shown in Figure 3.10 as an example for pp,  $\sqrt{s} = 7 \text{ TeV}$ , corresponding figures for other energies and collision systems

can be found in appendix D. For each cut variable the distribution was obtained with all other selection criteria applied. Note that there are strong correlations between some of the cuts. The distributions shown are integrated over the kinematic range  $0.15 < p_T < 50$  GeV/c and as a consequence are dominated by low  $p_T$  tracks. To illustrate the  $p_T$  dependence of the cut variables Figure 3.11 shows the fraction of tracks that is accepted by a given cut (again with all other cuts applied) as function of the reconstructed  $p_T$ . Fractions are for pp  $\sqrt{s} = 7$  TeV and shown separately for MC simulation and data (for other data and MC sets, see appendix D). Differences between MC and data are caused by the imperfection of the simulation and result in systematic uncertainties that are assessed via track cut variations. Figure 3.12 points out these differences in the ratio of fractions of accepted tracks in MC and data for each cut (pp,  $\sqrt{s} = 7$  TeV, additional figures in appendix D). Variations of track cuts that are used to estimate systematic uncertainties are included in the figure and show the sensitivity of the cuts to these variations. Differences in the double ratio correspond to systematic uncertainties, but this correspondence is not one-to-one. In the following sections the cuts are presented in more detail.

---

### 3.5.1 TPC cuts

---

The requirements of the TPC track refit and maximal  $\chi^2$  per TPC cluster are the minimal quality criteria needed to remove tracks which are not or not properly reconstructed in the TPC.

The selection of long tracks in the TPC is achieved through the cut on the number of crossed rows in the TPC. A track is accepted if the number of crossed padrows is at least 120 out of the total number of 159 padrows. The number of crossed rows  $n_{\text{rows}}$  is calculated from the number of all clusters that are assigned to the track  $n_{\text{cl}}$ , but taking into account clusters that are missing (for example because they are sub-threshold). Padrows, on which no cluster was found, but which have found clusters within  $\pm 2$  neighboring padrows, are counted as missing.

The number of findable cluster  $n_{\text{findable}}$  is the maximal number of possible clusters calculated from the track properties taking into account the geometrical effects of dead areas at the sector boundaries and the dependence of the maximal number of clusters on the polar track angle ( $\eta$ -acceptance) [159]. Dead channels or missing FECs in the TPC are considered as findable. The cut on the ratio  $n_{\text{rows}}/n_{\text{findable}}$  has a similar effect as a cut on the number of found/findable clusters, but takes into account sub-threshold clusters.

Shared clusters  $n_{\text{shared}}$  are clusters that belong to more than one track. Large fractions of shared clusters can originate from fake tracks or multiply reconstructed tracks and are removed by the corresponding cut on the fraction of shared clusters over all clusters  $n_{\text{shared}}/n_{\text{cl}}$ . While  $n_{\text{cl}}$  includes only clusters that contribute to the track fit,  $n_{\text{shared}}$  takes all clusters that are assigned to a track into account, therefore the ratio  $n_{\text{shared}}/n_{\text{cl}}$  can be larger than unity.

---

### 3.5.2 ITS cuts

---

Selection criteria for the ITS part of the track are the ITS refit requiring hits in at least two (out of six) layers of the silicon detector. At least one of these hits has to be in the two innermost layers. These innermost layers belong to the silicon pixel detector (SPD) and have the best spatial resolution. Together with the small radial distance from the primary vertex this

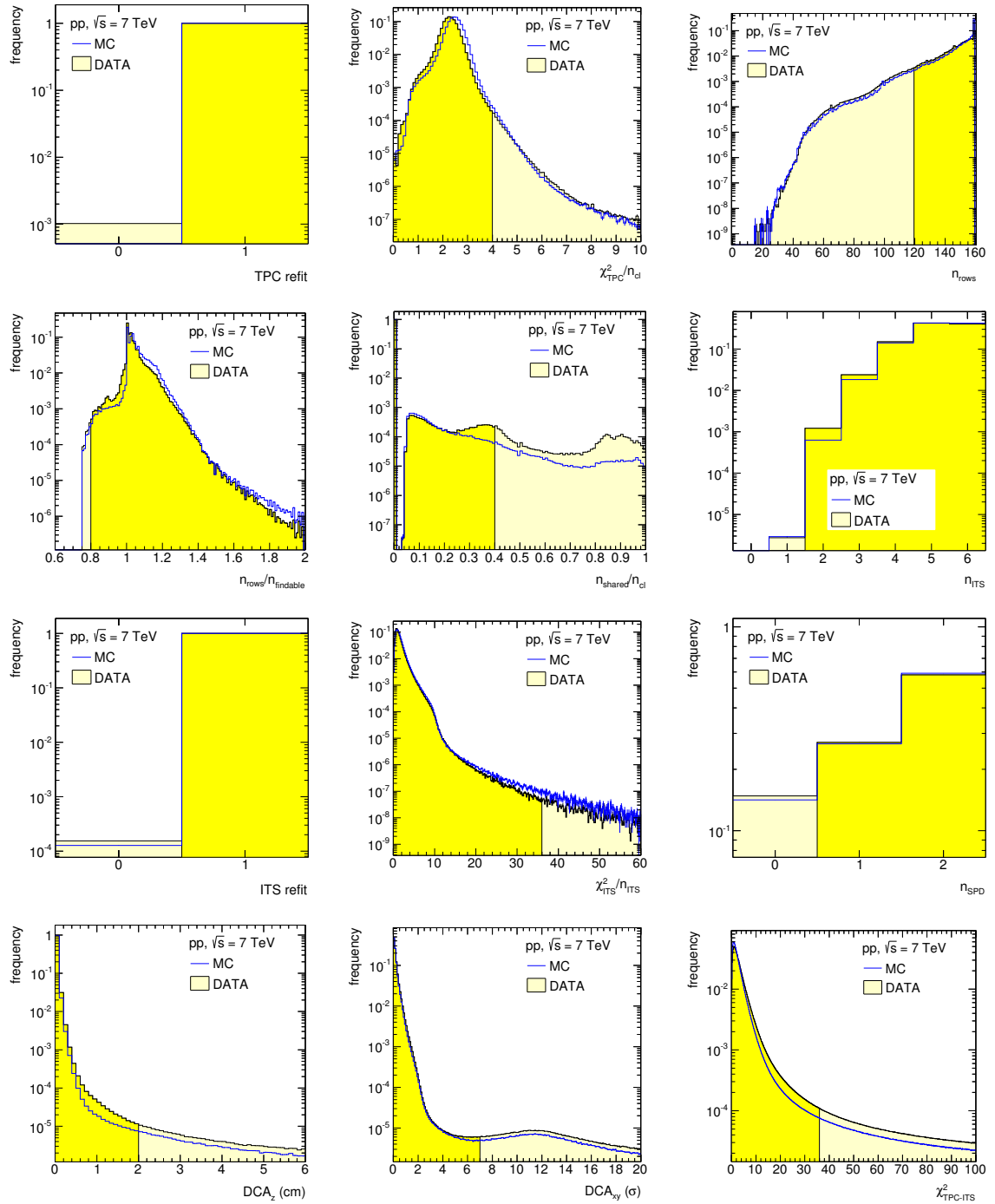


Figure 3.10.: Distributions of all track cut variables in MC simulation and data for  $pp, \sqrt{s} = 7$  TeV, integrated over the kinematic range  $0.15 < p_T < 50$  GeV/c and  $|\eta| < 0.8$ . As a consequence the distributions are dominated by tracks with low  $p_T$ . All distributions are normalized to an integral equal to unity. Note that the event numbers in MC and data are comparable in magnitude ( $\approx 10^8$  events each). For a given cut variable the distribution includes all tracks that fulfil the remaining track selection criteria. Ranges selected by the cuts are indicated in yellow.

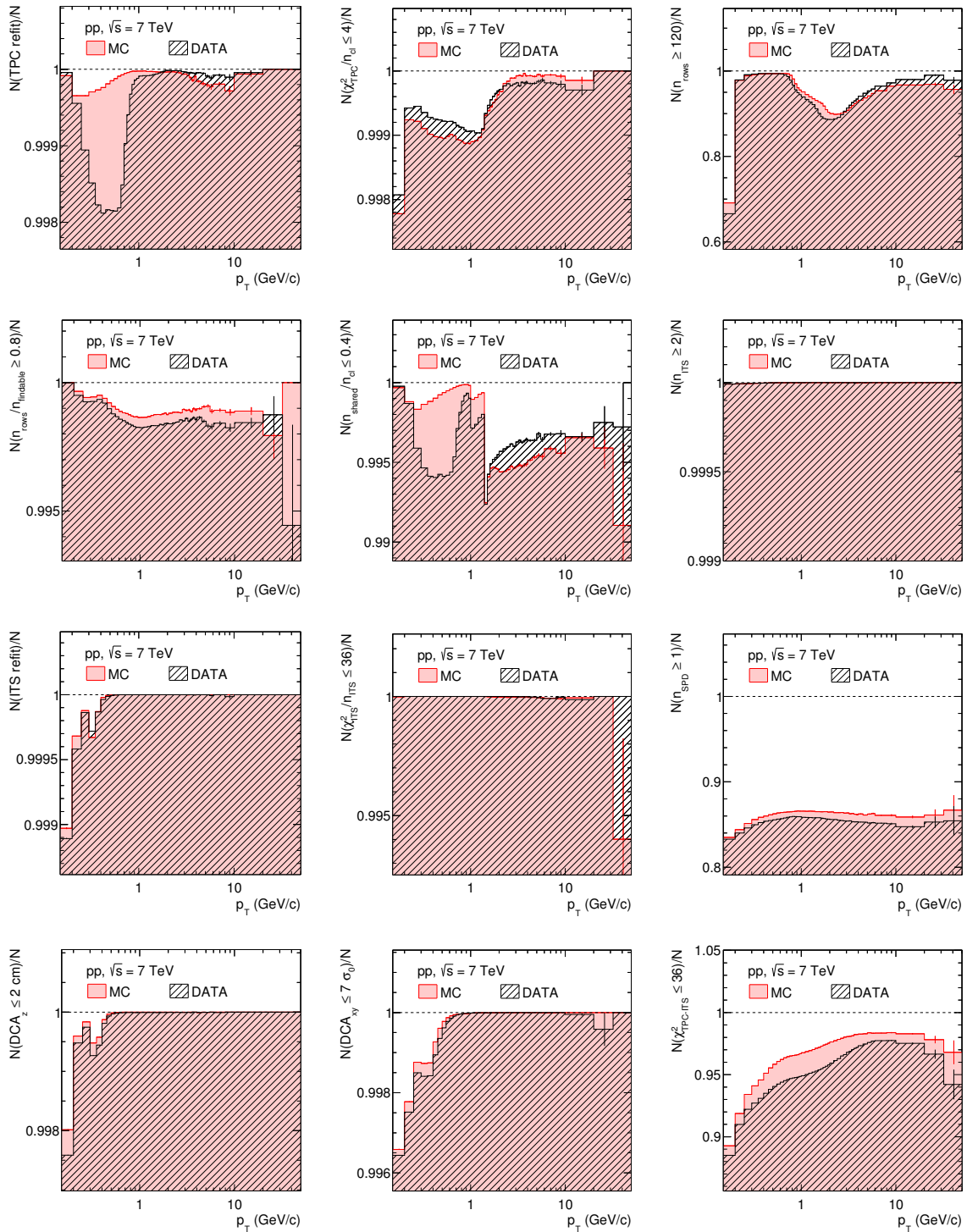


Figure 3.11.: Track cut performance in  $pp, \sqrt{s} = 7 \text{ TeV}$  data and MC simulation for all track cuts applied in the analysis. The fraction of tracks accepted by a given track cut is shown as a function of  $p_T$ , integrated over the pseudorapidity acceptance  $|\eta| < 0.8$ . For each track cut only tracks that pass all other selection criteria are considered. Note that the event numbers in MC and data are comparable in magnitude ( $\approx 10^8$  events each).

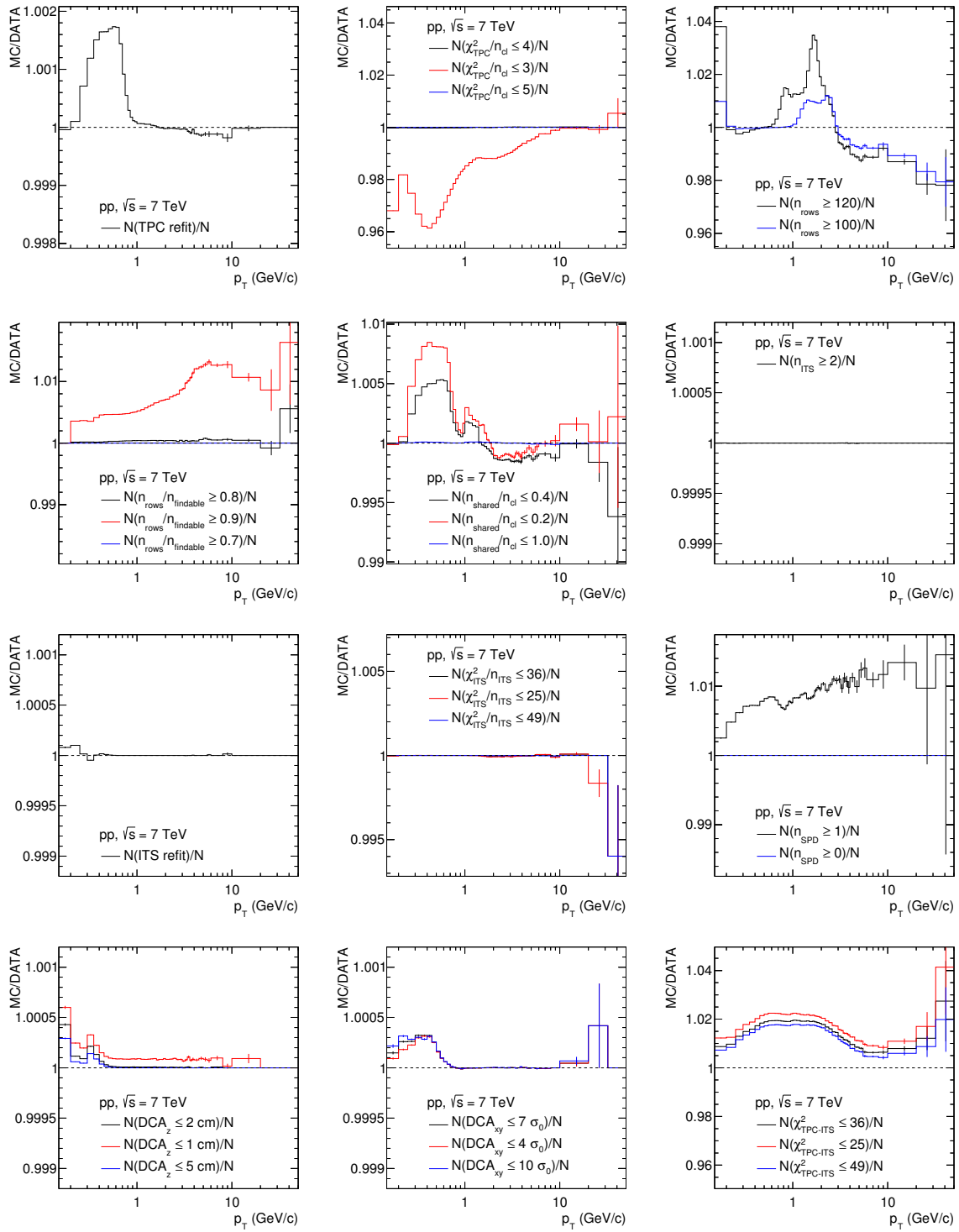


Figure 3.12.: Comparison of the fraction of tracks accepted by a given track cut in pp,  $\sqrt{s} = 7$  TeV MC simulation and data in terms of the double ratio  $(N_{\text{accepted}}/N_{\text{all}})_{\text{MC}}/(N_{\text{accepted}}/N_{\text{all}})_{\text{DATA}}$ . The black line corresponds to the nominal cut values, it is the ratio of the two histograms in Figure 3.11. In addition, alternative cuts shown as red line (more restrictive cut) and blue line (looser cut) display the sensitivity of the cut against variations. The alternative cut values are the ones used for the evaluation of systematic uncertainties.

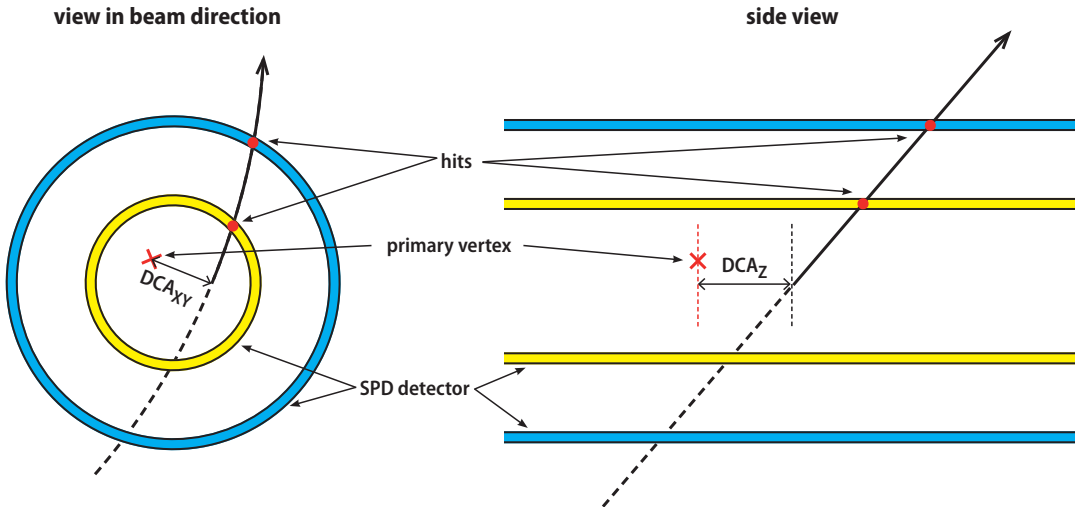


Figure 3.13.: Illustration of the transverse ( $DCA_{xy}$ ) and longitudinal ( $DCA_z$ ) impact parameters.

provides the good DCA resolution needed for the selection of primary particles. Tracks that have an exceptionally large  $\chi^2/\text{Cluster}$  in the ITS are likely to have wrong clusters assigned. As this can greatly influence the  $p_T$  resolution at large  $p_T$ , these tracks are also removed from the analysis.

### 3.5.3 Primary selection

High purity selection of primary charged particles is achieved with a  $p_T$  dependent cut on the distance of closest approach between the track and the primary vertex in the radial direction ( $DCA_{xy}$ ), corresponding to approximately seven standard deviations  $\sigma_0$  of the impact parameter resolution:

$$DCA_{xy} \leq 7 \cdot \underbrace{\left( 26 + \frac{50}{(p_T \text{ in GeV/c})^{1.01}} \right)}_{=\sigma_0} \mu\text{m} \quad (3.2)$$

In the longitudinal direction the cut on the impact parameter is  $DCA_z < 2 \text{ cm}$ . This is much less restrictive than the  $DCA_{xy}$  selection and removes tracks spiraling in the magnetic field of the detector.

With the two DCA cuts a cylinder around the reconstructed vertex is defined, with a radius depending on  $p_T$ , which tracks have to cross when they are propagated back to the interaction region. Figure 3.13 illustrates the geometry of the  $DCA_{xy}$  and  $DCA_z$ .

### 3.5.4 TPC-ITS $\chi^2$ cut

Tracks which have wrong ITS hits assigned or experienced scattering in the material between ITS and TPC can have a reconstructed momentum that is significantly different from the true one. In the case of a steeply falling  $p_T$  distribution, this can lead to an excess yield at large  $p_T$ , which is not cancelled by the  $p_T$  resolution correction.

The cut on the  $\chi^2_{\text{TPC-ITS}}$  variable removes these outliers, where  $\chi^2_{\text{TPC-ITS}}$  quantifies the difference of the track parameters between TPC-ITS and the TPC-constrained track, normalized to the covariance matrices.

The TPC-constrained track parameters are obtained from a track fit to the reconstructed TPC clusters, disregarding the ITS hits but using the reconstructed primary event vertex (track vertex if reconstructed, SPD vertex otherwise) as a constraint.

The squared distance (Mahalanobis [160] distance) is

$$\chi^2_{\text{TPC-ITS}} = \Delta \vec{v} \cdot \Sigma^{-1} \cdot \Delta \vec{v}^T \quad (3.3)$$

where  $\Delta \vec{v} = \vec{v}_{\text{TPC}_c} - \vec{v}_{\text{TPC-ITS}}$  is the difference between the five track parameters  $\vec{v} = (y, z, \sin \theta, \tan \lambda, 1/p_T)$  with TPC-constrained and TPC-ITS tracking. The combined covariance matrix is calculated treating the two tracks as uncorrelated as the sum of the individual covariance matrices  $\Sigma = \Sigma_{\text{TPC}_c} + \Sigma_{\text{TPC-ITS}}$ . The inverse of the covariance matrix is labeled  $\Sigma^{-1}$ .

The usage of the primary vertex to constrain the TPC stand-alone track is only valid for primary particles which are produced at the vertex. Tracks of secondary particles are mostly not pointing to the primary vertex yielding larger  $\chi^2_{\text{TPC-ITS}}$ . So the cut on this variable also helps to enhance the purity of primary tracks.

Tracks for which the TPC constrained fit fails or no  $\chi^2_{\text{TPC-ITS}}$  can be assigned are also excluded from the analysis.

---

### 3.5.5 Track cut performance

---

The effect of the track cuts on the tracking efficiency and contamination was studied using Monte Carlo simulations. Starting from all tracks (= no cuts) the cuts have been subsequently included one-by-one in a meaningful sequence.

The performance of the cuts in terms of the tracking efficiency for primary particles and contamination from secondaries is shown in Figure 3.14 as an example for pp collisions at  $\sqrt{s} = 7$  TeV. Corresponding figures for the the other energies and collision systems can be found in appendix E.

As some of the cuts have very little effect on the MC efficiency and contamination, and would not be distinguishable in the plots they are organized in the following groups for better visibility.

1. TPC basic cuts: TPC refit and  $\chi^2_{\text{TPC}}/n_{\text{cl}}$
2. TPC additional cuts:  $n_{\text{rows}}$ ,  $n_{\text{rows}}/n_{\text{findable}}$  and  $n_{\text{shared}}/n_{\text{cl}}$
3. selection of primaries with DCA cut corresponding to TPC resolution:  $\text{DCA}_z \leq 3 \text{ cm}$ ,  $\text{DCA}_{xy} \leq 3 \text{ cm}$
4. ITS basic cuts: ITS refit and  $\chi^2_{\text{ITS}}/n_{\text{ITS}}$
5. requirement of one hit in the SPD
6. selection of primaries with strict DCA cuts:  $\text{DCA}_z \leq 2 \text{ cm}$ ,  $\text{DCA}_{xy} \leq 7\sigma_0$  ( $p_T$  dependent)
7. outliers removal:  $\chi^2_{\text{TPC-ITS}}$

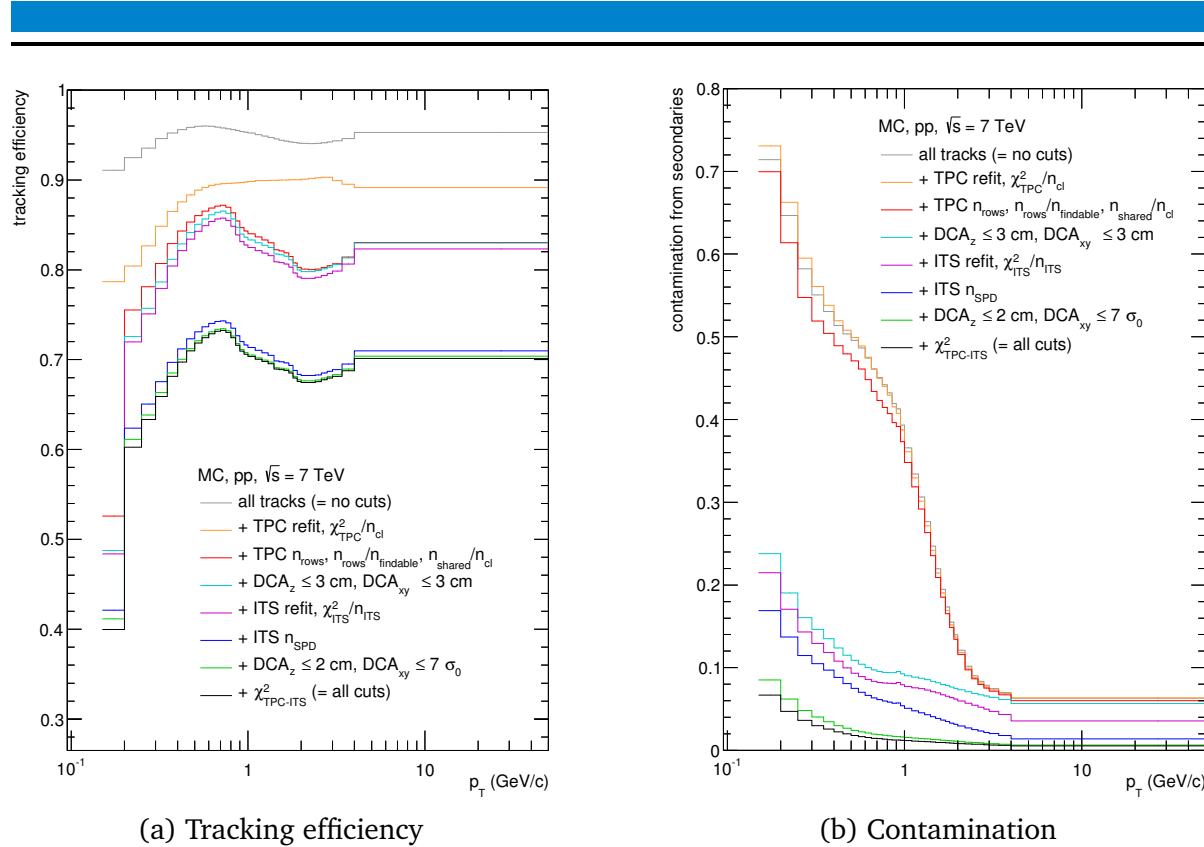


Figure 3.14.: Evolution of the tracking efficiency (a) and contamination (b) in pp collisions at  $\sqrt{s} = 7$  TeV simulated with PYTHIA and GEANT under the successive inclusion of the track selection criteria.

Two cuts have a dominant effect on the overall efficiency: the selection of long TPC tracks (120 crossed rows) and the requirement of a hit in one of the two layers of the SPD. The latter is caused by dead areas of the SPD detector, which increased with time because of damages in the cooling system and dead pixels. After a repair of the cooling system, most of the missing SPD parts could be recovered, clearly visible in the larger tracking efficiency for p–Pb in 2012. Most powerful for reducing the contamination from secondary particles are the cuts on the distance to the primary vertex (DCA), especially the tight ones possible only with ITS tracking information.

### 3.6 Corrections

From the analysis of the reconstructed data, an uncorrected (raw)  $p_T$  distribution is obtained that contains simply the number of tracks which have a reconstructed  $p_T$  in a certain interval. This distribution is obtained not only as a function of  $p_T$ , but also depending on geometric track variables like pseudorapidity  $\eta$ , polar angle  $\phi$  or event-specific variables like  $z$ -position of the reconstructed primary vertex  $V_z$  and the multiplicity (= number of all tracks in this event). In Pb–Pb collisions the centrality is used instead of the multiplicity.

The corrections for detector effects can be split into two groups:

1. effects on the single-track level, that can be  $p_T$  dependent and are relevant for the spectral shape and the normalization
2. effects on the event level relevant only for the overall normalization

system	$\sqrt{s_{\text{NN}}}$	event class	$p_{\text{T}}$ reach	efficiency	contamination	$p_{\text{T}}$ resolution correction
pp	0.9 TeV	INEL	0.15-20 GeV/c	39.5-73.2 %	0.7-6.5 %	<2.0 %
pp	2.76 TeV	INEL	0.15-32 GeV/c	36.1-67.5 %	0.9-6.9 %	<4.0 %
pp	7 TeV	INEL	0.15-50 GeV/c	39.9-73.2 %	0.8-6.7 %	<6.4 %
p-Pb	5.02 TeV	NSD, 2012	0.5-20 GeV/c	71.4-80.6 %	0.4-1.5 %	–
p-Pb	5.02 TeV	NSD, 2013	0.15-50 GeV/c	41.2-80.4 %	0.4-6.5 %	<1.9 %
Pb-Pb	2.76 TeV	0-5 %	0.15-50 GeV/c	36.9-69.3 %	0.7-13.4 %	<4.4 %
Pb-Pb	2.76 TeV	5-10 %	0.15-50 GeV/c	37.3-69.5 %	0.8-12.7 %	<4.7 %
Pb-Pb	2.76 TeV	10-20 %	0.15-50 GeV/c	37.6-69.8 %	0.8-11.8 %	<4.9 %
Pb-Pb	2.76 TeV	20-30 %	0.15-50 GeV/c	37.8-69.9 %	0.8-10.6 %	<5.0 %
Pb-Pb	2.76 TeV	30-40 %	0.15-50 GeV/c	38.0-70.1 %	0.7-9.6 %	<5.8 %
Pb-Pb	2.76 TeV	40-50 %	0.15-50 GeV/c	38.2-70.1 %	0.7-8.6 %	<5.8 %
Pb-Pb	2.76 TeV	50-60 %	0.15-50 GeV/c	38.3-70.3 %	0.9-7.8 %	<6.4 %
Pb-Pb	2.76 TeV	60-70 %	0.15-50 GeV/c	38.3-70.4 %	0.7-7.4 %	<7.1 %
Pb-Pb	2.76 TeV	70-80 %	0.15-50 GeV/c	38.2-70.6 %	0.7-7.0 %	<7.5 %

Table 3.6.: Numerical values of the corrections applied on the track level. All corrections are  $p_{\text{T}}$  dependent and correspond to the  $p_{\text{T}}$  ranges covered in the analysis which are quoted as well. Note that the smallest/largest correction do not correspond to the smallest/largest  $p_{\text{T}}$ .

In general, event effects can also influence on the spectral shape, these contributions have been separated from the pure normalization effect and taken into account in the systematic uncertainties (section 3.10.5).

### 3.7 Track-level corrections

The track level corrections taken into account are the tracking efficiency for primary tracks, the contamination of the reconstructed track sample from tracks which do not originate from primary particles and the resolution of the transverse momentum reconstruction. Table 3.6 gives an overview of the size of the track-level corrections.

#### 3.7.1 Tracking Efficiency

The correction for tracking efficiency is based on Monte Carlo information from simulated data using the full chain of Monte Carlo Event Generators (PYTHIA, HIJING, DPMJET) together with the detector simulation (based on GEANT) and the same reconstruction algorithms that are used for real data.

Within the acceptance defined by the kinematic range (usually  $0 \leq \phi < 2\pi$ ,  $|\eta| < 0.8$  and  $p_{\text{T}} > 0.15$  GeV/c) the overall efficiency accounts also for acceptance limitations. These can result from dead areas in the SPD and occur also at the edges of the TPC readout chambers. In this thesis the term *tracking efficiency* always refers to this overall efficiency.

The tracking efficiency  $\epsilon$  and corresponding multiplicative correction factor  $c_{\text{eff}}$  is obtained from simulations using all triggered events passing the event selection criteria. It depends on the kinematic variables  $p_{\text{T}}$ , pseudorapidity  $\eta$ , z-position of the primary vertex  $V_z$  and multiplicity class  $M$  and is calculated as the ratio of reconstructed primary tracks to generated primary particles:

$$\epsilon(p_{\text{T}}, \eta, V_z, M) = \frac{1}{c_{\text{eff}}(p_{\text{T}}, \eta, V_z, M)} = \frac{N_{\text{prim,rec}}^{\text{MC}}(p_{\text{T}}^{\text{MC}}, \eta^{\text{MC}}, V_z^{\text{MC}}, M)}{N_{\text{prim,gen}}^{\text{MC}}(p_{\text{T}}^{\text{MC}}, \eta^{\text{MC}}, V_z^{\text{MC}}, M)} \quad (3.4)$$

The corrections are calculated using histograms that are filled for all generated tracks (available through the particle stack) and in addition for tracks that have been reconstructed. All correction matrices are obtained using the true track parameters ( $p_{\text{T}}^{\text{MC}}, \eta^{\text{MC}}$ ) from the simulation. When the correction is applied to the data the reconstructed track parameters ( $p_{\text{T}}, \eta$ ) are used. In principal one could use the MC truth track parameters for the generated primaries and the measured parameters for the reconstructed primaries. Using this approach a combined effective correction for efficiency and resolution effects is obtained. The usage of the true track parameters, as it was done for this analysis, allows for a separate treatment of efficiency and momentum resolution effects. This is required since the  $p_{\text{T}}$  resolution is not properly modeled in the simulations and an effective correction depends also on the shape (steepness) of the spectrum, which is not well described by the MC generators used.

Multiplicity classes are defined in the same way in data and simulations. Not all of the variables in equation 3.4 need to be kept for the corrections. Even though efficiency itself is also strongly  $\phi$ -dependent, the fact that (averaged over many events) data and simulations have the same  $\phi$ -distribution of tracks (which is of course flat) allows to average over  $\phi$ . The same can be done for all variables whose distributions are either well described in simulations or for which the efficiency is constant. This is the case for the dependence of the efficiency on  $V_z$  where the simulations take the measured  $V_z$ -distribution as an input.

For pp and p–Pb no dependence of the efficiency on multiplicity was observed and an efficiency averaged over all  $M$ , and depending only on  $p_{\text{T}}$  and  $\eta$  has been used. For Pb–Pb efficiency corrections were evaluated in centrality intervals, which are chosen to have similar track multiplicities as the corresponding intervals in data.

As mentioned before the tracking efficiency depends also on the particle type under consideration. Figure 3.15 shows the  $p_{\text{T}}$  dependence of the tracking efficiency for different particles exemplary for pp with  $\sqrt{s} = 7$  TeV. PYTHIA6 and PHOJET have been used as event generators. Different low momentum cut-offs (increasing with particle mass) for pion, kaons and protons are visible, while at large momenta the efficiency is universal. The different  $p_{\text{T}}$  dependence of the kaon efficiency is a consequence of the decay probability (see also Figure 3.2). For the most frequently produces particles ( $\pi, K, p$ ) the simulated efficiencies do not depend on the employed event generator. For electrons, muons and strange baryons, labeled “other” in the plot, the difference between the generators is the result of varying relative production yields of these particles.

The overall efficiency for primary charged particles is the weighted average of the individual particle-type efficiencies weighted with their abundances. Except for the lower  $p_{\text{T}}$  bin, where it

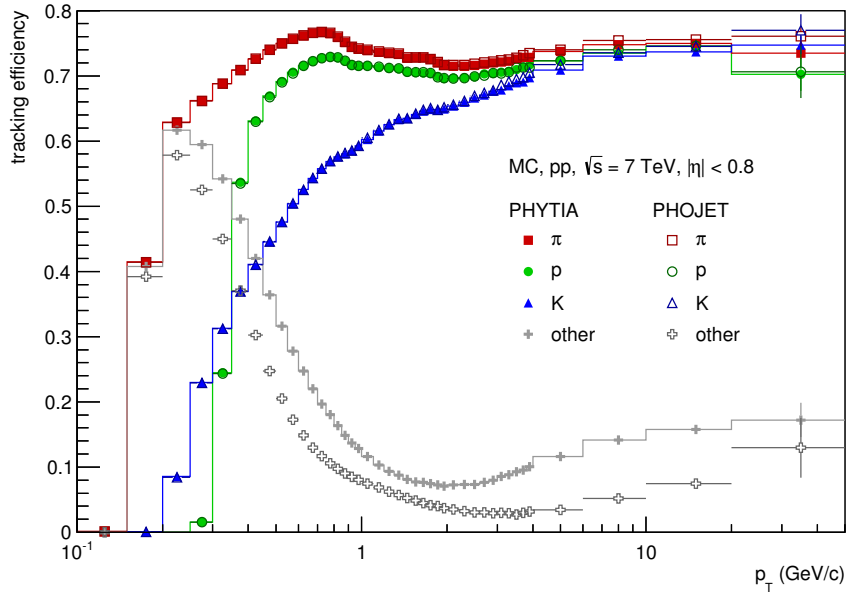


Figure 3.15.: Tracking efficiency for different primary charged particle species obtained from simulations of pp collisions at  $\sqrt{s} = 7$  TeV.

reaches only  $\approx 40\%$ , the tracking efficiency is generally in the range 55 – 80% for all energies and collisions systems.

The  $p_T$ -dependence of the tracking efficiency is shown in Figure 3.16 for pp collisions at the three energies. Efficiencies at 0.9 TeV and 7 TeV (2010 data) are very similar, while it is strikingly smaller for 2.76 TeV (2011 data). This is a result of the increased dead area of the SPD detector after the first heavy ion run. As the statistics available in the minimum bias simulations is limited at high  $p_T$  and no strong  $p_T$  dependence of the efficiency is seen above 4 GeV/c, a constant efficiency is assumed for  $p_T > 4$  GeV/c.

The centrality and  $p_T$  dependence of the overall tracking efficiency in Pb-Pb collisions is shown in Figure 3.17, there are only minor differences the different centrality classes. Figure 3.18 shows the ratio of the tracking efficiency in a given centrality interval to the average (minimum bias) efficiency. Efficiency variations for the different centralities are within  $\pm 2\%$  and exhibit only a marginal  $p_T$  dependence.

Similarly, Figure 3.19 visualizes the efficiencies obtained for p-Pb collisions in the different pseudorapidity intervals using the MC samples corresponding to the 2012 data. They are significantly larger as in the preceding pp and Pb-Pb data thanks to the increased active area of the SPD after a repair of the cooling system performed in the winter shutdown beginning of 2012.

For the study of the multiplicity dependence of the average transverse momentum (see section 5), which used the p-Pb data collected in 2013, the tracking efficiency was estimated based on the measured fractions of pions, protons and kaon [161]. The tracking efficiencies

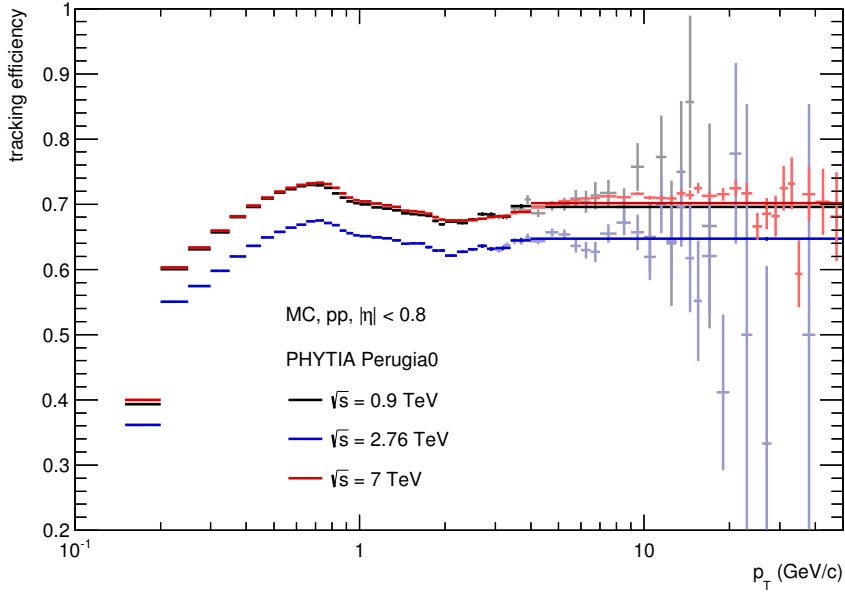


Figure 3.16.:  $p_T$  dependence of the tracking efficiency for primary particles as obtained from simulations of pp collisions at the various energies. The assigned averaged efficiencies for  $p_T > 4$  GeV/c that are used for the corrections are overlayed with the ones higher granularity  $p_T$  bins as used for the spectra.

for single particles are still based on simulations, but the measurement has been incorporated using a re-weighting procedure for the tracking efficiency:

$$\varepsilon_{\text{ch}}(p_T) = \varepsilon_{\text{other}}^{\text{MC}}(p_T) \cdot \frac{n_{\text{other}}^{\text{MC}}(p_T)}{n_{\text{all}}^{\text{MC}}(p_T)} + \frac{n_{\pi+\text{K}+\text{p}}^{\text{MC}}}{n_{\text{all}}^{\text{MC}}} \sum_{i=\pi, \text{K}, \text{p}} \varepsilon_i^{\text{MC}}(p_T) \cdot \frac{n_i^{\text{measured}}(p_T)}{n_{\pi+\text{K}+\text{p}}^{\text{measured}}(p_T)} \quad (3.5)$$

Here  $\varepsilon$  denotes the efficiency, that is always obtained from simulations, and the particle abundances are denoted by  $n$ . The sum (for the efficiency the weighted average) of primary particles that are not pion, kaons or proton are labeled *other*. The efficiencies in Equation (3.5) are only functions of  $p_T$ . For the dependence on  $\eta$  the shape obtained from MC simulations is used.

The measurement of identified particles [161] reports  $d^2N/(dydp_T)$  for the rapidity range  $0 < y < 0.5$ . For the use in Equation (3.5) the measured  $d^2N/(dydp_T)$  was fitted by a blast-wave [75] inspired function and converted to  $d^2N/(d\eta dp_T)$ . The effect of the difference in the acceptance ( $0 < y < 0.5$  vs.  $|\eta_{\text{cms}}| < 0.3$ ) has been neglected and the particle ratios were assumed to be equal in these two kinematic ranges. Outside the  $p_T$  range covered by the measurement, the particle fractions are assumed to remain constant. The relative difference between the pure MC efficiency and the re-weighted one turned out to be up to 2% at low  $p_T$  and drops below 0.5% for  $p_T > 3$  GeV/c.

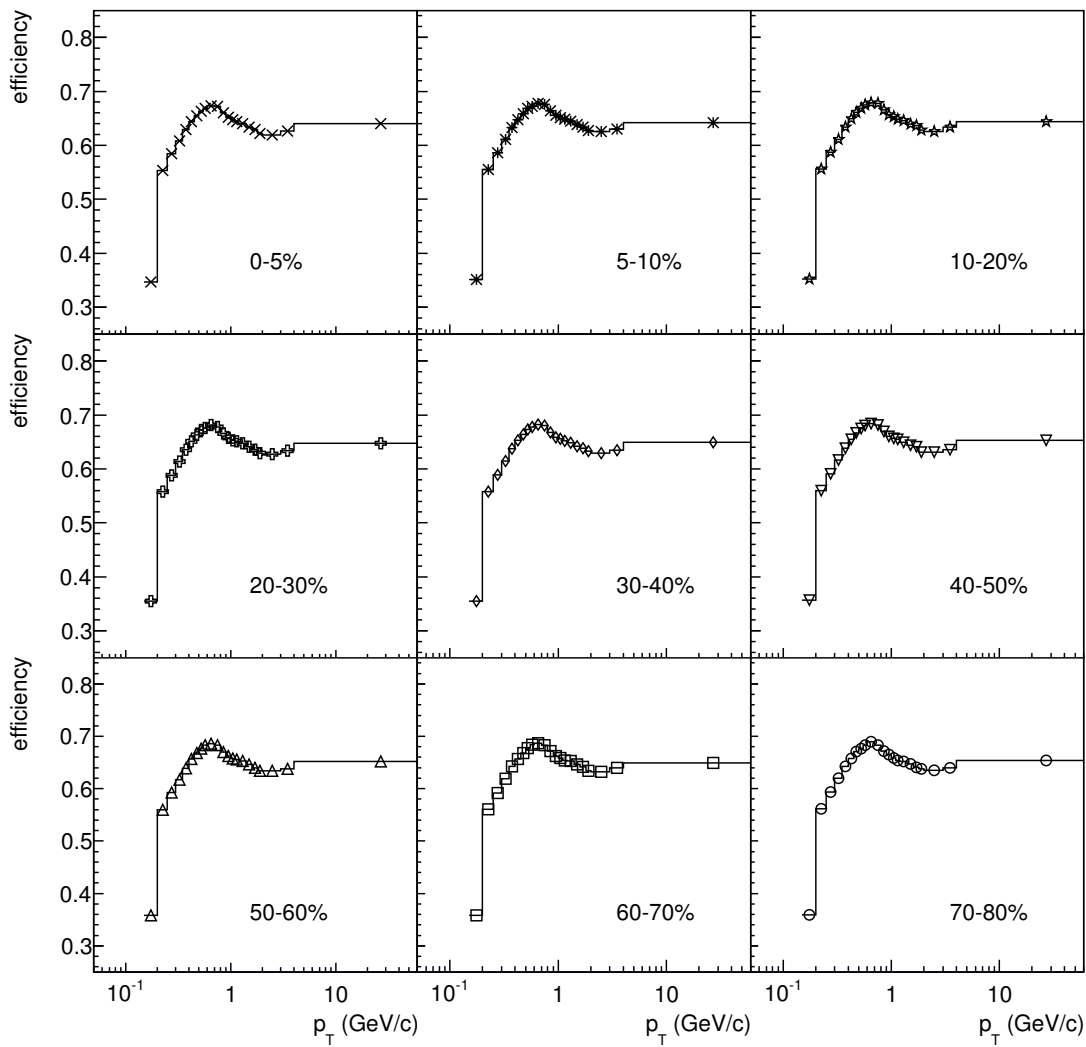


Figure 3.17.: Tracking efficiencies for primary charged particles in Pb–Pb collisions obtained from simulations with HIJING and GEANT3 for different centrality classes.

### 3.7.2 Contamination

#### Definition of secondary particles

Secondary particles are all particles that are reconstructed in the detector but not included in the definition of primary particles. This limits the definition of secondaries to charged particles. They can be subdivided by their production mechanism into two groups: 1) decay products and 2) interaction with the detector material.

Decay products are particles produced by the decay of primary particles, which can be charged (for example muons from  $\pi^+ \rightarrow \mu^+ \bar{\nu}_\mu$ ) or neutral (like  $K_S^0 \rightarrow \pi^+ \pi^-$ ). Particles originating from decays of secondaries are also secondaries, for example electrons from the decay of neutral pions, which are produced in the decay of kaons. ( $K_S^0 \rightarrow \pi^0 \pi^0$ ;  $\pi^0 \rightarrow e^+ e^- \gamma$ ).

In the interaction with the detector material, additional secondaries can be produced via electromagnetic or hadronic processes. Electromagnetic process include electrons from pair production ( $\gamma + \gamma^* \rightarrow e^+ e^-$ ), Compton scattering and production of delta rays. The domi-

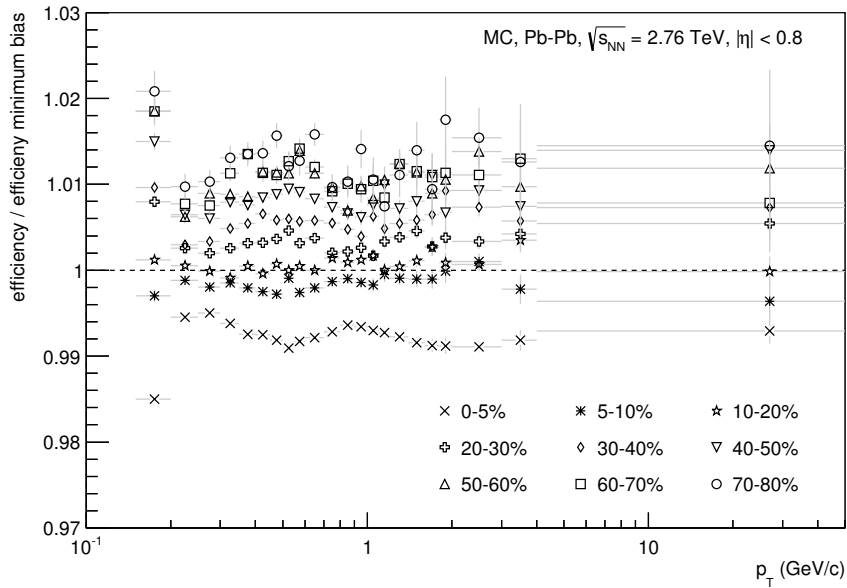


Figure 3.18.: Ratios of the tracking efficiencies for primary charged particles in different centrality intervals to the average (0-100%) efficiency obtained from simulations with HIJING and GEANT3.

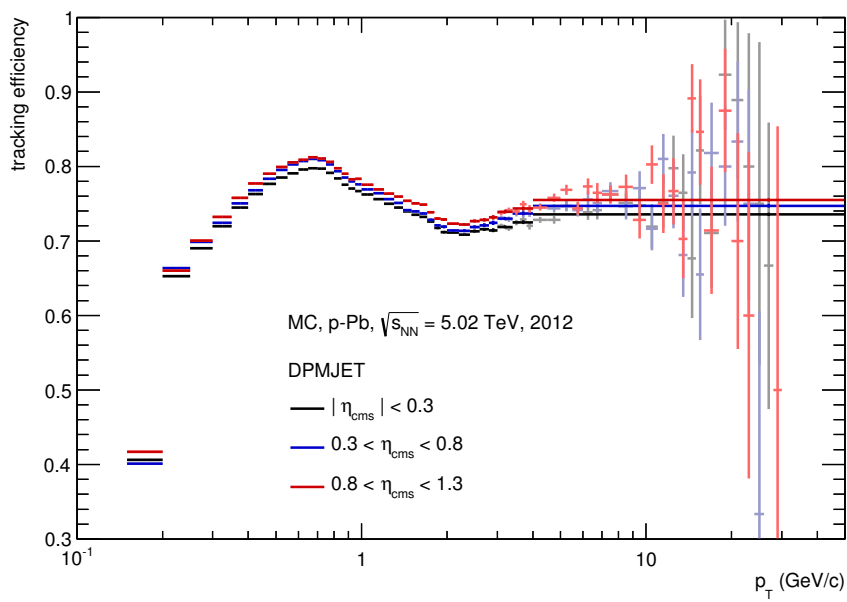


Figure 3.19.: Primary particle reconstruction efficiency in p-Pb collisions obtained from simulations with DPMJET for different pseudorapidity ranges as a function of  $p_T$ . The assigned averaged efficiencies of  $p_T > 4$  GeV/c are overlayed with the ones in finer  $p_T$  bins as used for the spectra.

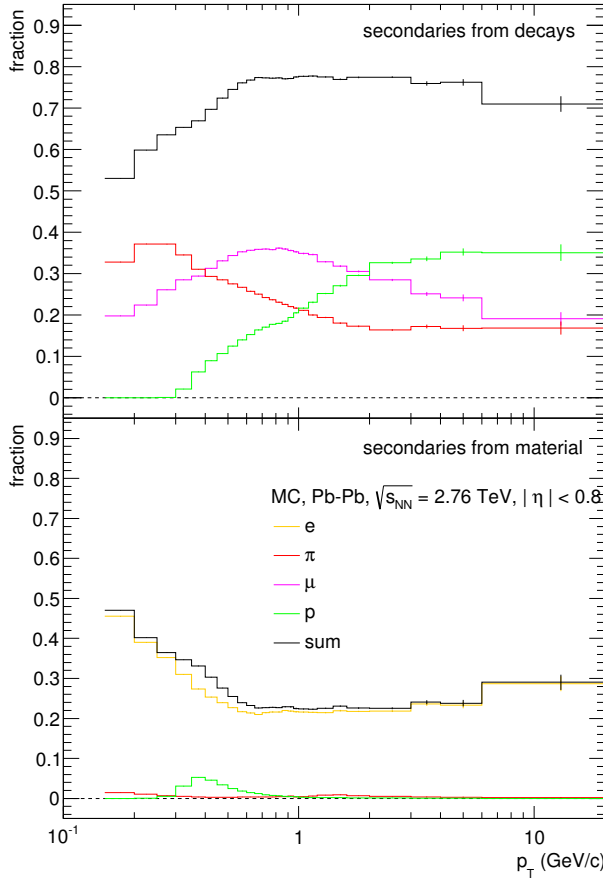


Figure 3.20.: Composition of secondary particles originating from particle decays (top panel) and interaction with the material (bottom panel) in minimum bias Pb–Pb collisions simulated with HIJING.

nant source of secondaries from material are electrons from pair production of photons from  $\pi^0 \rightarrow \gamma\gamma$  decays.

Figure 3.20 shows the fractions and composition of secondaries originating from decays (top panel) and material (bottom panel). As an example the case of simulated Pb–Pb collisions without centrality selection is taken. Secondary creation in the detector material is by far dominated by electrons, most of them created from conversion of photons from  $\pi^0$  decays. Knock-out protons from the material are only a small fraction, other contributions are negligible. Most of the secondaries (50–75%, depending on  $p_T$ ) are the result of weak decays of pions, kaons, and strange baryons.

### Correction for secondary particles

The secondary contamination  $\zeta$  is the fraction of reconstructed secondary particles  $N_{\text{sec,rec}}$  in the sample of all reconstructed particles  $N_{\text{prim,rec}} + N_{\text{sec,rec}}$  (primary and secondary):

$$\zeta = \frac{N_{\text{sec,rec}}}{N_{\text{prim,rec}} + N_{\text{sec,rec}}} \quad (3.6)$$

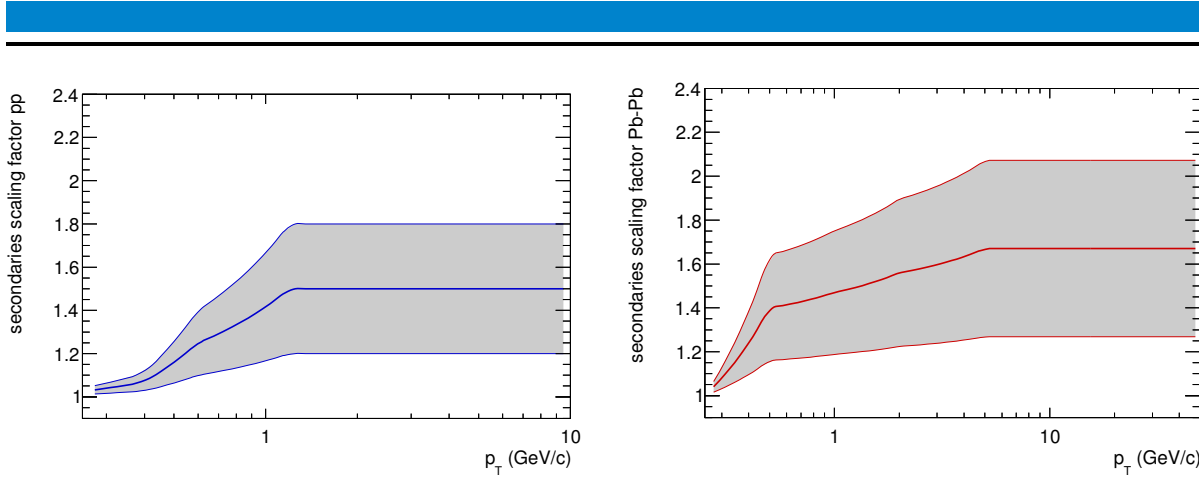


Figure 3.21.: Scaling factors for secondaries, applied in pp (left) and Pb–Pb (right) collisions. The gray band indicates the variation of the scaling factors for the evaluation of systematic uncertainties.

A sizeable fraction of the weak decays originate from the decay of neutral strange particles such as  $K^0$  or  $\Lambda$ . The yield of these strange particles is known to be underestimated in the event generators that were used to extract the corrections. To account for this the number of secondaries from MC has been scaled up by scaling factor derived from fits to the DCA distributions. These correction factors are shown in Figure 3.21. They depend only on  $p_T$  and are different for pp and Pb–Pb collisions. At the time the analysis was performed no measurements of strangeness production in p–Pb were known and no such correction was applied, but for the expected difference an appropriate systematic uncertainty was assigned.

The secondary contamination obtained from MC simulations was scaled up by  $s$ , leading to

$$\zeta(p_T, \eta, M) = 1 - c_{\text{sec}}(p_T, \eta, M) = \frac{s(p_T^{\text{MC}}) \cdot N_{\text{sec,rec}}^{\text{MC}}(p_T^{\text{MC}}, \eta^{\text{MC}}, M)}{N_{\text{prim,rec}}^{\text{MC}}(p_T^{\text{MC}}, \eta^{\text{MC}}, M) + s(p_T^{\text{MC}}) \cdot N_{\text{sec,rec}}^{\text{MC}}(p_T^{\text{MC}}, \eta^{\text{MC}}, M)} \quad (3.7)$$

Here, the superscript MC denotes Monte Carlo truth quantities. In the analysis the correction is applied as a correction factor  $c_{\text{sec}}$  equal to the fraction of primary particles in the overall sample (primary and secondary). It is also known as the *purity*.

As in the case of the tracking efficiency, the contamination is obtained from simulations in terms of the MC true variables  $p_T^{\text{MC}}$  and  $\eta^{\text{MC}}$ . When it is applied to the data, the corresponding reconstructed values of  $p_T$  and  $\eta$  are used.

The resulting contamination is of the order of 10% for the lowest  $p_T$  and quickly decreases below 1% for  $p_T$  above 2 GeV/c. The decrease towards larger transverse momenta is primarily a consequence of the steeply falling spectra and the decay kinematics (the energy is split between the daughter particles). In addition, the better impact parameter resolution for high  $p_T$  tracks leads to an improved selection of primary particles.

The overall contamination is shown in Figure 3.22 for pp collisions and in Figure 3.23 for p–Pb. The centrality and  $p_T$  dependence of the contamination for Pb–Pb collisions is shown

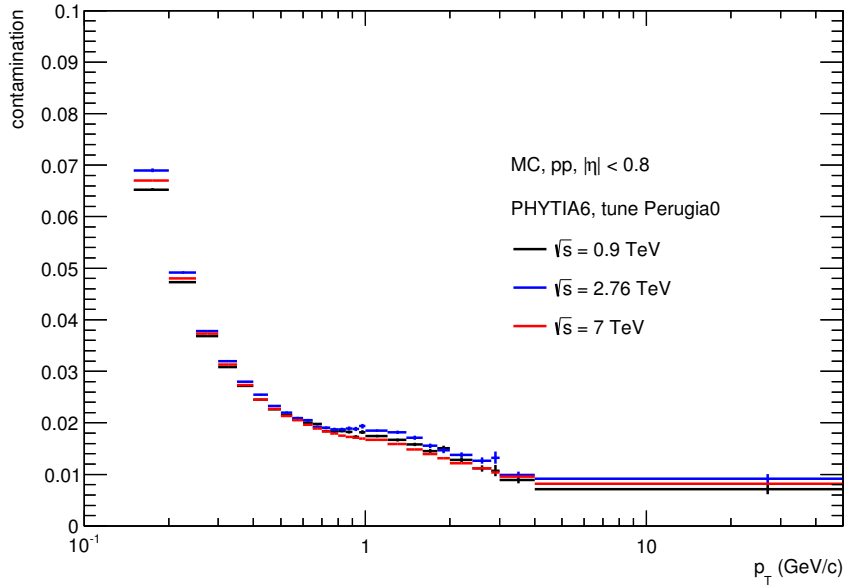


Figure 3.22.: Contamination of secondary tracks in pp collisions at the different energies from MC simulations with PYTHIA.

in Figure 3.24. One can note from the ratio in Figure 3.25 the contamination is significantly higher in more central collisions.

### 3.7.3 Fake tracks

Fake tracks (tracks which do not belong to a particle) and multiply reconstructed tracks are efficiently suppressed with the applied track cuts, especially the cut on the fraction of shared clusters in the TPC (see section 3.5.1). Figure 3.26 shows the fraction of multiply reconstructed tracks in simulated Pb–Pb collisions. The dependence on  $\eta$  reveals that almost all of these tracks are located around the central electrode. Overall the fraction of fake tracks is  $< 10^{-4}$  even for the most central collisions and no correction is required for these effects. In pp and p–Pb collisions the fraction of multiply reconstructed tracks is even smaller.

### 3.7.4 Transverse momentum resolution

For the measurement of  $p_T$  distributions up to very large momenta, a good transverse momentum resolution is a crucial part of the analysis. It is also indispensable that one knows the  $p_T$  resolution to be able to correct for the effect of a finite resolution. In the reconstruction procedure the Kalman filter is used to fit single hits in the TPC and ITS with tracks resulting in track parameters and error estimates (covariance matrix) for those parameters. The inverse of the transverse momentum  $1/p_T$  is one of this parameters and directly related to the track curvature. From the covariance  $\text{Cov}(1/p_T, 1/p_T)$  the relative  $p_T$  resolution is obtained as:

$$\frac{\sigma(p_T)}{p_T} \approx p_T \cdot \sigma(1/p_T) = p_T \cdot \sqrt{\text{Cov}(1/p_T, 1/p_T)}. \quad (3.8)$$

Figure 3.27 shows the relative  $p_T$  resolution as function of  $p_T$  for all data sets analyzed in this thesis (pp, p–Pb, Pb–Pb). For small momenta ( $p_T < 1$  GeV/c) the resolution is dominated

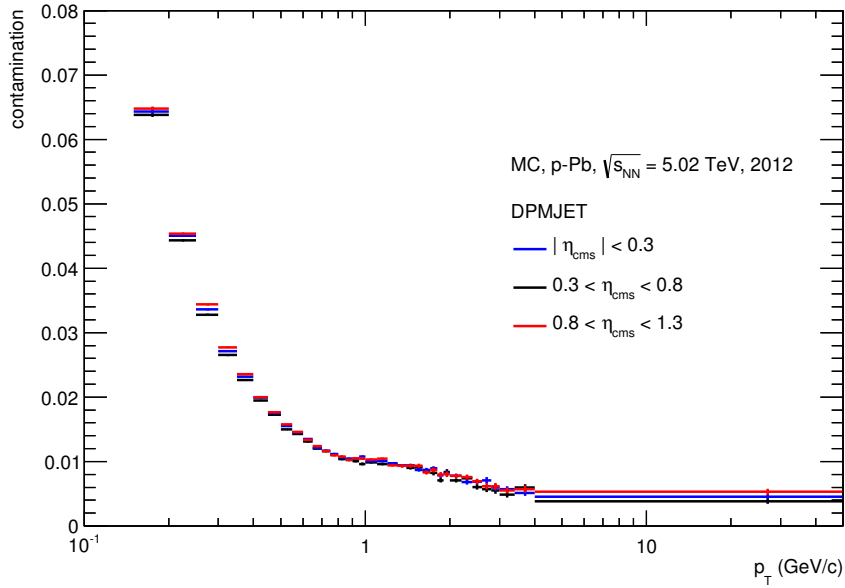


Figure 3.23.: Contamination from secondary particles in p–Pb collisions from simulations with DPMJET for different pseudorapidity ranges.

by multiple scattering and, as expected, no significant differences between the data sets are observed. In the scattering-dominated regime the resolution improves with increasing  $p_T$  to an optimum of  $\sigma(p_T)/p_T \approx 1\%$  around  $p_T = 1$  GeV/c. Towards larger momenta the resolution degrades and becomes limited by the spatial resolution of the measured track points. In the pp and Pb–Pb data sets the resolution at large  $p_T$  is comparable, with now dependence on the collision centrality. In the 2012 and 2013 data sets (p–Pb collisions) improvements in the reconstruction and calibration have lead to an improved resolution. At the highest momenta ( $p_T = 50$  GeV/c) the relative resolution is  $\sigma(p_T)/p_T \approx 10\%$  (2010), respectively  $\sigma(p_T)/p_T \approx 4\%$  (2013).

The resolution estimates from the covariance matrix of the tracks fits have been verified from the observed width of the neutral kaon decay  $K^0 \rightarrow \pi^+\pi^-$ , which are in agreement with the expectations from the covariance of the track fit<sup>3</sup>. For tracks reconstructed only with the TPC the resolution is verified also from the  $p_T$ -residuals of measured cosmic tracks that are independently reconstructed in the upper/lower half of the TPC.

The measured  $p_T$  distribution is a convolution of the true distribution with the transverse momentum resolution of the detector. The momentum resolution response function  $R(p_T)$  describes how detector and tracking algorithm affects the momentum resolution.

$$\left( \frac{dN}{d\eta dp_T} \right)_{\text{measured}}(p_T) = \left( \left( \frac{dN}{d\eta dp_T} \right)_{\text{true}} * R \right)(p_T) \quad (3.9)$$

For this analysis the momentum resolution function has been assumed to be a Gaussian in  $1/p_T$ , with no  $p_T$  shift and a width that depends on  $p_T$ . The unfolding procedure which was used to obtain back the true distribution is based on the observation that the transverse

<sup>3</sup> Described in the ALICE analysis notes [145, 146, 162].

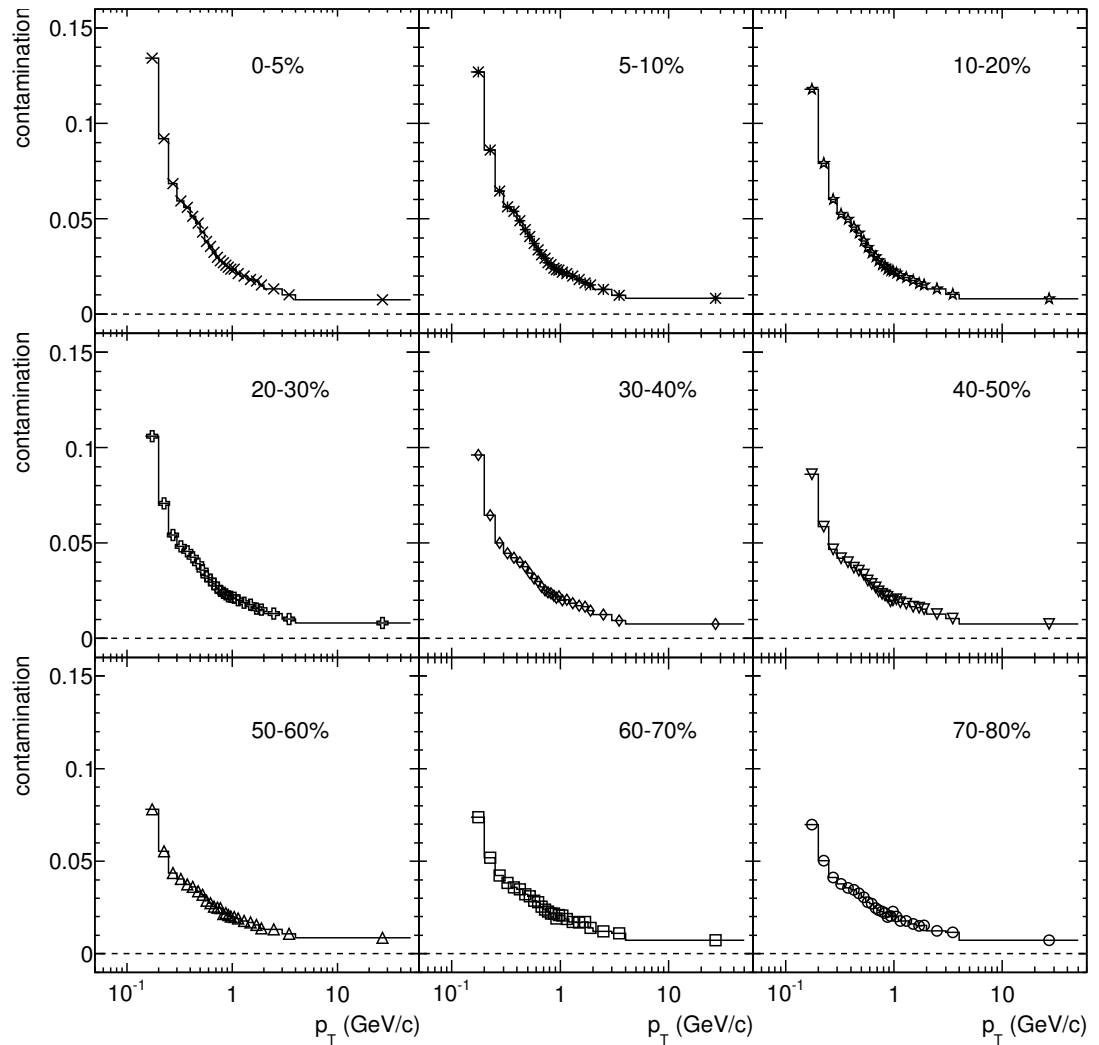


Figure 3.24.:  $p_T$  dependence of the contamination from secondaries in the reconstructed track sample in Pb–Pb collisions obtained from simulations using HIJING and GEANT3 for all centrality classes.

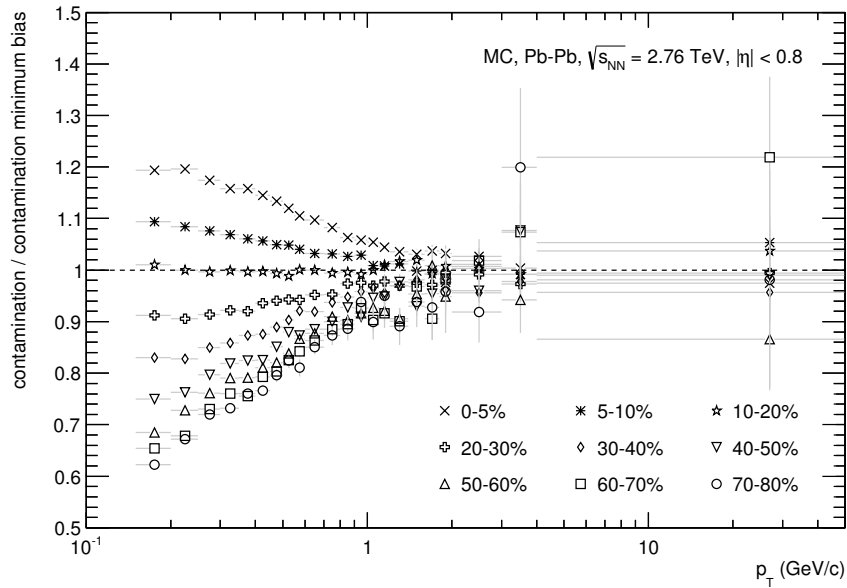


Figure 3.25.: Ratios of the contamination in different centrality intervals to the average (0-100%) contamination obtained from simulations with HIJING and GEANT3.

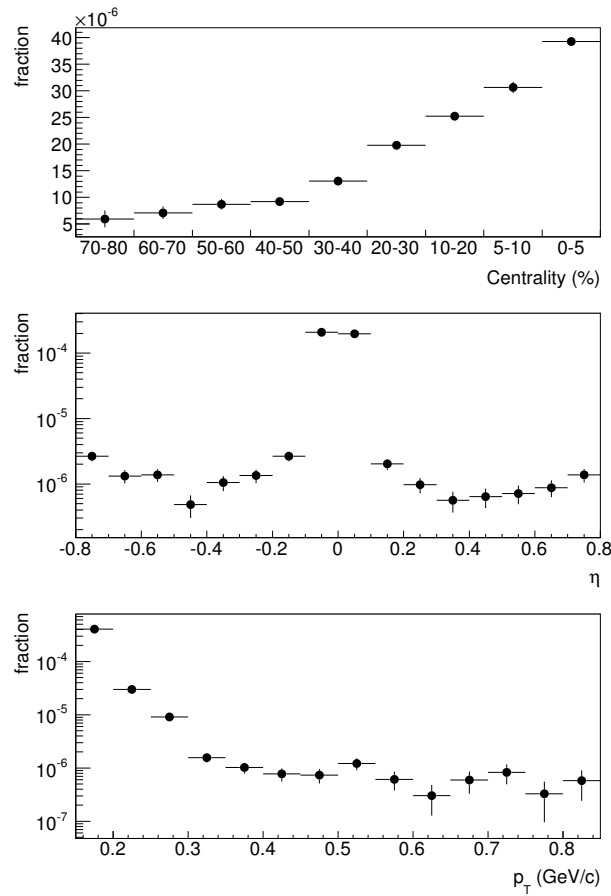


Figure 3.26.: Centrality (top), pseudorapidity (middle) and  $p_T$  (bottom) dependence of the fraction of tracks which are wrongly found multiple times in the reconstruction of simulated Pb–Pb collisions.

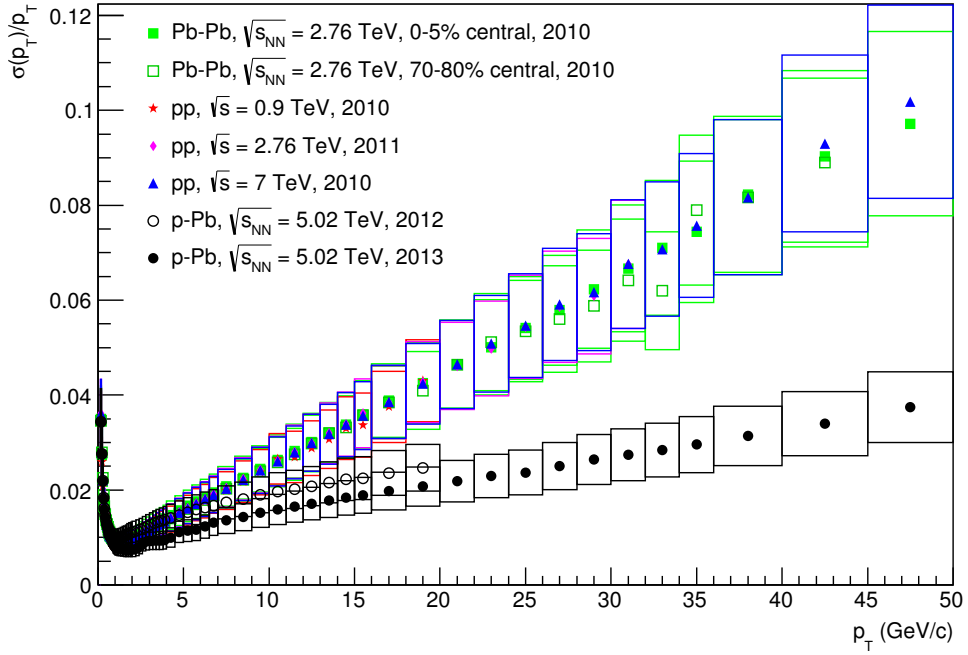


Figure 3.27.: Relative transverse momentum resolution  $\sigma(p_T)/p_T$  as function of  $p_T$  for pp, p–Pb and Pb–Pb collisions.

momentum smearing has only a small effect on the spectrum. This justifies the assumption that the ratio of the true  $p_T$  distribution to the measured one (which is the true spectrum folded with the resolution) is the same as the ratio of the measured  $p_T$  distribution to the measured one folded explicitly with the resolution. This allows to determine a correction factor based only on the measured information to be applied on the spectrum:

$$c_{\text{resolution}}(p_T) \equiv \frac{\left(\frac{dN}{d\eta dp_T}\right)_{\text{measured}}(p_T)}{\left(\left(\frac{dN}{d\eta dp_T}\right)_{\text{measured}} * R\right)(p_T)} \approx \frac{\left(\frac{dN}{d\eta dp_T}\right)_{\text{true}}(p_T)}{\left(\frac{dN}{d\eta dp_T}\right)_{\text{measured}}(p_T)} \quad (3.10)$$

While this procedure is not a genuine unfolding and, in general might not be applicable in all cases, it has the advantage of leaving the statistical uncertainties of each bin unaffected. Other unfolding procedures generally replace the statistical uncertainties with systematic ones. The drawbacks of the method described above can be overcome by turning it into an iterative procedure, where it is repeated with the unfolded distribution as a new input for the procedure until it converges.

### Application in this analysis

For the practical implementation of this procedure the measured spectra have been parameterized by a power law fit in the range  $p_T > 5\text{GeV}/c$  and folded with the  $p_T$  resolution obtained from the covariance matrix of the track fitting algorithm. The resulting correction factors depend on the spectral shape (larger corrections for the steeper falling spectra) and the  $p_T$  resolution. For the analysis of early (2012) p–Pb data, reaching only up to 20 GeV/c

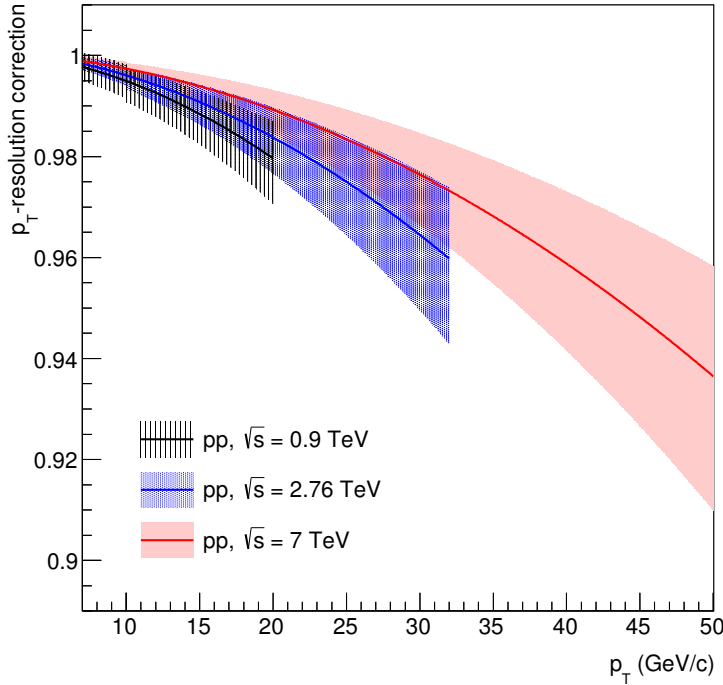


Figure 3.28.: Correction factors for the  $p_T$  resolution applied in pp.

in  $p_T$ , no correction has been applied, but a systematic uncertainty was assigned based on the anticipated correction.

The resulting correction factors depend on the shape of the  $p_T$  distribution and on the  $p_T$  resolution and are different for pp (Figure 3.28) and Pb–Pb (Figure 3.29).

### 3.7.5 Acceptance Corrections in p–Pb

The LHC has a 2-in-1 magnet design which provides the same magnet field strength in both beam-pipes. This results in different beam energies per nucleon for ions with different  $Z/A$  ratios. In the 2012 and 2013 p–Pb runs the beam energy was  $E/Z = 4$  TeV resulting in  $E_p = 4$  TeV and  $E_{Pb}/A = 1.58$  TeV with a nucleon-nucleon center-of-mass energy

$$\sqrt{s_{NN}} = \sqrt{((E_p/c, \vec{p}_p) + (E_{N,Pb}/c, \vec{p}_{N,Pb}))^2} = 5.02 \text{ TeV} \quad (3.11)$$

The nucleon-nucleon center-of-mass frame moves with  $|v_{cm}| \approx (208 - 82)/(208 + 82)c \approx 0.43c$ , corresponding to the rapidity<sup>4</sup>  $y_{cm} = -0.465$ , in the direction of the proton.

In case of symmetric collisions (like pp or Pb–Pb) the lab frame is the same as the nucleon-nucleon center-of-momentum frame. To obtain spectra that can be compared to pp, especially in terms of the nuclear modification factor  $R_{pPb}$ , the  $\eta$ -acceptance has to be identical.

For massless particles, the pseudorapidity equals the rapidity, thus  $\eta_{cms} = \eta_{lab} + y_{cm}$ . For the detector acceptance this translates the lab acceptance of  $|\eta_{lab}| < 0.8$  to approximately

<sup>4</sup> here the sign convention of ALICE is used.

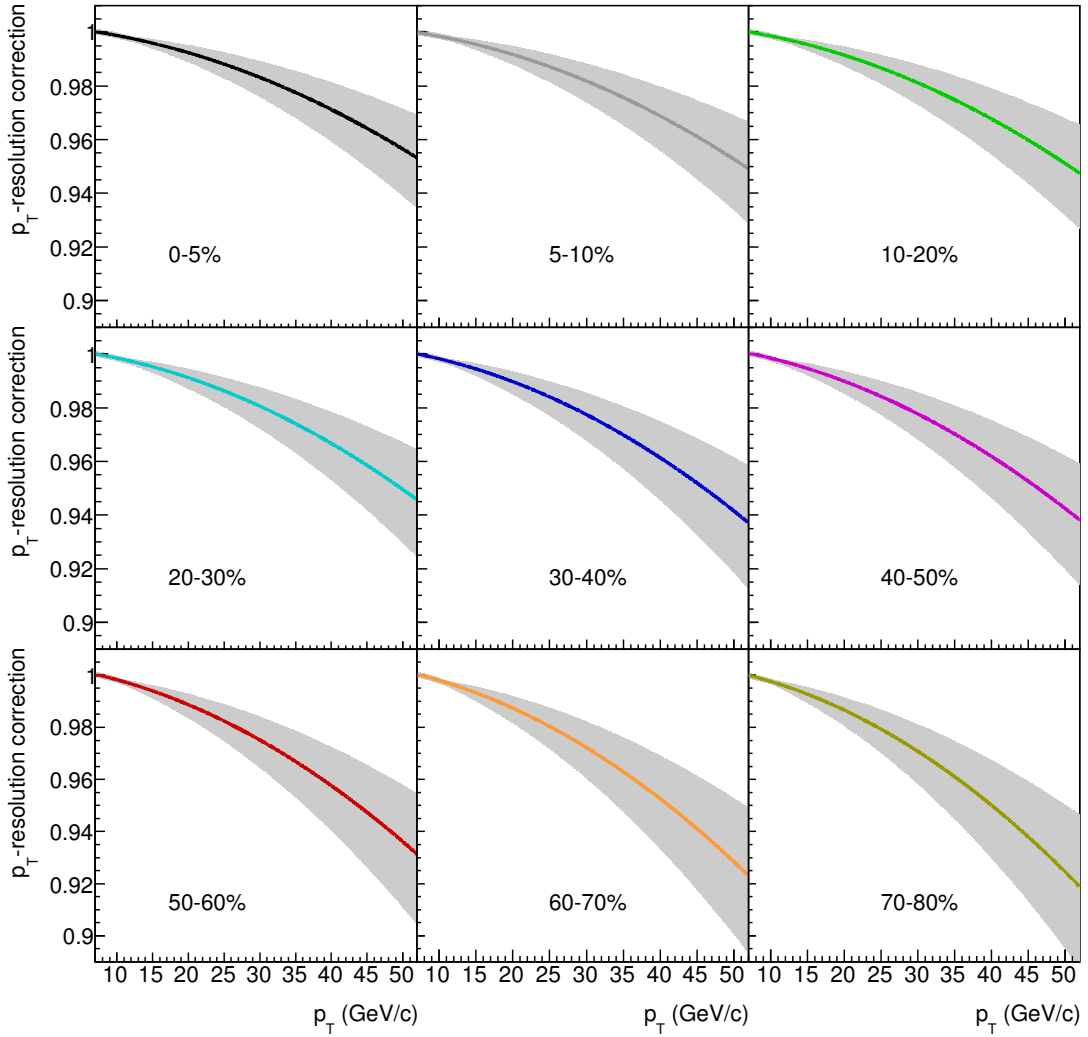


Figure 3.29.: Correction factors for the  $p_T$  resolution applied in Pb–Pb.

$-0.3 < \eta_{\text{cms}} < 1.3$  in the cm-frame. With pp collisions the overlap is  $|\eta_{\text{cms}}| < 0.3$  motivating this choice of the acceptance in the p–Pb analysis.

Since none of the measured particles is massless, the shift in  $\eta$  is only the first approximation. The proper transformation of  $\eta$  under a boost along the z-direction with rapidity  $y_{\text{cm}}$  is:

$$\sinh \eta_{\text{cms}} = \sinh(\eta_{\text{lab}} - y_{\text{cm}}) - \left( \sqrt{\frac{m^2}{p_T^2} + \cosh^2 \eta_{\text{lab}}} - \cosh \eta_{\text{lab}} \right) \sinh y_{\text{cm}} \quad (3.12)$$

where the first term corresponds to the shift and the second term is the additional correction, which can become arbitrary large.

In the center-of-momentum frame also the pseudorapidity acceptance depends on  $m/p_T$ . The analysis of  $p_T$  spectra integrates over the  $\eta$ -acceptance, and the boost causes that particles can be shifted, either within the acceptance, into the acceptance or out of the acceptance. Only the net effect is important, and has been included in the analysis as an additional *acceptance*

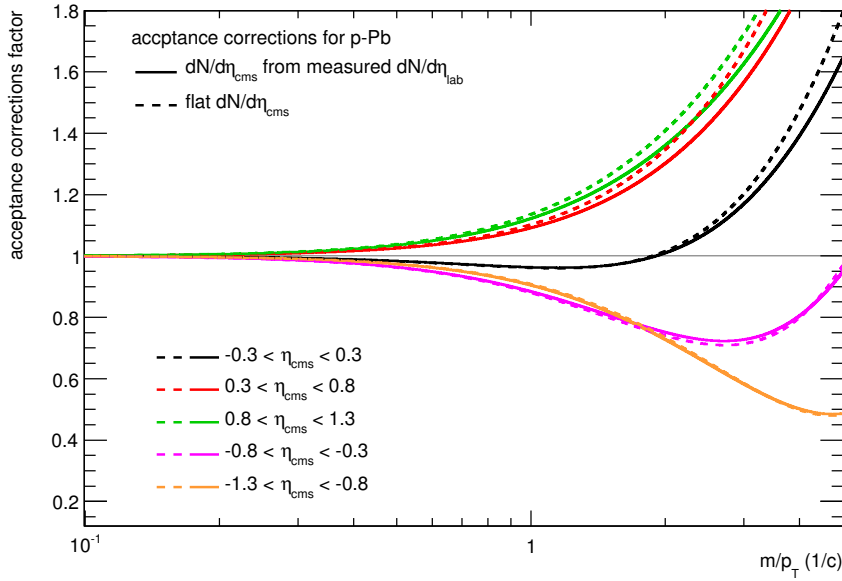


Figure 3.30.: Acceptance corrections for p–Pb to convert from  $\eta_{\text{lab}} + y_{\text{cm}}$  to  $\eta_{\text{cms}}$  for different pseudorapidity ranges as a function of  $m/p_{\text{T}}$ . The solid line corresponds to the measured  $dN/d\eta_{\text{lab}}$  [163], the dashed curve to a flat  $dN/d\eta_{\text{lab}}$ .

correction. This correction is calculated for each  $p_{\text{T}}$  bin, using the measured pseudorapidity distributions [163] and the primary particle composition from HIJING as input in a procedure described below.

Figure 3.30 shows the correction factors as a function of  $m/p_{\text{T}}$  for different ranges of  $\eta_{\text{cms}}$  using a realistic  $dN/d\eta_{\text{lab}}$  distribution that is used for the corrections and a flat  $dN/d\eta_{\text{lab}}$  demonstrating the dependence on the pseudorapidity distribution. Starting with the  $dN/d\eta_{\text{cms}}$  distribution as an input the correction factors  $c_{\text{acceptance}}$  are calculated as a function of  $m/p_{\text{T}}$  from the ratio of a proper transformation to  $dN/d\eta_{\text{lab}}$  (according to Equation (3.12)) to the distribution only shifted by  $y_{\text{cm}}$ :

$$c_{\text{acceptance}}(m/p_{\text{T}}) = \frac{\int_{\eta_1}^{\eta_2} dN/d\eta_{\text{cms}}(m/p_{\text{T}}) d\eta}{\int_{\eta_1+y_{\text{cm}}}^{\eta_2+y_{\text{cm}}} dN/d\eta_{\text{lab}}(m/p_{\text{T}}) d\eta} \quad (3.13)$$

Note that these correction factors are always averaged over a pseudorapidity  $\eta_1 < \eta_{\text{cms}} < \eta_2$  and are equal for all particles. The pseudorapidity distribution  $dN/d\eta_{\text{lab}}$  was measured only for inclusive charged particles [163] and is assumed to be the independent of the particle type.

The overall acceptance correction for all charged particles  $c_{\text{acceptance}}(p_{\text{T}})$  is obtained as a weighted average of the single particle corrections:

$$c_{\text{acceptance}}(p_{\text{T}}) = \sum_{i=\pi, K, p} \frac{n_i}{n_{\pi+K+p}} c_{\text{acceptance}}(m_i/p_{\text{T}}) \quad (3.14)$$

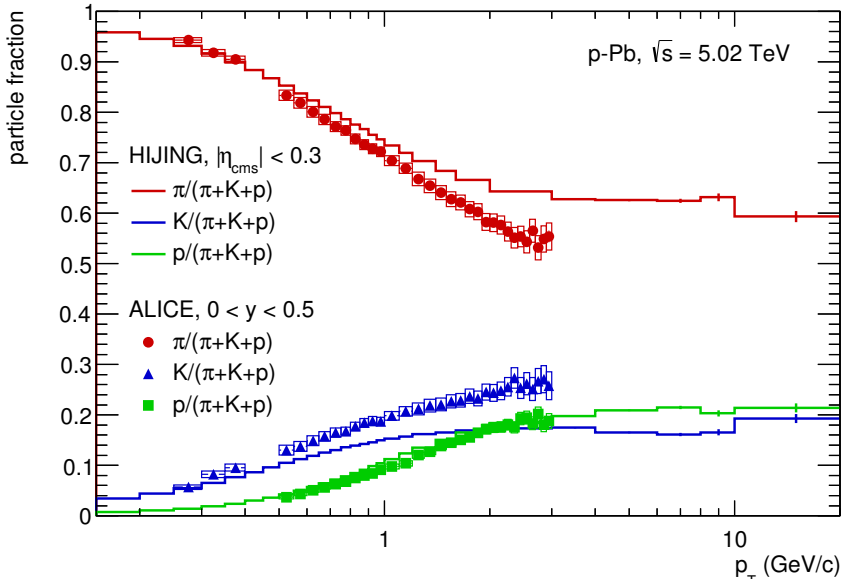


Figure 3.31.: The relative fraction of charged pion, kaons and protons as function of  $p_T$  from HIJING simulation and measured by ALICE [161].

The relative fractions of charged pion, kaons and protons have been taken from the simulations with the MC event generator HIJING and are shown in Figure 3.31 together with results later measured by ALICE [161].

The resulting overall corrections factors are shown in Figure 3.32 as a function of  $p_T$  for the relevant particle species and for inclusive charged particles, for the three different  $\eta_{\text{cms}}$  ranges considered. A clear mass-ordering of the corrections can be seen. For protons the correction is very large while for electrons it is negligible. At low  $p_T$  pions dominate the spectrum (cf. Figure 3.1) and prevent the corrections from becoming excessively large. In the range as used in the first publication ( $p_T > 500$  MeV/c) the correction is  $< 1\%$  for  $|\eta_{\text{cms}}| < 0.3$ , but ranges up to 3% for the more forward intervals of  $\eta_{\text{cms}}$ . The size and uncertainty of this correction at  $p_T < 500$  MeV/c was the reason to exclude this range in the first publication [164] of p-Pb results.

Measurements of identified pions, kaon, protons [161] became available after the results of the pilot run analysis have been published [164]. In the analysis of the 2013 p-Pb data (see sections 4.3.2 and 5) this has been incorporated also in the acceptance correction and where the particle fractions from HIJING simulation have been replaced by the measured particle composition, neglecting the difference in the rapidity interval. As apparent from Figure 3.31, the production of  $K^\pm$  is considerably underestimated in the HIJING simulation, however, the resulting acceptance corrections remain consistent with the ones shown in Figure 3.32 for  $p_T > 500$  MeV/c.

### 3.8 Event Level corrections

The event level corrections includes the efficiency of the trigger and the primary vertex reconstruction. For the normalization of the spectra it has to be taken into account that events are missing because they have not been triggered or lack a reconstructed vertex.

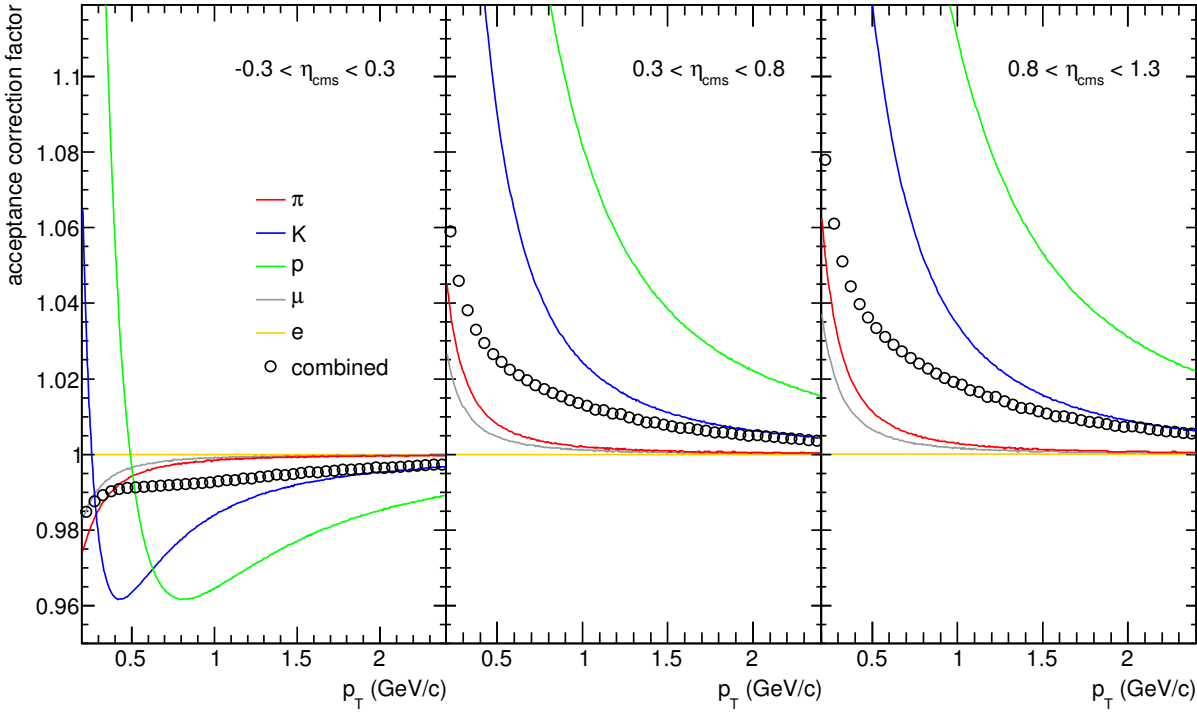


Figure 3.32.: Acceptance corrections for pion, kaons, protons, electrons and muons as function of  $p_T$  as well as the applied overall correction factor for the three analyzed pseudorapidity intervals.

The total number of events  $N_{\text{all}}$  consists of events that are triggered  $N_{\text{trigger}}$ , this includes events with a reconstructed vertex  $N_{\text{vertex}}$ , and events that are not triggered  $N_{\text{notrigger}}$ . The events which are triggered, but have no reconstructed primary vertex are referred to as *bin zero events*.

$$N_{\text{all}} = \underbrace{N_{\text{vertex}}^{\text{event}} + N_{\text{bin0}}^{\text{event}}}_{N_{\text{trigger}}^{\text{event}}} + N_{\text{notrigger}}^{\text{event}} \quad (3.15)$$

If the fraction of events which is not triggered on would be a random selection of all events, obviously there is no effect on the  $p_T$  spectrum, but this is not the case. Basically for all events which have a particle in the acceptance ( $p_T > 0.15 \text{ GeV}/c$ ,  $|\eta| < 0.8$ ) the trigger is fully efficient as shown in Figure 3.9. This is the reason why the trigger efficiency is almost exclusively affecting the overall normalization of the spectrum. Residual effects on the shape of the  $p_T$  distribution, the so-called *trigger bias*, are discussed in section 3.10.5.

With the trigger efficiency

$$\epsilon_{\text{trigger}} = \frac{N_{\text{trigger}}}{N_{\text{all}}}, \quad (3.16)$$

which has to be obtained from Monte Carlo simulations or from other measurements the total number of events is

$$N_{\text{all}} = \frac{N_{\text{vertex}} + N_{\text{bin0}}}{\epsilon_{\text{trigger}}}. \quad (3.17)$$

Only events which have a reconstructed z-position of the vertex located  $\pm 10$  cm around the nominal interaction point are considered in the analysis and contribute to the  $p_T$  distribution. For the corrections on the event level the same condition has to be applied, which is achieved by integrating the distributions of bin0, reconstructed and untriggered events over the corresponding  $V_z$  range:

$$N_{V_z < 10\text{cm}} = \int_{-10\text{cm}}^{+10\text{cm}} n_{\text{vertex}}(V_z) dV_z + \int_{-10\text{cm}}^{+10\text{cm}} n_{\text{bin0}}(V_z) dV_z + \int_{-10\text{cm}}^{+10\text{cm}} n_{\text{nottrigger}}(V_z) dV_z \quad (3.18)$$

Quantities available from the data are only

- $n_{\text{vertex}}(V_z)$ : The distribution of events which have a reconstructed primary vertex as function of the  $z$ -position of this vertex  $V_z$ . The integral corresponds to all events with a reconstructed vertex:  $N_{\text{vertex}} = \int n_{\text{vertex}}(V_z) dV_z$
- $N_{\text{bin0}}$ : The number of events which are triggered, but have no reconstructed primary vertex. Obviously, this is the integral over all values of  $V_z$ .

The distributions of bin0 events and untriggered events need additional input. A reasonable assumption is that the shape of the distributions is the same for all event classes, implying that the efficiencies for trigger and vertex do not depend on the position of the vertex. In this case  $N_{V_z < 10\text{cm}}$ , can be calculated as:

$$N_{\text{all}, V_z < 10\text{cm}} = \underbrace{\frac{N_{\text{vertex}} + N_{\text{bin0}}}{\varepsilon_{\text{trigger}}}}_{\text{all events}} \cdot \underbrace{\left( \frac{1}{N_{\text{vertex}}} \int_{-10\text{cm}}^{+10\text{cm}} n_{\text{vertex}}(V_z) dV_z \right)}_{\text{fraction of events with } V_z < 10 \text{ cm}} \quad (3.19)$$

However, as shown in Figure 3.8, there is a non-negligible dependence of the trigger and vertex reconstruction efficiencies on  $V_z$ . A possible way to take this into account, is to use the individual vertex distributions for the three event classes (reconstructed vertex, triggered but not vertex and not triggered) from Monte Carlo simulations in Equation (3.18).

All simulations are performed in a way that they are "anchored" to reconstructed real data and use the reconstructed  $z$ -vertex distributions from data as an input for the generation of simulated events. This leads to comparable  $z$ -vertex distributions in data and MC for all event classes. However, they are still slightly different, a consequence of the  $z$ -vertex-dependence in the trigger and vertex reconstruction efficiency as shown in Figure 3.8.

The approach in this analysis is to take this difference into account by using only the differences in shape of the event distributions from Monte Carlo, and not the distributions themselves. This is implemented by taking the ratios from MC and apply them as a correction in data.

The corrected shape of the bin0/untriggered events in data is then given by

$$s_{\text{bin0}}(V_z) = \underbrace{\frac{n_{\text{bin0}}^{\text{MC}}(V_z)}{n_{\text{vertex}}^{\text{MC}}(V_z)}}_{\text{from MC}} \cdot \underbrace{n_{\text{vertex}}(V_z)}_{\text{from data}} \quad (3.20)$$

$$s_{\text{nottrigger}}(V_z) = \frac{n_{\text{nottrigger}}^{\text{MC}}(V_z)}{n_{\text{vertex}}^{\text{MC}}(V_z)} \cdot n_{\text{vertex}}(V_z) \quad (3.21)$$

The integral of the distributions is normalized to the number of bin0/untriggered events from data to obtain the corrected  $V_z$  distributions:

$$n_{\text{bin0}}(V_z) = \underbrace{N_{\text{bin0}}}_{\text{normalization}} \cdot \underbrace{\frac{s_{\text{bin0}}(V_z)}{\int s_{\text{bin0}}(V_z) dV_z}}_{\text{shape}} \quad (3.22)$$

$$n_{\text{nottrigger}}(V_z) = \underbrace{\left( N_{\text{bin0}} + N_{\text{vertex}} \right)}_{\text{triggered events}} \cdot \underbrace{\left( \frac{1}{\varepsilon_{\text{trigger}}} - 1 \right)}_{\text{untriggered events}} \cdot \underbrace{\frac{s_{\text{nottrigger}}(V_z)}{\int s_{\text{nottrigger}}(V_z) dV_z}}_{\text{untriggered/triggered events shape}} \quad (3.23)$$

The z-Vertex dependence of the trigger efficiency is much smaller than that of the vertex reconstruction.

### 3.8.1 Trigger efficiency

The trigger efficiencies can be estimated using Monte Carlo simulations. They depend not only on the relative fractions of single, double and non-diffractive events but also on the event characteristics and on the event generator. Event fractions and trigger efficiencies for SD, DD, NSD and INEL are compiled in Table 3.7 (pp, 0.9 TeV), Table 3.8 (pp, 2.76 TeV) and Table 3.9 (pp, 7 TeV). For the normalization of the spectra to differential yields the trigger efficiencies estimated by ALICE were used, for the representation of the data as differential cross sections the trigger cross sections measured by ALICE (see below) were used.

The trigger cross sections of the minimum bias triggers were determined [165] using luminosity measurements with van der Meer scans [166] at  $\sqrt{s} = 2.76\text{TeV}$  and  $\sqrt{s} = 7\text{TeV}$ , and the inelastic cross section measured in  $p\bar{p}$  collisions by the UA5 experiment [167] together with a re-analysis [168] at  $\sqrt{s} = 0.9\text{TeV}$ . The Monte Carlo generators used in this study were PYTHIA6, Perugia0 tune [153–155] and PHOJET [156] with specially tuned diffractive mass distributions [165]. In the PYTHIA and PHOJET simulations listed for comparison in tables 3.7, 3.8 and 3.9 no such tuning has been performed, explaining the discrepancies in the event fraction and trigger efficiency.

The trigger cross sections used for normalization to the inelastic cross section are [165]

- pp,  $\sqrt{s} = 0.9\text{ TeV}$ :  $\sigma_{\text{MBOR}} = 47.8^{+2.5}_{-3.0} \text{ mb}$

PHOJET		PYTHIA Perugia0		ALICE measurement [165]		
process type	trigger efficiency	event fraction	trigger efficiency	event fraction	trigger efficiency	event fraction
	MB <sub>OR</sub>	$\sigma/\sigma_{\text{INEL}}$	MB <sub>OR</sub>	$\sigma/\sigma_{\text{INEL}}$	MB <sub>OR</sub>	$\sigma/\sigma_{\text{INEL}}$
SD	85.70 %	19.10 %	76.93 %	22.25 %		$0.21 \pm 0.03$
DD	97.71 %	6.39 %	91.54 %	12.21 %		$0.11 \pm 0.03$
ND	99.93 %	74.51 %	99.94 %	65.54 %		0.68
NSD	99.75 %	80.90 %	98.62 %	77.75 %		0.79
INEL	97.07 %		93.79 %		$91.0^{+3.2}_{-1.0}$	

Table 3.7.: Trigger efficiencies from pp MC 900 GeV. Results were obtained using the central ALICE MC productions LHC12e12 (PHOJET) and LHC12e13 (PYTHIA Perugia0).

PHOJET		PYTHIA Perugia0		ALICE measurement [165]		
process type	trigger efficiency	event fraction	trigger efficiency	event fraction	trigger efficiency	event fraction
	MB <sub>OR</sub>	$\sigma/\sigma_{\text{INEL}}$	MB <sub>OR</sub>	$\sigma/\sigma_{\text{INEL}}$	MB <sub>OR</sub>	$\sigma/\sigma_{\text{INEL}}$
SD	41.79 %	23.29 %	74.14 %	20.67 %		$0.20^{+0.07}_{-0.08}$
DD	95.75 %	5.63 %	89.05 %	12.78 %		$0.12 \pm 0.05$
ND	99.97 %	71.07 %	99.94 %	66.55 %		0.68
NSD	99.66 %	76.71 %	98.19 %	79.33 %		0.80
INEL	86.18 %		93.22 %		$88.1^{+5.9}_{-3.5}$	

Table 3.8.: Trigger efficiencies from pp MC 2.76 TeV. Results were obtained using the central ALICE MC productions LHC12f1b (PHOJET) and LHC11b10a (PYTHIA Perugia0).

PHOJET		PYTHIA Perugia0		ALICE measurement [165]		
process type	trigger efficiency	event fraction	trigger efficiency	event fraction	trigger efficiency	event fraction
	MB <sub>OR</sub>	$\sigma/\sigma_{\text{INEL}}$	MB <sub>OR</sub>	$\sigma/\sigma_{\text{INEL}}$	MB <sub>OR</sub>	$\sigma/\sigma_{\text{INEL}}$
SD	77.82 %	13.81 %	72.29 %	19.17 %		$0.20^{+0.04}_{-0.07}$
DD	93.39 %	5.07 %	86.94 %	12.97 %		$0.12^{+0.05}_{-0.04}$
ND	99.84 %	81.13 %	99.90 %	67.85 %		0.68
NSD	99.46 %	86.19 %	97.82 %	80.83 %		0.80
INEL	96.48 %		92.93 %		$85.2^{+6.2}_{-3.0}$	

Table 3.9.: Trigger efficiencies from MC pp 7 TeV. Results were obtained using the central ALICE MC productions LHC10f6 (PHOJET) and LHC10f6a (PYTHIA Perugia0).

- pp,  $\sqrt{s} = 2.76$  TeV:  $\sigma_{\text{MBOR}} = 55.4 \pm 1.0$  mb
- pp,  $\sqrt{s} = 7$  TeV:  $\sigma_{\text{MBOR}} = 62.2 \pm 2.2$  mb

The efficiency of the MBOR trigger is close to 100 % for events that have at least one track contributing to the  $p_{\text{T}}$  distribution ( $p_{\text{T}} > 0.15$  GeV/c,  $|\eta| < 0.8$ ). Thus the trigger efficiency affects only the normalization of the spectrum and is taken into account only in the event-level corrections. As the trigger efficiency is not exactly 100% even for  $\text{INEL} > 0$  events there is potentially a residual effect on the spectrum (see section 3.10.5).

The different trigger selection employed in p-Pb collisions (V0AND) has no sensitivity to pure single diffractive events. A normalization to INEL would be a correction purely based on Monte Carlo and amount to 2-3%, estimated with DPMJET and HIJING. Instead, the spectra are normalized to non-single-diffractive (NSD) events as defined in section 1.8. The trigger efficiency for NSD was estimated to 99.2% using simulations with the event generators PYTHIA, DPMJET and STARLIGHT with negligible contribution from single diffractive event or electromagnetic interactions [163].

In Pb–Pb collisions, within the centrality interval of 0-80% used for this analysis, both trigger and vertex reconstruction are fully efficient and there are no events without any track. Therefore a correction for trigger and vertex efficiency is not required and the proper normalization of the spectra to hadronic interactions is based only on the number of events passing event and centrality selection. Background from electromagnetic interactions become important for peripheral events (centrality > 90%) [144] and is thus not relevant for the event sample analyzed. The analysis is limited to 0-80% centrality to avoid possible contamination from electromagnetic dissociation, for the data recorded early the limit of the centrality range was required by the centrality selection. For the data analyzed the number of events in the 80-90% centrality interval is about 1.2% smaller than expected.

---

### 3.9 Application of track and event corrections

---

Starting point is the raw distribution  $N_{\text{raw}}(p_{\text{T}}, \eta, V_z, M)$  which is the number of tracks reconstructed with a given transverse momentum  $p_{\text{T}}$  and pseudorapidity  $\eta$  in an event with a z-coordinate of the primary vertex  $V_z$ , and a multiplicity class  $M$  given by a chosen multiplicity estimator. The implementation of the analysis is based on multi-dimensional histograms, where all variables are grouped into discrete intervals. The histogram binning defines the granularity of the applied corrections, in case of  $p_{\text{T}}$  this also defines the granularity of the measurement.

All corrections described in the sections above are applied to these raw distributions. The overall tracking efficiency effects (see section 3.7.1) are taken into account by the correction factor  $c_{\text{eff}}$  (Equation (3.4)) and the contamination from secondary particles present in the raw distribution (see section 3.7.2) yields the correction factor  $c_{\text{sec}}$  (Equation (3.7)). Smearing of the spectrum occurs due to finite  $p_{\text{T}}$  resolution (as discussed in section 3.7.4, the unfolding is encoded in an effective correction factor  $c_{\text{resolution}}$  (defined in Equation (3.10)). In case of p-Pb an additional correction factor  $c_{\text{acceptance}}$  (Equation (3.14)) is applied to account for the modified acceptance due to asymmetric collisions (see section 3.7.5).

The distribution  $N_{\text{corr}}$  including the track-level corrections is obtained as

$$N_{\text{corr}}(p_T, \eta, V_z, M) = N_{\text{raw}}(p_T, \eta, V_z, M) \cdot c_{\text{eff}}(p_T, \eta, M) \cdot c_{\text{sec}}(p_T, \eta, M) \cdot c_{\text{resolution}}(p_T, M) \cdot c_{\text{acceptance}}(p_T, \eta) \quad (3.24)$$

Here, the multiplicity class  $M$  denotes the centrality interval in Pb–Pb collisions. In pp and p–Pb collisions the raw and corrected distributions are kept in intervals of the multiplicity (number of reconstructed tracks in the acceptance) that are required to determine the multiplicity dependence of  $\langle p_T \rangle$  (section 5). However, the track-level corrections show no strong multiplicity dependence and are applied independent of multiplicity. The simulated distribution of primary vertex positions along  $z$  is almost equal (see remarks in section 3.8) to the measured distribution and there is no need to introduce a  $V_z$  dependence of the corrections. The granularity of the corrections in  $p_T$  and  $\eta$  is different for the various correction factors and data sets and governed by the statistics available in the simulation.

The resulting distribution is integrated over the acceptance defined by the acceptance cuts and is normalized to the proper number of events. Furthermore the  $p_T$  distribution is converted to a double-differential spectrum, dividing by the corresponding  $\eta$  and  $p_T$  intervals. However, it is not really differential in  $\eta$  as the average over the full  $\eta$ -range is taken.

$$\left( \frac{d^2 N_{ch}}{d\eta dp_T} \right)_M = \frac{1}{\Delta\eta} \frac{1}{N_{\text{event,corr}}} \sum_{\eta, V_z} \frac{1}{\Delta p_T} N_{\text{corr}}(p_T, \eta, V_z, M) \quad (3.25)$$

Here the division by  $\Delta p_T$  corresponds to a normalization to the bin width and  $\Delta\eta = \eta_{\text{max}} - \eta_{\text{min}}$  is the width of the pseudorapidity interval considered.

The normalization to the cross section is similar, in this case the number of events  $N_{\text{event,trigger}}$  entering the normalization only includes triggered events and a multiplication of the trigger cross section is  $\sigma_{\text{trigger}}$  required:

$$\frac{d^2 \sigma_{ch}}{d\eta dp_T} = \sigma_{\text{trigger}} \frac{1}{\Delta\eta} \frac{1}{N_{\text{event,trigger}}} \sum_{\eta, V_z} \frac{1}{\Delta p_T} N_{\text{corr}}(p_T, \eta, V_z) \quad (3.26)$$

The results are commonly presented in the following form as an approximation of the invariant yields or cross sections:

$$E \frac{d^3 \sigma_{ch}}{dp^3} \approx \frac{1}{2\pi p_T} \frac{d^2 \sigma_{ch}}{d\eta dp_T} \quad (3.27)$$

$$E \frac{d^3 N_{ch}}{dp^3} \approx \frac{1}{2\pi p_T} \frac{d^2 N_{ch}}{d\eta dp_T} \quad (3.28)$$

Note that there is no correction for finite  $p_T$  bin width and all results are understood to be averages over corresponding  $p_T$  intervals. It is a commonly used method to move data points of histogrammed data measured over wide bins either in  $x$  or in  $y$  direction to enable direct

contribution	pp 0.9 TeV	pp 2.76 TeV	pp 7 TeV
Event vertex selection	1.2	2.3	0.5
Trigger bias	negl.	negl.	negl.
Vertex bias	0.1-1	0.1-1.2	0.1-0.9
Track selection	2.5-5.5	2.3-5.1	1.9-4.3
Tracking efficiency	5	5	5
$p_T$ resolution	<1.7	<1.9	<2.6
Particle composition	1-2	1-2	1-2
Secondary particles	<0.3	<0.3	<0.3
Material budget	0.2-1.5	0.2-1.5	0.2-1.5
MC event generator	2.5	2-3.5	2-3.5
total $p_T$ dependent	6.7-8.3	6.4-8.0	6.6-7.9
additional normalization uncertainty	+5.1/-4.0	$\pm 1.9$	$\pm 3.6$

Table 3.10.: Systematic uncertainties in pp (all values in %).

comparisons to smooth frequency distributions. However, this *bin shift correction* requires assumptions on the shape of the underlying distribution [169]. Here, the ALICE common practise of not applying a bin shift correction is adapted and data points are drawn at the bin center. For comparisons of data to theory or models, the corresponding distributions are averaged over the  $p_T$  intervals given by the bin width of the measurement.

## 3.10 Systematic uncertainties

### 3.10.1 Overview

The possible sources of systematic uncertainties that have been studied in all collision systems are the event  $z$ -vertex selection, the track selection criteria, tracking efficiency,  $p_T$  resolution, material budget MC generator dependence and secondary particles. Centrality selection is present only in Pb–Pb collisions while trigger efficiencies are relevant in pp and p–Pb, but not in Pb–Pb. An additional source of systematic uncertainty in p–Pb collisions is related to the acceptance correction (section 3.7.5).

An overview of the systematic uncertainties is given in Table 3.10 for pp collisions at the three different energies, in Table 3.11 for p–Pb and in Table 3.12 for all centralities in Pb–Pb collisions.

### 3.10.2 Procedure

Most systematic uncertainties turn out to be asymmetric, in many cases this asymmetry is small compared to the magnitude of the uncertainty. For the combination of systematic uncertainties they have been symmetrized by using the larger deviation. This is mainly done for simplicity as

contribution	$ \eta_{\text{cms}}  < 0.3$	$0.3 < \eta_{\text{cms}} < 0.8$	$0.8 < \eta_{\text{cms}} < 1.3$	$\frac{0.3 < \eta_{\text{cms}} < 0.8}{ \eta_{\text{cms}}  < 0.3}$	$\frac{0.8 < \eta_{\text{cms}} < 1.3}{ \eta_{\text{cms}}  < 0.3}$
Event vertex selection	1-2	1-2	1-2	1	1
Trigger bias	<0.5	<0.5	<0.5	–	–
Vertex bias	<negl.	<negl.	<negl.	–	–
Track selection	0.9-2.7	1.1-2.6	1.2-3.2	1.2-2	1.2-2
Tracking efficiency	3	3	3	–	–
$p_{\text{T}}$ resolution	<2.8	<2.8	<2.8	<1.0	<1.0
Particle composition	2.2-3.1	2.1-3.1	2.1-3.1	0.1-0.3	0.1-0.3
Secondary particles	0.4-1.1	0.4-1.1	0.4-1.1	–	–
Material budget	0.2-0.5	0.2-0.5	0.2-0.5	–	–
MC event generator	1	1	1	1	1
Acceptance (conversion to $\eta_{\text{cms}}$ )	0.1-0.6	0.1-4.3	0.1-5.1	0.2-4.6	0.2-5.4
total $p_{\text{T}}$ dependent	5.2-5.5	5.1-6.7	5.6-7.0	2.2-5.1	2.2-5.9
additional normalization uncertainty	3.1	3.1	3.1	–	–

Table 3.11.: Systematic uncertainties in p-Pb (all values in %). The last two columns give the systematic uncertainties for the ratio of different pseudorapidity ranges, where correlated parts of the uncertainties cancel.

contribution	0-5%	5-10%	10-20%	20-30%	30-40%	40-50%	50-60%	60-70%	70-80%
Event vertex selection	3.2	3.2	3.3	3.3	3.3	3.3	3.4	3.4	3.4
Centrality selection	0.2	0.3	0.7	1.0	2.0	2.4	3.5	4.8	6.7
Track selection	4.1-7.3	4.1-7.3	4.0-6.9	3.9-6.6	3.8-6.3	3.8-6.1	3.7-6.1	3.7-6.1	3.6-6.0
Tracking efficiency	5	5	5	5	5	5	5	5	5
$p_T$ resolution	<1.8	<1.9	<1.9	<2.0	<2.3	<2.3	<2.7	<2.9	<3.0
Particle composition	0.6-10	0.6-10	0.6-9.6	0.6-9.3	0.6-9.0	0.6-8.7	0.5-8.4	0.5-8.1	0.5-7.7
Secondary particles	<1.0	<1.0	<1.0	<0.9	<0.9	<0.8	<0.8	<0.8	<0.7
Material budget	0.9-1.2	0.9-1.2	0.9-1.3	0.8-1.4	0.8-1.5	0.7-1.6	0.7-1.7	0.6-1.7	0.5-1.7
MC event generator	2.5	2.5	2.4	2.3	2.1	2.0	1.8	1.7	1.5
total for spectra	8.2-13.4	8.2-13.4	8.1-13.2	8.1-13.0	8.3-12.8	8.3-12.6	8.7-12.6	9.3-12.8	10.3-13.4

Table 3.12.: Systematic uncertainties in Pb-Pb (all values in %).

the introduction of asymmetric uncertainties has very little benefit for the analysis presented here. The treatment of asymmetric uncertainties comes with additional difficulties and implies some counterintuitive consequences [170, 171].

Within this analysis all contributions of systematic uncertainties are assumed to be Gaussian with their sizes corresponding to the standard deviation of the Gaussian. In some cases the uncertainties treated as standard deviations are rather representing maximal deviations. Along with the symmetrizing this has the effect that the estimated overall uncertainty estimate is rather conservative.

For combination of all contributions they have simply been added in quadrature. This is based on the assumption that the uncertainties are not only Gaussian but also uncorrelated. This might not always be the case but it is not feasible to evaluate all correlations among the various sources of systematic uncertainties.

Correlations of systematic uncertainties have been evaluated for the ratio of spectra in pp collisions at different energies and the ratio of different pseudorapidity ranges in p–Pb collisions.

The fact that all contributions including very tiny ones have been taken into account and added quadratically might seem to result in an inflation of the systematic uncertainties: the effect that with each contribution added the systematic uncertainty grows. From a practical point of view it turns out that there are some dominating sources of uncertainty, and many small ones that are approximately irrelevant when the squared sum is taken. As an illustration consider a large 5% uncertainty and small contributions of 0.1% each, you would need 100 of them to increase the overall uncertainty by 0.1%.

In Pb–Pb collisions a full evaluation of systematic uncertainties was performed for the most central (0–5%) and most peripheral (70–80%) centrality intervals. Uncertainties for the intermediate centralities have been interpolated using a conservative approach. Uncertainties related to centrality selection and  $p_T$  resolution have been evaluated individually for all centrality intervals.

In the following sections the individual contribution to the systematic uncertainties are described.

---

### 3.10.3 Event Selection

---

The effect of the selection of events based on the  $z$ -vertex position was studied by comparing  $p_T$  spectra obtained with the nominal selection criteria ( $|V_z| < 10$  cm) to those obtained with the alternative selections  $|V_z| < 5$  cm and  $|V_z| < 20$  cm. These cut variation is applied in a consistent way in data and simulation. In addition the selection was restricted to vertices reconstructed either with negative or positive  $z$ -coordinate.

The variation of the event selection is sensitive to a bias from the  $z$ -vertex dependence of the trigger or vertex reconstruction. In addition effects of the acceptance ( $V_z$  vs.  $\eta$ ) and the tracking the  $V_z$  dependence of the tracking efficiency influence the related systematic uncertainty.

---

### 3.10.4 Centrality selection in Pb–Pb

---

The centrality selection has been briefly described in section 2.7, for a detailed description see ref. [144]. In ALICE the scale of the centrality selection is defined by the anchor point, which

is taken at 90% of the hadronic cross section. Varying this anchor point by  $\pm 1\%$  shifts the centrality classes leading to changes in the  $p_T$  spectrum. The relative difference to the nominal spectrum has been assigned as systematic uncertainty related to the centrality selection.

An additional cross check of the centrality selection is the use of a different centrality estimators. This cross-check has been done comparing the spectra in bins of the VZERO multiplicities to centrality estimated by the second layer of the SPD. The observed differences range from  $<0.5\%$  for the most central collisions to  $2.6\%$  in the most peripheral one. In the first analysis of Pb–Pb data [172] the uncertainty related to the centrality selection has not been estimated from the variation of the anchor point but from the difference between the two centrality estimators leading to slightly different systematic uncertainties.

---

### 3.10.5 Trigger and Vertex

---

Effects of the trigger and vertex efficiency are only contributing to the systematic uncertainty in pp and p–Pb collisions. In Pb–Pb collisions, within the analyzed 0–80% centrality interval, the multiplicities are sufficiently large that both, trigger and vertex reconstruction, are fully efficient. Hence no bias from the trigger or vertex reconstruction is present and no systematic uncertainty assigned.

Uncertainties of the trigger efficiencies and cross sections [165] affect only the normalization and are discussed in section 3.8.1 for pp collisions.

In p–Pb the uncertainty of the trigger efficiency for NSD events was estimated [163] using control triggers from the ZDC and amounts to  $3.1\%$ .

An additional systematic uncertainty is associated with the multiplicity dependence of the trigger and vertex efficiencies as observed in pp collisions (see Figure 3.8). While the trigger is fully efficient for events with at least one charged particle in the acceptance for the vertex reconstruction this is not the entirely true. Events with low multiplicities are also characterized by a softer spectrum, as a consequence there is a net effect on the low  $p_T$  part of the spectrum. This effects are called *trigger bias* and *vertex bias*, they affect the shape of the  $p_T$  distribution. Both of these effects were estimated using MC simulations and contribute to the systematic uncertainty, in addition to the uncertainty of the trigger cross section.

Figure 3.33 shows the trigger and vertex biases for pp collisions at the different energies, as obtained from the comparison of  $p_T$  distributions before and after trigger and vertex selection is applied. While the trigger bias is negligibly small, the bias from the event vertex reconstruction contributes to the systematic uncertainties at the lowest  $p_T$  bins with up to about  $1\%$ .

With the higher multiplicity in p–Pb collisions the vertex bias is negligibly small. The trigger bias has been estimated from a comparison of events triggered with V0AND and V0OR, the systematic uncertainty amount to  $0.5\%$  only for  $p_T < 1\text{GeV}/c$ .

---

### Track Selection

---

Variation of all the track selection criteria (cuts) verify the stability of the results against reasonable variations of the cuts. Table 3.13 lists the nominal values and the variations of all track cuts that have been studied. Cut scenarios are modified simultaneously in data and in the sim-

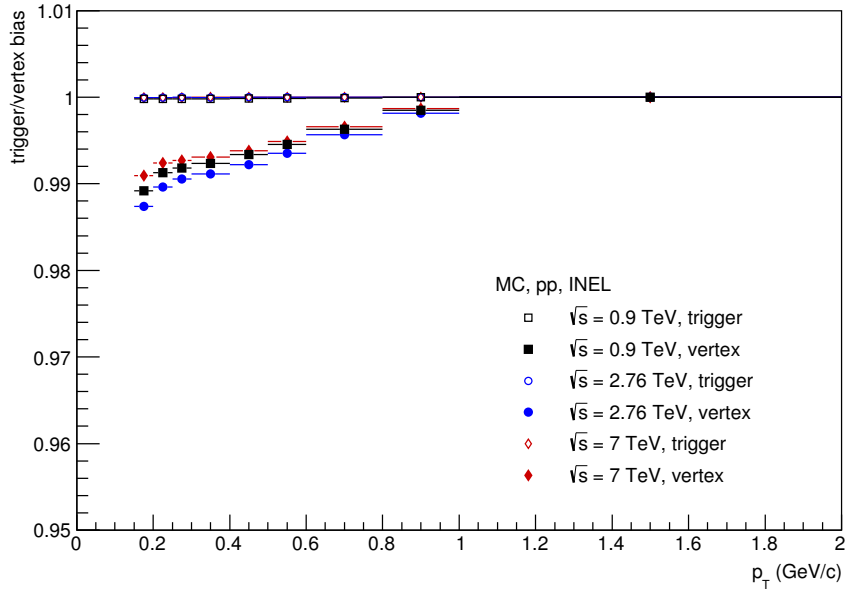


Figure 3.33.: Residual effect of the trigger and vertex reconstruction efficiencies on the  $p_T$  spectrum for pp collisions.

ulations from which the corrections are derived. The residual differences of the  $p_T$  spectra obtained with different cut scenarios, after applying all corrections, reflect imperfections in the simulations and is assigned as systematic uncertainty.

For cuts which have been varied in two directions, the larger discrepancy is assigned. The overall uncertainty related to track selection is taken as the squared sum of the single contributions. Typically at a given  $p_T$  only few of the cut variations contribute significantly to the systematic uncertainties.

### 3.10.6 Tracking efficiency

The corrections for the tracking (in)efficiency are determined from Monte Carlo simulations (see 3.7.1). These corrections rely on the proper description of the ALICE detector in the simulations.

To evaluate the systematic uncertainty related to this corrections a control variable that can be defined in the same way in data and MC is needed. The TPC→ITS matching efficiency can serve as this control variable. It is the probability that a given track that has been measured in the TPC has a matching hit in the ITS. It is calculated as the ratio of ESD tracks with TPC refit to ESD tracks with TPC and ITS refit. Table 3.14 lists the cuts that are used for the matching efficiency, including a rough selection of primary tracks based on the  $DCA_z$  and  $DCA_{xy}$ .

The matching efficiency obtained for data and MC is shown in Figure 3.34 for pp data, and in Figure 3.35 for all centrality classes in Pb–Pb data. Differences in MC and data are quantified in ratio (Figure 3.36). It is observed the matching efficiency is generally larger in MC as compared to DATA. The resulting discrepancy is reflecting the (in)accuracy of the tracking efficiency extracted from simulation and is assigned as a systematic uncertainty. In pp and Pb–Pb collisions the difference depends on  $p_T$  and centrality, ranging up to 5%, which is the value assigned as systematic uncertainty for all  $p_T$  bins.

track parameter		nominal	variation
$\chi^2$ per TPC cluster	$\chi^2_{\text{TPC}}/n_{\text{cl}}$	$\leq 4$	$\leq 3, \leq 5$
number of crossed rows in the TPC	$n_{\text{rows}}$	$\geq 120$	$\geq 100$
ratio of crossed rows to findable clusters in the TPC	$n_{\text{rows}}/n_{\text{findable}}$	$\geq 0.8$	$\geq 0.7, \geq 0.9$
fraction of shared TPC clusters	$n_{\text{shared}}/n_{\text{cl}}$	$\leq 0.4$	$\leq 0.2, \leq 1.0$
$\chi^2$ per ITS cluster	$\chi^2_{\text{ITS}}/n_{\text{ITS}}$	$\leq 36$	$\leq 25, \leq 49$
number of hits in the SPD	$n_{\text{SPD}}$	$\geq 1$	$\geq 0$
DCA to primary vertex in $z$	$\text{DCA}_z$	$\leq 2 \text{ cm}$	$\geq 1 \text{ cm}, \geq 5 \text{ cm}$
DCA to primary vertex in $xy$	$\text{DCA}_{xy}$	$\leq 7\sigma_0$	$\leq 4\sigma_0, \leq 10\sigma_0$
$\chi^2$ between TPC-ITS and TPC constrained track	$\chi^2_{\text{TPC-ITS}}$	$\leq 36$	$\leq 25, \leq 49$

Table 3.13.: Variations of the track cuts to determine the corresponding systematic uncertainties.

cut variable		cut value
TPC refit		required
number of crossed rows in the TPC	$n_{\text{rows}}$	$\geq 120$
ratio of crossed rows over findable clusters in the TPC	$n_{\text{rows}}/n_{\text{findable}}$	$\geq 0.8$
$\chi^2$ per TPC cluster	$\chi^2_{\text{TPC}}/n_{\text{cl}}$	$\leq 4$
fraction of shared TPC clusters	$n_{\text{shared}}/n_{\text{cl}}$	$\leq 0.4$
DCA to primary vertex in $xy$	$\text{DCA}_{xy}$	$\leq 3 \text{ cm}$
DCA to primary vertex in $z$	$\text{DCA}_z$	$\leq 3 \text{ cm}$
ITS refit		changed

Table 3.14.: Basic track selection used to determine the TPC-ITS matching efficiency.

In p–Pb the matching efficiency is larger compared to pp and Pb–Pb, a result of the increased fraction of the ITS being active. The systematic difference of the matching efficiencies is lower, resulting in a systematic uncertainty of 3%.

In MC the matching efficiency can be studied separately for primary and secondary particles. As exemplarily shown in Figure 3.37 for pp at  $\sqrt{s} = 2.76 \text{ TeV}$ , the matching efficiency is higher for primary particles compared to secondary particles. Part (but not all) of the discrepancy in the matching efficiency can thus be attributed to the larger amount of secondaries in data compared to MC.

### 3.10.7 $p_{\text{T}}$ resolution

The effect of finite  $p_{\text{T}}$  resolution and the correction procedure are described in section 3.7.4. The size of the correction depends on the momentum resolution, the shape of the  $p_{\text{T}}$  spectrum and limitations of the procedure itself. Systematic uncertainties that arise the corrections are dominated by the uncertainty of the transverse momentum resolution.

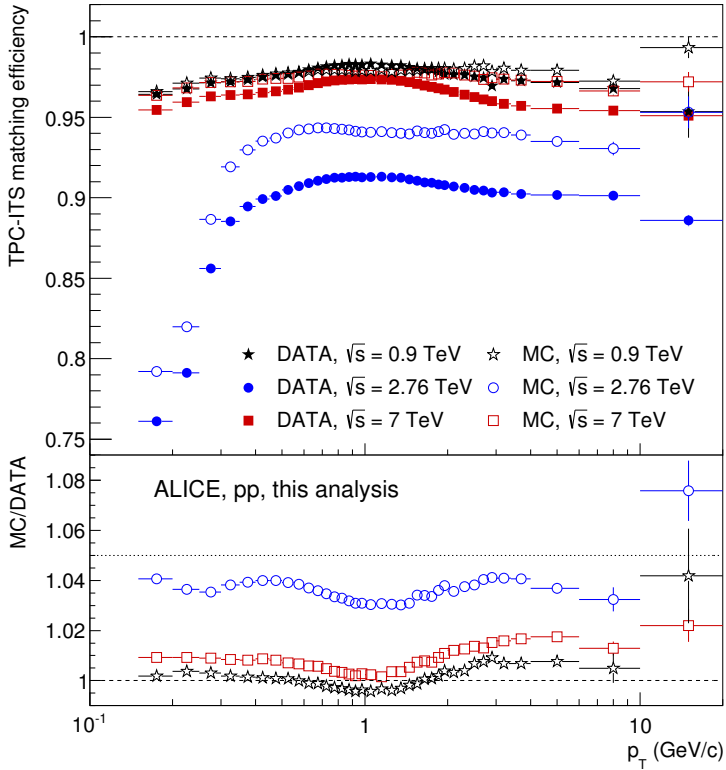


Figure 3.34.: Top: TPC-ITS matching efficiency in MC simulation with PYTHIA6 and data for Pb–Pb collisions at  $\sqrt{s} = 0.9, 2.76$  and  $7$  TeV.  
 Bottom: The ratio MC/DATA is an estimate of the systematic uncertainty related to the tracking efficiency. As a conservative estimate a relative uncertainty of 5% over the entire  $p_T$  range was assigned for all energies.

As there is no independent measurement of the  $p_T$  resolution the parameters obtained from the covariance matrix of the track fit have been verified via the reconstruction of strange particles ( $K_S^0, \Lambda$ ) in their decay into two charged particles. The width of the  $K_S^0$  and  $\Lambda$  peaks in the invariant mass spectrum is compared to the width expected from the error estimate of the track fit. This comparison<sup>5</sup> was performed as a function of the  $p_T$ , using the larger  $p_T$  of the two daughter tracks. Based on this procedure it was possible to confirm the resolution estimate from the covariance matrix up to  $p_T = 20$  GeV/c. Since this method requires the  $K_S^0$  or  $\Lambda$  to decay inside the ITS, it is statistically limited at larger  $p_T$ , where the probability of such decays gets tiny. For  $p_T < 50$  GeV/c the maximal relative systematic uncertainty for the  $p_T$  resolution was estimated to be 20%, based on the extrapolation from  $p_T < 20$  GeV/c.

In the unfolding procedure (section 3.7.4) the  $p_T$  resolution has been varied by  $\pm 20\%$  relative to the nominal value. This results in an uncertainty on the correction factors as indicated in Figure 3.29 (for Pb–Pb) and Figure 3.28 (for pp). The corresponding uncertainty on the  $p_T$  spectra is less than 3%.

An additional contribution to the systematic uncertainty is related to the procedure used to extract the corrections factors. This contribution is much smaller compared to the uncertainty of the  $p_T$  resolution and has been estimated in the following way. Two sources of systematic

<sup>5</sup> Details can be found in the ALICE analysis notes: [145, 146, 162]

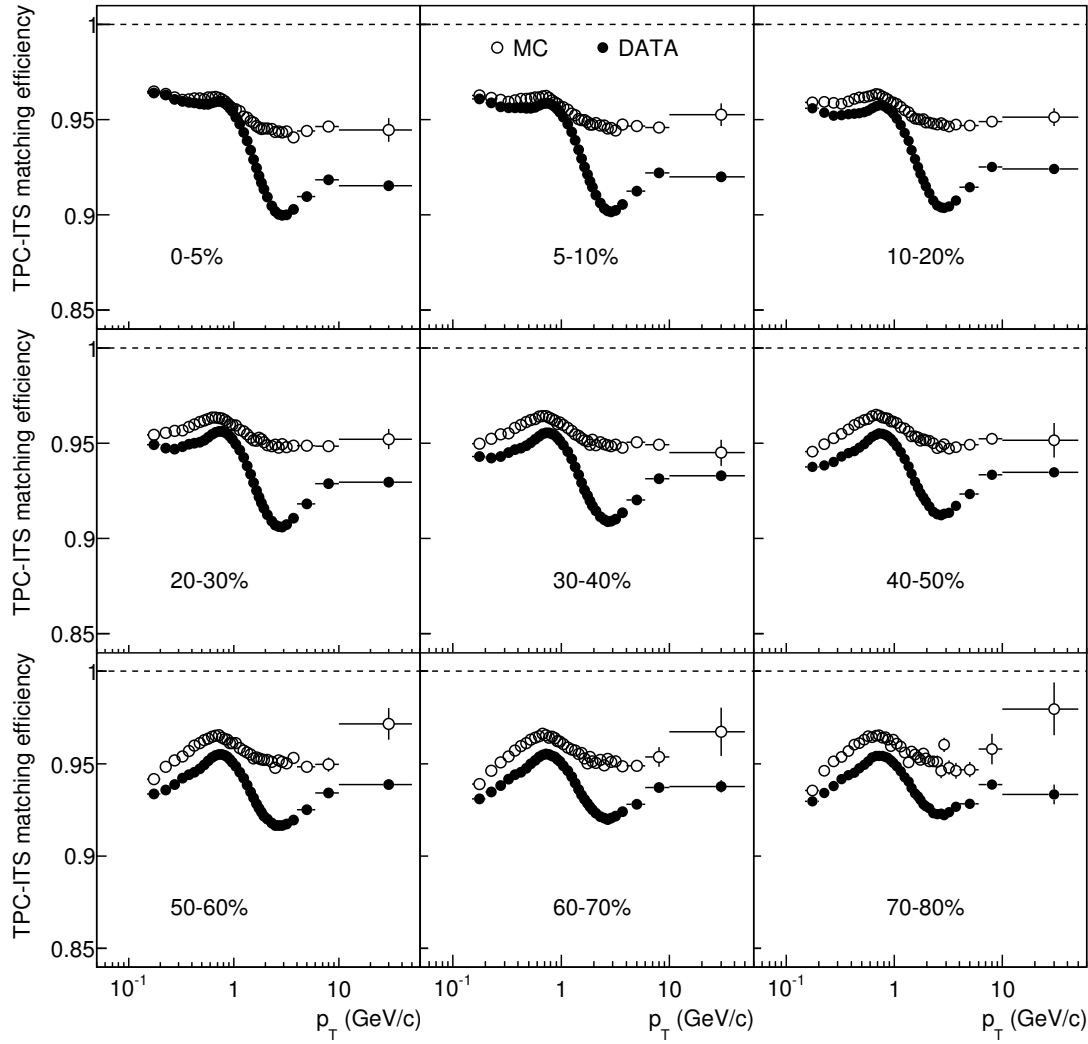


Figure 3.35.: Evolution of the TPC-ITS matching efficiency in data and MC simulations with centrality in Pb–Pb,  $\sqrt{s_{\text{NN}}} = 2.76$  TeV.

uncertainty have been evaluated: the influence of the steepness of the power law fit and the effect that the resolution correction (see equation 3.10 in section 3.7.4) is only a first order approximation, not a true unfolding.

The relevant fit parameter  $n$  of the power law fit to the data has been varied within its statistical uncertainty, reflecting the statistical uncertainties of the measured spectrum. The corrected spectra has been fitted again and the resulting change in slope has been used to estimate the second order correction to the  $p_{\text{T}}$  resolution. Both contributions (added quadratically) account for a relative uncertainty of 0.4–1.0% at the highest  $p_{\text{T}}$  covered. They have been included in the overall uncertainty of the  $p_{\text{T}}$  resolution correction.

In the reconstruction of 2012 p–Pb data the  $p_{\text{T}}$  resolution has been significantly improved compared to pp and Pb–Pb data (see Figure 3.27). The analysis of the 2012 p–Pb pilot run, was statistically limited to 20 GeV/c in  $p_{\text{T}}$  and no correction for finite  $p_{\text{T}}$  resolution has been applied. However, an uncertainty of up to 2.8% has been assigned representing an upper limit on the resolution correction.

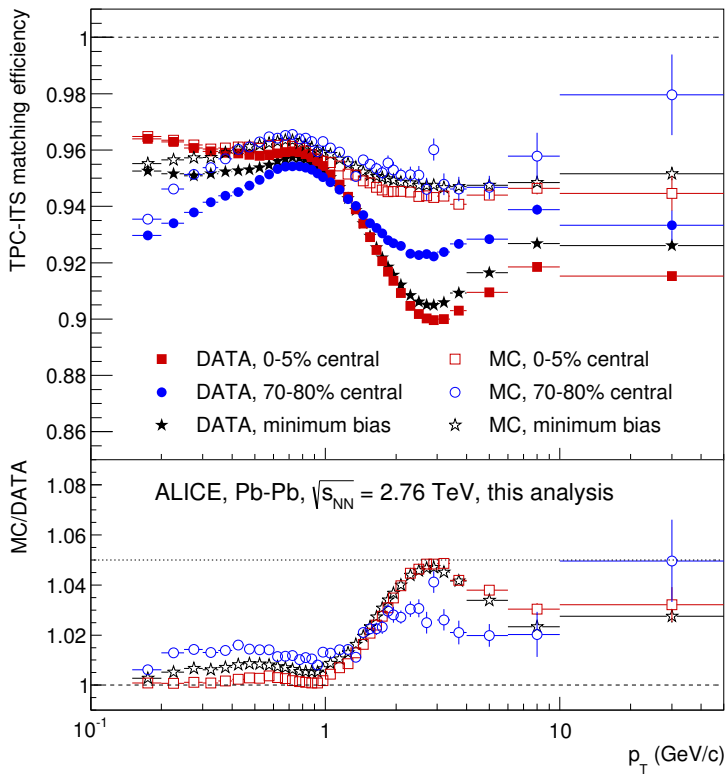


Figure 3.36.: Top: TPC-ITS matching efficiency in MC and data for Minimum Bias Pb-Pb collisions and two selected centrality intervals (most central and most peripheral). Bottom: The ratio MC/DATA is used to determine the systematic uncertainty related to the tracking efficiency. A relative uncertainty of 5% for the entire  $p_T$  range was assigned, independent of centrality.

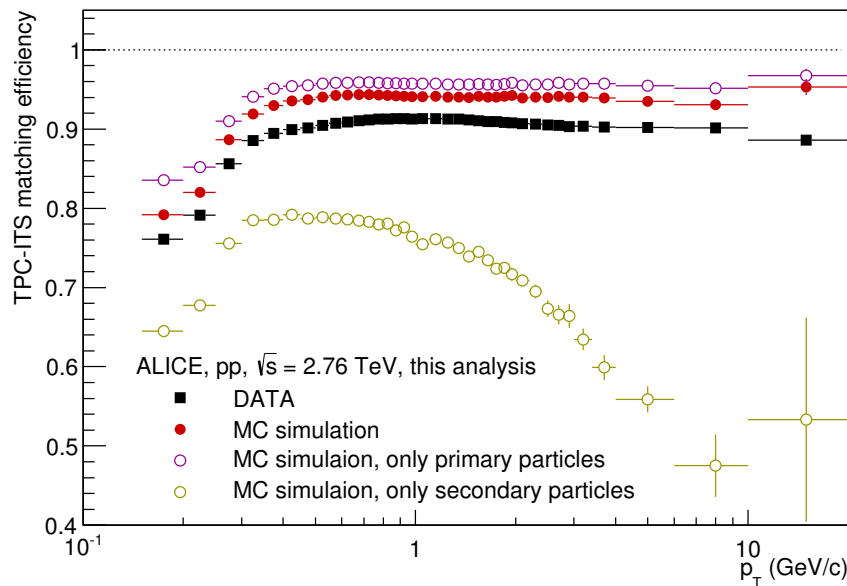


Figure 3.37.: The TPC $\rightarrow$ ITS matching efficiency for pp collisions at  $\sqrt{s} = 2.76$  TeV for data (LHC11a) and MC (LHC11b10a). For MC the matching efficiency is separately shown for primary and secondary charged particles. The reconstruction was performed without SDD.

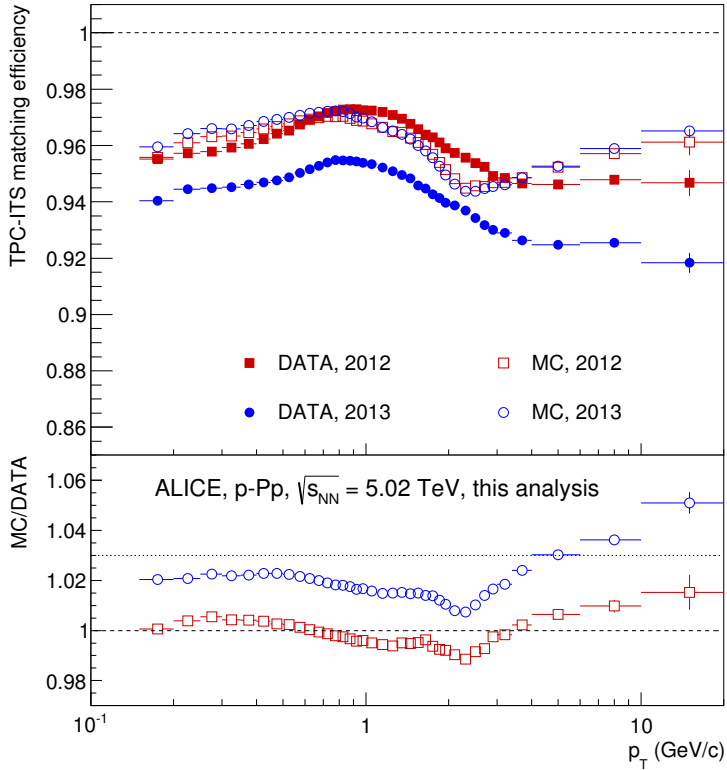


Figure 3.38.: Top: TPC-ITS matching efficiency in MC simulation with PYTHIA6 and data for Pb–Pb collisions at  $\sqrt{s} = 0.9, 2.76$  and  $7$  TeV.  
 Bottom: The ratio MC/DATA is an estimate of the systematic uncertainty related to the tracking efficiency. A relative uncertainty of 5% over the entire  $p_T$  range was assigned for all energies.

The  $p_T$  resolution in the 2013 p–Pb data is comparable to that in the 2012 data (or even slightly better). For the analysis of the multiplicity dependence of  $\langle p_T \rangle$  the 2013 data set has been used, but restricted to tracks with  $p_T < 10$  GeV/c, where the systematic uncertainty from  $p_T$  resolution is negligibly small. The analysis of 2013 data has been extended up to 50 GeV/c in  $p_T$  [173] with  $p_T$  resolution corrections are applied. With the improved  $p_T$  resolution the systematic uncertainty has also decreased and remains below 1.6%.

### 3.10.8 Material Budget

The amount of material, between the vertex and the detector as well as within the detector, can affect the measurement in several ways. The dominant effects are photon conversions that produce secondary electrons and multiple scattering of charged particles at low  $p_T$ . Also the energy loss of charged particles and hadronic interactions depend on the material budget. ALICE was designed with a very low material thickness of only 13%  $X_0$  up to the end of the TPC [111]. The radiation length  $X_0$  is characterizing the energy loss of high-energy photons (7/9 of the mean free path for pair production) and electrons (distance in which the energy drops to  $1/e$  by radiation) [174].

The radiation thickness of ALICE has been measured with a relative precision of  $\pm 6\%$  using reconstructed photon conversions [175]. Resulting systematic uncertainties of the spectra have been studied with special Monte Carlo productions.

Systematic uncertainties in pp collisions were evaluated for the first publication of  $p_T$  spectra at  $\sqrt{s} = 900$  GeV [176] with a relative variation of  $\pm 10\%$  corresponding to the uncertainty of the material budget measurements at that time. Systematic uncertainties on the  $p_T$  spectra evaluated for pp,  $\sqrt{s} = 900$  GeV are 0.2-1.5%, depending on  $p_T$ . These values have been assigned also for the other pp energies and for p-Pb collisions, where they amount to 0.2-0.5% for the 2012 data due to the restriction to  $p_T > 0.5$  GeV/c.

In the case of Pb-Pb the amount of material has been varied in the MC simulation<sup>6</sup> by  $\pm 7\%$  relative to the nominal value, resulting in an uncertainty of 0.5-1.7%, depending on  $p_T$  and centrality.

---

### 3.10.9 Particle composition

---

This contribution to the systematic uncertainty is related to the different composition of primary particles in the data compared to the Monte Carlo generator that was used to estimate efficiency corrections.

As shown in Figure 3.15 the efficiency is different for different particles. Mainly, two effects play a role. First, there is a  $p_T$  threshold that is required that a given particle leaves a track in the TPC that is sufficiently long (at least 120 crossed rows). This requires, neglecting the energy loss, a minimal  $p_T$  of about 150 MeV/c. When including the energy loss this cutoff is larger and depends also on the mass of the particle (as the specific energy loss depends on the velocity). As a result of the energy loss the  $p_T$  cutoff is approximately 150 MeV/c for pions, 200 MeV/c for kaons and 300 MeV/c for protons.

A second effect is visible for unstable particles like Kaons, arising from their decay. For large momenta ( $p_T > 4$  GeV/c) the efficiency is nearly constant and similar for all particle species. The lower efficiency for "other particles", that includes electrons, muons and strange baryons (visible in Figure 3.15 and labeled "other" in this plot) as well as the different shape is the result of the decay of the multi-strange baryons.

Efficiency corrections are obtained from Monte Carlo simulations and thus based on the particle composition in the event generator that is used. For the evaluation of the uncertainty related to this the relative fractions of the most abundant particles (pion, kaons and protons) are varied by  $\pm 30\%$  to account for the uncertainty in the particle composition. Figure 3.39 shows the variation of the particle fractions and the resulting variation of the efficiency in the case of Pb-Pb collisions. Similarly, particle ratios have been varied in pp and Pb-Pb.

At the time of the analysis no measurements of identified particle spectra were available. A comparison to the ALICE measurements is discussed in appendix C revealing a discrepancy to particle composition in the HIJING event generator that is exceeding the assumption used for the systematic uncertainties.

---

<sup>6</sup> The corresponding ALICE names of the MC productions are LHC10h8 (nominal), LHC10h9 (+7%) and LHC10h10 (-7%).

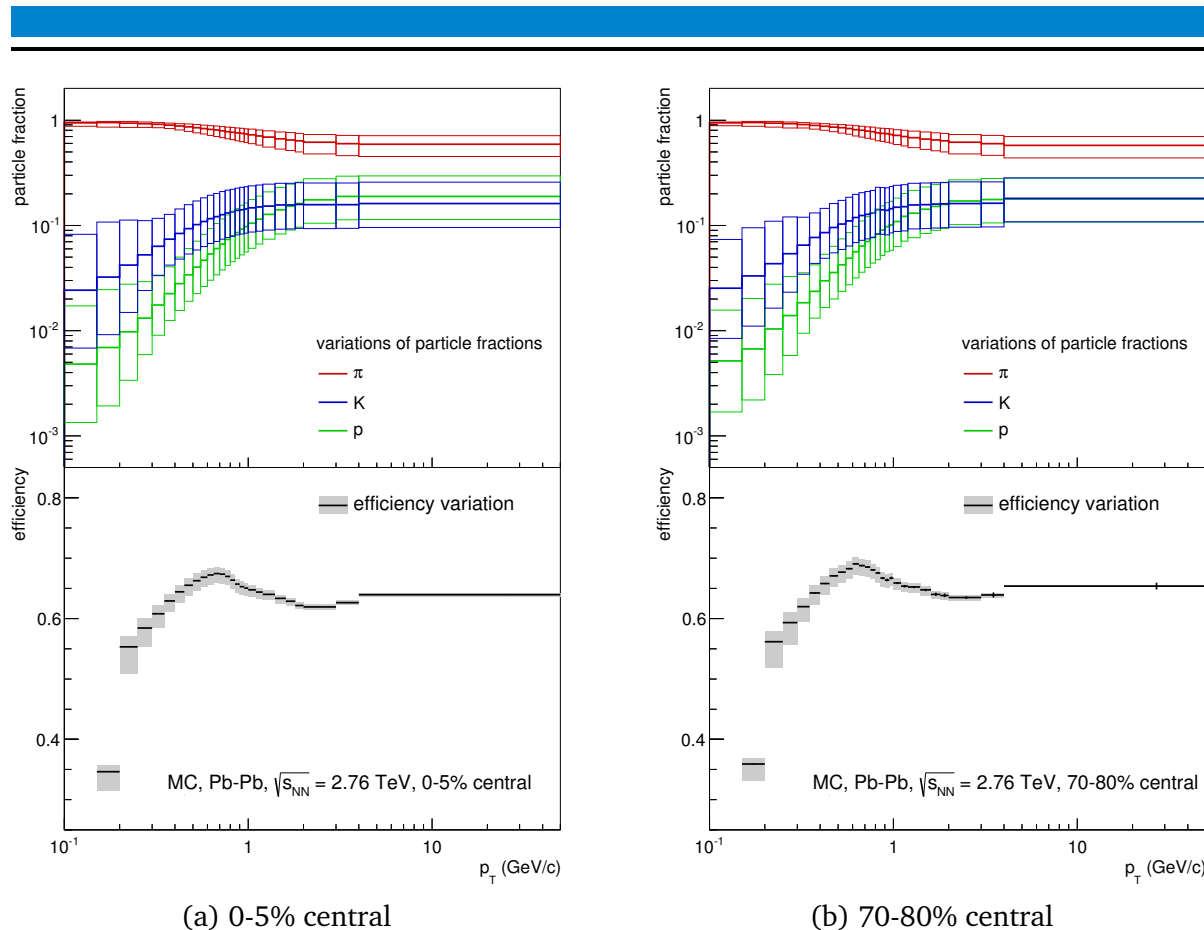


Figure 3.39.: Variation of the particle composition (top panels) and the resulting variation of the charged particle tracking efficiency (bottom panels) estimated for central (a) and peripheral (b) Pb–Pb collisions.

### 3.10.10 MC generator

All corrections obtained from simulations depend on the employed event generators in many respects: overall event shape, multiplicity distribution,  $dN/d\eta$  distribution, composition of primary and secondary particles, amount of secondary particles, amount and characteristics of diffractive events etc. Residual dependences of the analysis results on the Monte Carlo generator were studied using MC productions with alternative event generators.

For pp the generator was PHOJET<sup>7</sup> (instead of PYTHIA) to generate the corrections applied to the data at  $\sqrt{s} = 0.9$  and 7 TeV. For  $\sqrt{s} = 2.76$  TeV no PHOJET production was available at the time of the analysis, and the systematic uncertainty from the analysis of 7 TeV was assigned.

In p–Pb, HIJING<sup>8</sup> was used as an alternative to the default DPMJET, while in Pb–Pb HIJING is the default generator and DPMJET<sup>9</sup> was used as an alternative.

<sup>7</sup> ALICE productions LHC10e12 ( $\sqrt{s} = 900$  GeV) and LHC10f6 ( $\sqrt{s} = 7$  TeV)

<sup>8</sup> ALICE production: LHC12g1

<sup>9</sup> ALICE production: LHC10h2

---

### 3.10.11 Secondary particles

---

The scaling factors (Figure 3.21) applied on the secondary yield obtained from MC were varied by  $\pm 30\%$ , the resulting variations of the  $p_T$  spectra are assigned as systematic uncertainties. This applied to pp and Pb–Pb data, while in p–Pb, where no scaling factor applied by default, the scaling factor from Pb–Pb was used to determine the systematic uncertainty.

---

### 3.10.12 $p_T$ dependence of the systematic uncertainties

---

The  $p_T$  dependence of all contributions to the systematic uncertainties that are applied bin-by-bin (the normalization uncertainty not included) are shown in Figure 3.40 for pp. Likewise Figure 3.41 shows the contributions for p–Pb in three different bins of  $\eta_{\text{cms}}$  and Figure 3.42 for the most central and peripheral centrality bins of Pb–Pb. The total uncertainty (squared sum) has been flattened in the intermediate  $p_T$  region: The maximal uncertainty is assigned for a wider  $p_T$  range to avoid fluctuations from the track cut systematics resulting in odd-looking overall uncertainties.

Note that an uncertainty which is constant as a function of  $p_T$  does not imply a pure normalization effect. Only the systematic uncertainty related to centrality selection does affect primarily the normalization and is thus almost fully correlated between the bins. All other uncertainties assigned on the bin-by-bin level can potentially affect both, normalization and shape of the distribution. The systematic uncertainty related to centrality selection does affect essentially only the normalization and is thus highly correlated between the bins. It has been included but is nevertheless included in the bin-by-bin uncertainties.

---

### 3.10.13 Ratios of spectra at different pseudorapidities in p–Pb

---

Besides the three pseudorapidity intervals, also the ratios of spectra at the two forward pseudorapidities to those at midrapidity  $0.3 < \eta_{\text{cms}} < 0.8/|\eta_{\text{cms}}| < 0.3$  and  $0.8 < \eta_{\text{cms}} < 1.3/|\eta_{\text{cms}}| < 0.3$  have been evaluated, systematic uncertainties for these ratios partially cancel. Values are listed in Table 3.11.

The overall normalization uncertainty is fully correlated between the different  $\eta_{\text{cms}}$  intervals and fully cancels. Uncertainties related to the trigger and vertex bias, the tracking efficiency (evaluated from the TPC-ITS track matching efficiency), the underestimation of secondary particles in the simulation and the uncertainty of the material budget are assumed to be independent of  $\eta$  and canceled in the ratio. Variation of the event vertex selection, track selection and particle composition was evaluated thoroughly and resulted in a significant reduction of the systematic uncertainties. The uncertainty related to the MC event generator has been adopted unmodified from the analysis of the spectra themselves. The acceptance correction at the central and forward pseudorapidities are different in sign (cf. Figure 3.32) and are added linearly.

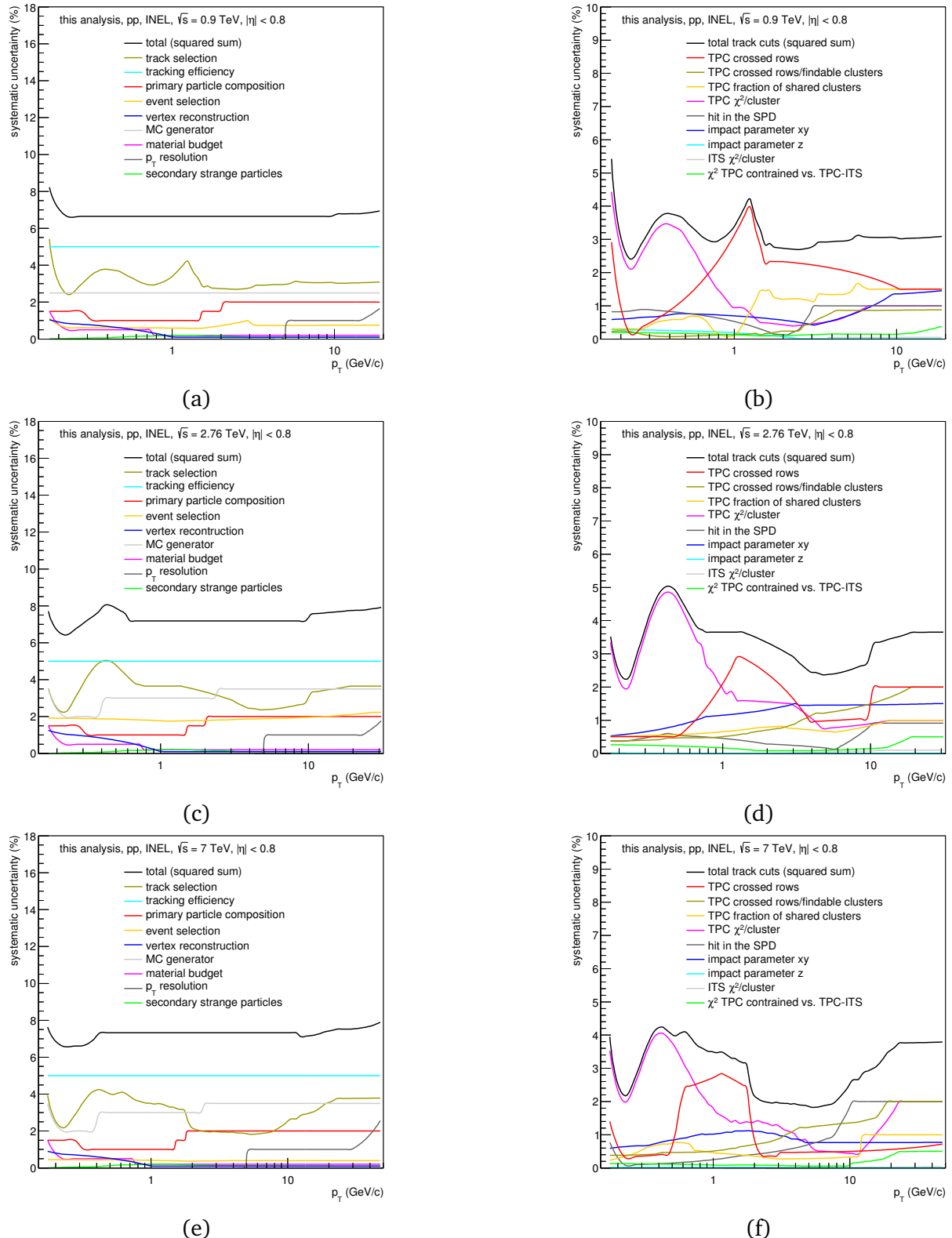


Figure 3.40.: Contributions to the systematic uncertainties in pp collisions at the different energies:  $\sqrt{s} = 0.9$  TeV (a, b),  $\sqrt{s} = 2.76$  TeV (c, d) and  $\sqrt{s} = 7$  TeV (e, f). Plots on the left side show all contributions to the systematic uncertainties, plots on the right show contributions from the variations of track cuts.

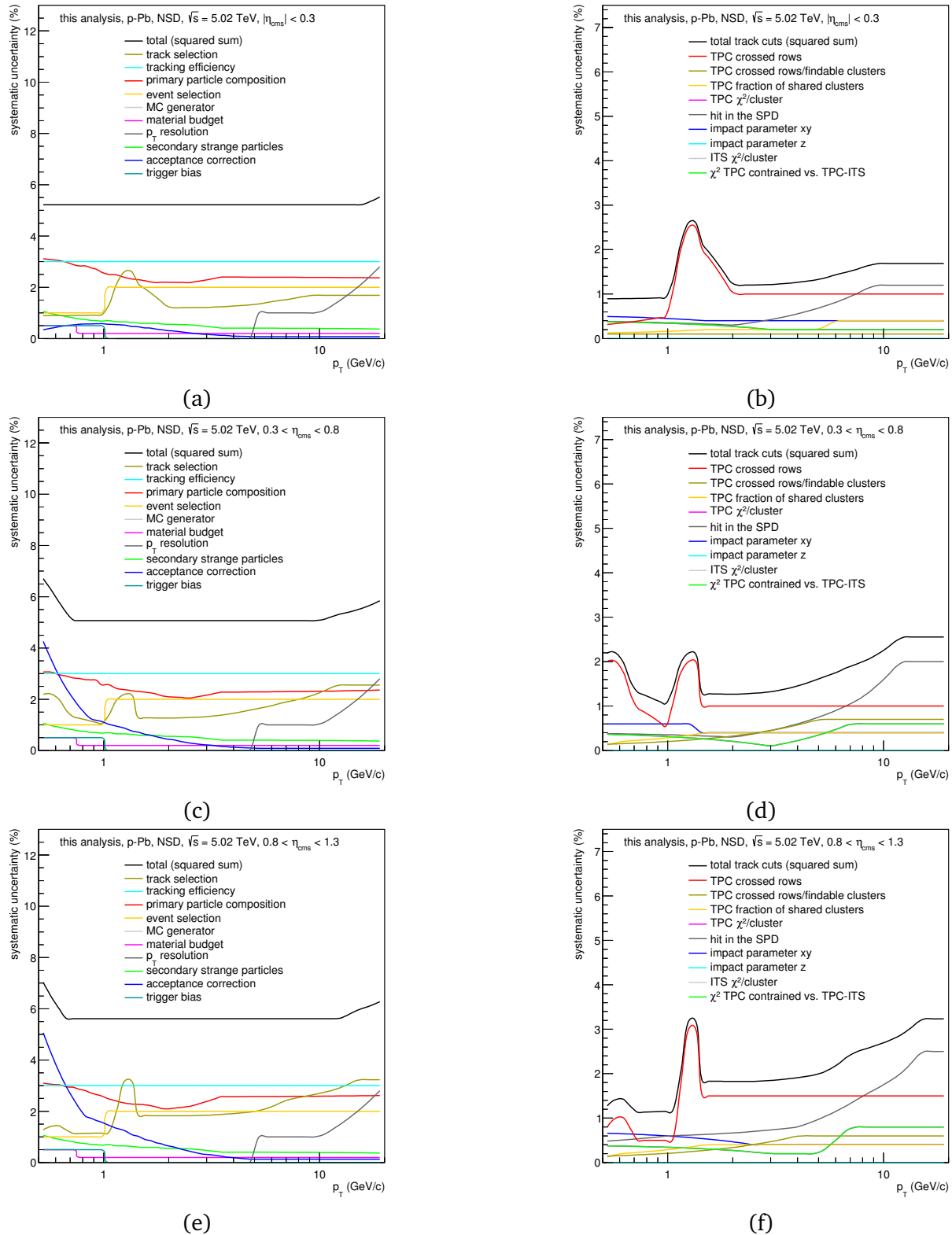
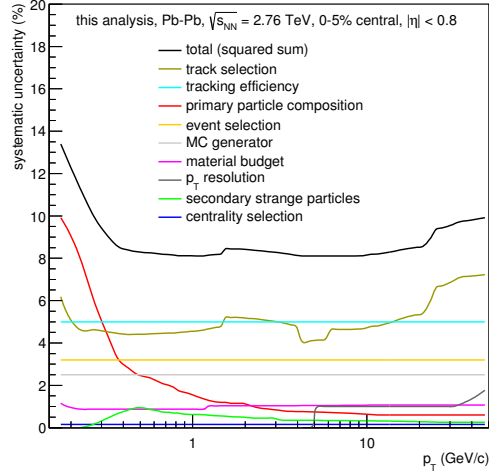
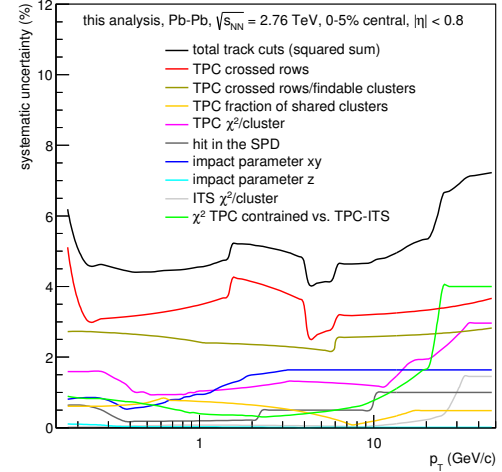


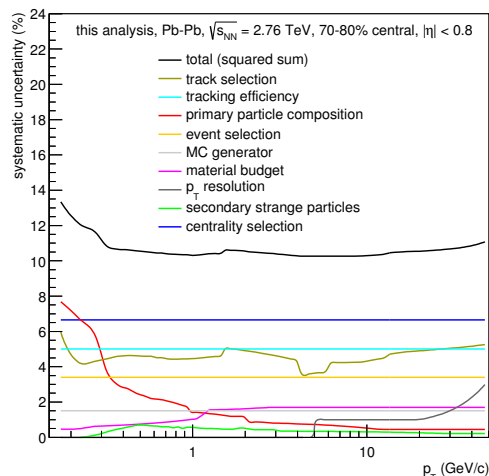
Figure 3.41.: Contributions to the systematic uncertainties in p-Pb collisions at  $\sqrt{s_{NN}} = 5.02$  TeV for the three intervals of  $\eta_{\text{cms}}$ :  $|\eta_{\text{cms}}| < 0.3$  (a, b),  $0.3 < \eta_{\text{cms}} < 0.8$  (c, d) and  $0.8 < \eta_{\text{cms}} < 1.3$  (e, f). Plots on the left side show all contributions to the systematic uncertainties, plots on the right show contributions from the variations of track cuts.



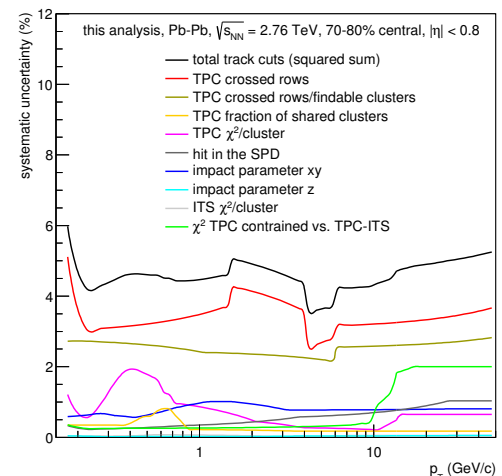
(a)



(b)



(c)



(d)

Figure 3.42.: Contributions to the total systematic uncertainties as a function of  $p_T$  for 0-5% central (a) and 70-80% peripheral (c) Pb-Pb collisions are shown on the left plots. The single contributions to the systematics from cut variations are shown on the right plots for central (b) and peripheral (d).



## 4 Results

In this section results of charged particle transverse momentum spectra are presented for all collision systems and energies. For Pb–Pb collisions this includes the centrality dependence of the  $p_T$  spectra. Results in p–Pb and Pb–Pb collisions are compared to those obtained from pp collisions in terms of the nuclear modification factor. In addition, comparisons to theoretical models and predictions as well as other measurements are presented. The  $p_T$  spectra and nuclear modification factors have been published in [164, 173, 177, 178].

The evolution of the average transverse momentum  $\langle p_T \rangle$  as a function of the charged particle multiplicity  $\langle N_{ch} \rangle$  is described in the separate chapter 5 with results presented in section 5.3.

### 4.1 pp collisions

Differential cross sections have been measured for inelastic pp collisions at  $\sqrt{s} = 0.9, 2.76$  and  $7$  TeV in the pseudorapidity ranges  $|\eta| < 0.8$  and  $|\eta| < 0.3$ . The measurements cover different transverse momentum ranges:  $0.15 < p_T < 20$  GeV/c at  $\sqrt{s} = 0.9$  TeV,  $0.15 < p_T < 32$  GeV/c at  $\sqrt{s} = 2.76$  TeV and  $0.15 < p_T < 50$  GeV/c at  $\sqrt{s} = 7$  TeV. These results have been published in [178] and are used for the construction of a pp reference spectrum needed to calculate the nuclear modification factors  $R_{AA}$  and  $R_{pPb}$ . The  $p_T$  distributions measured in pp collisions are compared to NLO pQCD calculations and simulations with Monte Carlo event generators. In addition to cross sections also differential yields for all energies are presented in this thesis. The  $p_T$  range of the differential yield at  $\sqrt{s} = 0.9$  TeV has been extended compared to the results obtained from the 2009 data taking period, published earlier in [176].

Figure 4.1 shows the differential yield ( $|\eta| < 0.8$ ) of primary charged particles measured in inelastic pp collisions at  $\sqrt{s} = 0.9$  TeV in comparison to different Monte Carlo (MC) event generators: PHOJET [156], PYTHIA8 [179] and PYTHIA6 [32, 153]. The comparison to PYTHIA6 includes the tunes D6T [180] and Perugia0 [155, 181]. For the comparison to the MC generators the statistical and systematic uncertainties of the measurement have been added in quadrature. Events generated with PYTHIA6, tune Perugia0 have been used to determine the corrections. PHOJET was used as an alternative to estimate the systematic uncertainties related to the event generator. Equivalent comparisons to the same MC generators are shown in Figure 4.2 for  $\sqrt{s} = 2.76$  TeV and Figure 4.3 for  $\sqrt{s} = 7$  TeV.

None of the MC generators is able to reproduce the data within the uncertainties of the measurement. Overall, the agreement between data and models is better at  $\sqrt{s} = 0.9$  TeV and the discrepancies rise for the higher energies.

For the comparison with MC generators it is instructive to consider the normalization and shape separately. Here the term normalization refers to the  $p_T$ -integrated yield. On the normalization to the number of inelastic events diffractive processes have a large impact, recall that about 30% of all inelastic events are single or double diffractive (see section 3.8.1). The overall shape of the  $p_T$  spectrum is dominated by non-diffractive collisions, as diffractive events produce only few particles at mid-rapidity. Estimates based on PYTHIA simulations show that

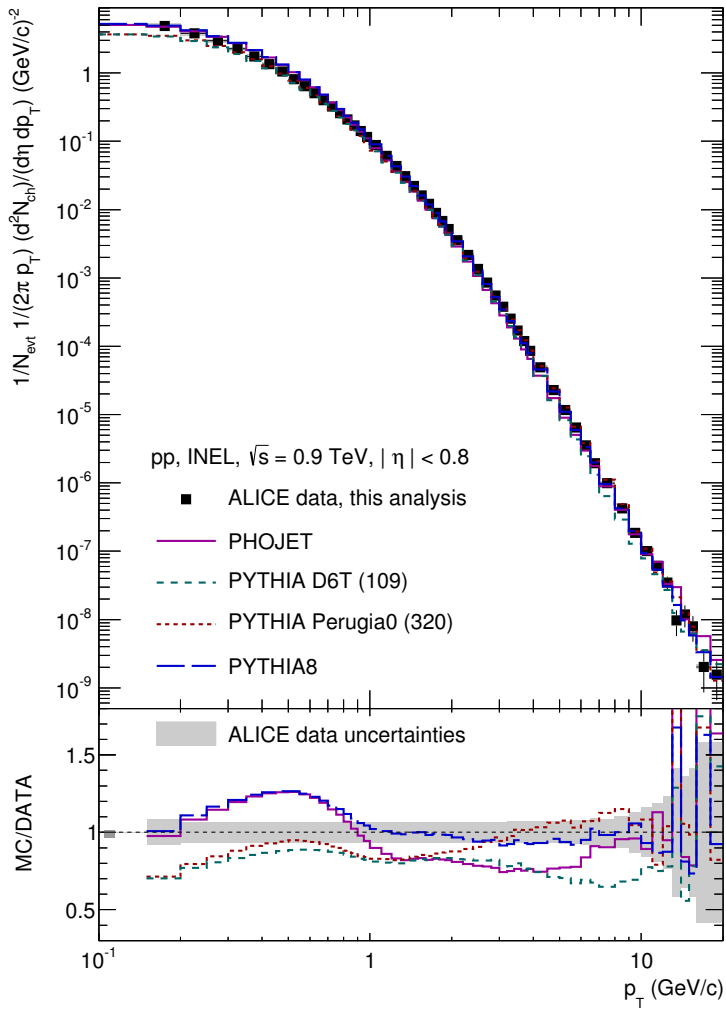


Figure 4.1.: Differential yield measured in pp collisions at  $\sqrt{s} = 0.9$  TeV in comparison to Monte Carlo generators. Uncertainties in the lower panel are statistical and systematic uncertainties added in quadrature. The additional asymmetric normalization uncertainty of the data amounts to  $+1.1\%/-3.4\%$  and is shown as a box near  $p_T = 0.1$  GeV/c.

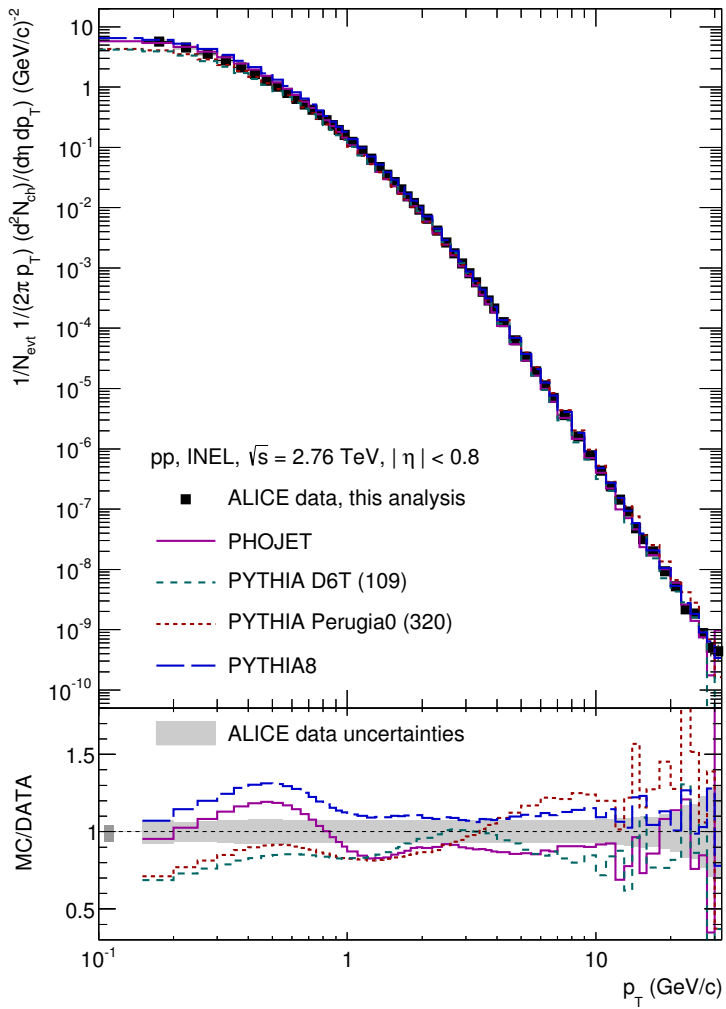


Figure 4.2.: Differential yield measured in pp collisions at  $\sqrt{s} = 2.76$  TeV in comparison to Monte Carlo generators. Uncertainties in the lower panel are statistical and systematic uncertainties added in quadrature. The additional asymmetric normalization uncertainty of the data amounts to  $+4.1\%/-6.3\%$  is shown as a box near  $p_T = 0.1$  GeV/c.

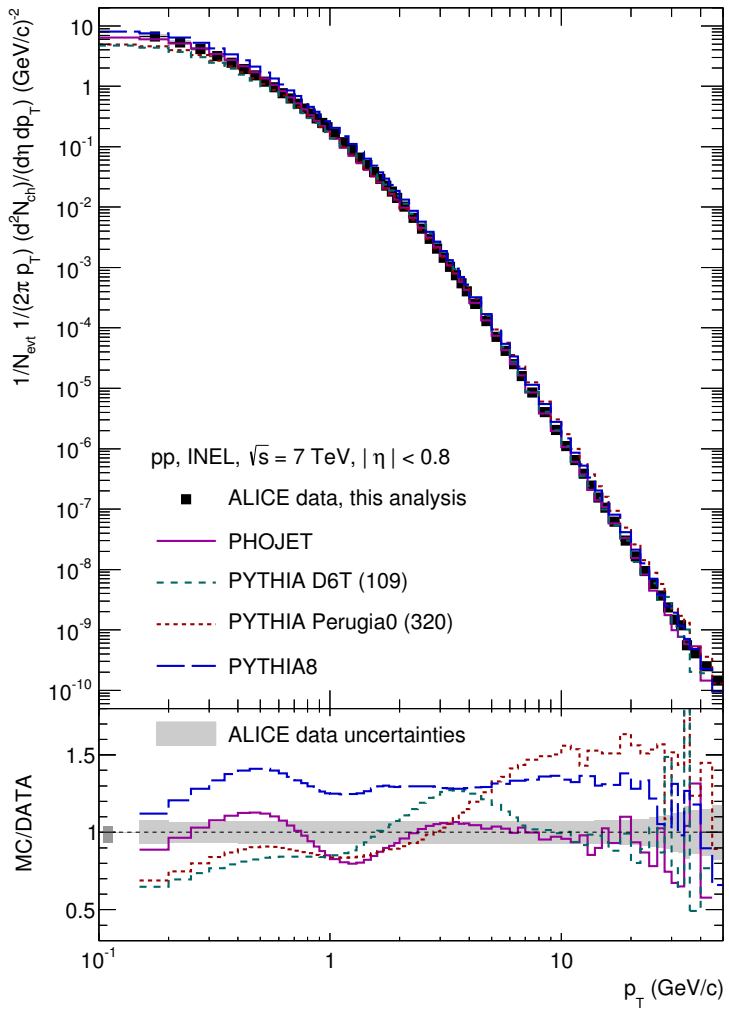


Figure 4.3.: Differential yield measured in pp collisions at  $\sqrt{s} = 7$  TeV in comparison to Monte Carlo generators. Uncertainties in the lower panel are statistical and systematic uncertainties added in quadrature. The additional asymmetric normalization uncertainty of the data amounts to  $+3.7\%/-6.8\%$  and is shown as a box near  $p_T = 0.1$  GeV/c.

the contribution from diffraction is negligible for  $p_T$  above 1 GeV/c. At  $p_T$  below 1 GeV/c diffractive events also contribute to the shape of the spectrum, but on a rather limited scale (up to 7%). Since the MC generators have difficulties describing diffraction [165] it is not unexpected that they are not able to get the normalization right.

It is also useful to distinguish between the low  $p_T$  (soft) and high  $p_T$  (hard) parts of the spectrum, as they are handled differently in the MC generators. At low  $p_T$  phenomenological approaches are used, while at high  $p_T$  methods of perturbative QCD are applicable and incorporated in the generators.

The PYTHIA tune D6T is rather old but has been used earlier [176] to estimate the corrections. This tune shows large deviations in the normalization, but gives a reasonable description of the shape at  $\sqrt{s} = 0.9$  TeV. However, at higher energies the differences in the shape become more pronounced. PYTHIA, tune Perugia0, is very similar to D6T for  $p_T < 1$  GeV/c, with the same discrepancy in normalization. At high  $p_T$  the two tunes differ by up to 60% (at  $\sqrt{s} = 7$  TeV). Perugia0 overestimates the yield at high  $p_T$  for 2.76 and 7 TeV. At 0.9 TeV it agrees within the uncertainties of the data. Both PYTHIA6 tunes underestimate the total yield by about 20%, nearly independent of  $\sqrt{s}$ .

PYTHIA8 provides the best description of the shape above 1 GeV/c in  $p_T$ , but overestimated the total yield, especially at the higher energies.

At all three collision energies PHOJET gives a better description of the normalization compared to the PYTHIA tunes employed. Surprisingly, the agreement with the data (regarding only normalization) improves with larger  $\sqrt{s}$ . The shape of the spectrum is reproduced within 30%, above  $p_T = 2$  GeV/c the shape is well described

The mechanism of color reconnection (CR) in PYTHIA8 is introduced in the context of average transverse momentum  $\langle p_T \rangle$  presented in chapter 5. Comparisons in Figures 4.1, 4.2 and 4.3 were obtained with color reconnection, which is the default in PYTHIA8. As discussed later (Chapter 5) with color reconnection a proper description of the  $N_{ch}$  dependence of the average transverse momentum is observed. To see the effect on the  $p_T$  spectra, Figure 4.4 shows the ratio of spectra from PYTHIA8 with and without color reconnection to the measured spectra for all three energies. Note that this particular comparison is for  $|\eta| < 0.3$  and the event class INEL > 0, containing only events that have at least one charged particle produced within the defined acceptance. In this case the acceptance is chosen as  $p_T > 0.15$  GeV/c and  $|\eta| < 0.3$ .

The effect of color reconnection leads to the production of less particles with larger transverse momenta as seen in Figure 4.4. This significantly improves the description of the data. A remarkable feature of the spectra is seen at low  $p_T$ : with CR the difference in shape between data and PYTHIA8 at low  $p_T$  does not depend on  $\sqrt{s}$ .

In Figure 4.5 the measured differential cross sections for all energies are shown and compared to NLO pQCD calculations [182]. The  $p_T$  spectra at all energies exhibit an approximate power law behavior at large  $p_T$ , this is expected from the pQCD scaling behavior, known as  $x_T$  scaling [183–187]. A fit of a power law function for  $p_T > 5$  GeV/c

$$\frac{1}{2\pi p_T} \frac{d^2\sigma}{d\eta dp_T} = A \cdot p_T^{-n} \quad (4.1)$$

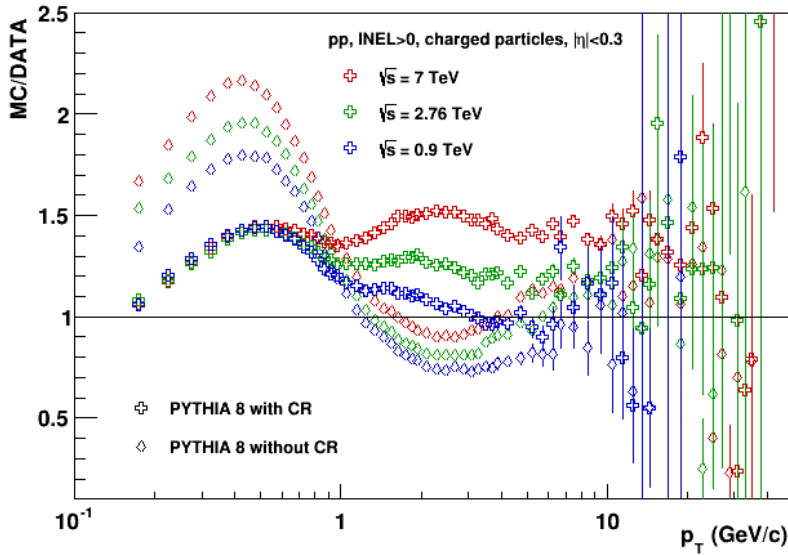


Figure 4.4.: Comparison of measured transverse momentum spectra of pp collisions at  $\sqrt{s} = 0.9$ , 2.76 and 7 TeV to spectra from PYTHIA8 obtained with (open crosses) and without (open diamonds) color reconnection. All ratios are for  $\text{INEL} > 0$  events (at least one charged particle in the acceptance) and the pseudorapidity range  $|\eta| < 0.3$ . Only statistical uncertainties are shown.

is in good agreement with the data, the obtained  $n$  of the fits are listed in Table 4.1 and are compatible with the values obtained from the NLO calculations [182, 188]. Systematic uncertainties quoted in Table 4.1 correspond to the maximal possible deviation compatible with the given  $p_T$ -dependent systematic uncertainties. In the NLO calculations the power  $n$  has a dependence on  $p_T$  itself, with the smallest  $n$  at  $p_T = 5 \text{ GeV}/c$  and the largest  $n$  at the maximal  $p_T$  covered in the measurement. As shown in Table 4.1 only a weak scale dependence of  $n$  in the range  $p_T/2 < \mu < 2p_T$  is observed. The maximal relative variation of  $n$  1% (5%) for  $\mu = 2p_T$  ( $\mu = p_T/2$ ).

At low  $p_T$ , the spectra have an approximately exponential shape. An approximate parameterization over the full  $p_T$  range can be achieved with the Tsallis function [189] or the modified Hagedorn function [190] which is used to construct a pp reference (see section 4.2). These parameterizations describe the data within  $\pm 20\%$  over the full  $p_T$  range. Characteristics of these functions is the exponential behavior at low  $p_T$  and a power law behavior at large  $p_T$ .

The measured differential cross section at all three collision energies are compared to calculations in next-to-leading order (NLO) perturbative QCD [182, 188], as shown in Figure 4.5. The NLO calculations are based on collinear factorization and use the CTEQ6.6M parton distribution functions [191] and the DSS fragmentation functions [192, 193] with the factorization, renormalization and fragmentation scales  $\mu_f = \mu_r = \mu_{f'} = \mu = p_T$ . They cover only the range  $p_T > 3 \text{ GeV}/c$ . At lower momenta, pQCD is not expected to be reliable. For the comparison to NLO calculations the measured data points are fitted with a modified Hagedorn function (see Equation (4.2)) to avoid that fluctuations in the data obfuscate the comparison. The ratios in the lower panels of Figure 4.5 reveal that the cross sections are not well described by the

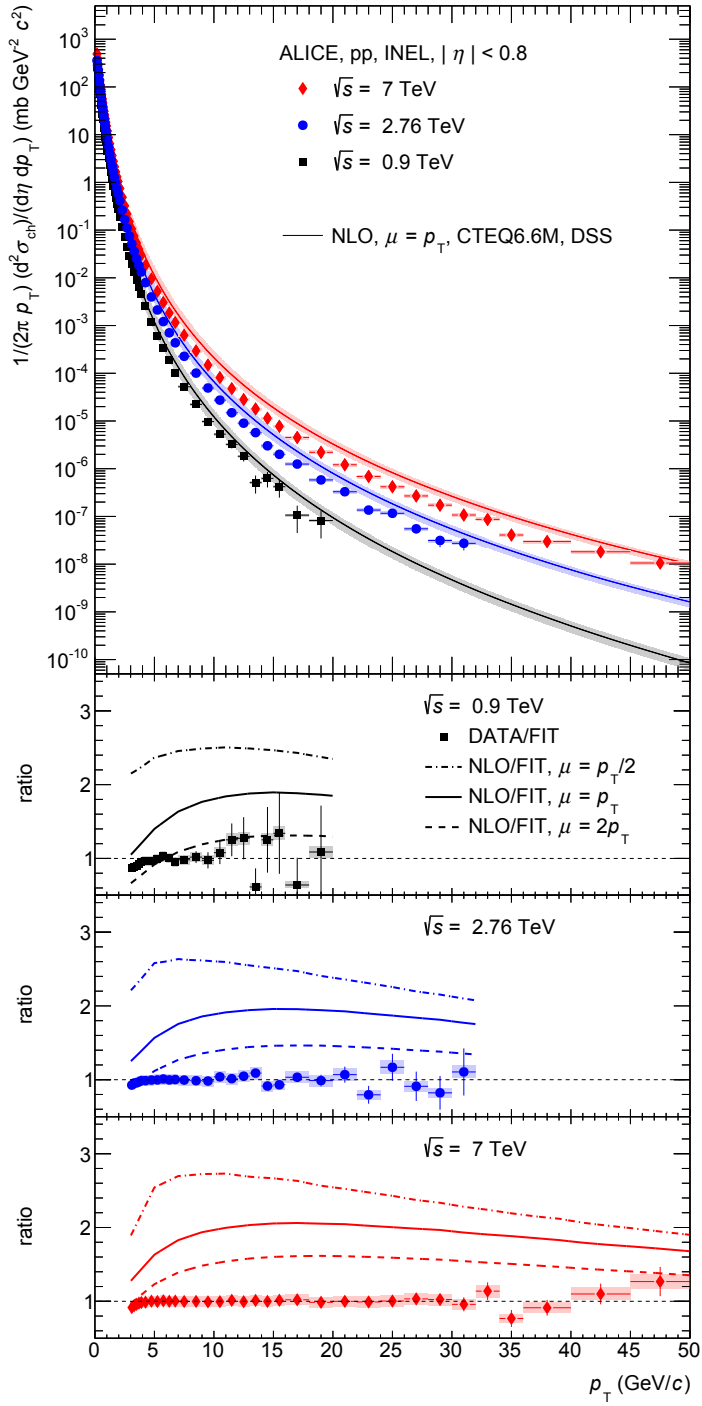


Figure 4.5.: Top: Differential cross section measured in pp collisions at  $\sqrt{s} = 0.9$ , 2.76 and 7 TeV in comparison to NLO calculations [182] for the same energies. The shaded band around the NLO calculations corresponds to a variation of the scale  $p_T/2 < \mu < 2p_T$ .

Bottom: Ratio of the NLO calculations (lines) and the data (points) to modified Hagedorn parameterization that is fitted to the data. Statistical (systematic) uncertainties of the data are shown as error-bars (filled boxes). The ratio NLO/FIT is shown for the scale  $\mu = p_T$  and the variations  $\mu = p_T/2$  and  $\mu = 2p_T$ . The additional overall normalization uncertainty of the data is not shown.

$\sqrt{s}$	$p_T$	$n$ from data	$n$ from NLO		
			$\mu = p_T$	$\mu = p_T/2$	$\mu = 2p_T$
0.9 TeV	5-20 GeV/c	$6.98 \pm 0.08(\text{stat.}) \pm 0.12(\text{syst.})$	6.49-7.22	6.84-7.30	6.44-7.22
2.76 TeV	5-32 GeV/c	$6.35 \pm 0.01(\text{stat.}) \pm 0.11(\text{syst.})$	5.96-6.78	6.24-6.83	5.92-6.76
7 TeV	5-50 GeV/c	$6.29 \pm 0.01(\text{stat.}) \pm 0.11(\text{syst.})$	5.63-6.53	5.80-6.57	5.61-6.51

Table 4.1.: Results of a power law fit to the measured  $pp$  differential cross section. For comparison the power of fits to the NLO calculations [182] are listed for different scales  $\mu$ . The ranges given for the NLO calculations correspond to the variation of  $n$  within the indicated  $p_T$  range. Smaller (larger) values of  $n$  correspond to lower (higher)  $p_T$ .

calculation. It is noticeable that the ratio NLO/FIT is almost independent of  $\sqrt{s}$ . Above 10 GeV in  $p_T$  the NLO calculations over-predict the measured cross section approximately by a factor 2, but describe the shape of the  $p_T$  spectrum rather well. Towards the largest  $p_T$  there is trend of reduced discrepancy between NLO and data. At lower  $p_T < 10$  GeV/c the discrepancy of NLO and data is reduced as well, but the shape of the distribution is not well described.

Other measurements of hadrons at the LHC show similar discrepancies between NLO pQCD calculations and the measured cross sections. About a factor 2 overprediction has been observed in measurements of neutral pions [194] from ALICE and charged particles from CMS [195, 196].

Since pQCD calculations are scale dependent a variation of the scales to  $\mu = 2p_T$  and  $\mu = p_T/2$  gives an estimate of the theoretical uncertainty. In the lower panel of Figure 4.5 the ratios are also shown with the alternative scales. Note that uncertainties of the parton distribution functions or fragmentation functions, which are obtained from fits to measured data, are not included in this uncertainty since the scale uncertainty is dominating the overall uncertainty [197]. The scale uncertainties decrease, as expected, for larger  $p_T$  and larger  $\sqrt{s}$ ; for the largest  $p_T$  they are on the order of 20-30%. The choice of a larger scale  $\mu = 2p_T$  reduces the discrepancy between data and NLO, but no agreement can be claimed. For a reduced scale of  $\mu = p_T/2$  the discrepancy between data and NLO grows. This could be caused by the fact that the involved partonic scale of the jet is larger than the  $p_T$  of the measured hadrons. The poor description of the LHC data with NLO pQCD has been attributed to the gluon-to-hadron fragmentation function in [198].

The ratio NLO/DATA shown in the lower panel of Figure 4.5 is almost independent of the collision energy. This equivalently signifies that the  $\sqrt{s}$  dependence of the cross section follows the NLO prediction. This is emphasized by the ratios of differential cross sections at different  $\sqrt{s}$  shown in Figure 4.6, where the agreement between data and NLO calculations is much better compared to the spectra themselves. For the ratio 2.76 TeV to 7 TeV the difference between NLO and data is below 5%, while being significantly larger for the ratios involving the 0.9 TeV data (up to approximately 15%). The double ratio of (2.76 TeV data to 7 TeV data) to (2.76 TeV NLO to 7 TeV NLO) is consistent with unity.

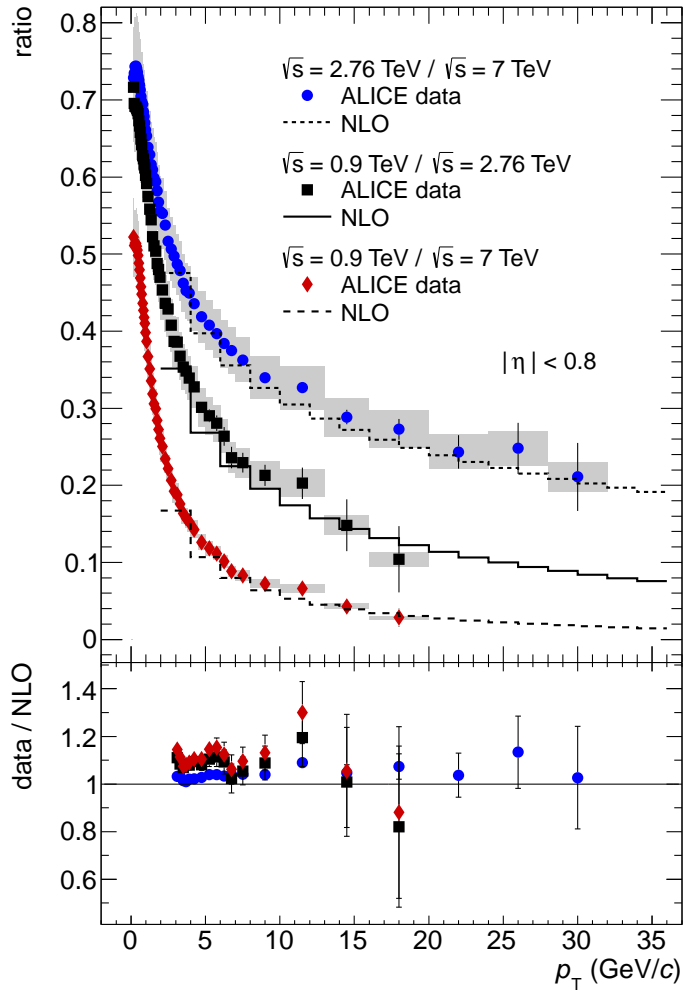


Figure 4.6.: Top: The ratio of differential cross sections at different  $\sqrt{s}$  for inelastic pp collisions from measurement (filled symbols) and NLO calculations (histogrammed lines). Systematic uncertainties (excluding the normalization uncertainties) of the data are shown as gray boxes, statistical uncertainties as lines. Note that part of the systematic uncertainties are correlated between the energies and cancel in the ratio. Bottom: The ratio data/NLO of the ratios from the top panel.

Figure published in [178].

---

## 4.2 Construction of pp references

---

To enable the comparison of particle production in p–Pb and Pb–Pb to pp in terms of the nuclear modification factors, a pp reference spectrum is required.

For the first publication of  $R_{AA}$  [172] no measurement of pp collisions at the same collision energy was available. The pp reference spectrum in the range 0.15–20 GeV/c was obtained as a power law interpolation between the invariant yields measured at  $\sqrt{s} = 0.9$  TeV and  $\sqrt{s} = 7$  TeV. To account for the uncertainty of this method, alternative choices for the pp reference were included in this publication. The The interpolation method described in [172] has not been used since the measurements of pp collisions at  $\sqrt{s} = 2.76$  TeV were available.

In the following publications of  $R_{AA}$  [177] and  $R_{pPb}$  [164] the used pp references were based exclusively on the measured differential cross section as presented in the previous section. The methods used to obtain the pp references at  $\sqrt{s} = 2.76$  TeV and 5.02 TeV are published in [178], and will be briefly described in the following.

---

### 4.2.1 pp reference for $\sqrt{s} = 2.76$ TeV

---

With the analyzed data sample, the cross section measurement of pp  $\sqrt{s} = 2.76$  TeV is limited by statistics to  $p_T < 32$  GeV/c, with considerable statistical uncertainties of about 30% at the largest  $p_T$ . For the calculation of the nuclear modification factor  $R_{AA}$  this would limit the  $p_T$  reach and introduce large statistical uncertainties at high  $p_T$ . Recall, that in Pb–Pb collisions the  $p_T$  reach is up to 50 GeV/c. In order to show  $R_{AA}$  also up to 50 GeV/c, a pp reference spectrum is needed also for  $p_T > 32$  GeV/c.

To extend the pp reference up to 50 GeV/c, the measured spectrum has been parameterized by the so-called modified Hagedorn function [190]

$$\frac{d^2\sigma}{d\eta dp_T} = A \cdot \frac{p_T}{m_T} \left( 1 + \frac{p_T}{p_0} \right)^{-n} \quad (4.2)$$

for  $p_T > 5$  GeV/c. Here, the  $m_T$  is the transverse mass  $m_T = \sqrt{m^2 + p_T^2}$  and  $m = 140$  MeV/c, corresponding to the pion mass, is used.

At low  $p_T$  the modified Hagedorn function behaves like an exponential in  $p_T$ , while at high  $p_T$  it has a power law behavior. For the  $p_T$  range used in the fit ( $> 5$  GeV/c), the spectrum exhibits an approximate power law behavior. In this case the exponential part of the modified Hagedorn function acts as a correction that improves the fit at the lower end of the  $p_T$  range.

In the range  $0.15 < p_T < 5$  GeV/c the measured differential cross section is used as the pp reference while for  $5 < p_T < 50$  GeV/c the parameterization is used. Above 32 GeV/c in  $p_T$  this parameterization is actually an extrapolation. The fit range of the parameterization has been varied to  $p_T > 3$  GeV/c and  $p_T > 7$  GeV/c to estimate the additional systematic uncertainty related to this procedure. Systematic and statistical uncertainties from the spectra are propagated to the parameterization/extrapolation.

Figure 4.7 shows the measured cross section for  $|\eta| < 0.8$  at  $\sqrt{s} = 2.76$  TeV together with the modified Hagedorn parameterization of the high  $p_T$  part and the extrapolation up to 50

GeV/c in  $p_T$ . The bottom panel of Figure 4.7 shows the ratio fit/data that demonstrates the quality of the fit. Systematic uncertainties of both, the measurement and the parameterization/extrapolation are also shown.

The total  $p_T$ -dependent systematic uncertainty of the pp reference spectrum ranges from 6.4% at low  $p_T$  up to 19% at  $p_T = 50$  GeV/c. In addition, the normalization to inelastic events comes with a relative uncertainty of 1.9%, fully correlated between the  $p_T$  bins.

Considering that the reference is not measured in the full  $p_T$  range and based partially on an parameterization/extrapolation it is desirable to check the consistency with other approaches.

Figure 4.8 shows the ratio of alternative references to the reference described above. The alternative references shown are: a measurement by CMS [196], the results at  $\sqrt{s} = 7$  TeV scaled to 2.76 TeV using the ratio obtained from NLO calculations, simulations with PYTHIA8 [179] and the interpolation between yields as used for the first publication of  $R_{AA}$  [172]. Systematic uncertainties of the reference are shown without the overall normalization uncertainty of 1.9%.

The CMS collaboration has measured the  $p_T$  distribution of charged particles in pp collisions at  $\sqrt{s} = 2.76$  TeV [196], though in a slightly wider pseudorapidity range of  $|\eta| < 1$ . It agrees within the overall uncertainty (additional systematic uncertainty of the CMS reference is 6%). For  $p_T < 6$  GeV/c the two measurements are in excellent agreement, while for larger  $p_T$  the CMS data is below the ALICE reference.

As discussed in the previous section, the NLO calculations are able to describe the evolution of the differential cross section with  $\sqrt{s}$ . This allows to scale the differential cross section measured at  $\sqrt{s} = 7$  TeV, by the the ratio from NLO calculations to obtain the cross section at  $\sqrt{s} = 2.76$  TeV:

$$\left( \frac{d^2\sigma}{d\eta dp_T} \right)_{\sqrt{s}=2.76\text{TeV}} = \underbrace{\left( \frac{d^2\sigma}{d\eta dp_T} \right)_{\sqrt{s}=7\text{TeV}}}_{\text{measurement}} \cdot \frac{\left( \frac{d^2\sigma}{d\eta dp_T} \right)_{\text{NLO}, \sqrt{s}=2.76\text{TeV}}}{\underbrace{\left( \frac{d^2\sigma}{d\eta dp_T} \right)_{\text{NLO}, \sqrt{s}=7\text{TeV}}}_{\text{ratio from NLO calculation}}} \quad (4.3)$$

The  $p_T$  interval of  $3 < p_T < 50$  GeV/c for the scaled reference is the maximal overlap of the NLO calculation (starting from 3 GeV/c in  $p_T$ ) and the 7 TeV measurement (up to 50 GeV/c in  $p_T$ ). The reference obtained with this approach agrees well with the actual pp reference over the full  $p_T$  range.

As described in the previous section PYTHIA8 is able to describe the shape of the  $p_T$  spectrum at  $\sqrt{s} = 2.76$  TeV very well for  $p_T > 1$  GeV/c, but with a normalization about 10% above the data. A reference obtained from PYTHIA8 simulations agrees with the nominal reference for  $p_T > 15$  GeV/c. The shape is well described also at lower  $p_T$ .

The power law interpolation between the differential yields at  $\sqrt{s} = 0.9$  TeV and 7 TeV used in [172] differs from the current reference.

The final pp reference at  $\sqrt{s} = 2.76$  TeV, including the extrapolation is shown in Figure 4.9.

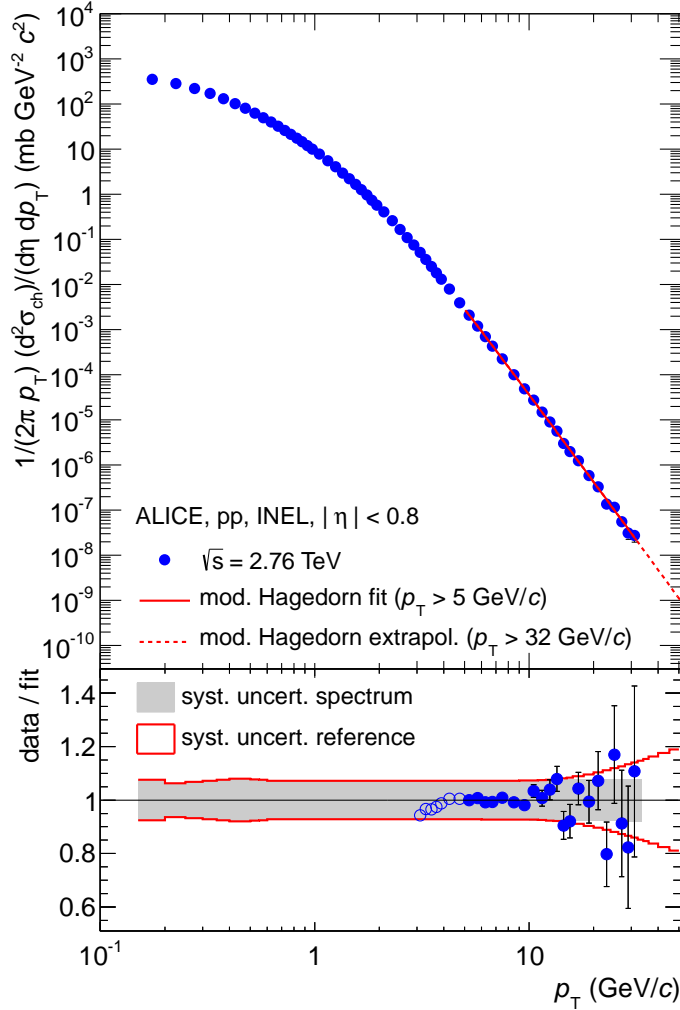


Figure 4.7.: Top: Differential cross section of charged particles measured in inelastic pp collisions at  $\sqrt{s} = 2.76$  TeV. The line shows the parameterization by a modified Hagedorn function fitted to the data for  $p_T > 5$  GeV/c. Above  $p_T = 32$  GeV/c the parameterization is extrapolated to  $p_T = 50$  GeV/c, indicated as a dashed line. Bottom: Ratio of the data points to the parameterization. The filled band around unity shows the systematic uncertainties of the data (excluding the normalization uncertainty). The lines show the systematic uncertainty of the reference, including the uncertainty of the parameterization and extrapolation. Data points which are used for the fit are shown as full circles. To estimate the uncertainty of the parameterization the fit range was changed to  $p_T > 3$  GeV/c, these data points are shown as open circles.

Figure published in [178].

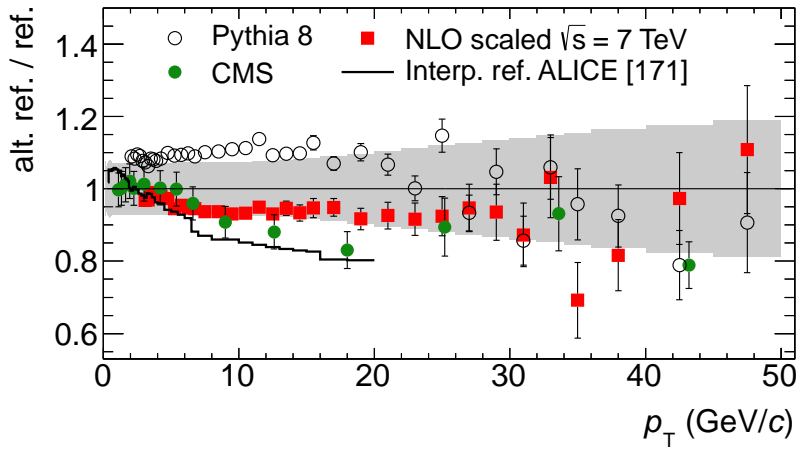


Figure 4.8.: Comparison of alternative pp references at  $\sqrt{s} = 2.76$  TeV discussed in the text to the chosen one in term of the ratio. The gray band around unity shows the  $p_T$  dependent uncertainty of the reference. Additional normalization uncertainties are not shown. Error-bars shown for the CMS reference are statistical and systematic uncertainties added in quadrature.

Figure published in [178].

#### 4.2.2 pp reference for $\sqrt{s} = 5.02$ TeV

For the calculation of  $R_{p\text{Pb}}$ , a pp reference spectrum at  $\sqrt{s} = 5.02$  TeV for  $|\eta| < 0.3$  is needed. As there is no measurement at this collision energy, the spectra measured at  $\sqrt{s} = 7$  TeV and 2.76 TeV in the pseudorapidity range  $|\eta| < 0.3$  are used to construct the reference spectrum with a combination of different approaches applied at different  $p_T$  ranges.

At large  $p_T$  ( $> 5$  GeV/c), where pQCD calculations are reliable the NLO cross sections [182] are used to scale down the 7 TeV data:

$$\left( \frac{d^2\sigma}{d\eta dp_T} \right)_{\sqrt{s}=5.02\text{TeV}} = \underbrace{\left( \frac{d^2\sigma}{d\eta dp_T} \right)_{\sqrt{s}=7\text{TeV}}}_{\text{measurement}} \cdot \frac{\left( \frac{d^2\sigma}{d\eta dp_T} \right)_{\text{NLO}, \sqrt{s}=5.02\text{TeV}}}{\underbrace{\left( \frac{d^2\sigma}{d\eta dp_T} \right)_{\text{NLO}, \sqrt{s}=7\text{TeV}}}_{\text{ratio from NLO calculation}}} \quad (4.4)$$

This method makes use of the measurement of 7 TeV extending up to 50 GeV/c in  $p_T$ . As statistical uncertainties become significant for  $p_T > 20$  GeV/c also in the 7 TeV data, the resulting 5.02 TeV spectrum has been parameterized in the range  $20 < p_T < 50$  GeV/c by a power law function:

$$\frac{d^2\sigma(p_T)}{d\eta dp_T} = A \cdot p_T^{-n}. \quad (4.5)$$

This parameterization was intended to serve as a pp reference for  $20 < p_T < 50$  GeV/c.

At  $p_T < 5$  GeV/c the NLO calculations are not reliable, as evident from the increasing scale uncertainties (see Figure 4.5). In this range the differential cross section at  $\sqrt{s} = 5.02$  TeV

is constructed from the data at  $\sqrt{s} = 2.76$  and  $7$  TeV assuming a power law behavior of the differential cross section as a function of  $\sqrt{s}$  for fixed  $p_T$ :

$$\frac{d^2\sigma(\sqrt{s})}{d\eta dp_T} \propto \sqrt{s}^n. \quad (4.6)$$

The pp reference spectrum in the range  $0.15 < p_T < 5$  GeV/c is obtained from this power law interpolation for each  $p_T$  bin.

The systematic uncertainty of the pp reference is determined by the maximal relative systematic uncertainty of the data at  $\sqrt{s} = 2.76$  and  $7$  TeV in the range  $p_T < 5$  GeV/c. For  $p_T > 5$  GeV the uncertainty of the underlying  $\sqrt{s} = 7$  TeV measurement is added in quadrature with the uncertainty from a scale variation of  $p_T/2 < \mu < 2p_T$  in the NLO calculation. In addition, the difference between the power law interpolation and the NLO scaling in the overlap region of  $3 < p_T < 5$  GeV/c is assigned as an uncertainty of the method and added quadratically. Statistical uncertainties of the measured data at  $\sqrt{s} = 2.76$  TeV and  $\sqrt{s} = 7$  TeV are independent and propagated to the pp reference according to Equation (4.6) for  $p_T < 5$  GeV/c. Above  $p_T = 5$  GeV the relative statistical uncertainties are identical to the ones of the  $\sqrt{s} = 7$  TeV data.

The pp reference spectrum for  $\sqrt{s} = 5.02$  TeV and  $|\eta| < 0.3$  is shown in Figure 4.9 together with the power law parameterization. The ratio DATA/FIT in the bottom panel of Figure 4.7 demonstrates that the high  $p_T$  part of the spectrum is well described by the power law function. While only data points above  $20$  GeV/c in  $p_T$  are used for the fit, the extrapolation of the fit towards lower  $p_T$  is in remarkable agreement with the data (open points in Figure 4.9).

The overall systematic uncertainty (excluding normalization) of the pp reference spectrum amounts to 6.7-8.4% for the full  $p_T$  range of  $0.15 < p_T < 50$  GeV/c and is shown as gray band in the lower panel of Figure 4.9. The publication of  $R_{pPb}$  [164] covers only the range  $0.5 < p_T < 20$  GeV/c, in this range the uncertainty of the reference amounts to 7.7-8.2%. The additional normalization uncertainty of 3.6% is identical to the one in pp at  $\sqrt{s} = 7$  TeV. Also the statistical uncertainties at high  $p_T$  are fixed from the 7 TeV pp data. They remain below 5% for  $p_T < 20$  GeV/c and reach 16% at 50 GeV/c.

For the second publication of p-Pb spectra with the extended kinematic range of  $0.15 < p_T < 50$  GeV/c the power law parameterization of the pp reference has not been adopted to calculate the nuclear modification factor. Instead, the pp reference spectrum for the full acceptance  $|\eta| < 0.8$  was used, since only a weak pseudorapidity dependence of the  $p_T$  spectra for  $|\eta| < 0.8$  is observed [173].

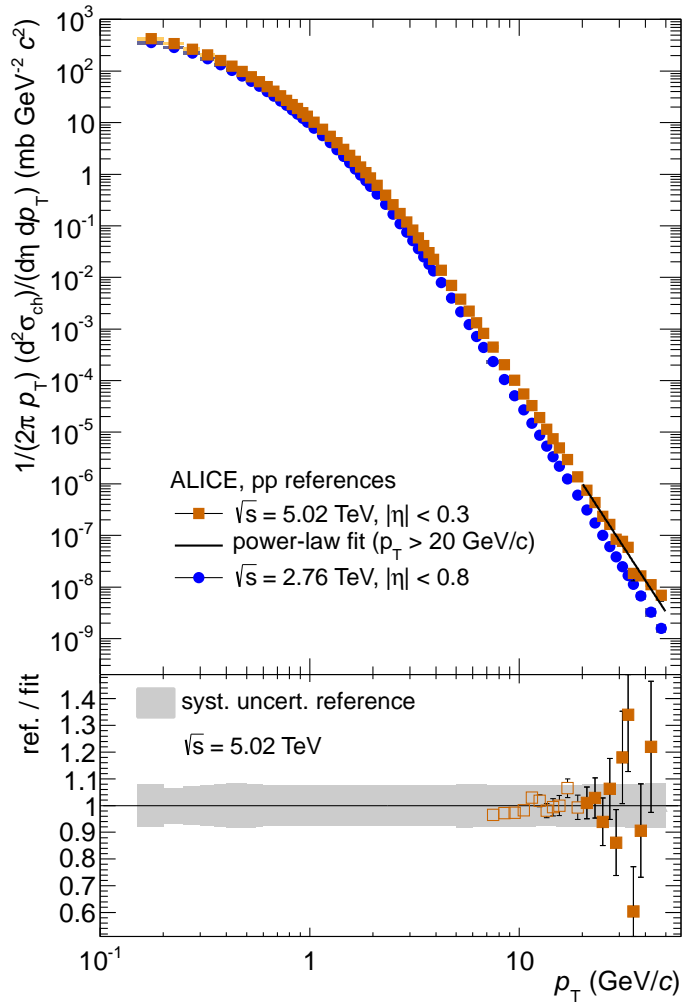


Figure 4.9.: Top: Constructed pp references for  $\sqrt{s} = 2.76$  TeV ( $|\eta| < 0.8$ ) and  $5.02$  TeV ( $|\eta| < 0.3$ ) as described in the text. The power law parameterization of the reference at  $\sqrt{s} = 5.02$  TeV is shown for  $p_T > 20$  GeV/c. Bottom: Ratio of the reference at  $\sqrt{s} = 5.02$  TeV obtained from NLO-scaling to the power law parameterization. The band around unity shows the systematic uncertainty of the 5.02 TeV reference.

Figure published in [178].

## 4.3 p–Pb collisions

In non-single-diffractive (NSD) p–Pb collisions at  $\sqrt{s_{\text{NN}}} = 5.02$  TeV  $p_{\text{T}}$  spectra of charged particles have been measured in three pseudorapidity intervals covering the kinematic range  $-0.3 < \eta_{\text{cms}} < 1.3$ , with positive  $\eta_{\text{cms}}$  defined in the direction of the Pb ion<sup>1</sup>. This range corresponds approximately to the pseudorapidity interval of  $|\eta_{\text{lab}}| < 0.8$  covered by the detector. In this section the results are presented as differential yields and, utilizing the pp reference measurements described in the previous section, in terms of the nuclear modification factor  $R_{\text{pPb}}$ .

The results based on the data from the 2012 p–Pb pilot run have been published in [164] for  $0.5 < p_{\text{T}} < 20$  GeV/c. Results obtained from the 2013 high statistics p–Pb run extending the  $p_{\text{T}}$  range to  $0.15 < p_{\text{T}} < 50$  GeV/c are published in [173]. In both cases only minimum bias (MB) triggered collisions were analyzed.

### 4.3.1 2012 pilot run

The differential yields measured in NSD p–Pb collisions at  $\sqrt{s_{\text{NN}}} = 5.02$  TeV are shown in the upper panel of Figure 4.10 for three intervals of pseudorapidity  $|\eta_{\text{cms}}| < 0.3$ ,  $0.3 < \eta_{\text{cms}} < 0.8$  and  $0.8 < \eta_{\text{cms}} < 1.3$ . Shown in the same figure is the pp reference for  $|\eta_{\text{cms}}| < 0.3$ , which is calculated as the cross section for inelastic (INEL) collisions at  $\sqrt{s} = 5.02$  TeV (as shown in Figure 4.9) scaled by the average nuclear overlap  $\langle T_{\text{pPb}} \rangle$ . The agreement of the scaled pp reference with the p–Pb spectrum at high  $p_{\text{T}}$  is remarkable, while at low  $p_{\text{T}}$  the p–Pb data shows a deviation from the scaled pp reference.

From the ratio of spectra at different intervals of  $\eta_{\text{cms}}$  shown in the bottom panel of Figure 4.10 the evolution of the spectrum as a function of pseudorapidity is illustrated. Systematic uncertainties of the ratios are reduced with respect to the uncertainties of the differential yields, as part of the uncertainties are correlated (see section 3.10.13 for a detailed description). At more forward pseudorapidities (Pb side) the overall integrated charge particle yield is increases, consistent with the results of the  $dN_{\text{ch}}/d\eta_{\text{lab}}$  measurement [163], and a gradual softening of the particle production is observed. Overall, the variation of the spectra with  $\eta_{\text{cms}}$  is small with a maximal difference at the lowest  $p_{\text{T}}$  of 4% (8%) for  $0.3 < \eta_{\text{cms}} < 0.8$  ( $0.8 < \eta_{\text{cms}} < 1.3$ ). Nevertheless, this little variation is larger than what is observed in pp collisions (2% at lowest  $p_{\text{T}}$ ).

Nuclear effects are quantified in terms of the nuclear modification factor  $R_{\text{pPb}}$ , which is defined as the ratio of differential yields in p–Pb collisions to that in pp collisions, scaled by the average number of binary nucleon-nucleon collisions  $\langle N_{\text{coll}} \rangle$  in one p–Pb collision. Equivalently, the pp reference can be calculated as the cross section scaled by the average nuclear overlap  $\langle T_{\text{pPb}} \rangle$

$$R_{\text{pPb}}(p_{\text{T}}) = \frac{d^2N_{\text{ch}}^{\text{pPb}}/d\eta dp_{\text{T}}}{\langle N_{\text{coll}} \rangle \cdot d^2N_{\text{ch}}^{\text{pp}}/d\eta dp_{\text{T}}} = \frac{d^2N_{\text{ch}}^{\text{pPb}}/d\eta dp_{\text{T}}}{\langle T_{\text{pPb}} \rangle \cdot d^2\sigma_{\text{ch}}^{\text{pp}}/d\eta dp_{\text{T}}} \quad (4.7)$$

<sup>1</sup> This sign convention is used in this thesis and in the first p–Pb publication [164]. It is opposite to the more common convention in [173], where positive  $\eta_{\text{cms}}$  corresponds to the direction of the proton.

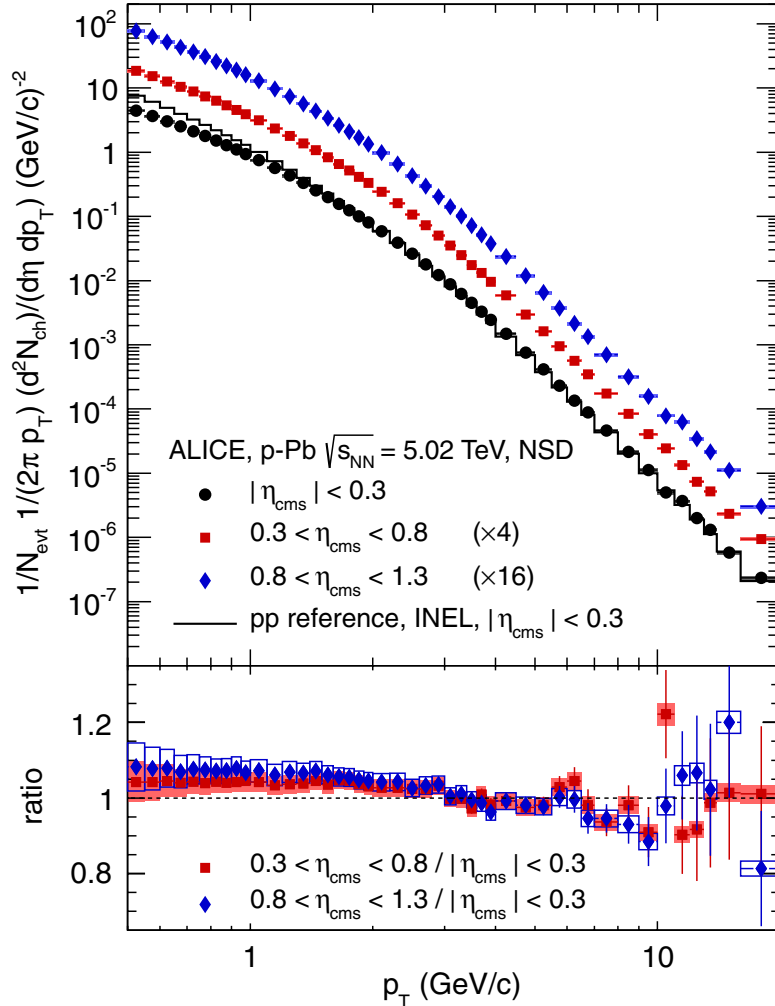


Figure 4.10.: Top: Measured differential charged particle yields in non-single-diffractive (NSD) p-Pb collisions in three ranges of  $\eta_{\text{cms}}$ . Results for  $0.3 < \eta_{\text{cms}} < 0.8$  and  $0.8 < \eta_{\text{cms}} < 1.3$  are scaled for better visibility. Both, statistical and systematic uncertainties are smaller than the symbol size. The reference spectrum for inelastic (INEL) pp collisions at the equivalent collision energy and identical pseudorapidity range is shown as black line (without uncertainties) in comparison. Overall normalization uncertainties of the p-Pb spectra and pp reference are not shown.

Bottom: Ratio of the differential yields measured at moderately forward rapidities to those at mid-rapidity. Statistical uncertainties of the ratio are shown as error-bars and systematic uncertainties as boxes.

Figure published in [164]

To determine  $R_{p\text{Pb}}$ , the pp reference obtained from the differential cross section is used.  $\langle T_{p\text{Pb}} \rangle$  is calculated from a MC Glauber model with the average taken over all events with at least one binary nucleon-nucleon collision (see section 1.7 for a description of the MC Glauber model). In minimum bias (0-100% central) p–Pb collisions the numerical values obtained with a nucleon-nucleon cross section of  $\sigma_{\text{NN}} = 70 \pm 5 \text{ mb}$  are  $\langle T_{p\text{Pb}} \rangle = 0.0983 \pm 0.0035 \text{ mb}^{-1}$  for the nuclear overlap. The corresponding number of binary collisions is  $\langle N_{\text{coll}} \rangle = 6.9 \pm 0.7$ , and  $N_{\text{part}} = N_{\text{coll}} + 1$ .

The fact that for p–Pb the spectra are presented in NSD collisions is due to the trigger used in p–Pb (see sections 3.4.1 and 3.8.1 for a description of the trigger). These spectra are compared to inelastic (INEL) pp collisions in terms of  $R_{p\text{Pb}}$ . Clearly it would be preferable to to this comparison using also INEL p–Pb collisions. Invariant yields from NSD and INEL p–Pb collisions can differ in shape and normalization.

Differences of the shape are only affecting the low  $p_{\text{T}}$  part of the spectrum as diffractive events do not produce high momentum particles in the central rapidity. Estimates with the MC event generator DPMJET show that the difference in shape is below 0.5% at the lowest  $p_{\text{T}}$ . Above 2 GeV/c in  $p_{\text{T}}$  no difference in shape is observed in the simulation.

The difference in the normalization of the invariant yield to NSD and INEL events, which is the fraction of pure single diffractive events<sup>2</sup>, is significant. With the MC event generators HIJING and DPMJET is was estimated that the INEL yield is 3-4% lower compared to the NSD yield. This number is consistent with the fraction of single-diffractive events measured in pp collisions at 7 TeV (approximately 20%) combined with the fraction of p–Pb collisions in which only a single nucleon-nucleon collision occurs, as estimated from the Glauber MC approach (also approximately 20%). Note that independent of the choice of events in p–Pb collisions (i.e. NSD or INEL), the pp reference should always be for INEL events.

The measured  $R_{p\text{Pb}}$  with NSD event selection is shown in Figure 4.11. For  $p_{\text{T}} > 2 \text{ GeV/c}$  it is consistent with unity indicating that no strong nuclear effects are present in p–Pb collisions at large transverse momenta. Below 2 GeV/c in  $p_{\text{T}}$  the nuclear modification factor drops to about 0.6 at  $p_{\text{T}} = 0.5 \text{ GeV/c}$ . A fit to the flat region of the measured  $R_{p\text{Pb}}$  in the range  $6 < p_{\text{T}} < 20 \text{ GeV/c}$  yields an average of  $\langle R_{p\text{Pb}} \rangle = 1.06 \pm 0.01(\text{stat.}) \pm 0.10(\text{syst.}) \pm 0.06(\text{norm.})$ .

An enhancement of high  $p_{\text{T}}$  particle yields in p–A collisions was first observed in fixed target experiments [199, 200] and is commonly referred to as *Cronin effect* or *Cronin enhancement*. In d–Au collisions at  $\sqrt{s_{\text{NN}}} = 200 \text{ GeV}$  such an enhancement of the nuclear modification factor  $R_{\text{dAu}}$  was observed for  $p_{\text{T}} > 2 \text{ GeV/c}$  by the RHIC experiments [201–204]. A maximal of about 1.4 was observed for  $3 < p_{\text{T}} < 5 \text{ GeV/c}$ , while lower  $p_{\text{T}}$  below 2 GeV/c the nuclear modification factor was less than unity. For neutral pions, PHENIX measured an  $R_{\text{dAu}}$  that is consistent with unity [202].

Only a hint of a Cronin-type enhancement at intermediate  $p_{\text{T}}$  is seen in the minimum bias data presented here. Within the systematic uncertainties the data is also consistent with no Cronin effect at all. A comparison of the results to the nuclear modification factor measured in  $\sqrt{s_{\text{NN}}} = 0.2 \text{ TeV}$  d–Au collisions at RHIC [201, 202] is shown in Figure 4.12.

<sup>2</sup> Collisions of p–Pb are called pure single diffractive if they appear like single diffractive nucleon-nucleon collisions to the detector. This is the case if all of the underlying nucleon-nucleon collision are single diffractive with all non-diffracting nucleons moving in the same direction.

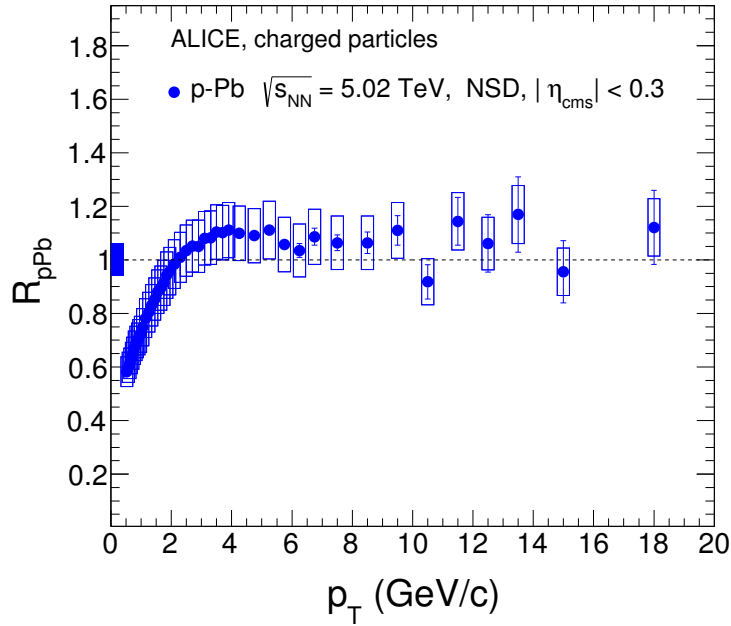


Figure 4.11.: The nuclear modification factor of charged particles as a function of  $p_T$  measured in NSD p–Pb collisions at  $\sqrt{s} = 5.02$  TeV, averaged over the pseudorapidity range  $|\eta_{\text{cms}}| < 0.3$ . Statistical uncertainties are drawn as vertical error bars, systematic uncertainties as open boxes. The filled box at  $p_T = 0$  shows the additional normalization uncertainty of 6%.

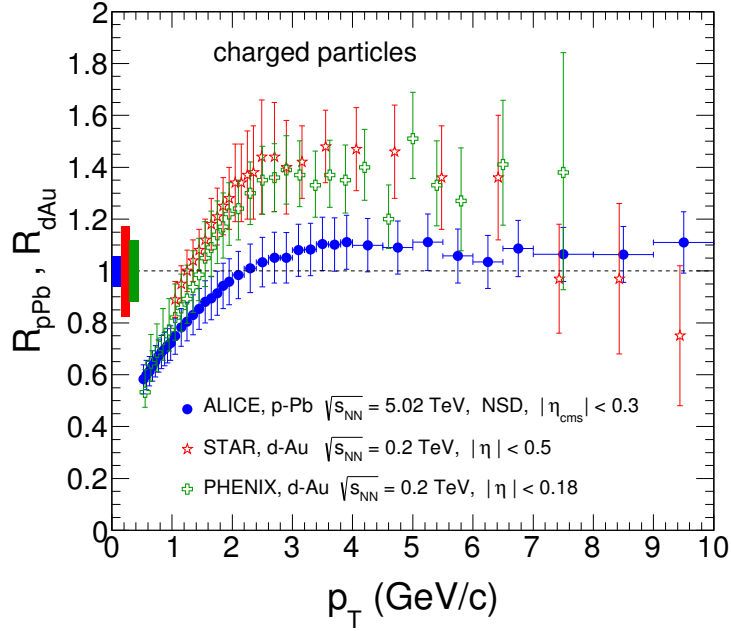


Figure 4.12.: Comparison of the nuclear modification factors measured in  $\sqrt{s_{\text{NN}}} = 5.02$  TeV p–Pb collisions at the LHC [164] to those measured in  $\sqrt{s_{\text{NN}}} = 0.2$  TeV d–Au collisions at RHIC by the STAR [201] and PHENIX [202] collaborations. Error bars show statistical and systematic uncertainties added in quadrature. The additional normalization uncertainties of 6% (ALICE), 17.4% (STAR) and 11.8% (PHENIX) are shown as filled boxes near  $p_T = 0$ .

In Figure 4.13  $R_{\text{pPb}}$  is compared to theoretical predictions from various models. Predictions based on gluon saturation models in the Color Glass Condensate (CGC) framework are shown in the top panel of Figure 4.13. The calculation in the framework of the running coupling Balitsky-Kochegov (rcBK) model [205] slightly under-predict the data. The prediction from the Monte Carlo rcBK (rcBK-MC) [206] agrees with the data within the large uncertainties of the model. Calculations from the impact parameter dependent dipole saturation model (IP-Sat) [205] are consistent with the data, as well as other CGC predictions [207] not shown in the figure.

The center panel of Figure 4.13 shows predictions for  $\pi^0$  from next-to-leading order (NLO) pQCD with the EPS09s nuclear parton distribution functions [50] which are in agreement with the data. The EPS09s calculations for  $\pi^0$  show no Cronin enhancement, in agreement with measured  $R_{\text{pPb}}$  of identified  $\pi^\pm$  [208]. The prediction from leading order (LO) pQCD with cold nuclear matter effects [209] including the isospin effect, Cronin effect, cold nuclear matter energy loss and dynamical shadowing shows a larger suppression at high  $p_T$  than observed in the data.

In the bottom panel of Figure 4.13 predictions from HIJING 2.1 [210, 211] are shown with different options: default (with shadowing parameter  $s_g = 0.28$ ), with decoherent hard scattering (DHC), DHC without shadowing, DHC without shadowing and independent fragmentation. None of the HIJING predictions is consistent with the data. With shadowing the  $R_{\text{pPb}}$  is under-predicted in a wide range of  $p_T$  and without shadowing a large Cronin enhancement in the intermediate  $p_T$  region is predicted, that is not seen in the data.

---

### 4.3.2 2013 run with extended $p_T$ range

---

With the large statistics p–Pb data sample collected in 2013 the  $p_T$  range of the measurement could be extended up to  $p_T = 50$  GeV/c. Preliminary results for the measured relative fractions of  $\pi$ ,  $K$ ,  $p$  were included in the efficiency and acceptance corrections and allowed to reduce the lower threshold to  $p_T = 0.15$  GeV/c. Increasing the range also towards low  $p_T$  is important for the analysis of  $\langle p_T \rangle$ , as this quantity is dominated by the soft part of the spectrum. Hence the results from the 2013 run are used for the  $\langle p_T \rangle$  analysis (see chapter 5).

In the analysis of the 2012 pilot run data, the pp reference spectrum for  $R_{\text{pPb}}$  covers the same pseudorapidity as the p–Pb measurement ( $|\eta_{\text{cms}}| < 0.3$ ). Results from the 2013 run were obtained with the pp reference in a larger pseudorapidity interval ( $\eta < 0.8$ ), to minimize statistical uncertainties in the reference. The power law parameterization discussed in section 4.2.2 has not been used.

Figure 4.14 shows the  $R_{\text{pPb}}$  extracted from the 2013 p–Pb run in the pseudorapidity range  $|\eta_{\text{cms}}| < 0.3$ . The upper plot illustrates the extension to larger  $p_T$ . The representation in logarithmic  $p_T$  scale (bottom plot) demonstrated the extension of the measurement towards lower  $p_T$  and the consistency of the two measurements. At low and intermediate  $p_T$  both analysis are in perfect agreement. Small differences are seen in the trend toward large  $p_T$  and are partially caused by differences in the reconstruction of simulated collisions used for corrections.

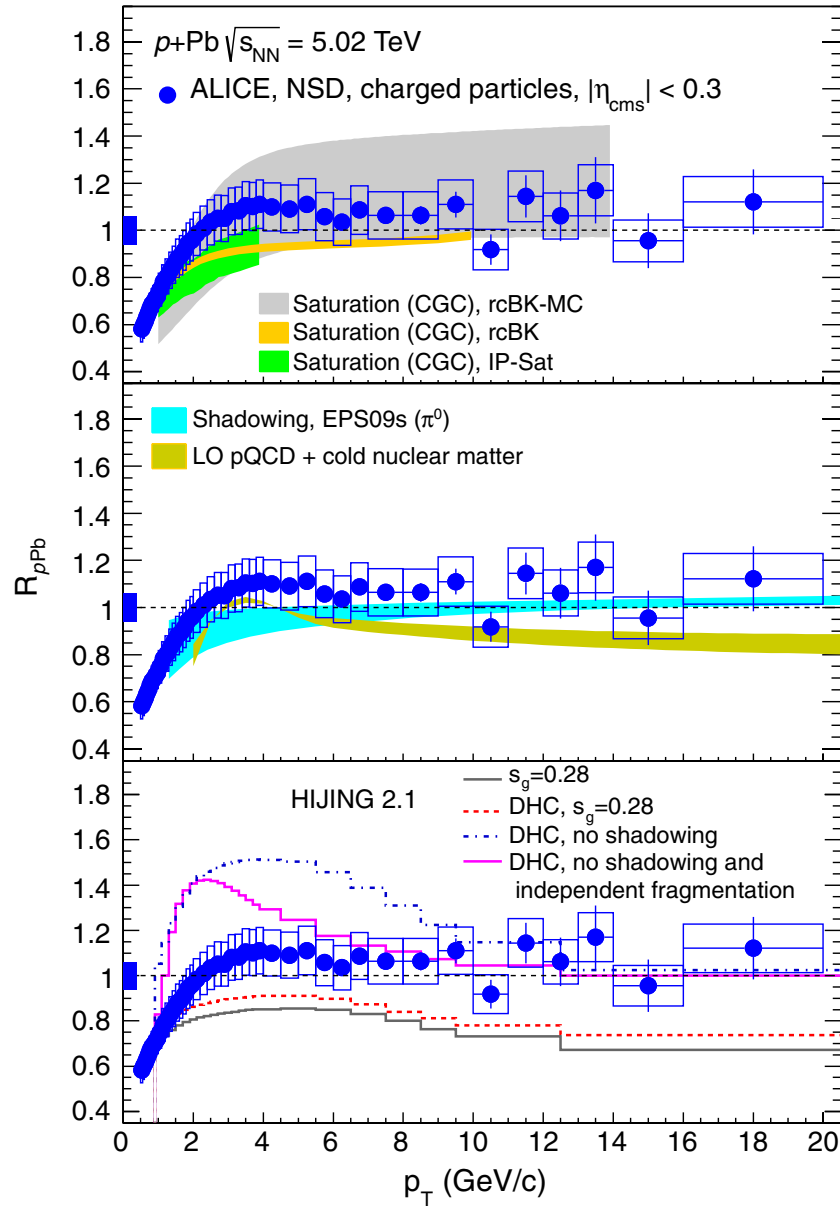


Figure 4.13.:  $R_{pPb}$  measured for charged particles in NSD events in comparison to model calculations. Systematic uncertainties of the data are shown as open boxes, statistical uncertainties as vertical bars. The systematic uncertainty of the normalization is shown as a box around unity at  $p_T = 0$ .

Figure published in [164].

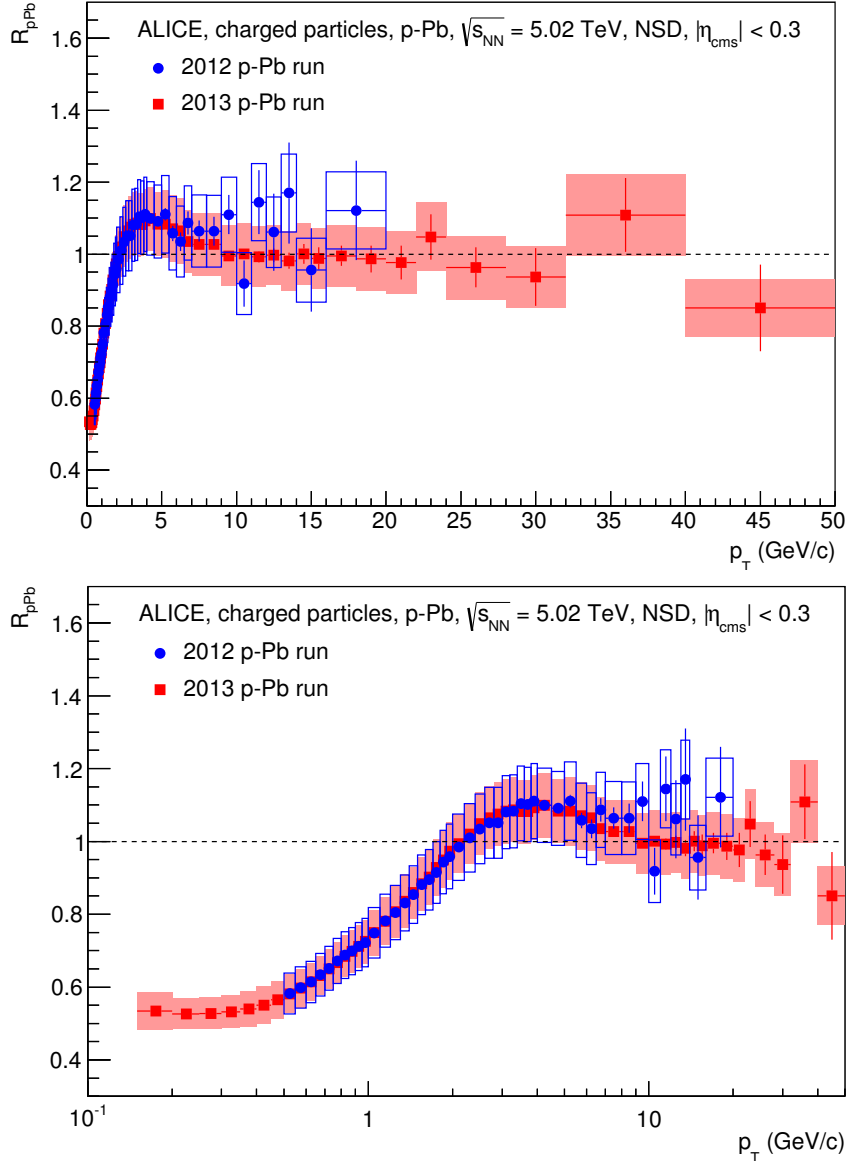


Figure 4.14.:  $R_{pPb}$  from the analysis of the 2013 data [173] in comparison to results from the 2012 pilot run [164]. Both measurements are for  $|\eta_{cms}| < 0.3$ , but the pp reference spectrum for 2012  $R_{pPb}$  is taken at  $|\eta| < 0.3$ , while the 2013 results use the pp reference in  $|\eta| < 0.8$ . Systematic uncertainties are shown as boxes and statistical uncertainties vertical lines. Note that the systematic uncertainties of the two measurements are correlated to a large extend. The top (bottom) plot is in linear (logarithmic) scale in  $p_T$  to demonstrate the extended  $p_T$  reach. The additional normalization uncertainty of 6%, which is common to both measurements and fully correlated between them, is not shown.

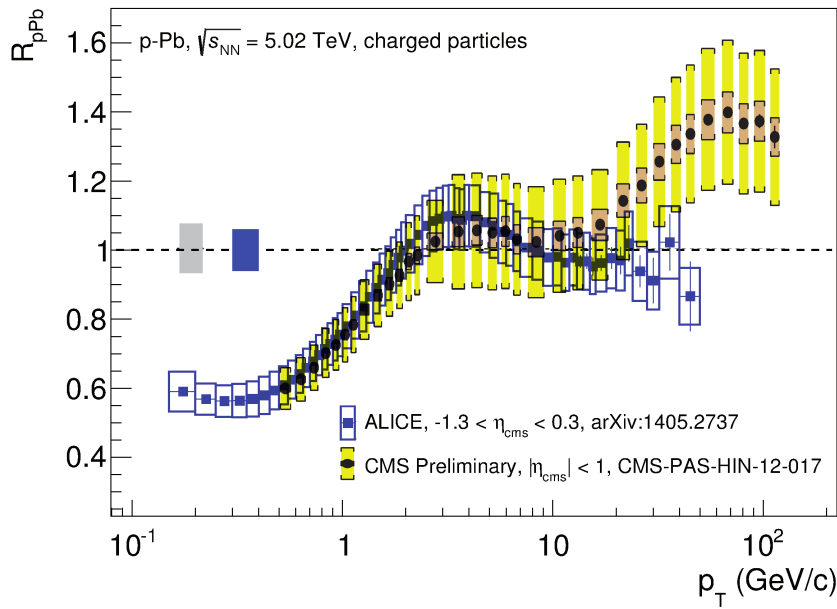


Figure 4.15.: Comparison of  $R_{p\text{Pb}}$  from 2013 ALICE data to preliminary results measured by the CMS Collaboration [212]. The pseudorapidity range is slightly different with  $|\eta_{\text{cms}}| < 1$  for the CMS data and  $-0.3 < \eta_{\text{cms}} < 1.3$  for the ALICE results. Overall normalization uncertainties are shown as boxes around  $R_{p\text{Pb}} = 1$ .

The nuclear modification factor remains consistent with unity also above 20 GeV/c in  $p_{\text{T}}$ . Also the EPS09s calculations [50] remain in agreement with the extended measurement also for  $p_{\text{T}} > 20$  GeV/c. Average values of  $R_{p\text{Pb}}$  in  $|\eta_{\text{cms}}| < 0.3$  in selected  $p_{\text{T}}$  ranges are:

- $\langle R_{p\text{Pb}} \rangle = 0.995 \pm 0.007(\text{stat.}) \pm 0.084(\text{syst.}) \pm 0.060(\text{norm.})$  for  $10 < p_{\text{T}} < 20$  GeV/c
- $\langle R_{p\text{Pb}} \rangle = 0.990 \pm 0.031(\text{stat.}) \pm 0.090(\text{syst.}) \pm 0.060(\text{norm.})$  for  $20 < p_{\text{T}} < 28$  GeV/c
- $\langle R_{p\text{Pb}} \rangle = 0.969 \pm 0.056(\text{stat.}) \pm 0.090(\text{syst.}) \pm 0.060(\text{norm.})$  for  $28 < p_{\text{T}} < 50$  GeV/c

Preliminary results on  $R_{p\text{Pb}}$  at  $\sqrt{s_{\text{NN}}} = 5.02$  TeV have also been presented by the other LHC experiments CMS [212] and ATLAS [213, 214]. The CMS results are for  $|\eta_{\text{cms}}| < 1$  and ATLAS presented  $R_{p\text{Pb}}$  in the centrality interval 0-90% for the rapidity range  $|y_{\text{cms}}| < 0.5$ . Both experiments observe a rise of  $R_{p\text{Pb}}$  above unity for  $p_{\text{T}} > 30$  GeV/c and a continuing increase up to  $R_{p\text{Pb}} \approx 1.4$  at  $p_{\text{T}} = 100$  GeV/c. This trend is not seen in the ALICE data, but within the statistic and systematic uncertainties of the measurements no discrepancy can be claimed. A direct comparison of the ALICE results to the CMS measurement is shown in Figure 4.15. At  $p_{\text{T}} < 20$  GeV/c both measurements are in remarkable agreement, towards larger  $p_{\text{T}}$  the different trend start to be visible. Differences between ALICE and CMS at large  $p_{\text{T}}$  are present in the p-Pb spectra as well as in the pp reference, but with opposite sign and accumulate in  $R_{p\text{Pb}}$ .

#### 4.4 Pb–Pb collisions

In heavy-ion Pb–Pb collisions  $p_{\text{T}}$  spectra of charged particles, averaged over the pseudorapidity range  $|\eta| < 0.8$  were measured as a function of the centrality for the 0-80% most central

collisions. The results agree with the identified charged particle production measured at low  $p_T$  [215] (see appendix B for details). ALICE results on identified particle production at high  $p_T$  [216] are based on the results presented here.

Early results obtained shortly after the first collisions have been published in [172] for two selected centrality classes (0-5% and 70-80%) covering the range  $0.3 < p_T < 20$  GeV/c. For this publication, which was released shortly after the first Pb–Pb data taking (end of 2010), only part of the recorded data was available for analysis. The pp reference was based on a power law interpolation between the yields measured in pp collisions at  $\sqrt{s} = 0.9$  and 7 TeV and scaled with  $\langle N_{\text{coll}} \rangle$ .

Results including the full statistics of the 2010 Pb–Pb run and the a pp reference spectrum based on the results of the  $\sqrt{s} = 2.76$  TeV data (section 4.1) have been published in a follow-up paper [177]. This measurement extends the covered  $p_T$  range to  $0.15 < p_T < 50$  GeV/c and includes the full centrality dependence of the spectra in nine centrality intervals. All Pb–Pb results that are presented in this thesis correspond to this second publication.

Figure 4.16 shows the  $p_T$ -differential yield of charged particles and its evolution with centrality with systematic and statistic uncertainties added in quadrature. In this figure, the pp reference spectrum, scaled by the nuclear overlap function  $\langle T_{\text{AA}} \rangle$ , is shown in comparison, without the uncertainties.

In peripheral collisions, the spectra exhibits a similar shape as the pp reference with a power law behavior at large  $p_T$  above 5 GeV/c. With increasing centrality the spectra deviate more and more from the power law shape, with a strongest effect around  $p_T = 7$  GeV/c. The soft part below 2 GeV/c in  $p_T$  shows a suppression of particle production already in peripheral collisions that is increasing towards more central collisions.

Differences of particle production in pp and heavy ion collisions are commonly quantified by the nuclear modification factor  $R_{\text{AA}}$ .  $R_{\text{AA}}$  is calculated as the ratio of the differential yields in Pb–Pb collisions to the differential cross section in pp collisions scaled by the average nuclear overlap  $\langle T_{\text{AA}} \rangle$ . This is equivalent to the pp yield scaled by  $\langle N_{\text{coll}} \rangle$ .

$$R_{\text{AA}}(p_T) = \frac{d^2N_{\text{ch}}^{\text{Pb–Pb}}/d\eta dp_T}{\langle N_{\text{coll}} \rangle \cdot d^2N_{\text{ch}}^{\text{pp}}/d\eta dp_T} = \frac{d^2N_{\text{ch}}^{\text{Pb–Pb}}/d\eta dp_T}{\langle T_{\text{AA}} \rangle \cdot d^2\sigma_{\text{ch}}^{\text{pp}}/d\eta dp_T} \quad (4.8)$$

The nuclear overlap is calculated from a Monte Carlo Glauber model (see section 1.7) in intervals of the impact parameter that correspond to the measured centrality. In Table 4.2 averaged values of the nuclear overlap function  $T_{\text{AA}}$ , number of binary collisions  $N_{\text{coll}}$  and number of participating nucleons  $N_{\text{part}}$  are given for all centrality intervals.

The resulting nuclear modification factors are shown in Figure 4.17 for all centrality intervals. Even in the most peripheral collisions (70-80%), a significant suppression ( $R_{\text{AA}} \approx 0.7$ ) is observed with only a weak  $p_T$  dependence above  $p_T > 2$  GeV/c. Below 2 GeV/c in  $p_T$  the suppression increases slightly. Even in peripheral collisions at the highest  $p_T$ ,  $R_{\text{AA}}$  appears to remain below unity. Taking into account both  $p_T$  dependent and overall normalization systematic uncertainties  $R_{\text{AA}}$  at high  $p_T$  in peripheral collisions is consistent with unity as well.

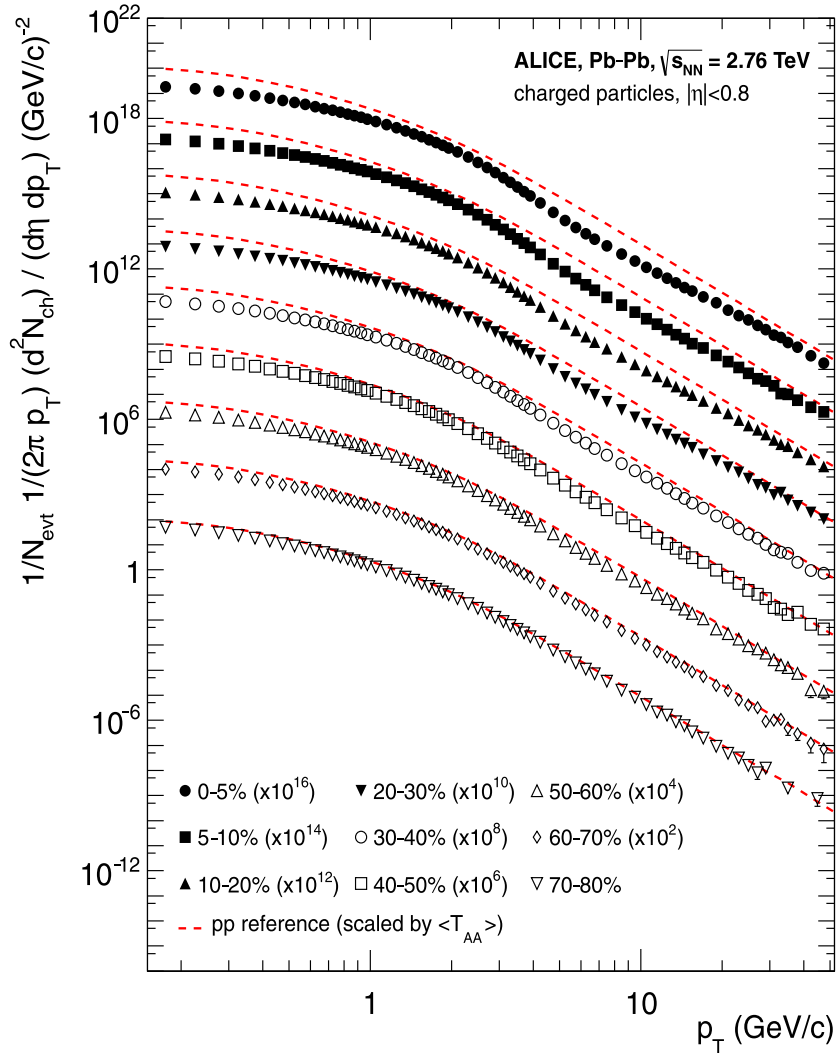


Figure 4.16.:  $p_T$ -differential yields of charged particles measured at mid-rapidity ( $|\eta| < 0.8$ ) in  $\sqrt{s} = 2.76$  TeV Pb–Pb collisions for nine centrality intervals scaled by arbitrary factors for better visibility. Uncertainties are systematic and statistical ones added in quadrature. Shown as dashed lines without uncertainties is the differential cross section in pp collisions, scaled by the average nuclear overlap  $\langle T_{AA} \rangle$  for each centrality.

Figure published in [177].

Centrality interval	$b$ (fm)	$\langle N_{\text{part}} \rangle$	$\langle N_{\text{coll}} \rangle$	$\langle T_{\text{AA}} \rangle$ (mb $^{-1}$ )
0-5%	0-3.50	$383 \pm 3$	$1687 \pm 198$	$26.4 \pm 1.1$
5-10%	3.50-4.95	$330 \pm 5$	$1320 \pm 154$	$20.6 \pm 0.9$
10-20%	4.95-6.98	$261 \pm 4$	$923 \pm 100$	$14.4 \pm 0.6$
20-30%	6.98-8.55	$186 \pm 4$	$559 \pm 56$	$8.7 \pm 0.4$
30-40%	8.55-9.88	$129 \pm 3$	$321 \pm 31$	$5.0 \pm 0.2$
40-50%	9.88-11.04	$85 \pm 3$	$172 \pm 15$	$2.68 \pm 0.14$
50-60%	11.04-12.09	$53 \pm 2$	$85 \pm 8$	$1.32 \pm 0.09$
60-70%	12.09-13.06	$30.0 \pm 1.3$	$39 \pm 4$	$0.59 \pm 0.04$
70-80%	13.06-13.97	$15.8 \pm 0.6$	$15.8 \pm 1.3$	$0.24 \pm 0.03$

Table 4.2.: Centrality intervals sliced in the corresponding impact parameter range. Average number of participating nucleons  $\langle N_{\text{part}} \rangle$ , average number of binary nucleon-nucleon collisions  $\langle N_{\text{coll}} \rangle$  and nuclear overlap function  $\langle T_{\text{AA}} \rangle$  are calculated from Monte Carlo Glauber model. The indicated systematic uncertainties are explained in the text. For the calculation of  $R_{\text{AA}}$  only  $\langle T_{\text{AA}} \rangle$  is used.

Towards more central collisions the overall suppression gradually increases and a characteristic shape with a minimum around  $p_{\text{T}} = 6\text{-}7$  GeV/c develops.

In the most central (0-5%) collisions a strong ( $R_{\text{AA}} \approx 0.2$ ) suppression of particle production is observed at the lowest  $p_{\text{T}}$ , followed by a relative maximum in  $R_{\text{AA}}$  around 2 GeV/c in  $p_{\text{T}}$ . A minimum in  $R_{\text{AA}}$  (maximal suppression) is observed around  $p_{\text{T}} = 6\text{-}7$  GeV/c with  $R_{\text{AA}} \approx 0.13$ . Towards higher transverse momenta  $R_{\text{AA}}$  rises approximately linearly with  $p_{\text{T}}$  up to  $R_{\text{AA}} \approx 0.4$  at 30 GeV/c. For  $p_{\text{T}}$  above 30 GeV the data is consistent with a constant nuclear modification factor of  $R_{\text{AA}} \approx 0.4$ . Within the statistical uncertainties also a continued, but less steep rise of  $R_{\text{AA}}$  cannot be excluded.

In the region around the first maximum in  $R_{\text{AA}}$  ( $p_{\text{T}} \approx 2$  GeV/c) effects from collective expansion (radial flow) change the shape of the  $p_{\text{T}}$ -spectrum which results in the relative maximum seen in  $R_{\text{AA}}$ . As expected for collective effects, a strong centrality dependence is observed. The effect of radial flow depends on the particle mass, and thus also on the primary particle composition.

The centrality dependence of  $R_{\text{AA}}$  is shown in Figure 4.18 for different intervals of  $p_{\text{T}}$  (5-7 GeV/c, 15-20 GeV/c, 20-30 GeV/c and 30-50 GeV/c) as a function of  $\langle N_{\text{part}} \rangle$  and  $dN_{\text{ch}}/d\eta$ . The average number of participants  $\langle N_{\text{part}} \rangle$  (as listed in Table 4.2) is obtained from the same Glauber MC calculations. The centrality can also be expressed in terms of the average charged particle pseudorapidity density  $dN_{\text{ch}}/d\eta$  which has been measured by ALICE [115].  $N_{\text{part}}$  is an approximation of the initial volume, while  $dN_{\text{ch}}/d\eta$  is a measure for the entropy/energy density.

In the  $p_{\text{T}}$  interval of maximal suppression ( $5 < p_{\text{T}} < 7$  GeV/c) the strongest centrality dependence is observed. With increasing  $p_{\text{T}}$ , a reduced, but still significant centrality dependence is seen.

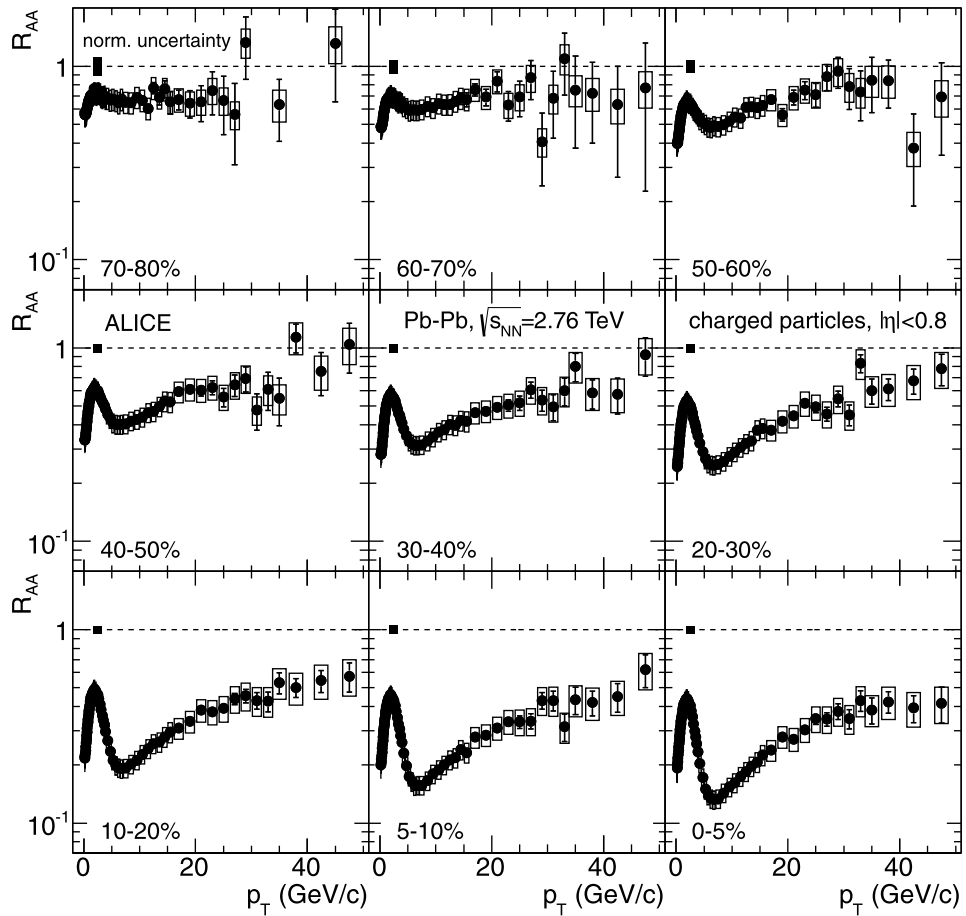


Figure 4.17.: The nuclear modification factor  $R_{AA}$  of charged particles as a function of  $p_T$  measured in Pb–Pb collisions at  $\sqrt{s_{NN}} = 2.76$  TeV four nine centrality intervals. Statistical uncertainties are shown as vertical error bars, systematic uncertainties as open boxes. The filled boxes at  $R_{AA} = 1$  shows the additional normalization uncertainty of 4.5–11% arising from the pp reference normalization and  $\langle T_{AA} \rangle$ . Figure published in [177].

The comparison to PHENIX results [217] shown in Figure 4.18 for  $5 < p_T < 7$  GeV/c shows that the suppression is stronger at LHC than at RHIC when compared as the same value of  $\langle N_{\text{part}} \rangle$ . Suppression of charged particle production at LHC and RHIC is comparable at similar values of  $dN_{\text{ch}}/d\eta$ .

A comparison of  $R_{AA}$  in most central (0-5%) collisions to results from CMS [196] is shown in Figure 4.19. At low  $p_T$  there is an excellent agreement between the two measurements. At the highest  $p_T$  (30-50 GeV), the  $R_{AA}$  measured by ALICE is around 0.4, while the value measured by CMS is slightly above this and is around 0.5. However, within the systematic uncertainties of the measurements these two values are compatible. The differences in  $R_{AA}$  seems to be largely due to differences the pp references (see also the comparison in Figure 4.8).

In Figure 4.19  $R_{AA}$  measured in most central (0-5%) collisions is also compared to predictions from different parton energy loss models [218–223]. All models are able to describe qualitatively the rise of  $R_{AA}$  with increasing  $p_T$ , but none of them in in agreement with the data over the full  $p_T$  range.

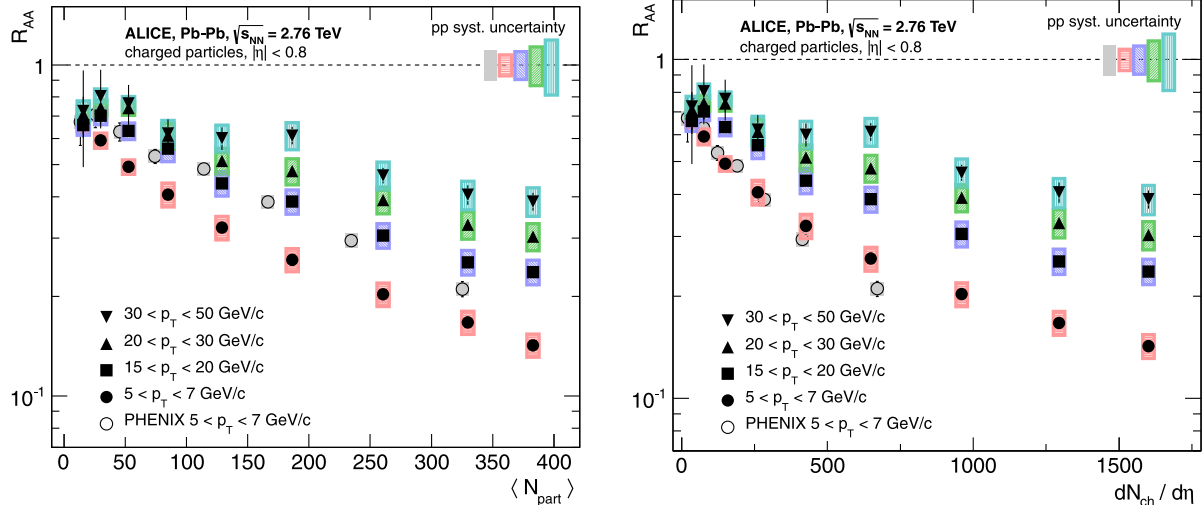


Figure 4.18.: Nuclear modification factor of charged particles measured in  $\sqrt{s_{\text{NN}}} = 2.76 \text{ TeV}$  Pb–Pb collisions for different  $p_{\text{T}}$  intervals and comparison to  $R_{\text{AA}}$  measured in  $\sqrt{s_{\text{NN}}} = 0.2 \text{ TeV}$  Au–Au collisions by PHENIX [217].  $R_{\text{AA}}$  is shown as a function of the average number of participants  $\langle N_{\text{part}} \rangle$  (left) and the average charged particle pseudorapidity density  $dN_{\text{ch}}/d\eta$  (right). Uncertainties of the Pb–Pb spectra are shown as boxes around the data; the boxes at  $R_{\text{AA}} = 1$  are the systematic uncertainties of the pp reference. Overall normalization uncertainties are not shown. Values of  $dN_{\text{ch}}/d\eta$  are from [115], uncertainties of  $dN_{\text{ch}}/d\eta$  are not shown.

Figure published in [177].

The higher twist (HT) approach by Chen et al. [220] is a NLO pQCD based model with jet quenching incorporated via induced gluon radiation in medium-modified fragmentation functions. The jet transport parameter  $\hat{q}$  encoding the medium effects is proportional to the initial medium density. It is determined from hadron suppression data measured in Au–Au collisions at RHIC with the medium density scaled to LHC energies using the  $dN_{\text{ch}}/d\eta$  measured in Pb–Pb collisions by ALICE. The evolution of the bulk medium is modeled in 3+1D ideal hydrodynamic simulation, constrained from  $dN_{\text{ch}}/d\eta$  at  $\sqrt{s} = 2.76 \text{ TeV}$ . Calculation from this model are shown in Figure 4.19 for two initial densities ( $\hat{q}_0 t_0 = 1$  and  $1.4 \text{ GeV}^2$ ). The lower density is in good agreement with the data for  $p_{\text{T}} > 7 \text{ GeV}/c$ , the higher density overpredicts the suppression for  $p_{\text{T}} < 30 \text{ GeV}/c$ .

Another HT radiative energy loss calculation by Majumder et al. [223] uses a 2+1D viscous hydrodynamic evolution of the medium with CGC initial conditions and model parameters adjusted from soft hadron yields an elliptic flow. The entropy-density dependent transport parameter  $\hat{q}$  is obtained from  $R_{\text{AA}}$  measured in Au–Au collisions at RHIC and extrapolated to LHC energies. This calculation shows a rise of  $R_{\text{AA}}$  with  $p_{\text{T}}$  that is stronger than seen in the data and too little suppression at largest  $p_{\text{T}}$ .

The calculations of  $R_{\text{AA}}$  with only elastic energy loss [219], YaJEm-D (Renk [218, 219]) and ASW [222] by Renk et al. use a 2+1D ideal hydrodynamic description of the bulk medium that is able to describe elliptic flow and particle multiplicities at RHIC and the LHC. The initial state is modeled combining gluon saturation and pQCD with EPS09s for nuclear effects. Elas-

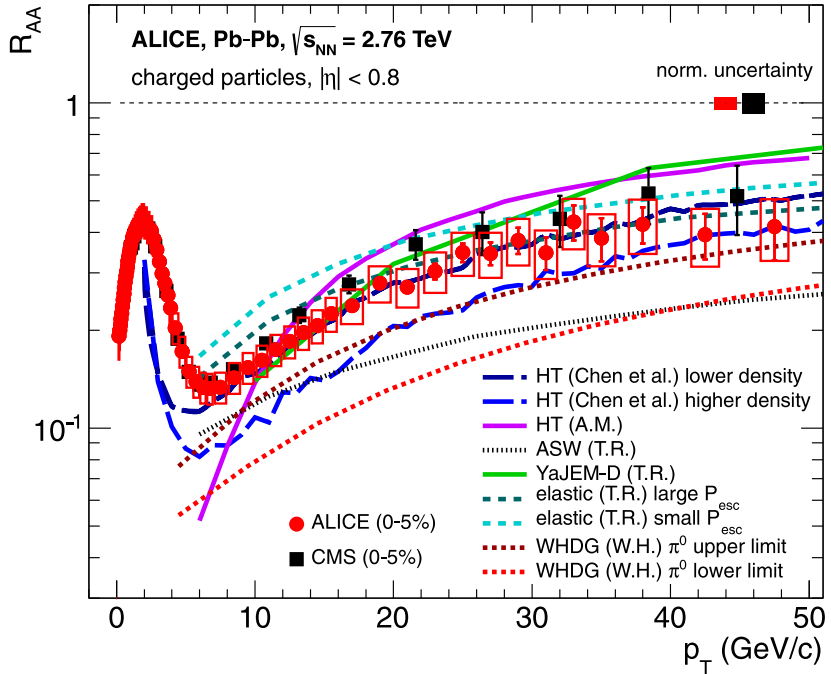


Figure 4.19.:  $R_{AA}$  for charged particles in most central (0-5%) Pb-Pb collisions at  $\sqrt{s_{NN}} = 2.76$  TeV compared to results from the CMS collaboration [196] and model calculations (see text). The boxes (vertical error bars) for ALICE represent systematic (statistical) uncertainties. The vertical lines for CMS are systematic and statistical uncertainties added in quadrature. The uncertainties of the overall normalization are shown as filled boxes at  $R_{AA} = 1$ .

Figure published in [177].

tic energy loss is modeled in a phenomenological approach controlled by three parameters: the average energy loss per scattering, the strength of fluctuations in the energy loss and the magnitude of the escape probability. In Figure 4.19 the elastic energy loss is shown for two different parameter sets corresponding to large and small escape probabilities  $P_{esc}$ . The adjustment of the remaining two parameters lead to the counterintuitive result that a larger escape probability leads to stronger suppression is a caused by the larger mean energy loss. Both elastic energy loss scenarios under-predict the suppression at  $p_T < 20$  GeV/c. The YaJEM-D Monte Carlo code is an pQCD based model for radiative energy loss simulating the parton shower evolution as series of parton splitting with splitting functions modified by the medium. The formation length of partons it forced to be contained inside the medium. YaJEM-D predicts a too strong rise of  $R_{AA}$  with  $p_T$  and underestimates the suppression at high  $p_T$ . Without the formation time constraint the standard version YaJEM (not included in Figure 4.19) shows a much slower rise of  $R_{AA}$  with  $p_T$  [219]. Radiative energy loss from quenching weights calculated in the ASW formalism [222] results in a larger suppression of particle production than seen in the data over the entire  $p_T$  range.

The predictions from Horowitz et al. in the WHDG/DGLV framework [221] of opacity expansion incorporate both, radiative and elastic energy loss, as well as fluctuations of the geometry. The medium evolution is treated as 1D Bjorken expansion with an initial state calculated in the optical Glauber approach and an initial density constrained from PHENIX  $\pi^0$  measurements

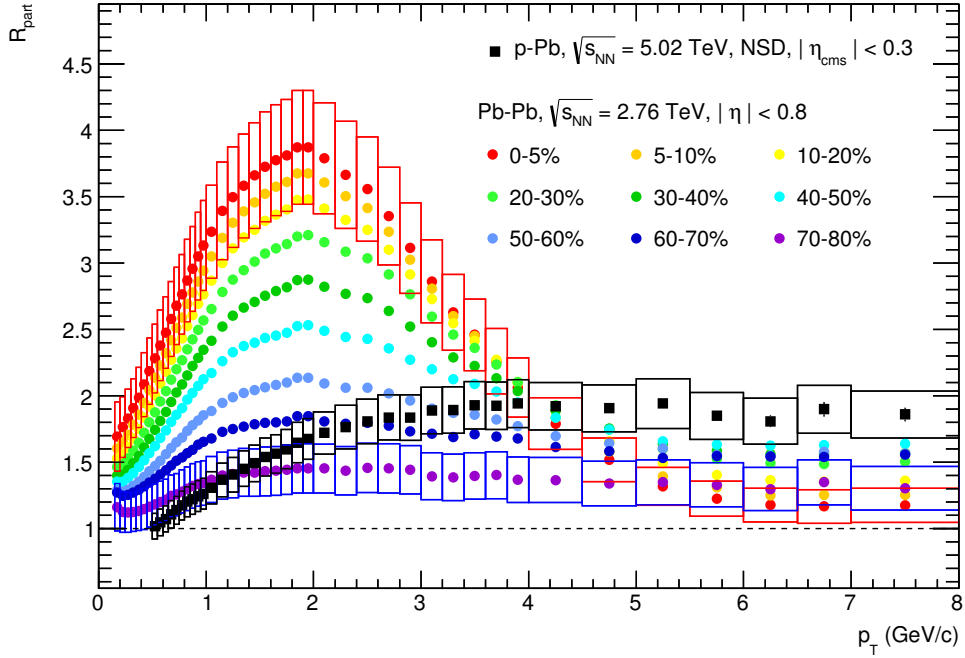


Figure 4.20.:  $R_{\text{part}}$ : ratio of spectra in Pb–Pb and p–Pb collisions to those in pp collisions, scaled by  $\langle N_{\text{part}} \rangle$ . Systematic uncertainties are shown as boxes only for p–Pb, central (0–5%) and peripheral (70–80%) Pb–Pb collisions to improve visibility. Normalization uncertainties are not shown.

and  $dN_{\text{ch}}/d\eta$  at  $\sqrt{s} = 2.76$  TeV. The WHDG calculations, which are shown for the upper and lower limits of the extrapolation to LHC in Figure 4.19, exhibit a larger suppression than seen in the data.

Only a subset of the existing jet quenching models are shown in Figure 4.19. Calculations of  $R_{\text{AA}}$  by Zapp et al. [224] assuming a Bjorken expanding medium with the JEWEL framework [225] for medium effects are consistent with the data for  $p_{\text{T}} > 10$  GeV/c.

In the low  $p_{\text{T}}$  part of the spectrum soft processes dominate particle production and binary collision scaling is not expected to hold, as soft processes rather scale with the average number of participating nucleons  $\langle N_{\text{part}} \rangle$  [226]. A hint of this can be seen in the minimum value of  $R_{\text{AA}}$  in most central collisions, which is around 0.13 and no so different from 0.11 expected from participant scaling. As observed in measurements of  $dN_{\text{ch}}/d\eta$  [114–116] scaling with  $\langle N_{\text{part}} \rangle$  is approximately working for peripheral collisions, while for central collisions the overall yield is about a factor 2 larger compared to participant scaling. A better description can be achieved in a two-component model including soft ( $\propto N_{\text{part}}$ ) and hard ( $\propto N_{\text{coll}}$ ) particle production.

The soft to semi-hard part ( $p_{\text{T}} < 8$  GeV/c) of the  $p_{\text{T}}$ -spectrum in Pb–Pb is shown in Figure 4.20 as the ratio to pp, scaled by  $\langle N_{\text{part}} \rangle$ . The ratio  $R_{\text{part}}$  is calculated equivalently to  $R_{\text{AA}}$ , but assuming participant scaling.

$$R_{\text{part}}(p_{\text{T}}) = \frac{2 \cdot d^2 N_{\text{ch}}^{\text{Pb–Pb}} / d\eta dp_{\text{T}}}{\langle N_{\text{part}} \rangle \cdot d^2 N_{\text{ch}}^{\text{pp}} / d\eta dp_{\text{T}}} \quad (4.9)$$

As seen in Figure 4.20 there is an approximate scaling with the number of participants at the lowest  $p_T$ , within a factor 1.7, in Pb–Pb collisions. In the intermediate region around  $p_T \approx 2\text{GeV}/c$  an enhancement of particle production towards more central collisions is seen, compared to participant scaling. At higher  $p_T$ , in the region  $4 < p_T < 8\text{ GeV}/c$ , again an approximate scaling with  $\langle N_{\text{part}} \rangle$  is observed. The  $R_{\text{part}}$  for p–Pb collisions, shown for comparison in Figure 4.20, shows a very different behavior with  $N_{\text{part}}$  scaling at low  $p_T$  and a smooth transition to  $N_{\text{coll}}$  scaling at high  $p_T$ .



# 5 Multiplicity dependence of the average transverse momentum

The average transverse momentum  $\langle p_T \rangle$ , which is the first moment of the  $p_T$  distribution, is dominated by the low  $p_T$  part of the spectrum since most particles are produced at low transverse momenta. But, in contrast to  $dN_{\text{ch}}/d\eta$ , it is much more influenced by the high  $p_T$  partons that fragment into hadrons with large  $p_T$ . This becomes important when studying  $\langle p_T \rangle$  as a function of the charged particle multiplicity  $N_{\text{ch}}$ . In pp collisions a large multiplicity event contains a hard parton collision that fragments into many particles.

The analysis of  $\langle p_T \rangle$  as a function of  $N_{\text{ch}}$  allows to study the interplay between soft and hard processes in a unique way.

## 5.1 Analysis

For this study the analysis of the transverse momentum spectra as described in chapter 3 was performed as a function of multiplicity with the number of reconstructed tracks in the acceptance  $N_{\text{acc}}$  used as a multiplicity estimator. The acceptance is defined by the transverse momentum  $p_T > 0.15 \text{ GeV}/c$  and the pseudorapidity  $|\eta| < 0.3$ . Spectra, that are corrected for tracking efficiency and contamination from secondary particles, are obtained with the procedures described in chapter 3. Note that in pp and p–Pb collisions the dependence of the correction factors for efficiency and secondary particle contamination on multiplicity is negligible and hence the minimum bias corrections have been applied to all multiplicity classes.

As a starting point, fully corrected spectra as a function of the reconstructed number of charged particles  $N_{\text{acc}}$  are obtained. Corrections affecting only the normalization are irrelevant for the mean of the distribution and have not been included in this analysis.

Two corrections affect the normalization: trigger efficiency and vertex reconstruction efficiency. As apparent from Figure 3.9 (in section 3.4.3) the trigger is fully efficient for events with one particle in the acceptance, for the vertex reconstruction this is only the case for three or more particles. As a result the spectra obtained for  $N_{\text{ch}} > 3$  also have the correct normalization.

The  $\langle p_T \rangle$  as a function of  $N_{\text{acc}}$  was obtained from the measured, histogrammed, yields as the  $p_T$  average over the range  $0.15 < p_T < 10 \text{ GeV}/c$ :

$$\langle p_T \rangle (N_{\text{acc}}) = \frac{\sum_{p_T} \frac{d^2 N_{\text{ch}}(p_T, N_{\text{acc}})}{d\eta dp_T} \cdot p_T \cdot \Delta p_T}{\sum_{p_T} \frac{d^2 N_{\text{ch}}(p_T, N_{\text{acc}})}{d\eta dp_T} \cdot \Delta p_T} \quad (5.1)$$

Here  $\Delta p_T$  is the width of the  $p_T$  interval, and  $p_T$  corresponds to the bin center.

As a result of the finite, non-uniform efficiency and the  $p_T$  cutoff at about  $0.15 \text{ GeV}/c$  events with the same reconstructed multiplicity  $N_{\text{acc}}$  correspond to a range of events with different

$N_{\text{ch}}$ . To deconvolute this dependence and obtain  $\langle p_{\text{T}} \rangle$  as a function of  $N_{\text{ch}}$ , a re-weighting procedure is employed as described in [176]:

$$\langle p_{\text{T}} \rangle(N_{\text{ch}}) = \sum_{N_{\text{acc}}} R(N_{\text{ch}}, N_{\text{acc}}) \cdot \langle p_{\text{T}} \rangle(N_{\text{acc}}) \quad (5.2)$$

Here  $R(N_{\text{ch}}, N_{\text{acc}})$  is the multiplicity correlation matrix. Note that this re-weighting procedure is not a genuine unfolding, but rather an approximation.

$R(N_{\text{ch}}, N_{\text{acc}})$  is obtained from Monte Carlo simulations of the detector response as the probability to reconstruct  $N_{\text{acc}}$  particles for a given  $N_{\text{ch}}$  of generated particles. Since  $N_{\text{ch}}$  refers to all charged particles the multiplicity correlation matrix contains a combined correction for efficiency, secondaries and the  $p_{\text{T}}$ -cutoff and is thus strongly MC dependent. In particular it depends on the shape of the  $p_{\text{T}}$  spectrum as a function of  $N_{\text{ch}}$ .

Each row of the correlation matrix is normalized to

$$\sum_{N_{\text{acc}}} R(N_{\text{ch}}, N_{\text{acc}}) = 1 \quad (5.3)$$

To overcome statistical uncertainties and populate the correlation matrix also at large values of  $N_{\text{ch}}$  that are not reached by the MC productions each  $N_{\text{acc}}$  distribution for a given  $N_{\text{ch}}$  (i.e. each column of the correlation matrix) is parameterized by a Gaussian distribution in  $N_{\text{acc}}$  that is characterized by a mean  $\mu$  and a standard deviation  $\sigma$ .

The mean  $\mu$  extracted in this way has an approximately linear dependence on  $N_{\text{ch}}$  and corresponds to the combined corrections for efficiency, contamination and low- $p_{\text{T}}$  cutoff. The standard deviation  $\sigma$  of the Gaussian fit is of statistical origin (fluctuations) and scales like  $\sqrt{N_{\text{ch}}}$ , as expected from basic Poisson statistics.

The  $N_{\text{ch}}$  dependence of the mean  $\mu$  is parameterized by a linear function  $\mu = a + b \cdot N_{\text{ch}}$ . For the standard deviation  $\sigma$  a linear dependence on the square root of  $N_{\text{ch}}$  is assumed:  $\sigma = c + d \cdot \sqrt{N_{\text{ch}}}$ . These parameterization can be easily extrapolated to larger  $N_{\text{ch}}$ . At lower  $N_{\text{ch}}$  this procedure avoids statistical uncertainties in the entries of  $R$ . The parameterization of the multiplicity correlation matrix obtained from simulations is used in the re-weighting of  $\langle p_{\text{T}} \rangle$ . Figure 5.1 shows an example of the  $N_{\text{ch}}$  dependence of the average  $\mu(N_{\text{acc}})$  and its standard deviation (width)  $\sigma(N_{\text{acc}})$  along with the parameterizations.

An example of the multiplicity correlation matrix from simulations is shown in Figure 5.2 for p–Pb collisions. The right plot of Figure 5.2 shows the raw correlation matrix revealing the limiting statistics at large multiplicities. On the left plot of Figure 5.2  $R$  is shown after applying the parameterization and extrapolation procedure described above.

To assess systematic uncertainties related to this re-weighting procedure different Monte Carlo generators are used in the simulation. The simulated measurements generated with one generator were re-weighted using the correlation matrix obtained with the other generator and vice versa. The difference between the true  $\langle p_{\text{T}} \rangle$  obtained directly from the MC generator and the  $\langle p_{\text{T}} \rangle$  obtained after simulation of the detector and the re-weighting with  $R$  from a different generator is assigned as systematic uncertainty.

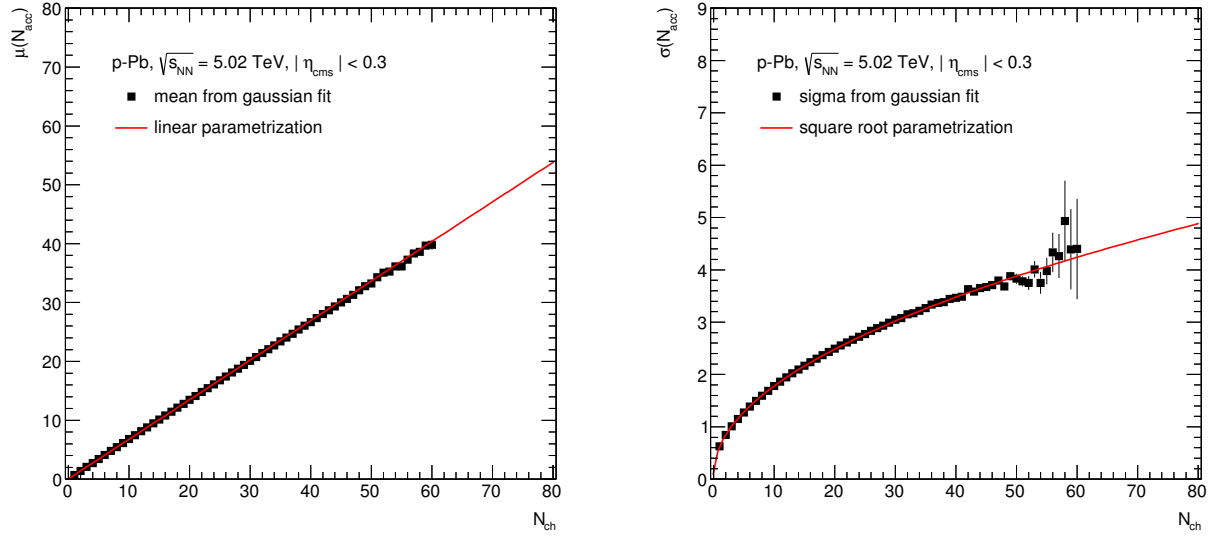


Figure 5.1.: Average number of reconstructed tracks  $\mu(N_{\text{acc}})$  as a function of  $N_{\text{ch}}$  (left) and the standard deviation  $\sigma(N_{\text{acc}})$  (right) extracted from Gaussian fits to slices of the multiplicity correlation matrix. The parameterizations used for smoothing and extrapolation of the correlation matrix are shown as red lines.

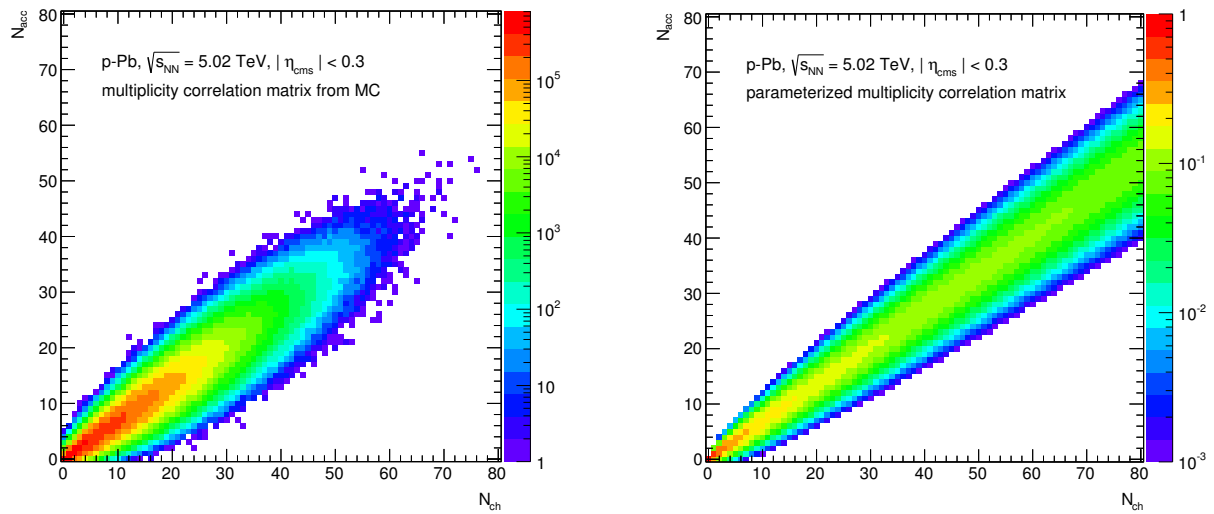


Figure 5.2.: Left: The multiplicity correlation matrix as obtained from MC simulations. Right: The correlation matrix  $R(N_{\text{acc}}, N_{\text{ch}})$  after normalization and parameterization (see text) as it is used for the re-weighting of  $\langle p_{\text{T}} \rangle$ .

Contribution	pp	p-Pb	Pb-Pb
Track Selection	0.5-1.8%	0.8-1.0%	1.1-1.2%
Particle Composition	0.2-0.4%	0.7-0.8%	0.2-0.3%
Tracking efficiency	0.1%	0.2%	0.1%
Monte Carlo generator	$\leq 0.2\%$	0.1-0.2%	0.2%
Re-weighting procedure	2.3-4.1%	1.3-1.8%	0.5-1.2%
total	2.4-4.5%	1.8-2.2%	1.2-3.0%

Table 5.1.: Relative systematic uncertainties on  $\langle p_T \rangle$  in pp, p-Pb and Pb-Pb collisions. The given ranges correspond to the  $N_{\text{ch}}$  ranges covered, for pp also the energy dependence is included.

In the case of pp collisions PHOJET and PYTHIA6 tune Perugia0, are used, while for p-Pb and Pb-Pb estimates of the systematic uncertainty are based on differences between DPMJET and HIJING.

The total uncertainties consist of two contributions, one coming from the re-weighting procedure as described above. The other one is the uncertainty in  $\langle p_T \rangle (N_{\text{acc}})$  and is a direct consequence of the systematic uncertainties on the spectra themselves.

Any uncertainty that changes only the normalization does not affect  $\langle p_T \rangle$ , and any correlation of an uncertainty between the  $p_T$  bins will reduce the relative uncertainty on  $\langle p_T \rangle$ . For a proper estimate of the uncertainty on  $\langle p_T \rangle$  arising from the spectra, for each contribution to the systematic uncertainty (as described in section 3.10), the spectra have been varied accordingly and after the re-weighting procedure described above the difference obtained in  $\langle p_T \rangle$  is assigned as a systematic uncertainty related to the given contribution.

All contributions to the systematic uncertainty of  $\langle p_T \rangle$  were estimated in this way and added in quadrature. Note that for most of these uncertainties almost no dependence on  $N_{\text{ch}}$  is observed. Overall systematic uncertainties on  $\langle p_T \rangle$  are summarized in Table 5.1. In Pb-Pb collisions also electromagnetic interactions contribute to events with very few tracks (up to 4). An additional correction and systematic uncertainty has been added based on the difference between the two centrality intervals 0-90% and 0-100%. Contamination from electromagnetic processes is only present in the most peripheral 90-100% centrality interval [144].

As a cross check of the re-weighting method described above a different approach has been implemented to transform  $\langle p_T \rangle (N_{\text{acc}})$  to  $\langle p_T \rangle (N_{\text{ch}})$  using the average  $N_{\text{ch}}$  that corresponds to a given  $N_{\text{acc}}$ . For every value of  $N_{\text{acc}}$ , the corresponding fully corrected and properly normalized spectrum was integrated to obtain the average  $N_{\text{ch}}$ . To determine the yield in the unmeasured part of the spectrum below  $p_T = 0.15$  GeV/c the spectra were parameterized by a modified Hagedorn function [190] (see Equation (4.2)) in the range  $0.15 < p_T < 1$  GeV/c. This parameterization was extrapolated down to  $p_T = 0$  and integrated in the range  $0 < p_T < 0.15$  GeV/c.

Note that in this alternative procedure the values of  $\langle p_T \rangle$  for a given measured multiplicity class is directly obtained from the spectrum (no re-weighting), but yields fractional values

for the average true multiplicity  $N_{\text{ch}}$ . Results for  $\langle p_{\text{T}} \rangle (N_{\text{ch}})$  are fully consistent with the ones obtained with the re-weighting method.

## 5.2 Glauber Model for average transverse momentum

In a simple approach Pb–Pb or p–Pb collisions can be described as an incoherent superposition of independent nucleon-nucleon collisions. This can be implemented in a Monte Carlo Glauber Model and applied to various observables.

In the case of the average transverse momentum as a function of multiplicity the  $\langle p_{\text{T}} \rangle$  in p–Pb and Pb–Pb collisions can be constructed from  $\langle p_{\text{T}} \rangle (N_{\text{ch}})$  in pp collisions, with additional knowledge of the multiplicity distribution in pp collisions.

This approach allows to quantify the expectation for  $\langle p_{\text{T}} \rangle$  in p–Pb and Pb–Pb collisions for pure  $N_{\text{coll}}$  scaling in absence of any nuclear effects and has been implemented in a Monte Carlo Model.

The model follows a Monte Carlo approach and works in the following steps:

1. the number of binary collisions  $N_{\text{coll}}$  is calculated from a MC Glauber model
2. for each of the binary collisions a random multiplicity is drawn sampling the pp multiplicity distribution
3. for the given multiplicity the corresponding  $\langle p_{\text{T}} \rangle$  is taken
4. the overall multiplicity  $N_{\text{ch}}$  is calculated as the sum over the multiplicities of individual NN collisions
5. the corresponding  $\langle p_{\text{T}} \rangle$  is calculated as the weighted sum over the  $\langle p_{\text{T}} \rangle$  of the individual NN collisions
6. the final  $\langle p_{\text{T}} \rangle$  for a given  $N_{\text{ch}}$  is the average over all events in this multiplicity class is taken

For the Glauber part of the calculation a Woods-Saxon distribution of the nucleons is assumed for the lead nucleus following the radial density profile

$$\rho(r) = \frac{\rho_0}{1 + e^{(r-r_0)/a}} \quad (5.4)$$

Here,  $r_0 = 6.62$  fm is the nuclear radius and  $a = 0.546$  fm is the skin thickness. The maximal nuclear density  $\rho_0$  determines the normalization and is not relevant for the MC implementation. In addition, two nucleons are required to have a minimal distance  $d_{\text{min}} = 0.4$ , i.e. a generated nucleus is rejected if any pair of nucleons has a distance  $d < d_{\text{min}}$ . The inelastic nucleon-nucleon cross section  $\sigma_{\text{NN}}^{\text{inel}} = 64$  mb was used for  $\sqrt{s_{\text{NN}}} = 2.76$  TeV, and  $\sigma_{\text{NN}}^{\text{inel}} = 70$  mb for  $\sqrt{s_{\text{NN}}} = 5.02$  TeV. Numerical values for all parameters are identical to the ones used in the centrality determination by ALICE [144].

As an input for the model, the multiplicity distributions measured by ALICE in inelastic pp collisions at  $\sqrt{s} = 2.36$  TeV and 7 TeV [227, 228] are used to model Pb–Pb collisions at  $\sqrt{s_{\text{NN}}} = 2.76$  TeV and p–Pb collisions at  $\sqrt{s_{\text{NN}}} = 5.02$  TeV. For the  $\langle p_{\text{T}} \rangle$  as a function of  $N_{\text{ch}}$  the measured values [229] are used as input. Results of the the measurement at  $\sqrt{s} = 2.36$  TeV are available for inelastic collisions; for  $\sqrt{s} = 7$  TeV results are for inelastic events with at least

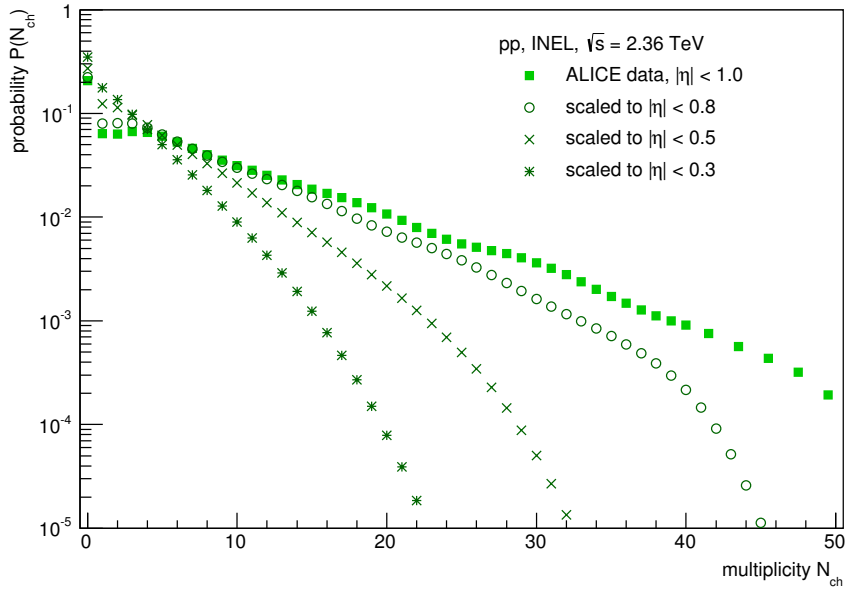


Figure 5.3.: Measured multiplicity distribution [227] for  $|\eta| < 1.0$  and distributions obtained from binomial scaling to smaller pseudorapidity intervals. Neither systematic nor statistical uncertainties are shown.

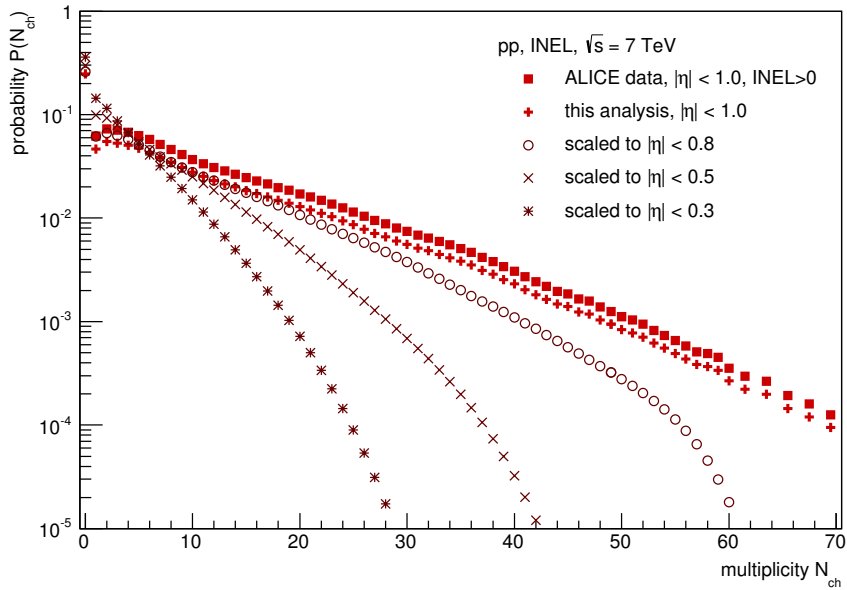


Figure 5.4.: Measured multiplicity distribution [228] in  $\text{INEL} > 0$  events for  $|\eta| < 1.0$  and distributions obtained from binomial scaling to smaller pseudorapidity intervals. The data points labeled “this analysis” have been derived from the normalization of the transverse momentum spectra measured in INEL pp collisions and the published ALICE results for  $\text{INEL} > 0$ . Uncertainties are not shown.

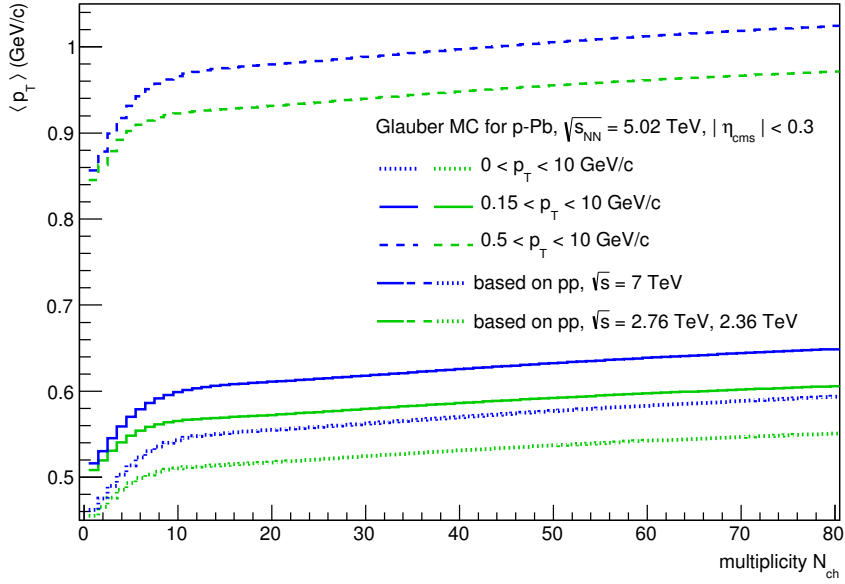


Figure 5.5.: Distribution of the average transverse momentum  $\langle p_T \rangle$  as a function of multiplicity  $N_{ch}$  obtained from the Glauber overlap model for p–Pb collisions. The green (blue) lines show the results that are obtained using the multiplicity distributions measured in pp collisions at  $\sqrt{s} = 2.36$  TeV ( $\sqrt{s} = 7$  TeV) and the measured  $\langle p_T \rangle$  ( $N_{ch}$ ) values from pp collisions at  $\sqrt{s} = 2.76$  TeV ( $\sqrt{s} = 7$  TeV) as in input. Results for different  $p_T$  ranges are shown in different line styles. Uncertainties have not been evaluated and are not shown.

one charged particle in the acceptance of  $|\eta| < 1.0$  (INEL>0). For the MC Glauber calculation also events with  $N_{ch} = 0$  have to be taken into account. The relative fraction of these events has been derived from the normalization of the  $p_T$  spectra (described in section 3.8). These  $N_{ch} = 0$  events are also included in 5.4, which has been normalized<sup>1</sup> to  $\int P(N_{ch}) = 1$ .

The input multiplicity distributions have been measured using the SPD silicon detector for an acceptance of  $|\eta| < 1.0$  (see Figure 5.3, Figure 5.4). They also take into account collisions that do not produce any charged particles in the acceptance. To estimate the particle production in the limited acceptance of  $|\eta| < 0.3$  resp.  $|\eta| < 0.8$  a flat distribution in  $dN/d\eta$  is assumed with a binomial probability density function i. e. for each simulated particle a random number is drawn to decide if it is produced inside the acceptance. The multiplicity distributions arising from this approach are shown in Figures 5.3 and 5.4.

The resulting average transverse momenta are shown in Figure 5.5 for simulated p–Pb collisions. All curves are for  $|\eta_{cms}| < 0.3$ , the average is over different  $p_T$  ranges corresponding to the different input measured in pp collisions. Two versions of the calculation are shown based on input from pp collisions at different collision energy. The difference is dominated by the different multiplicity distributions, while the  $\langle p_T \rangle$  as a function of  $N_{ch}$  there is only a tiny difference between the two energies. For comparisons to p–Pb measurements at  $\sqrt{s_{NN}} = 5.02$  TeV, the  $\sqrt{s} = 7$  TeV multiplicity distribution and  $\langle p_T \rangle$  are used. Equivalent calculations for Pb–Pb collisions are shown in Figure 5.6.

<sup>1</sup> The resulting  $\langle p_T \rangle(N_{ch})$  of the Monte Carlo model calculation does not depend on the normalization.

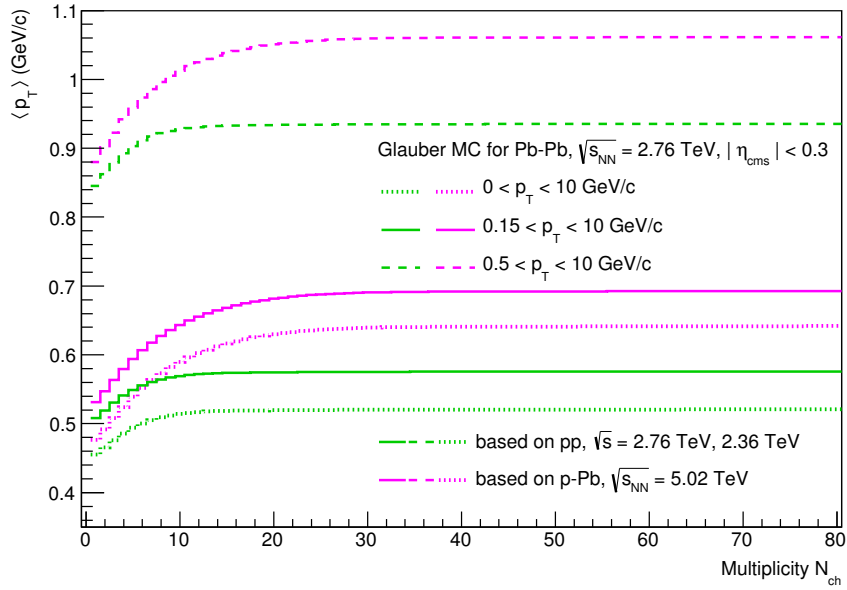


Figure 5.6.: The average transverse momentum  $\langle p_T \rangle$  as a function of multiplicity  $N_{ch}$  obtained from the Glauber overlap model for Pb–Pb collisions. The green lines show the results that are obtained using the multiplicity distributions measured in pp collisions at  $\sqrt{s} = 2.36$  TeV and the measured  $\langle p_T \rangle$  ( $N_{ch}$ ) values from pp collisions at  $\sqrt{s} = 2.76$  TeV as in input. In addition, Glauber calculations based on p–Pb collisions at  $\sqrt{s_{NN}} = 5.02$  TeV are shown in magenta. Results for different  $p_T$  ranges are shown in different line styles. Uncertainties have not been evaluated and are not shown.

Both calculations show some characteristic features. At the lowest  $N_{ch}$  there is a region in which the  $\langle p_T \rangle$  increases strongly with multiplicity, similar to the pp input. Here, a rise in  $N_{ch}$  can be attributed primarily to a higher multiplicity in the underlying nucleon-nucleon collision. At  $N_{ch}$  around 5-10 a substantial flattening of  $\langle p_T \rangle$  ( $N_{ch}$ ) is observed indicating the transition to the region in which larger multiplicities are produced by a larger number of binary collisions. For Pb–Pb collisions,  $\langle p_T \rangle$  at large  $N_{ch}$  is nearly independent of  $N_{ch}$ . In the case of p–Pb collisions  $\langle p_T \rangle$  increases further with rising  $N_{ch}$  up to the highest multiplicities. This behavior is expected, as the maximal number of binary nucleon-nucleon collisions in a p–Pb collision is small, too small to produce large values of  $N_{ch}$  from "average" minimum bias NN collisions alone. In addition to many binary collisions  $N_{coll}$  also the individual NN collisions are biased towards higher multiplicities, i.e. harder events with a larger average transverse momentum.

In a similar way collisions of two Pb nuclei can be considered as a superposition of p–Pb collisions if only one of the colliding nuclei is split into single nucleons. This concept could encode part of the modifications observed in Pb–Pb. In this case the MC Glauber model is utilized to determine the number of p–Pb collisions in a Pb–Pb collisions, which is equivalent to the number of participants  $N_{part}$  of either of the two nuclei.

Since measurements of fully-corrected multiplicity distributions in p–Pb collisions are not yet publicly available, distributions extracted from the transverse momentum analysis have been used to demonstrate the concept. These distributions are corrected for efficiency, contamina-

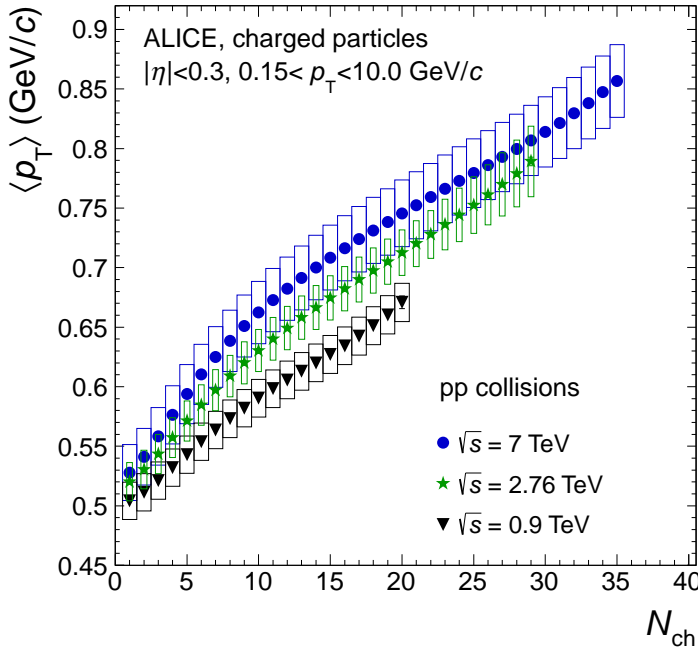


Figure 5.7.: The average transverse momentum  $\langle p_T \rangle$  of charged particles as a function of the charged-particle multiplicity  $N_{ch}$  measured in pp collisions at  $\sqrt{s} = 0.9, 2.76$  and  $7$  TeV.  $\langle p_T \rangle$  is averaged over the kinematic range  $|\eta| < 0.3$  and  $0.15 < p_T < 10$  GeV/c, the multiplicity  $N_{ch}$  corresponds to the same pseudorapidity range but is integrated over all momenta, down to  $p_T = 0$ . The systematic uncertainties are shown as open boxes around the data points, statistical uncertainties are smaller than the symbol size.

Figure published in [229].

tion and  $p_T$ -cutoff (acceptance), but do not take into account resolution effects of the response matrix.

Results are shown in Figure 5.6. The simulation of Pb–Pb collisions as an overlap of p–Pb collisions leads to a significantly larger  $\langle p_T \rangle$  compared to the expectations from incoherent pp collisions. Compared to the measured results (see following section), this approach over-predicts the  $\langle p_T \rangle$  in Pb–Pb collisions.

### 5.3 Results

The average transverse momentum  $\langle p_T \rangle$  as a function of the multiplicity  $N_{ch}$  were measured for charged particles and are shown in Figure 5.7 for pp collisions at  $\sqrt{s} = 0.9, 2.76$  and  $7$  TeV. A strong and approximately linear increase of  $\langle p_T \rangle$  with rising  $N_{ch}$  is observed in pp collisions at all energies. For a given  $N_{ch}$  also a small increase of  $\langle p_T \rangle$  with increasing  $\sqrt{s}$  is observed.

A comparison of the results in pp collisions at  $\sqrt{s} = 7$  TeV to p–Pb  $\sqrt{s_{NN}} = 5.02$  TeV and Pb–Pb  $\sqrt{s_{NN}} = 2.76$  TeV is shown in Figure 5.8.

In p–Pb collisions, the rise of  $\langle p_T \rangle$  as a function of  $N_{ch}$  is very similar to that observed in pp collisions for  $N_{ch}$  up to  $15$ . For events with larger multiplicity the rise of  $\langle p_T \rangle$  is much less pronounced. The latter can be attributed to the fact that in p–Pb collisions a high multiplicity

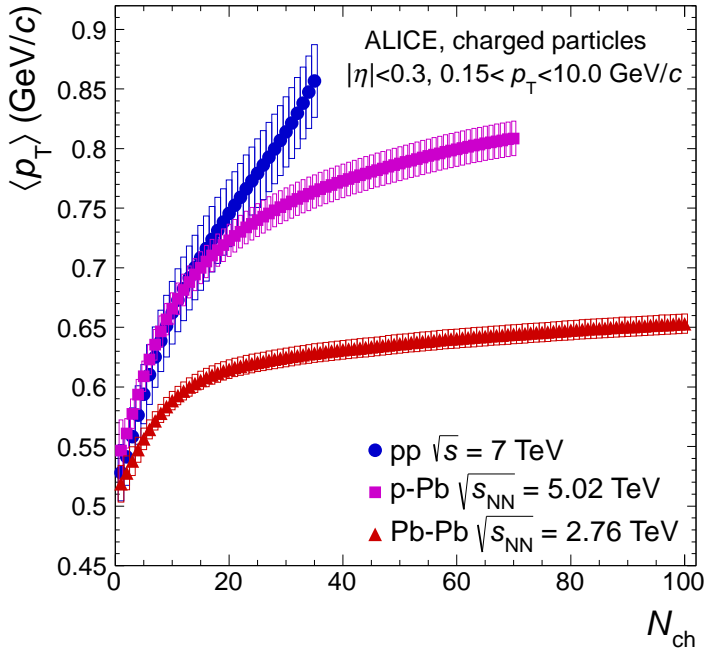


Figure 5.8.: Comparison of the average transverse momentum  $\langle p_T \rangle$  as a function of the charged particle multiplicity  $N_{ch}$  in pp  $\sqrt{s} = 7$  TeV, p-Pb  $\sqrt{s_{NN}} = 5.02$  TeV and Pb-Pb  $\sqrt{s_{NN}} = 2.76$  TeV collisions.  $\langle p_T \rangle$  is averaged over  $\eta_{cms} < 0.3$  and  $0.15 < p_T < 10$  GeV/c,  $N_{ch}$  is the integrated yield in  $\eta_{cms} < 0.3$  and  $p_T > 0$ . Systematic uncertainties are shown as open boxes around the data, statistical uncertainties are negligible.

Figure published in [229].

events contains a larger number of nucleon-nucleon collisions, while in pp large multiplicities require hard collisions.

Pb-Pb collisions show a lower  $\langle p_T \rangle$  and much smaller rise of  $\langle p_T \rangle$  with multiplicity. Above  $N_{ch} = 20$ ,  $\langle p_T \rangle$  is not completely flat as expected from the simple Glauber model, but keeps increasing up to the largest  $N_{ch}$ . Note that  $N_{ch} = 100$  corresponds approximately to 50% centrality.

Figure 5.9 shows the comparison of the results in pp, p-Pb and Pb-Pb collisions to those obtained from model calculations. Comparison of pp results to PYTHIA8 are shown with and without color reconnection (CR) [230] and highlights the significance of this mechanism for the description of  $\langle p_T \rangle$  as a function of  $N_{ch}$  within this generator.

Results from p-Pb and Pb-Pb collisions are compared to the Monte Carlo event generators EPOS [231], DPMJET [158], HIJING [157] and AMPT [232]. In addition, the expectations from the incoherent overlap of pp collisions, as obtained from the Glauber MC approach described in the previous section, are shown for p-Pb and Pb-Pb collisions.

Except for EPOS, the predictions from all event generators for p-Pb and Pb-Pb, are similar in shape and comparable in magnitude to the expectation from the simple Glauber calculation. EPOS gives a good description of  $\langle p_T \rangle$  in pp and p-Pb collisions but fails to describe Pb-Pb.

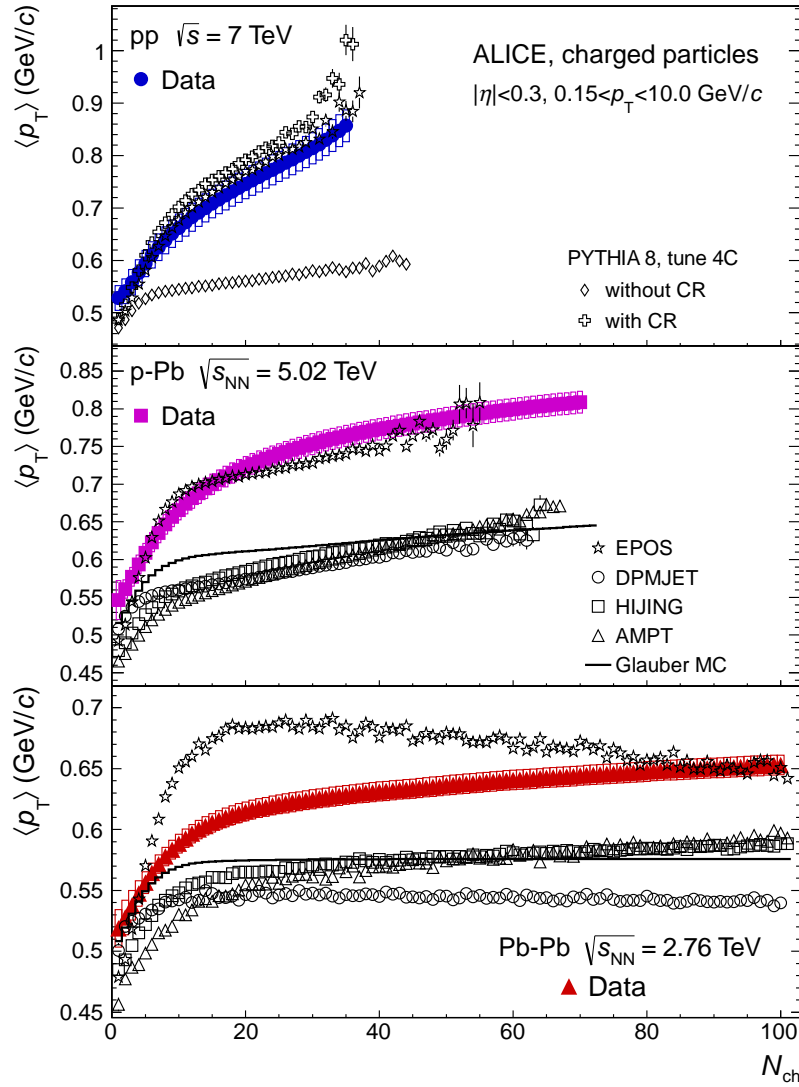


Figure 5.9.: Measured average transverse momentum  $\langle p_T \rangle$  as a function of charged particle multiplicity  $N_{ch}$  for the different collisions systems in comparison to calculation from models. Systematic uncertainties are shown as open boxes. Top panel: pp collisions at  $\sqrt{s} = 7$  TeV in comparison to the PYTHIA8 Monte Carlo Event generator, tune 4C with and without color reconnection (CR). Middle and Bottom panel: Comparison to the Monte Carlo Event generators EPOS, DPMJET, HIJING and AMPT for p-Pb collisions at  $\sqrt{s_{NN}} = 5.02$  TeV (middle panel) and Pb-Pb collisions at  $\sqrt{s_{NN}} = 2.76$  TeV (bottom panel). The expectations from an incoherent superposition of nucleon-nucleon collisions calculated in a Glauber approach (see section 5.2) are shown as lines.

Figure published in [229].

In the calculations assuming an incoherent superposition of pp collisions,  $\langle p_T \rangle$  for a given  $N_{\text{ch}}$  is dominated by multiple soft (low multiplicity) nucleon-nucleon collisions. A deviation from binary collisions scaling is expected at low  $p_T$ , with rather an approximate participant scaling.

At low  $p_T$ , a deviation from  $N_{\text{coll}}$  scaling, namely a nuclear modification factor less than unity at low  $p_T$ , is observed in p–Pb collisions (see section 4.3). Since this soft part of the spectrum dominates the average transverse momentum  $\langle p_T \rangle$ , a larger measured  $\langle p_T \rangle$  is expected compared to the calculation from an incoherent superposition of pp collisions. Taking the  $R_{\text{pPb}}$  measured in minimum bias collisions as an estimator of this deviation from  $N_{\text{coll}}$  scaling into account in the Glauber MC leads to larger values of  $\langle p_T \rangle$  for all  $N_{\text{ch}}$ . However, the increase in  $\langle p_T \rangle$  is too small to describe the data the discrepancy in shape of  $\langle p_T \rangle$  ( $N_{\text{ch}}$ ) remains.

The results from Pb–Pb collisions shown in Figures 5.9 and 5.8 cover only semi-central to peripheral centralities (approximately 50–100%). For the extension to more central collisions the  $\langle p_T \rangle$  (for  $|\eta| < 0.8$ ) was extracted as a function of collision centrality from the  $p_T$  distributions presented in section 4.4 (published in [177]). The corresponding average  $N_{\text{ch}}$  (for  $|\eta| < 0.3$ ) is obtained from the ALICE measurements of  $dN_{\text{ch}}/d\eta$  [115] (for  $|\eta| < 0.5$ ) according to  $N_{\text{ch}}(|\eta| < 0.3) = dN_{\text{ch}}/d\eta \cdot 0.6$ . Note that around mid-rapidity the pseudorapidity density of charged particles shows only little dependence on  $\eta$  [116]. The results are shown in Figure 5.10 along with the higher granularity measurement for  $|\eta| < 0.3$  and compared to expectations from the Glauber calculation (see section 5.2), the Monte Carlo event generators AMPT, HIJING and DPMJET as well as a calculation in the b-CGC model [233]. The b-CGC calculation is in agreement with  $\langle p_T \rangle$  measured in pp, p–Pb and  $N_{\text{ch}} < 100$  Pb–Pb collisions (see Ref. [233]), but predicts a continued increase of  $\langle p_T \rangle$  with  $N_{\text{ch}}$  that is inconsistent with the data.

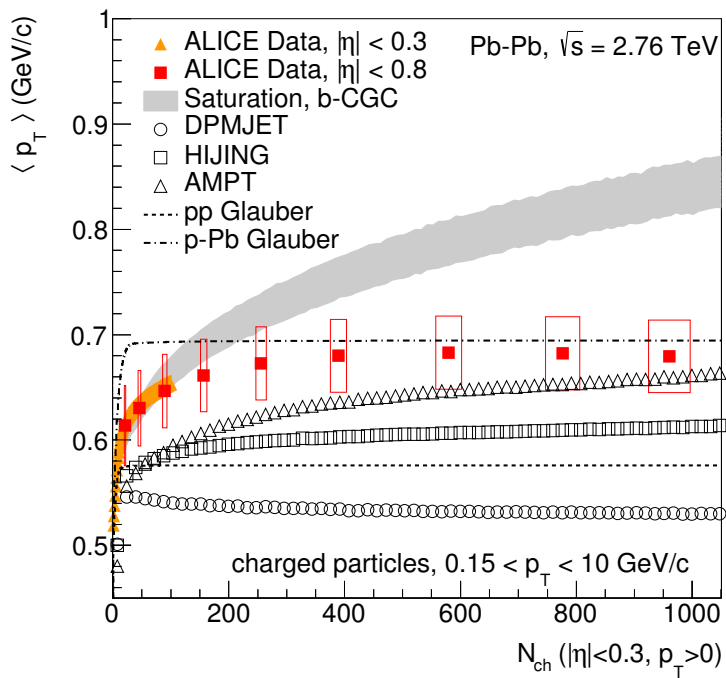


Figure 5.10.: The average transverse momentum  $\langle p_T \rangle$  of charged particles as a function of the charged-particle multiplicity  $N_{ch}$  measured in Pb-Pb collisions at  $\sqrt{s_{NN}} = 2.76$  TeV in comparison to expectations from an incoherent superposition of pp and p-Pb collisions (calculated from the Glauber model described in section 5.2), the MC event generators DPMJET, HIJING and AMPT and a model based on gluon saturation [233]. Systematic uncertainties shown for the data in centrality intervals ( $|\eta| < 0.8$ ) are the maximal deviations allowed by the systematic uncertainties of the  $p_T$ -spectra and represent the most conservative estimate.



## 6 Summary and Conclusions

Transverse momentum ( $p_T$ ) distributions at midrapidity have been measured for inelastic (INEL) pp collisions at  $\sqrt{s} = 0.9, 2.76$  and  $7$  TeV, in non-single-diffractive (NSD) p–Pb collisions at  $\sqrt{s_{NN}} = 5.02$  TeV and in 0–80% central Pb–Pb collisions at  $\sqrt{s} = 2.76$  TeV. The measurements cover the pseudorapidity ranges  $|\eta| < 0.8$  (pp, Pb–Pb) respectively  $-0.3 < \eta_{\text{cms}} < 1.3$  (p–Pb) and are presented as differential cross sections (pp) respectively differential yields (pp, p–Pb, Pb–Pb). They cover  $0.5 < p_T < 20$  GeV/c (p–Pb 2012),  $0.15 < p_T < 20$  GeV/c (pp  $\sqrt{s} = 0.9$  TeV),  $0.15 < p_T < 32$  GeV/c (pp  $\sqrt{s} = 2.76$  TeV) and  $0.15 < p_T < 50$  GeV/c (pp  $\sqrt{s} = 7$  TeV, Pb–Pb, p–Pb 2013), respectively. Results include the evolution of particle production with centrality in Pb–Pb collisions and with pseudorapidity in p–Pb collisions. The nuclear modification factors  $R_{AA}$  and  $R_{pPb}$  were calculated using the measurements in pp collisions as a reference. In addition,  $p_T$  spectra were obtained as a function of the number of reconstructed charged particles that allowed to extract the multiplicity dependence of the average transverse momentum.

In pp collisions, NLO calculations [197] fail to describe the measured differential cross section. The large discrepancy of about a factor for  $\sqrt{s} = 7$  TeV seen with  $\mu = p_T$  is reduced to about a factor 1.5 if the scale is changed to  $\mu = 2p_T$ . It seems that this scale is more appropriate, likely because the hard partonic scale involved in the production of hadrons at a given  $p_T$  is larger than the  $p_T$  of the final state hadron. The variation of the NLO cross sections with  $\mu$  reflects the rather large theoretical uncertainties of the calculation, which are about a factor 2 larger than the systematic uncertainties of the measurement. The shape of the  $p_T$  spectrum is much better predicted by NLO pQCD for  $p_T > 10$  GeV/c, also the relative dependence of the cross section on  $\sqrt{s}$  is well described. In particular, the increase from 2.76 TeV to 7 TeV is in reasonable agreement with the data.

The Monte Carlo event generators PYTHIA6 (tunes D6T, Perugia0) [155], PYTHIA8 [179] and PHOJET [156] give a better description of the spectra compared to the NLO calculations, however, none of the studied generators is consistent with the data over the entire range of  $p_T$ . The MC generators describe the increase of differential yields with  $\sqrt{s}$  reasonably well in the non-perturbative regime ( $p_T < 1$  GeV/c). At large  $p_T > 5$  GeV/c the energy dependence of the spectra is not well described by the MC generators, in contrast to the NLO pQCD calculations.

Monte Carlo event generators need some further tuning, but  $p_T$  spectra are among the observables that are already rather well described. The discrepancy of almost a factor 2 between data and NLO calculations is not observed for jet spectra [234]. This points to a problem in the leading hadron fragmentation function, which seems to be too hard. The good description of the relative  $\sqrt{s}$  dependence observed for the NLO calculations allows to scale measured pp spectra to other collision energies.

The measurements of the average transverse momentum  $\langle p_T \rangle$  as a function of multiplicity  $N_{\text{ch}}$  is dominated by the low- $p_T$  soft part of the spectrum but also significantly influenced from jets arising from hard pQCD processes. Especially the increase of  $p_T$  with  $N_{\text{ch}}$  can be attributed to contributions from jets, which increase the number of high  $p_T$  particles in the sample.

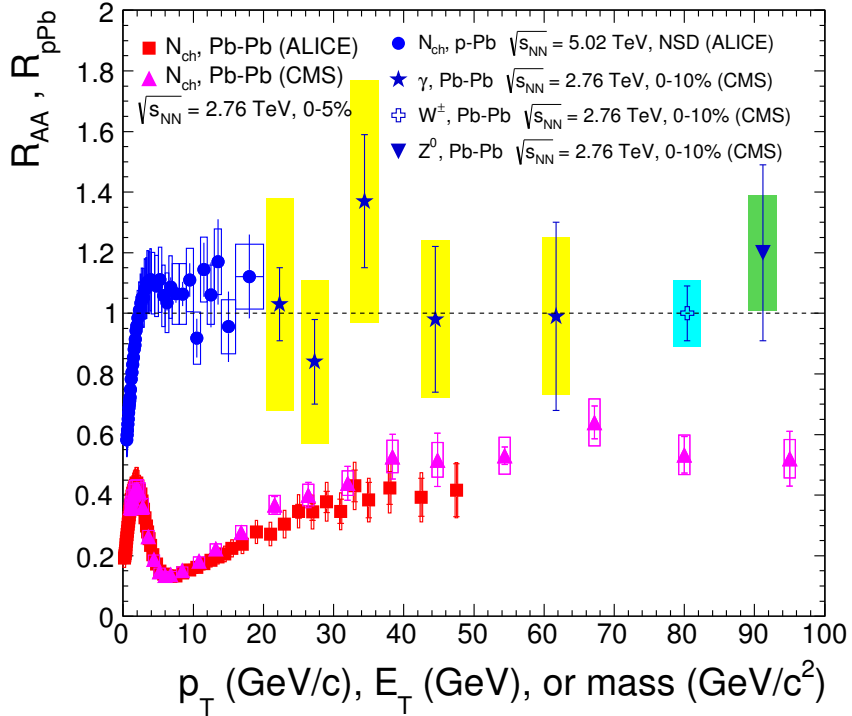


Figure 6.1.: Nuclear modification factors of charged particles as a function of  $p_T$  measured with ALICE in minimum bias p–Pb collisions ( $\sqrt{s_{NN}} = 5.02$  TeV) and 0–5% central Pb–Pb collisions ( $\sqrt{s_{NN}} = 2.76$  TeV) compared to Pb–Pb results from CMS:  $R_{AA}$  ( $p_T$ ) of charged particles in 0–5% central collisions [196],  $R_{AA}$  ( $E_T$ ) of isolated photons (0–10% centrality) [236],  $R_{AA}$  of  $W^\pm$  [237] and  $Z^0$  bosons [238] (0–10% centrality) drawn at the respective boson masses.

The strong increase seen in the the multiplicity dependence of  $\langle p_T \rangle$  in pp collisions, is well described by PYTHIA8, if color reconnection is turned on. PYTHIA6 without color reconnection tuned to available data is able to describe most observables but fail for  $\langle p_T \rangle$  ( $N_{ch}$ ), as stated in [181]. This color reconnection introduces an interaction between different parton-parton interactions and can be interpreted as a collective behavior. Long range correlations were also observed by the CMS experiment in high multiplicity pp collisions [235]. They are similar to long range correlations that are a characteristic observation in heavy-ion collisions and there commonly attributed to flow. However, the interpretation of these results in pp is not yet clear and also models based on the CGC are able to describe the  $\langle p_T \rangle$  ( $N_{ch}$ ) measurements well [233].

Nuclear modification factors obtained in central Pb–Pb and minimum bias p–Pb collisions are shown in Figure 6.1 that neatly summarize results combined from all three collision systems. Measurements of  $R_{AA}$  for charged particles (0–5% centrality), direct photons and weak bosons (0–10% centrality) in Pb–Pb collisions come from the CMS Collaboration [196, 236–238] and are included in the figure. Charged particle  $R_{AA}$  measurements by the two experiments are in agreement within the uncertainties, however, the CMS  $R_{AA}$  is slightly larger at high  $p_T$  (ALICE:  $R_{AA} \approx 0.4$ , CMS:  $R_{AA} \approx 0.5$ ).

The results on  $R_{ppb}$  (as shown in Figure 6.1) show that there are no strong initial state effects and binary collision scaling is a valid assumption for the initial production of particles at high

$p_T$  in hard QCD processes. A strong anti-shadowing effect with  $R_{p\text{Pb}} > 1$  for charged particles at  $p_T > 30$  GeV/c that was observed by the CMS and ATLAS experiments [212, 214] is not seen in the ALICE data, a measurement of  $R_{p\text{Pb}}$  for charged jets [239] is consistent with unity up to  $p_{T,\text{jet}} = 90$  GeV/c.

The Cronin enhancement, i. e. an  $R_{p\text{Pb}}$  above unity at intermediate  $p_T$ , is much smaller compared to results at lower energies [201–204], a result which can be explained by the much harder spectrum at LHC energies, diminishing the effect of  $k_T$ -broadening [240]. Measurements of  $R_{p\text{Pb}}$  for identified light hadrons [208] show a significant Cronin enhancement for protons and  $\Xi$  mesons, but not for kaons or pions. Thus a small enhancement has to be present also for charged particles. The biased nuclear modification factor  $Q_{p\text{Pb}}$  of charged particles [241] shows an increase of the enhancement from peripheral to central collisions.

Overall the  $R_{p\text{Pb}}$  shows a behavior that matches the most naive expectation for p–Pb collisions: scaling with  $N_{\text{part}}$  at low  $p_T$  and scaling with  $N_{\text{coll}}$  at high  $p_T$  with a smooth transition in between. The results show that other cold nuclear matter effects, like shadowing or energy loss in nuclear matter are, at least, small in magnitude. This has relevant implications for the interpretation of results from Pb–Pb collisions.

The basic idea of binary collisions scaling is also supported in Pb–Pb collisions by the observation that the  $R_{AA}$  for isolated photons [236], W and Z bosons [237, 238] is compatible with unity (see Figure 6.1). These results for hard probes which are not taking part in the strong interaction demonstrate that binary collision scaling is valid for processes with large momentum transfer also in Pb–Pb collisions and that the geometrical properties  $N_{\text{coll}}$  or  $T_{AA}$  extracted from the Glauber model approach match the experimental data. There is one difference between charged hadrons and photons, W and Z bosons worth mentioning: High  $p_T$  hadrons originate from even-higher  $p_T$  partons, i.e. quarks or gluons. They can be produced in all partonic collisions (quark-quark as well as gluon-gluon or gluon-quark). At LHC most jets originate from gluons, with increasing  $p_T$  the fraction of jets from quarks increases [221]. Hard probes that are not subject to QCD interactions ( $\gamma, Z^0, W^\pm$ ) can, in the lowest order diagrams, only be produced by collisions of quarks, because these carry electric and weak charges. Gluons do not and can't couple directly to electric and weak charges. In higher order diagrams this is possible (for example the Higgs production from gluon fusion  $gg \rightarrow H$  via a heavy quark loop) and also gluon-quark processes can contribute. But differences between jets and color-neutral probes remain in the sense that jets (or equivalently charged hadrons) are more sensitive to the gluon distributions while  $\gamma, Z^0, W^\pm$  are probing the quark content of the colliding nucleons.

Particle production at low  $p_T$ , and in particular the strong correlation between the average transverse momentum  $\langle p_T \rangle$  and the multiplicity  $\langle N_{\text{ch}} \rangle$  observed in p–Pb collisions can not be explained with binary collision scaling. Results on  $\langle p_T \rangle$  can be interpreted as an initial state effect in the context of gluon saturation [233] or as final state collective effects. For instance the Monte Carlo event generator EPOS [231], which includes also a fluid dynamic description in proton-nucleus collisions if the energy density is high enough, is able to reproduce the observed  $\langle p_T \rangle$  ( $N_{\text{ch}}$ ).

In central (0-5%) Pb–Pb collisions a strong suppression of particle production at large  $p_T$  is observed. This can be attributed to energy loss of high energy partons traversing the QGP medium that is produced in the collision. The nuclear modification factor in central collisions (0-5%) has a minimum of  $R_{AA} \approx 0.13$  at  $p_T = 6-7$  GeV/c and a rises for  $p_T > 7$  GeV/c

to about  $R_{AA} \approx 0.4$  for  $30 < p_T < 50$  GeV/c. The suppression gradually decreases with decreasing centrality but remains substantial also for peripheral collisions, with  $R_{AA} \approx 0.65$  at  $p_T = 6$  GeV/c in 70-80% central collisions.

The production of initial partons at large transverse momenta is qualitatively described by pQCD. The fact that in p–Pb collisions  $R_{pPb}$  of charged particles is compatible with unity at large transverse momenta, shows that the quite simple approach of the Glauber model works as no deviations from naive binary collision scaling are observed. Note that this does not need to be true for centrality or multiplicity selected p–Pb collisions. Furthermore, the results from p–Pb collision indicate that at high  $p_T$  nuclear initial state effects (like saturation or  $k_T$ -broadening) are also negligible in Pb–Pb collision and that suppression of particle production in Pb–Pb collisions is truly a final state effect. In Pb–Pb the idea of binary collision scaling is supported by measurements of probes that have little interaction with the medium as they have no color charge. In particular measurements of isolated photons, W and Z bosons are in agreement with binary collisions scaling. The observed suppression of charged particles can be described by attributed to energy loss of high energy partons with the QCD medium that is created in such collisions leading to parton energy loss. The effects of energy loss depend on the interactions with the medium and the medium properties itself. Most of the energy loss models are different in both aspects, the mechanism of the energy loss and the properties and evolution of the medium. Nevertheless the characteristic rise of  $R_{AA}$  (which was not observed at RHIC) seems to be a generic feature of all model calculations. This rise can be fully attributed to the harder spectrum of the initial parton production at LHC [224, 225]. The fact that the suppression of particle production at large  $p_T$  is stronger compared to RHIC energies, although the harder production spectrum would suggest a larger  $R_{AA}$ , is a sign of the higher initial density and longer lifetime of the QGP at LHC [221]. This idea is supported by the strong increase in  $dN_{ch}/d\eta$  [114], which is related to the initial density in a fluid dynamic description.

Additional constrains of the models are given by the measurement of the harmonic flow coefficients at large  $p_T$  or the dependence of  $R_{AA}$  on the event plane angle (related to the path length in the medium). At high energy elliptic flow is not created by pressure gradients and the different expansion velocities of the medium. Instead, the different track length in the medium lead to a suppression that depends on the relative orientation of the parton to the reaction plane. A complete model of parton energy loss that confidently allows to extract medium properties needs to be able to describe not only  $R_{AA}$  of charged particles and jets, but also the angular correlations at high  $p_T$ .

## 7 Outlook

While the results presented in this thesis are an important step, the charged particle analysis can still be improved and extended to further constrain theoretical models of pp, p–Pb and Pb–Pb collisions. Especially in the case of  $R_{AA}$  and  $R_{pPb}$  improved precision measurements with smaller uncertainties will allow to exclude models that are currently consistent with the data. In p–Pb it will be possible to distinguish between CGC or shadowing/anti-shadowing and in Pb–Pb the data will allow to extract more details on mechanism of energy loss (pQCD, AdS/CFT, elastic, radiative). Especially towards larger  $p_T$  theoretical predictions for  $R_{AA}$  differ significantly: from a continued rise of  $R_{AA}$ , even above unity, as predicted by JEWEL [224] to a flattening or even a decreasing  $R_{AA}$  [242].

For the measurements of charged particles two key issues have to be addressed: the improvement of precision and the extension to higher transverse momenta. To improve the precision at low and intermediate  $p_T$  a significant reduction of systematic uncertainties is required. At high  $p_T$ , the improvements in the precision and extension of the  $p_T$  reach requires both, higher statistics data and improved systematic uncertainties. In principle it should be possible to extend the  $p_T$  reach to 100 GeV/c. In the analysis of  $\langle p_T \rangle$  as a function of  $N_{ch}$ , improved precision at low  $p_T$  is most important, especially when the extrapolation to  $p_T = 0$  is used. Here, also extension to lower  $p_T$  (80 MeV/c) would slightly reduce the uncertainty of the measurement.

The remainder of this section contains a technical outlook on the future potentials for the analysis of inclusive charged particles in ALICE. Clearly, at low and intermediate  $p_T$  the study of identified particle production provides more differential information and it might not be worth the effort required to further improve the accuracy of charged particle results. At the high  $p_T$  limit, particle identification is much more difficult and currently hadrons in ALICE can be identified up to  $p_T = 20$  GeV/c [216]. Here, the analysis of inclusive charged particles has the advantage of smaller systematic and statistical uncertainties and can cover larger  $p_T$ . In this context it is worth mentioning that for  $\pi$ , K, p measurements of the nuclear modification factors  $R_{AA}$  and  $R_{pPb}$  do not differ from those of charged particles for  $p_T > 10$  GeV/c [208, 216].

In the following this section is organized as follows. First the possibilities of further analysis and future options are discussed for the different collision systems separately (sections 7.1, 7.2 and 7.3). Secondly, different possibilities (common to all collision systems) to reduce the systematic uncertainties (section 7.4) and statistical (section 7.5) uncertainties of the measurement are described. In the last section 7.6 future running scenarios are briefly described with their potential for the high  $p_T$  analysis.

### 7.1 pp collisions and pp reference

The main motivation to improve the measurements of pp collisions is to obtain a better constrained reference for the calculation of  $R_{AA}$  and  $R_{pPb}$  and extend this reference towards larger transverse momenta, possibly up to  $p_T = 100$  GeV/c. The uncertainties of the pp reference at  $\sqrt{s} = 2.76$  TeV (as needed for  $R_{AA}$ ) are dominated by the systematic uncertainties of the

measurement. At high  $p_T$  the use of a parameterization and extrapolation adds additional uncertainties yielding about 20% at 50 GeV/c, plus the normalization uncertainty that comes on top of that. A significant reduction of the systematic uncertainty (a factor two is a reasonable goal) is needed as well as an extension of the pp measurement towards larger  $p_T$  and improved statistics at high  $p_T$ . Currently the measurement at  $\sqrt{s} = 2.76$  TeV is statistically limited to  $p_T < 32$  GeV/c.

The pp results presented in this thesis are based only on a part of all data that has been collected so far. At  $\sqrt{s} = 7$  TeV about  $100 \cdot 10^6$  minimum bias events have been used in the analysis and there is still about a factor 3 more data available collected in 2010. The main focus of the 2011 pp running was on rare triggers, the amount of minimum bias triggered events is comparable to that recorded in 2010. The usage of triggered data for  $p_T$  spectra is not straight-forward and requires a detailed understanding of the trigger bias. For  $\sqrt{s} = 2.76$  TeV data, it has been considered to include data triggered with the EMCAL neutral energy jet trigger, but turned out to be not feasible. Extending the measurements of  $\langle p_T \rangle$  to larger  $N_{ch}$  could be achieved with events recorded with high multiplicity triggers, but these triggers are sensitive also to pile-up events.

Collisions at  $\sqrt{s} = 8$  TeV have been recorded in 2012. The sample of Minimum Bias data was mostly collected with the V0AND trigger and suffers from high LHC background due to the high luminosity delivered for the other experiments. Compared to the other experiments a smaller luminosity was achieved in the ALICE interaction region using satellite bunches for collisions. The analysis of the Minimum Bias data alone does not seem to be worth the effort as the data at  $\sqrt{s} = 7$  TeV were recorded at more favorable running and detector conditions (lower luminosity, lower background) and contain more Minimum Bias events. The difference in  $\sqrt{s}$  between 7 and 8 TeV is also too small to be useful as an extension of the energy dependence. pp data recorded at  $\sqrt{s} = 8$  TeV with the TRD charged jet trigger on the other hand could lead to a significant extension of the  $p_T$  range and a better statistical precision.

A rather small sample (about  $20 \cdot 10^6$ ) of Minimum Bias pp collisions at  $\sqrt{s} = 2.76$  TeV have been collected in a short pp run in 2013. This amount of data does not allow a significant improvement with respect to current data in terms of statistics.

Concerning the  $\sqrt{s} = 5.02$  TeV pp reference required for  $R_{ppb}$ , the most desirable solution would be a dedicated period of pp collisions at the same collision energy that should allow to gather significant statistics, possibly with a suitable trigger to increase statistics at large transverse momenta. Such a measurement could also serve as a baseline for future Pb–Pb collisions at the full LHC energy of  $\sqrt{s_{NN}} = 5.52$  TeV and might be carried out in the upcoming run II of the LHC.

Uncertainties in the normalization of the spectra are likely to remain at the current level. Similarly, for the calculation of the nuclear overlap  $\langle T_{ppb} \rangle$  and  $\langle T_{AA} \rangle$  no significant reduction of systematic uncertainties is expected.

A rather straightforward extension of the analysis is the addition of new event classes (NSD<sup>1</sup>, INEL>0). Results for these event classes could serve as an additional constraint for Monte Carlo generators and simplify the comparison to other LHC experiments. The uncertainty of the overall normalization is closely related to the characteristics of diffractive processes. For

<sup>1</sup> Results of 2009 data at  $\sqrt{s} = 0.9$  TeV are published in [176] also for non single diffractive events.

event classes like NSD or INEL>0 the MB trigger is more efficient thus they have the potential advantage of reduced normalization uncertainties.

The  $\langle p_T \rangle$  analysis in pp could easily be extended to include the pseudorapidity dependence.  $\langle p_T \rangle$  averaged over different  $p_T$  ranges focussing on different (soft, intermediate, hard) parts of the spectra or higher order moments of the  $p_T$  distribution can also be obtained easily, but it remains unclear if this would really provide new insights. The measurement of  $p_T$  spectra as a function of multiplicity gives the most complete information and was already performed in the course of the analysis of  $\langle p_T \rangle$  but spectra themselves have not been published so far. A difficulty here is the unfolding of the  $N_{ch}$  intervals, for  $\langle p_T \rangle$  this was approximated by a reweighting procedure.

---

## 7.2 p–Pb collisions and $R_{p\text{Pb}}$

---

In p–Pb collisions an improved precision at intermediate  $p_T$  is required to confirm the existence of a small Cronin-type enhancement of  $R_{p\text{Pb}}$  and quantify its magnitude. As the systematic uncertainties in p–Pb and pp spectra are of the same size, also the pp reference needs to be improved as described above to significantly reduce the systematic uncertainties of  $R_{p\text{Pb}}$ . The separation of uncertainties correlated between the two measurements, could lead to cancellations in the ratio  $R_{p\text{Pb}}$ .

The surprising of  $R_{p\text{Pb}} > 1$  at high  $p_T$  observed by the CMS Collaboration in a preliminary analysis [212], is not seen in the ALICE data. However, the results of ALICE and CMS are in marginal agreement within the systematic and statistical uncertainties. Larger statistics data and smaller systematic uncertainties are essential to confirm, or exclude, a possible inconsistency between the two experiments. A possible extension of the  $p_T$  range towards larger  $p_T$  requires substantially more statistics at high  $p_T$  and an extended  $p_T$  range of the pp reference.

With all Minimum Bias p–Pb data already analyzed, higher statistics could be achieved only with the analysis of TRD and/or EMCal jet triggered data. The events collected with the charged jet TRD trigger have a smaller bias compared to the neutral jet EMCal trigger, but corresponds to an integrated luminosity lower by about a factor ten.

With the analysis of Pb–p data (directions of p and Pb beams are swapped) in addition to p–Pb data, the pseudorapidity coverage of the measurements can be extended to  $|\eta_{\text{cms}}| < 1.3$ . In that way the  $\langle p_T \rangle$  can be measured as a function of (pseudo-)rapidity over a wide range. A further extension of the  $\eta$  range is possible if the track cuts, which require long tracks in the TPC, are released. Recall, that the reason for these cuts is the momentum resolution at high  $p_T$ , which is of no relevance for  $\langle p_T \rangle$ . The  $y$  or  $\eta$  dependence of  $\langle p_T \rangle$  is an interesting opportunity as it could help to distinguish between Color Glass Condensate (CGC) and hydrodynamic models, as proposed in [243].

The analysis of  $p_T$  spectra and  $R_{p\text{Pb}}$  as a function of centrality (defined in multiplicity intervals measured with different detectors) is a natural extension of the current Minimum Bias analysis and currently in progress. Preliminary results for  $Q_{p\text{Pb}}$  have already been presented [241].  $Q_{p\text{Pb}}$  is calculated in the same way as  $R_{p\text{Pb}}$ , but contains a bias from the centrality selection in p–Pb (more details can be found in [244]).

---

### 7.3 Pb–Pb collisions and $R_{AA}$

---

The current analysis is based only on the data collected in the 2010 Pb–Pb run of the LHC. In the second data taking period end of 2011 the LHC was running with increased luminosity and a larger data sample was collected with VZERO centrality triggers for central (0-10%) and semi-central (0-50%) collisions. In these centrality intervals higher statistics are available, about a factor 10 for the most central collisions, and an extension of the  $p_T$  coverage up to 100 GeV/c seems feasible. The improved  $p_T$  resolution required for measurements at  $p_T$  significantly exceeding 50 GeV/c will be available in the near future.

An extended range of charged hadron  $R_{AA}$  will complement the measurements of jet  $R_{AA}$  and serve as cross check of results from other experiments that already cover this range [196]. A Significantly higher precision in the present  $p_T$  range (halving the uncertainties) will allow to restrict theoretical models further and exclude part of them. Both, extended  $p_T$  range, and improved precision require the same also for the pp reference spectrum. The dependence of  $R_{AA}$  on the reaction plane can provide information on the path length dependence of the medium-induced energy loss

---

### 7.4 Possibilities for smaller systematic uncertainties

---

Improvements of systematic uncertainties require significant additional effort and have to focus on the largest contributions. Dominating uncertainties are the corrections for efficiency and systematic uncertainties from cut variations in the whole  $p_T$  range and the  $p_T$  resolution correction at large  $p_T$ . In addition, contributions from particle composition and secondary contamination are relevant mostly at low and intermediate  $p_T$ .

Possible reduction of systematic uncertainties could arise from new and improved track cuts and changes in the data reconstruction and simulations that lead to better agreement between simulation and data. In particular the description of the detector response in the simulations needs to be improved, e.g. by including ion tail cancellation and cross-talk effects. In addition the discrepancies between Monte Carlo event generators used for simulations and the measurements have to be reduced. The inclusion of measured results for identified particle production, in particular the composition of primary particles, allows more precise corrections and thus lower systematic uncertainties.

---

#### Transverse momentum resolution

---

The  $p_T$  resolution can be significantly improved with a new reconstruction, that includes a better parameterization of the space point resolution. These improvements have already been incorporated in the reconstruction of the p–Pb data, improving the  $p_T$  resolution at high  $p_T$  by about a factor 3 compared to previous pp and Pb–Pb data (see Figure 3.27 in section 3.7.4). During the long shutdown 1 (LS1) of the LHC (ending early 2015) it is intended to reconstruct most of the data recorded by ALICE again. This reprocessing, with all the improvements in the tracking and reconstruction software that have been made in the past years, will lead to significantly better performance, in particular an improved  $p_T$  resolution. Better alignment of the ITS with respect to the TPC also improves the  $p_T$  resolution.

If hits in the TRD are included in the track fitting procedure the  $p_T$  resolution will benefit from the larger lever arm. The improvement will depend on the space point resolution in the

TRD and the alignment with respect to the TPC. The fact that the TRD does not have full  $2\pi$  azimuthal coverage to date does not represent a major problem for a single particle analysis.

However, the verification of the  $p_T$  resolution estimate from the track covariance matrix (see section 3.7.4) remains an issue. The cross check done so far was based on the invariant mass peaks of 2-particle-decays of  $K_S^0$  and  $\Lambda$ , but this method can not be extended to the highest  $p_T$ . A trigger for cosmic muons crossing the TPC and ITS, running during ordinary data taking would be the optimal solution in the future. The difference of the  $p_T$  measured in the upper and lower half of the detector for a cosmic particle is a direct measurement of the  $p_T$  resolution. This method has already been applied for tracks in the TPC, where the long integration time allows to use cosmic tracks that are unavoidably part of the collision events.

---

### Inclusion of identified particle measurements

---

The analysis of charged particle spectra presented in this thesis was completed before several measurements of identified particle spectra, in particular charged pions, proton, kaons [161, 215, 216] and (multi-)strange baryons [245–247] were available. Incorporating this additional knowledge into the charged particle analysis helps to improve its precision.

The dominant effects depending on the particle composition are efficiency and secondary corrections, and, in the case of p–Pb, also acceptance corrections. Preferably the inclusion of the measurements is achieved via tuning of Monte Carlo generators, as this would directly decrease discrepancies between data and simulation. As a workaround, correction factors for efficiency, contamination and acceptance, that are obtained from MC simulations, can be rescaled properly taking into account measured particle compositions. However, the usage of such effective corrections is not feasible for application to all MC-related quantities. Not only the corrections, but all systematics (for example cut variations or matching efficiency) depend on the primary and secondary particle composition. Including effective corrections to all of them would inflate the number of such effective corrections.

In the analysis of the 2013 p–Pb data, preliminary measurements of  $\pi$ ,  $K$ ,  $p$  transverse momentum spectra have already been taken into account for the efficiency and acceptance corrections (see section 3.7.1). The analysis of pp and Pb–Pb collisions include a scaling factor for the contamination from secondaries to account for the strangeness production, which is underestimated in the MC generators (see section 3.7.2).

---

### Track cut modifications

---

A modification of the track selection criteria could help to reduce systematic uncertainties and overcome shortcomings of the Monte Carlo description of the detector.

In particular, a cut on the track length in the active area of the TPC has been recently proposed [248] and is currently under investigation. This cut is designed to remove tracks which cross TPC sector boundaries under small angles resulting in a large fraction of the track located either in the inactive zone between two sectors or in the vicinity of such a sector boundary, where the performance of the TPC is worst. Since the cut variable itself is defined purely by geometry, the description in the simulations is much better compared to cuts which involve also quantities depending on physical processes like energy loss of the particle or detector response.

Another possible improvement could come from a moderate cut on the number of clusters used for tracking, to remove outliers tracks with have an exceptional low number of clusters assigned. Recall that the  $p_T$  resolution depends also on  $\sqrt{n_{\text{cl}}}$ . A more restrictive cut on the ratio  $n_{\text{rows}}/n_{\text{findable}}$  has a similar effect and could be used in addition.

A major part of the track cut systematic uncertainties is due to the rather large cut on the number of crossed rows in the TPC. In the combination with the cut on the active length, the requirement of a large number of crossed rows could be relaxed to reduce systematic uncertainties at intermediate  $p_T$ . With a  $p_T$  dependent cut on  $n_{\text{rows}}$  it is possible to keep the requirement of long tracks at high  $p_T$  where the momentum resolution is crucial, but improve at low and intermediate  $p_T$ . Especially at the lowest  $p_T < 200$  MeV/c the current cut is on the edge of the kinematic limit, a looser cut would increase the efficiency to a level comparable to that at  $p_T > 200$  MeV/c.

---

### MC simulations

---

Improvements in the simulations would also help to reduce systematic uncertainties. In particular the use of improved Monte Carlo generators, that are tuned to reproduce the available measurements, and a more accurate description of detector geometry and response.

Better tuned or different generators need to reproduce the correct composition of primary particles, which are only poorly described by the generators that were used. In particular simulations with a proper baryons/meson ratio and correct production of strangeness will improve the corrections for efficiency and contamination and reduce the discrepancy in the TPC-ITS track matching between simulation and data. The re-weighting procedures for efficiency and contamination would become obsolete.

A better description of the detector geometry, (mis-)alignment, material budget and response (for example the error parameterization of space point resolution) will also result in smaller systematic uncertainties.

Most simulations currently available suffer from low statistics at large  $p_T$ , especially when obtained differentially also in other variables like pseudorapidity, multiplicity and  $z$ -position of the primary vertex. In this case the large statistical uncertainties of the efficiency mask potential systematic effects. This strongly affects the corresponding corrections at high  $p_T$ , which is averaged over a rather wide interval of  $p_T$ . For a reliable extraction of correction factors the available statistics of simulated events should be at least as large as in data, in order not to have uncertainties dominated by MC statistics. Another possible solution to this are simulations which have an enhanced contribution at high  $p_T$ .

### Efficiency

The efficiency is the main correction and has a large systematic uncertainty assigned. Improvements of the efficiency correction are possible from better detector calibration and improved MC simulations that have the correct particle composition. The reweighting of the efficiencies as described above is also an alternative. This reweighting could in principle also be applied to improve the agreement between data and simulation in the TPC-ITS track matching efficiency which is used to estimate systematic uncertainties on the the tracking efficiency.

Another inaccuracy comes from the efficiencies of strange baryons ( $\Sigma^\pm$ ,  $\Xi^-$ ,  $\Omega^-$ ) which are non-zero at large  $p_T$ . For these particles a  $p_T$  dependence of the efficiency and particle fractions extended to larger  $p_T$  could improve the accuracy especially at large  $p_T$ .

Generally the description of efficiency at high  $p_T$  would benefit from larger MC statistics or dedicated high  $p_T$  enhanced productions. As high  $p_T$  particles are mostly embedded in a jet, the influence of the local track density on the efficiency needs to be considered.

### Contamination

Secondary particles mostly affect the spectrum at the lowest  $p_T$ . An improved MC description of strangeness would render the effective correction applied to scale the secondaries unnecessary. This helps to reduce systematic uncertainties at low  $p_T$ .

---

### Correlated uncertainties

---

Another potential improvement of the measurement could come from separation of systematic uncertainties that are correlated between the  $p_T$  bins. These could be incorporated into the normalization uncertainty and improve the accuracy in the measurement of the  $p_T$  shape.

Even more benefits will arise from the study of systematic uncertainties correlated between different systems (i.e. pp and p–Pb as well as pp and Pb–Pb), as they partially cancel in the ratios  $R_{AA}$  and  $R_{pPb}$ . Similar cancellations have already been exploited for the ratios of spectra at different energies in pp and ratios at different pseudorapidity in p–Pb.

---

## 7.5 Possibilities for larger statistics data

---

To extend the analysis towards larger  $p_T$  requires an improvement of  $p_T$  resolution as described above and higher statistics at large  $p_T$ . If the data recorded with the jet or high multiplicity triggers are included in the analysis this would enhance the statistics at large  $p_T$  and could allow measurements up to 100 GeV/c in  $p_T$ . However, most triggers can have a bias on the  $p_T$  spectrum. A trigger on single high  $p_T$  hadrons would not contain such a bias.

While the TRD was designed from the beginning to be used as a trigger detector for electrons, in the 2013 p–Pb data taking it was also used as a jet trigger. In principle, it could also be used to trigger on single high  $p_T$  charged particles.

---

## 7.6 Future running

---

### Run 2

After the LS1, LHC will resume operation in 2015 with pp collisions at or close to the design energy of  $\sqrt{s} = 13\text{--}14$  TeV, with the full design luminosity of  $L = 10^{34}\text{cm}^{-2}\text{s}^{-2}$ . In the following run 2 also p–Pb and Pb–Pb collisions at the full energy are foreseen. This will allow to study heavy ion collisions at unprecedented high energy. Measurements of charged particle spectra will be extended to higher  $\sqrt{s_{NN}}$ . A pp data taking at  $\sqrt{s} \approx 5$  TeV is also under consideration and can serve as a reference for the p–Pb data already collected and Pb–Pb data at full energy. For the first time at LHC this allows comparisons of pp, p–Pb and Pb–Pb at the same  $\sqrt{s_{NN}}$ .

---

### Run 3 and 4

During the LS2 (2018) ALICE will install some major detector upgrades, see [249] for details. This including a completely new inner tracking system [250] and substantial upgrade of the TPC [251]. With the TPC running in a continuous mode, ALICE will be able to inspect 50 kHz of minimum bias Pb–Pb interactions. Corresponding upgrades of the readout and trigger system [252] will allow all events reconstructed online including online calibration. The focus of ALICE during this run will be on observables for which no triggering is possible and thus require huge statistics of minimum bias data. Typical examples are low mass di-leptons and  $J/\Psi$  down to  $p_T = 0$ .

For the runs 3 and 4 also collisions of lighter ions (Ar–Ar and p–Ar) are under consideration.

# A List of runs used in the analysis

## Data sets

Table A.1 shows a list of data sets and MC productions used for the analysis of Pb–Pb, p–Pb pp spectra described in this thesis. The MC productions are anchored to the appropriate data period and reconstruction pass. The event generators used for the productions are HIJING (Pb–Pb), DPMJET (p–Pb) and PYTHIA (pp). Runs and production used only for the evaluation of systematic uncertainties are not listed.

All runs have been selected for the analysis, which were not flagged as “bad runs” in the run condition table (RCT) at the time of the analysis. Some runs have been flagged as “bad” after the analysis has been frozen. It was decided to include these runs in the selection based on the output of the PWGPP-QA train and a run-by-run check of the resulting  $p_T$ -spectra. Short runs and runs with pending data quality assessment have not been generally excluded. A complete list of the ALICE run numbers for the runs used is given below.

system	$\sqrt{s_{\text{NN}}}$	year	data sample	MC sample	MC generator	remarks
pp	0.9 TeV	2010	LHC10c, pass3	LHC10e13	PYTHIA6	
pp	2.76 TeV	2011	LHC11a, pass2	LHC11b10a	PYTHIA6	without SDD
pp	7 TeV	2010	LHC10d, pass2	LHC10f6a	PYTHIA6	
p–Pb	5.02 TeV	2012	LHC12g, pass2	LHC12g4	DPMJET	for $R_{p\text{Pb}}$
p–Pb	5.02 TeV	2013	LHC13b, pass3	LHC13b2_efix_p1	DPMJET	only for $\langle p_T \rangle$
p–Pb	5.02 TeV	2013	LHC13c, pass2	LHC13b2_efix_p1	DPMJET	only for $\langle p_T \rangle$
Pb–Pb	2.76 TeV	2010	LHC10h, pass2	LHC11a10a	HIJING	

Table A.1.: ALICE names of the analyzed pp data sets and the corresponding MC samples used for corrections.

## pp – 900 GeV

DATA:

118506, 118507, 118512, 118518, 118556, 118558, 118560, 118561, 121039, 121040

MC:

118506, 118507, 118512, 118518, 118556, 118558, 118560, 118561, 121039, 121040

pp – 2.76 TeV

## DATA:

146746, 146747, 146748, 146801, 146802, 146803, 146804, 146805, 146806, 146807, 146817, 146824, 146856, 146858, 146859, 146860

MC:

146746, 146747, 146748, 146801, 146802, 146803, 146804, 146805, 146806, 146807, 146817, 146824, 146856, 146858, 146859, 146860

pp – 7 TeV

## DATA:

122374, 122375, 124751, 125023, 125085, 125097, 125100, 125134, 125296, 125630, 125632, 125633, 125842, 125843, 125844, 125847, 125848, 125849, 125850, 125851, 125855, 126004, 126007, 126008, 126073, 126078, 126081, 126082, 126088, 126090, 126097, 126158, 126160, 126168, 126283, 126284, 126285, 126351, 126352, 126359, 126403, 126404, 126405, 126406, 126407, 126408, 126409, 126422, 126424, 126425, 126432

MC:

122374, 122375, 124751, 125023, 125085, 125097, 125100, 125101, 125134, 125296, 125628, 125630, 125632, 125633, 125842, 125843, 125844, 125847, 125848, 125849, 125850, 125851, 125855, 126004, 126007, 126008, 126073, 126078, 126081, 126082, 126088, 126090, 126097, 126158, 126160, 126168, 126283, 126284, 126285, 126359, 126403, 126404, 126405, 126406, 126407, 126408, 126409, 126422, 126424, 126425, 126432

p-Pb 2012

## DATA:

188359, 188362

MC:

188359, 188362

---

---

---

## p–Pb 2013

---

DATA:

195344, 195346, 195351, 195389, 195390, 195391, 195478, 195479, 195480, 195481, 195482, 195483, 195529, 195531, 195566, 195567, 195568, 195592, 195593, 195596, 195633, 195635, 195644, 195673, 195675, 195677

MC:

195344, 195346, 195351, 195389, 195390, 195391, 195478, 195479, 195480, 195481, 195482, 195483, 195529, 195531, 195566, 195567, 195568, 195592, 195593, 195596, 195633, 195635, 195644,

---

---

---

## Pb–Pb

---

DATA:

137161, 137162, 137231, 137232, 137235, 137236, 137243, 137366, 137430, 137431, 137432, 137434, 137439, 137440, 137441, 137443, 137530, 137531, 137539, 137541, 137544, 137546, 137549, 137595, 137608, 137638, 137639, 137685, 137686, 137691, 137692, 137693, 137704, 137718, 137722, 137724, 137751, 137752, 137848, 138190, 138192, 138197, 138201, 138225, 138275, 138364, 138396, 138438, 138439, 138442, 138469, 138534, 138578, 138579, 138582, 138583, 138621, 138624, 138638, 138652, 138653, 138662, 138666, 138730, 138732, 138837, 138870, 138871, 138872, 139028, 139029, 139036, 139037, 139038, 139042, 139105, 139107, 139173, 139308, 139309, 139310, 139311, 139314, 139328, 139329, 139360, 139437, 139438, 139439, 139440, 139465, 139503, 139504, 139505, 139507, 139510

MC:

138653, 138662, 138666, 138730, 138732, 138837, 138871, 138872, 139028, 139029, 139036, 139037, 139038, 139042, 139105, 139107, 139173, 139309, 139310, 139314, 139328, 139329, 139360, 139437, 139438, 139440, 139465, 139503, 139505, 139507, 139510

## B Comparison of Pb–Pb results to the ALICE identified charged particle measurement

The ALICE experiment has also published a measurement on centrality dependence of identified charged hadron production in Pb-Pb collisions [215] containing  $p_T$  distributions of pions, kaons and protons. Since these particles account for the majority of primary charged particles produced in a heavy-ion collision, a comparison to the results from this analysis is an obvious thing to do and provides a cross-check of both measurements.

The two measurements are performed in a slightly different acceptance: for this analysis a pseudorapidity  $|\eta| < 0.8$  was selected, while the identified particles are measurement in the rapidity interval  $|y| < 0.5$ . Within these small intervals around mid-rapidity, particle production, both in terms of  $dN/d\eta$  and  $dN/dy$  is approximately flat in (pseudo-)rapidity [116]. In the charged particle analysis the relative difference between the  $p_T$  distributions  $dN/dp_T d\eta$  measured in the two pseudorapidity intervals  $|\eta| < 0.8$  and  $|\eta| < 0.5$  is up to 1% in the  $p_T$  range<sup>1</sup> of  $0.3 < p_T < 3$  GeV/c for all centralities. The spectrum in the narrow  $\eta$  range is slightly harder.

To allow a direct comparison of the two measurements,  $dN/dy dp_T$  was translated to  $dN/d\eta dp_T$  for each particle type separately prior to summation. Given the flatness of the rapidity distribution, the average  $y = 0.25$  along with the particle masses were used for this. Systematic uncertainties of the  $\pi + K + p$  spectrum were calculated as the weighted average from the uncertainties of the single spectra.

Figures B.1 and B.2 show the comparison of the charged particle  $p_T$  spectra to those obtained from the sum of pions, kaons and protons for central (0-5%) and peripheral (70-80%) collisions.

The relative differences between the two independent measurements is up to  $\approx 5\%$  and within the systematic uncertainties of either of the two measurements. These uncertainties are likely to contain also correlated parts. It is remarkable that the charged particle yields are partially lower than the cumulative yields of  $\pi$ ,  $K$  and  $p$ . In MC simulations with HIJING the sum of  $\pi$ ,  $K$ ,  $p$  account to more than 99% of all primary charged particles at low  $p_T < 0.5$  GeV/c and about 95% at  $p_T = 3.0$  GeV/c, independent of centrality.

<sup>1</sup> In this range spectra for all species ( $\pi$ ,  $K$ ,  $p$ ) are available.

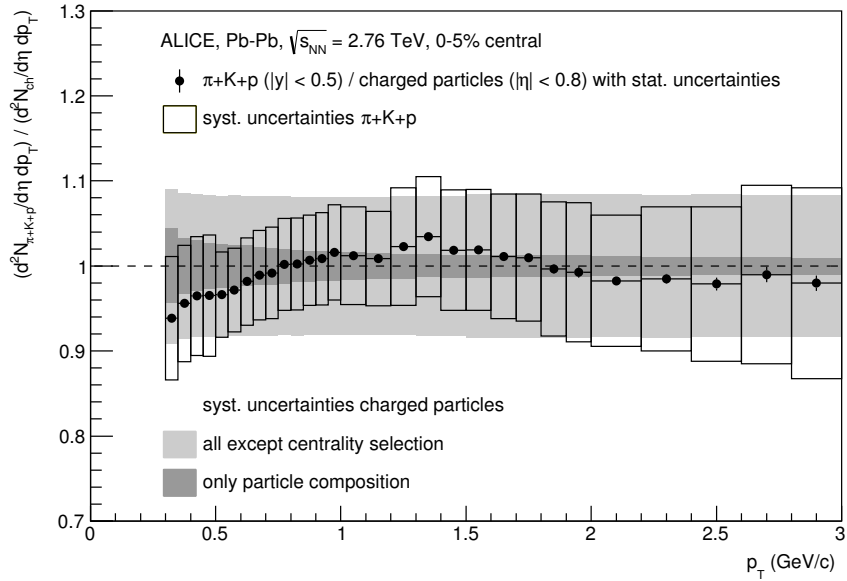


Figure B.1.: Comparison of  $p_T$  spectra obtained in this analysis to ALICE measurements of pion,kaons, protons [215] for 0-5% central Pb-Pb collisions.

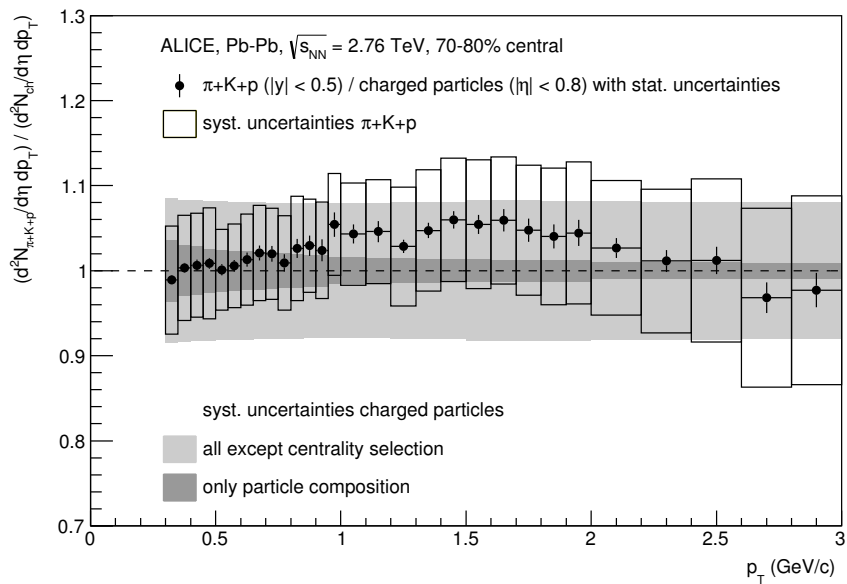


Figure B.2.: Comparison of  $p_T$  spectra obtained in this analysis to ALICE measurements of pion,kaons, protons [215] for 70-80% central Pb-Pb collisions.

## C Comparison of HIJING particle composition to the ALICE measurement

As described in section 3.7.1 the efficiency corrections differ for the various particle species and the overall corrections are based on the primary particle fractions generated with HIJING. The measurement of  $\pi$ ,  $K$ ,  $p$  spectra [215], which became available only after the publication of charged particle spectra, allow to review the assumptions made for the charged particle measurement. A comparison of the the production of kaons and protons relative to pions is shown in figures C.1 and C.2 for central and peripheral Pb-Pb collisions. The comparisons exhibit a significant discrepancy between the ALICE measurement and HIJING. Several generic features can be identified: 1. HIJING overpredicts the kaon and proton fractions at low  $p_T$ , but underpredicts them at high  $p_T$ . 2. The effect is more pronounced in central compared to peripheral collisions. 3. The discrepancy for protons is larger than for kaons. This can be explained by the formation of radial flow (boost of particles in a common velocity field), an effect which is not included in HIJING.

For the evaluation of systematic uncertainties (section 3.10.9) the particle fractions have been varied within the limits indicated in Figs. C.1/C.2. Although the discrepancy between DATA and MC significantly exceeds this variation of the particle composition, the effect on the combined charged particle efficiency of up to 3% remains and within the systematic uncertainties assigned to particle composition. At low  $p_T$  the fraction of  $p$  is small, while at high  $p_T$  the difference of efficiency between the particle species is small.

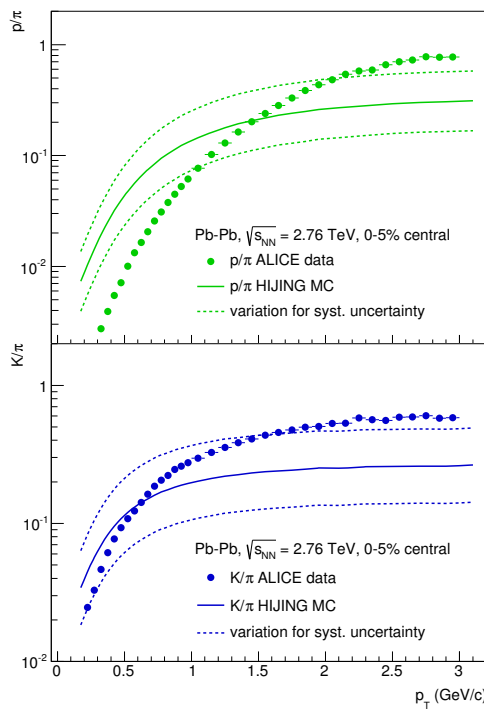


Figure C.1.: Comparison of particle composition in HIJING to ALICE measurements [215] for 0-5% central Pb-Pb collisions.

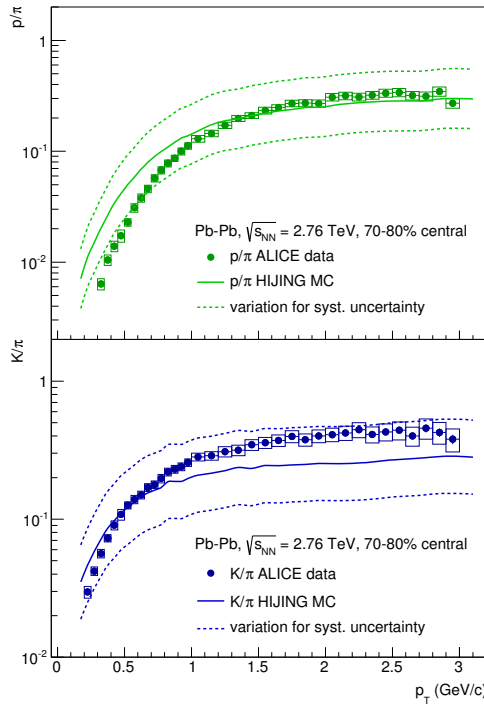


Figure C.2.: Comparison of particle composition in HIJING to ALICE measurements [215] for 70-80% central Pb-Pb collisions.

---

---

## D Distributions of cut variables

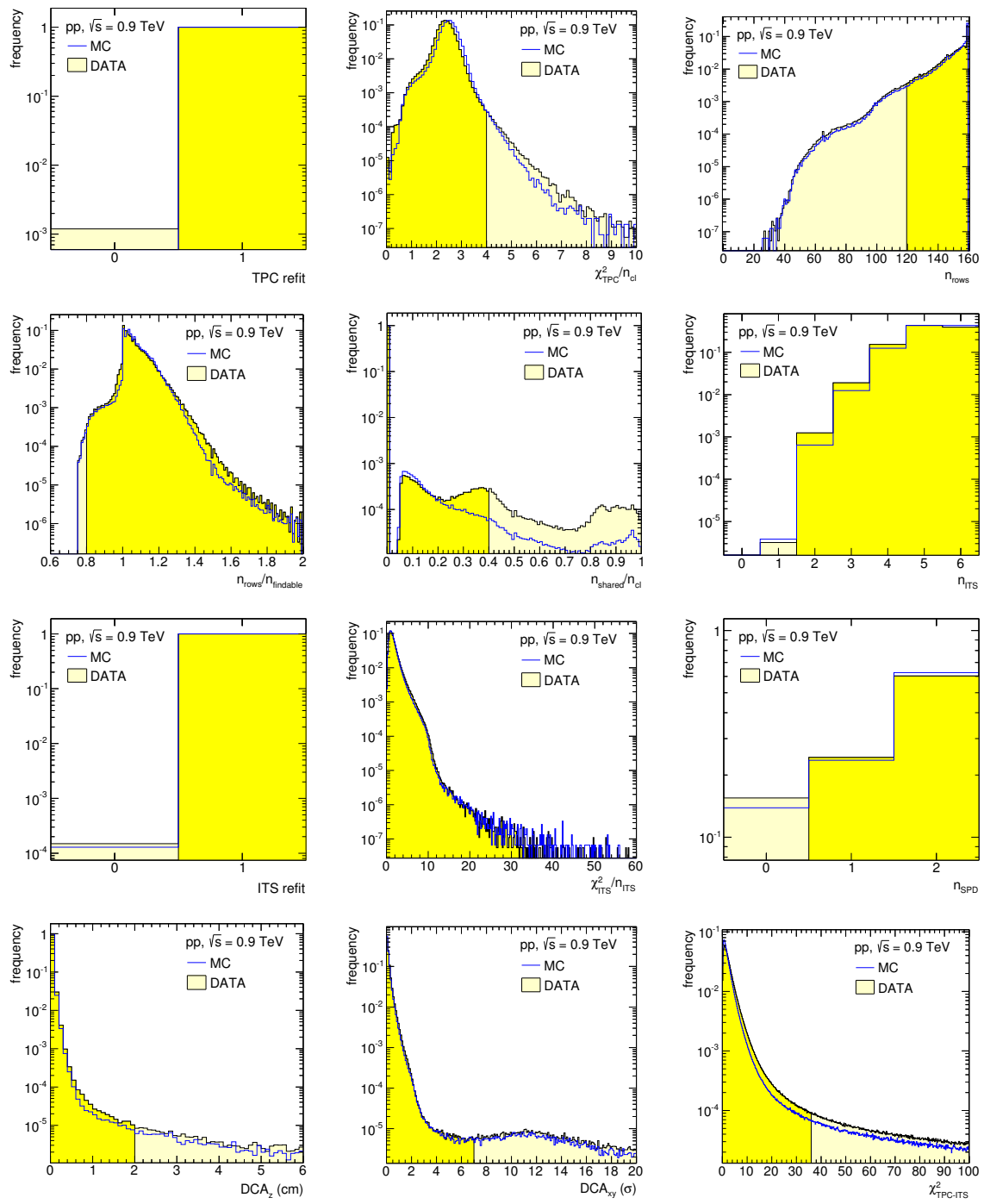


Figure D.1.: Distributions of all track cut variables in MC simulation and data for pp,  $\sqrt{s} = 0.9$  TeV, integrated over the kinematic range  $0.15 < p_T < 20$  GeV/c and  $|\eta| < 0.8$ . As a consequence the distributions are dominated by tracks with low  $p_T$ . All distributions are normalized to an integral equal to unity. Note that the event numbers in MC and data are comparable in magnitude ( $\approx 5 \cdot 10^6$  events each). For a given cut variable the distribution includes all tracks that fulfil the remaining track selection criteria. Ranges selected by the cuts are indicated in yellow.

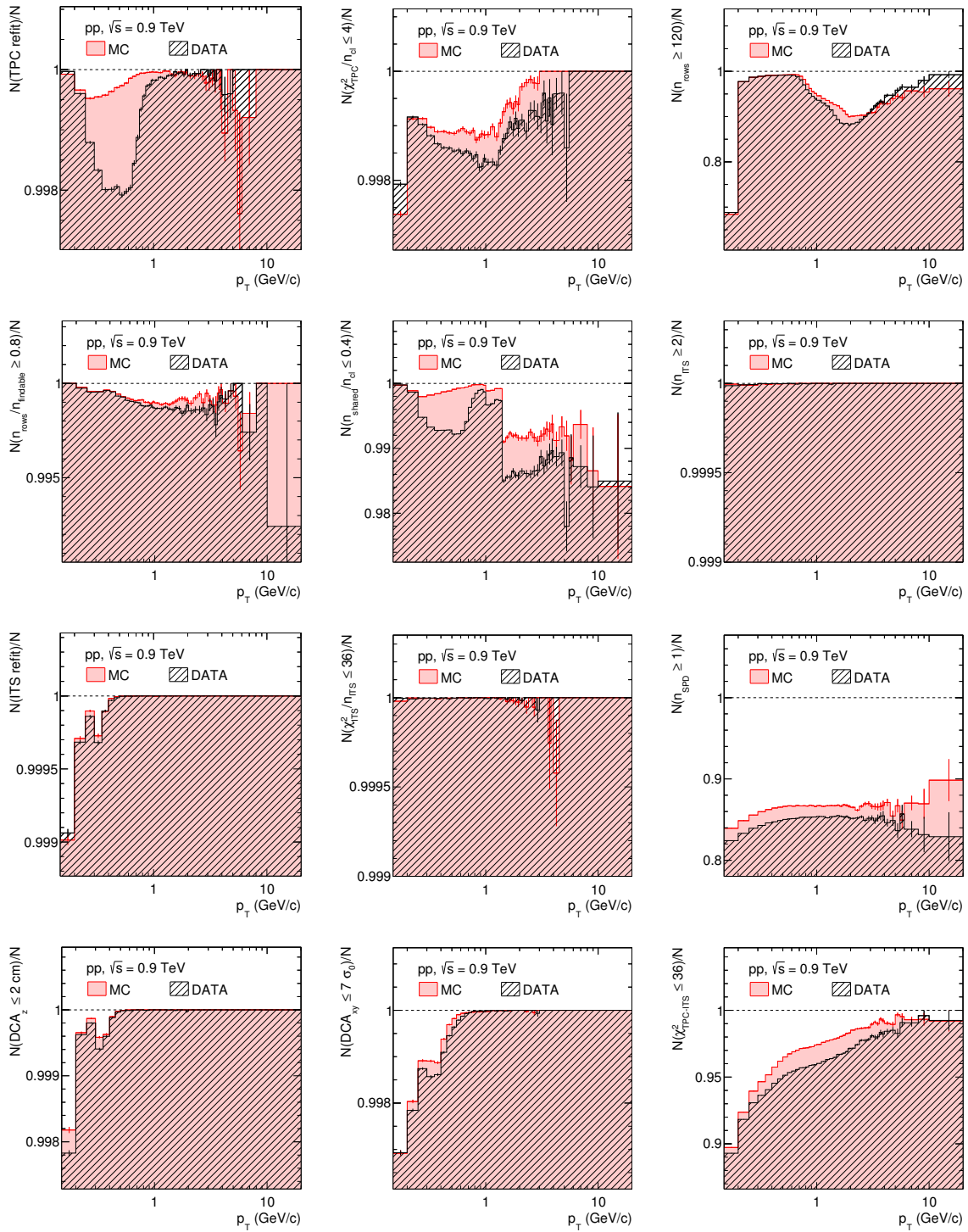


Figure D.2.: Track cut performance in  $\text{pp, } \sqrt{s} = 0.9 \text{ TeV}$  data and MC simulation for all track cuts applied in the analysis. The fraction of tracks accepted by a given track cut is shown as a function of  $p_T$ , integrated over the pseudorapidity acceptance  $|\eta| < 0.8$ . For each track cut only tracks that pass all other selection criteria are considered. Note that the event numbers in MC and data are comparable in magnitude ( $\approx 5 \cdot 10^6$  events each).

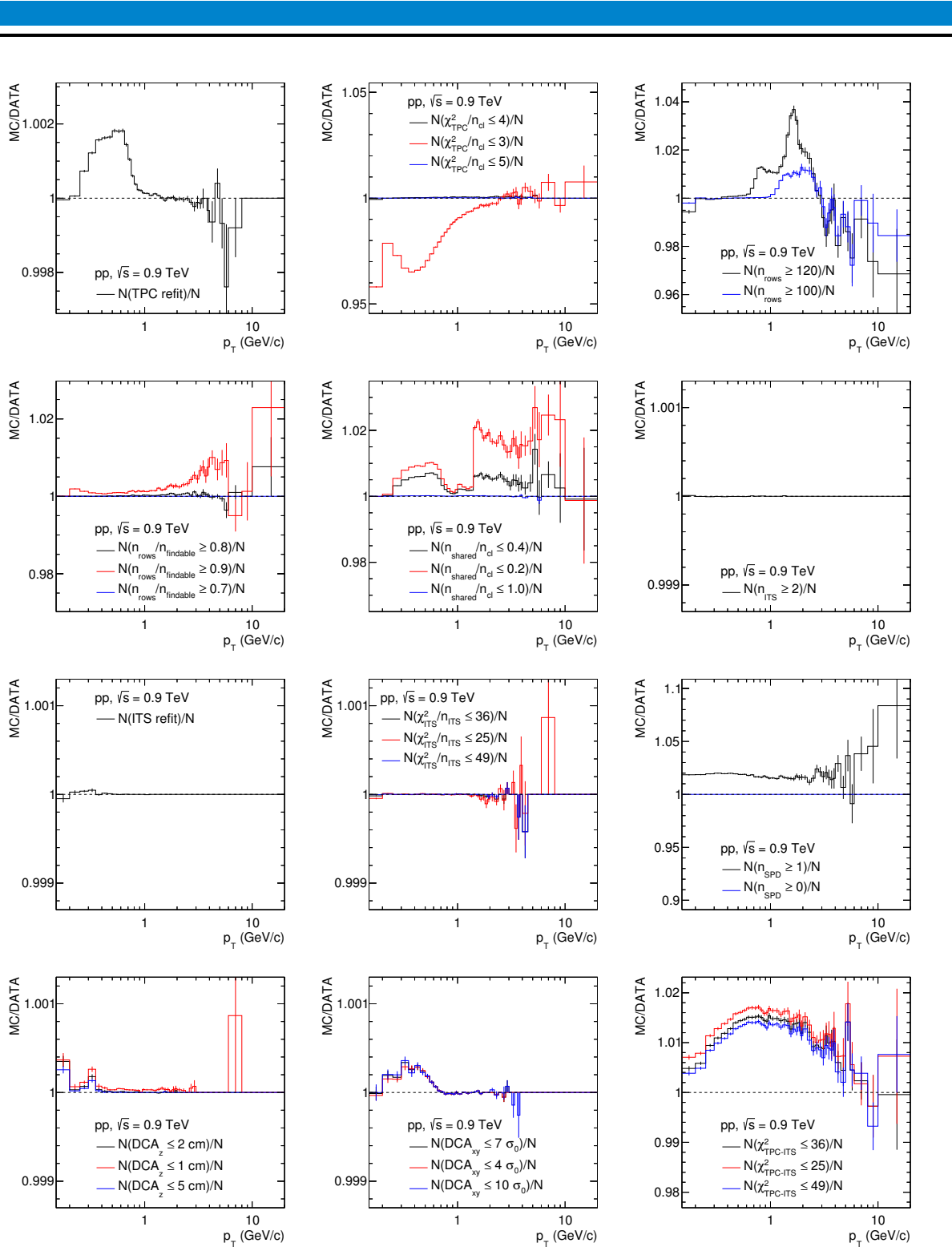


Figure D.3.: Comparison of the fraction of tracks accepted by a given track cut in  $pp, \sqrt{s} = 0.9$  TeV MC simulation and data in terms of the double ratio  $(N_{\text{accepted}}/N_{\text{all}})_{\text{MC}}/(N_{\text{accepted}}/N_{\text{all}})_{\text{DATA}}$ . The black line corresponds to the nominal cut values, it is the ratio of the two histograms in Figure D.2. In addition, alternative cuts shown as red line (more restrictive cut) and blue line (looser cut) display the sensitivity of the cut against variations. The alternative cut values are the ones used for the evaluation of systematic uncertainties.

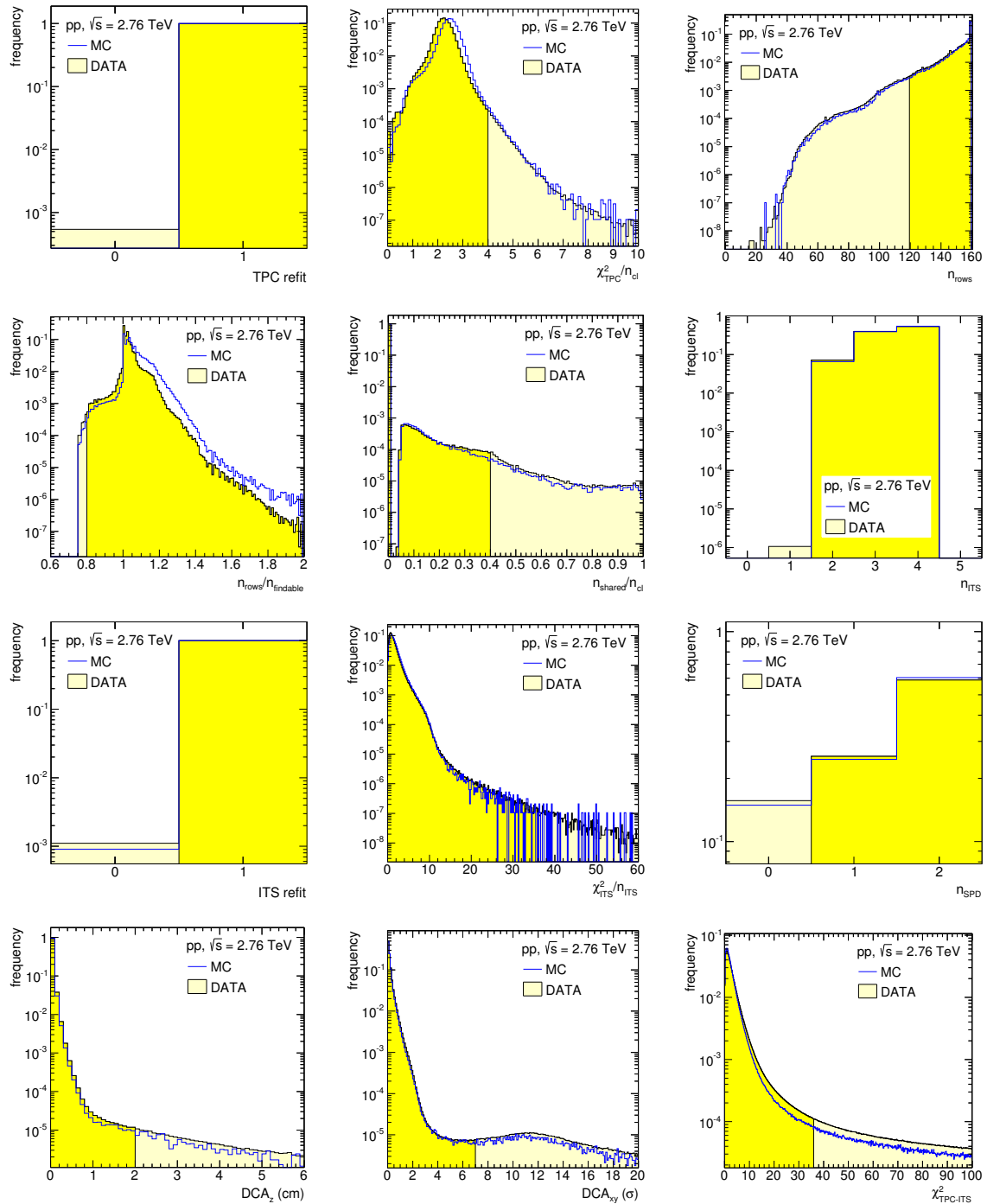


Figure D.4.: Distributions of all track cut variables in MC simulation and data for pp,  $\sqrt{s} = 2.76$  TeV, integrated over the kinematic range  $0.15 < p_T < 32$  GeV/c and  $|\eta| < 0.8$ . As a consequence the distributions are dominated by tracks with low  $p_T$ . All distributions are normalized to an integral equal to unity. Note that the event numbers in MC are about a factor 20 lower compared to data (MC:  $\approx 2.5 \cdot 10^6$  events, data:  $\approx 5 \cdot 10^7$  events). For a given cut variable the distribution includes all tracks that fulfil the remaining track selection criteria. Ranges selected by the cuts are indicated in yellow.

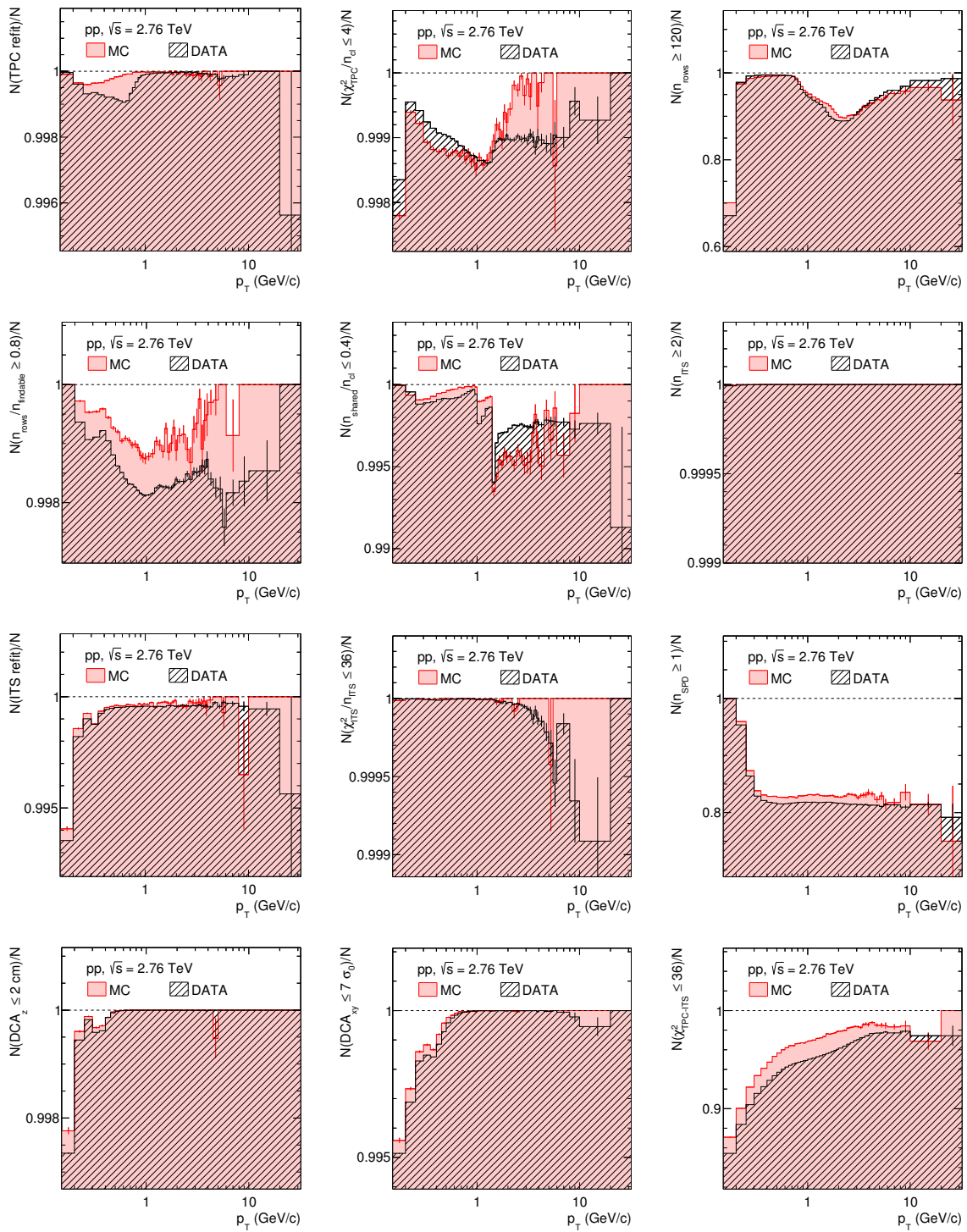


Figure D.5.: Track cut performance in pp,  $\sqrt{s} = 7$  TeV data and MC simulation for all track cuts applied in the analysis. The fraction of tracks accepted by a given track cut is shown as a function of  $p_T$ , integrated over the pseudorapidity acceptance  $|\eta| < 0.8$ . For each track cut only tracks that pass all other selection criteria are considered. Note that the event numbers in MC are about a factor 20 lower compared to data (MC:  $\approx 2.5 \cdot 10^6$  events, data:  $\approx 5 \cdot 10^7$  events).

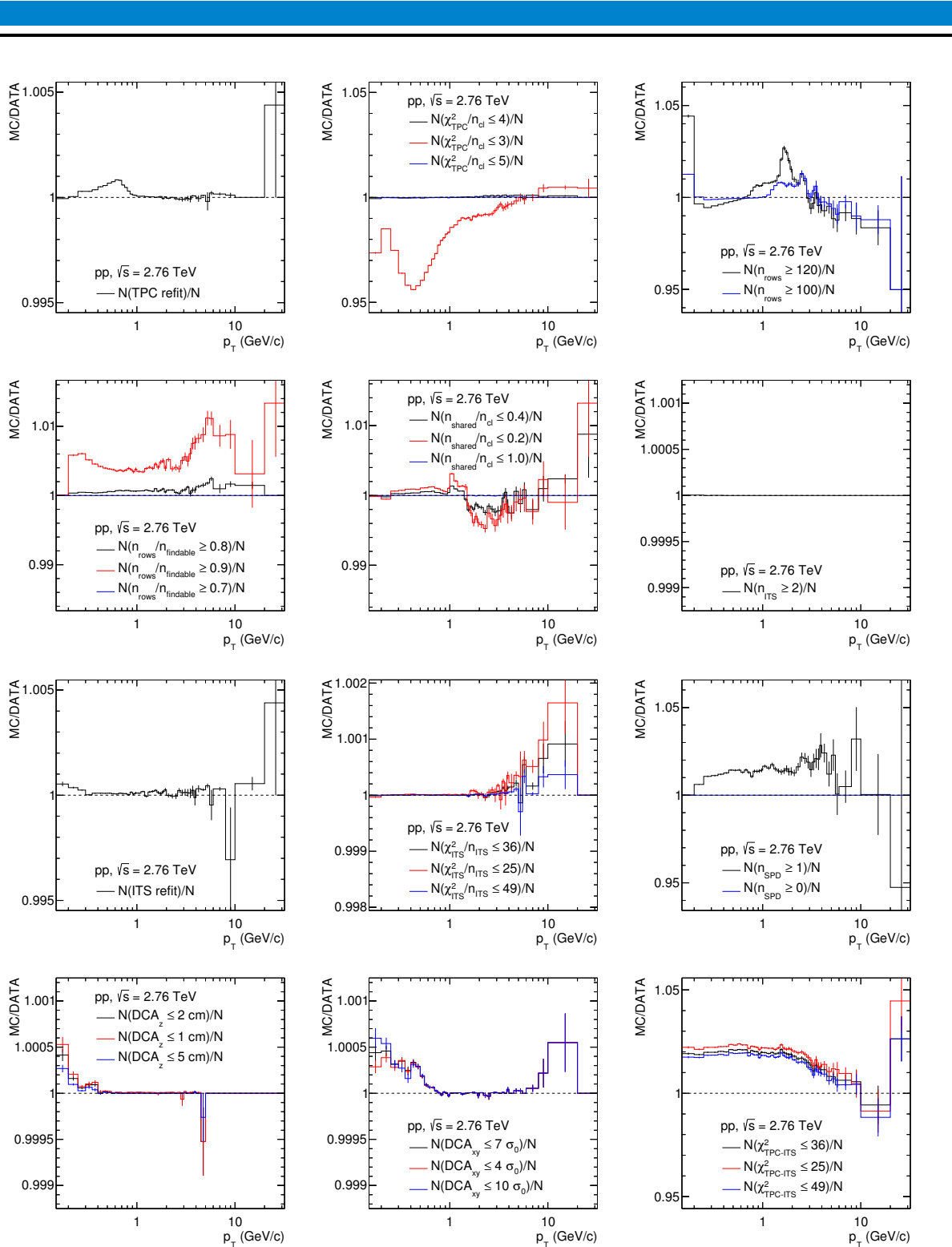


Figure D.6.: Comparison of the fraction of tracks accepted by a given track cut in pp,  $\sqrt{s} = 2.76$  TeV MC simulation and data in terms of the double ratio  $(N_{\text{accepted}}/N_{\text{all}})_{\text{MC}}/(N_{\text{accepted}}/N_{\text{all}})_{\text{DATA}}$ . The black line corresponds to the nominal cut values, it is the ratio of the two histograms in Figure D.5. In addition, alternative cuts shown as red line (more restrictive cut) and blue line (looser cut) display the sensitivity of the cut against variations. The alternative cut values are the ones used for the evaluation of systematic uncertainties.

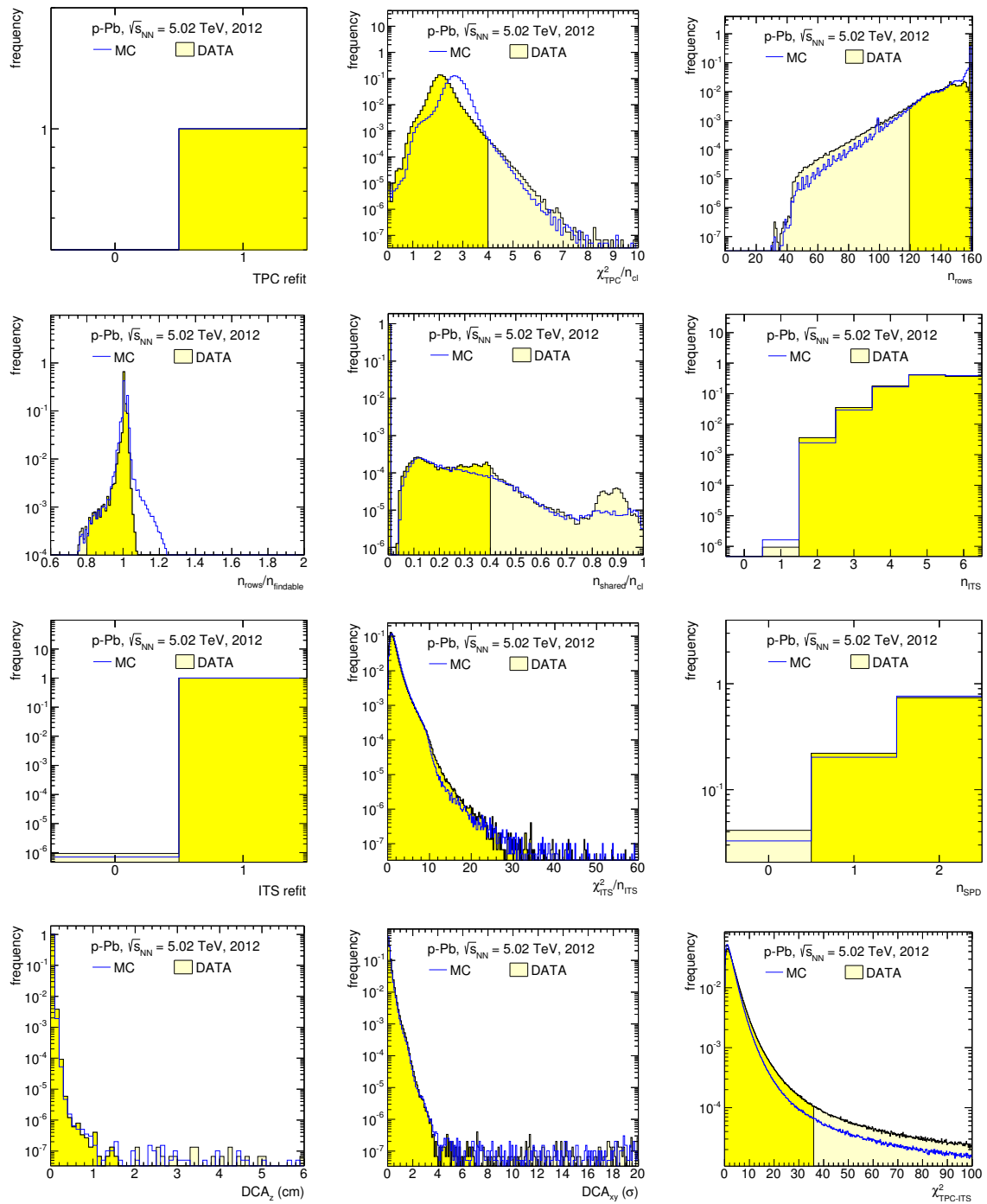


Figure D.7.: Distributions of all track cut variables in MC simulation and data for p-Pb,  $\sqrt{s_{NN}} = 5.02$  TeV using the 2012 data and MC sets. The distributions are normalized to an integral equal to unity and integrated over the kinematic range  $0.5 < p_T < 20$  GeV/c and  $|\eta_{\text{lab}}| < 0.8$ . As a consequence the distributions are dominated by tracks with low  $p_T$ . Note that the event numbers in MC and data are comparable in magnitude (MC:  $\approx 2.3 \cdot 10^6$  events, data:  $\approx 1.5 \cdot 10^6$  events). For a given cut variable the distribution includes all tracks that fulfil the remaining track selection criteria. Ranges selected by the cuts are indicated in yellow.

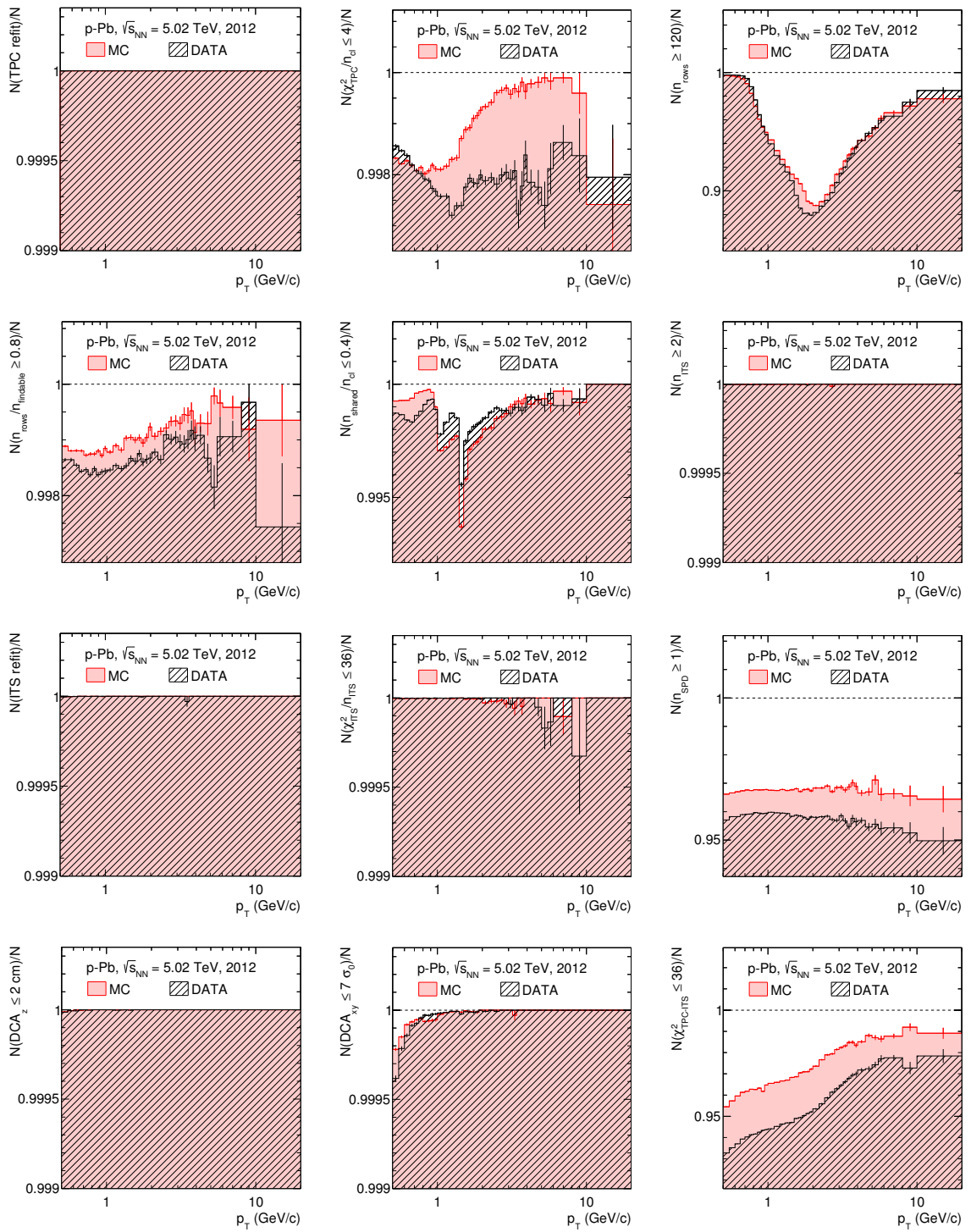


Figure D.8.: Track cut performance in p-Pb,  $\sqrt{s_{NN}} = 5.02$  TeV data and MC simulation for all track cuts applied in the analysis using the 2012 data and MC sets. The percentage of tracks removed by a given track cut is shown as a function of  $p_T$ , integrated over the pseudorapidity acceptance  $|\eta_{\text{lab}}| < 0.8$ . For each track cut only tracks that pass all other selection criteria are considered. Note that the event numbers in MC and data are comparable in magnitude (MC:  $\approx 2.3 \cdot 10^6$  events, data:  $\approx 1.5 \cdot 10^6$  events).

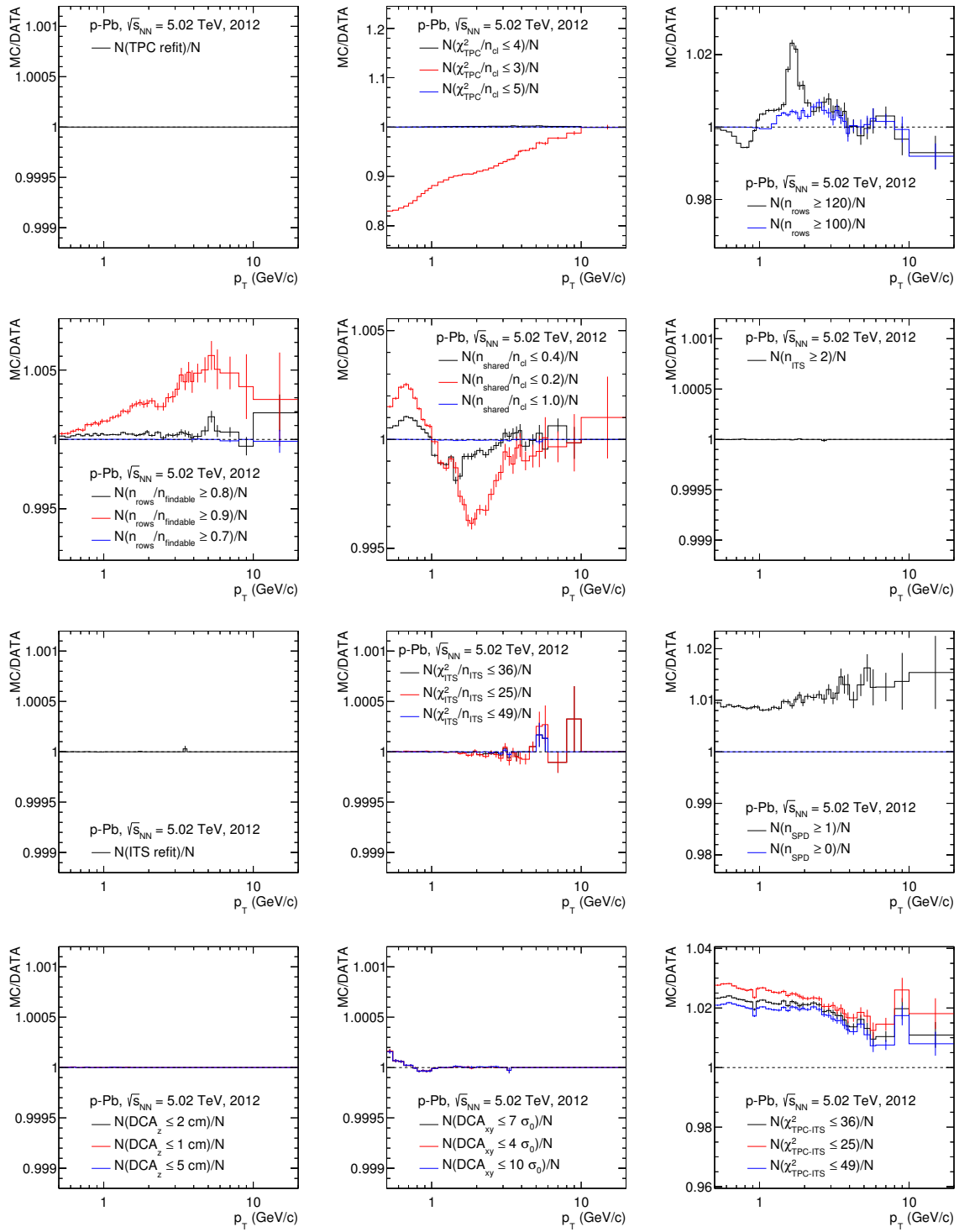


Figure D.9.: Comparison of the fraction of tracks accepted by a given track cut in the 2012 sets of p-Pb,  $\sqrt{s_{NN}} = 5.02$  TeV MC simulation and data in terms of the double ratio  $(N_{\text{accepted}}/N_{\text{all}})_{\text{MC}}/(N_{\text{accepted}}/N_{\text{all}})_{\text{DATA}}$ . The black line corresponds to the nominal cut values, it is the ratio of the two histograms in Figure D.8. In addition, alternative cuts shown as red line (more restrictive cut) and blue line (looser cut) display the sensitivity of the cut against variations. The alternative cut values are the ones used for the evaluation of systematic uncertainties.

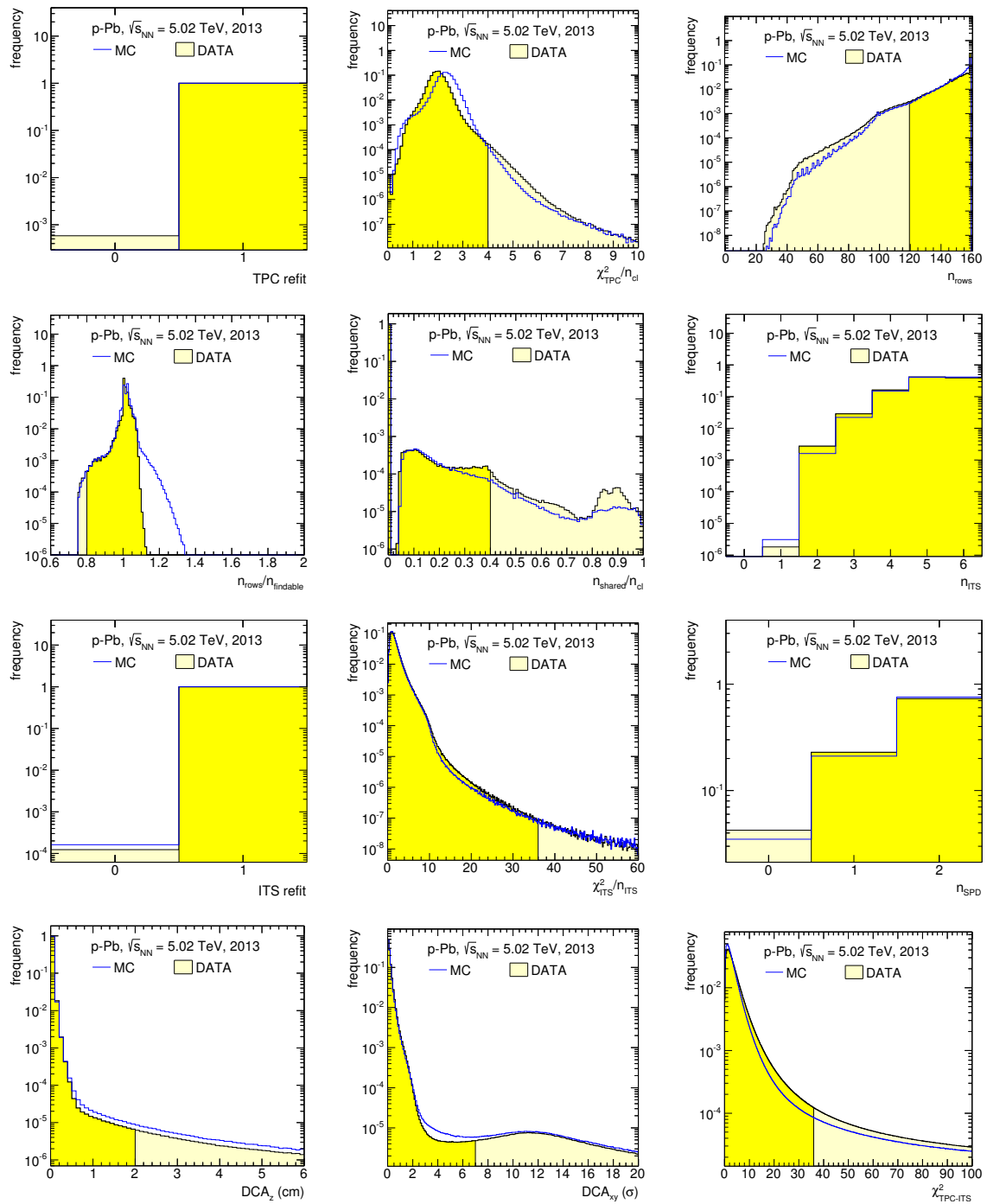


Figure D.10.: Distributions of all track cut variables in MC simulation and data for p-Pb,  $\sqrt{s_{NN}} = 5.02$  TeV using the 2013 data and MC sets. The distributions are normalized to an integral equal to unity and integrated over the kinematic range  $0.15 < p_T < 50$  GeV/c and  $|\eta_{\text{lab}}| < 0.8$ . As a consequence the distributions are dominated by tracks with low  $p_T$ . Note that the event numbers in MC and data are comparable in magnitude (MC:  $\approx 70 \cdot 10^6$  events, data:  $\approx 100 \cdot 10^6$  events). For a given cut variable the distribution includes all tracks that fulfil the remaining track selection criteria. Ranges selected by the cuts are indicated in yellow.

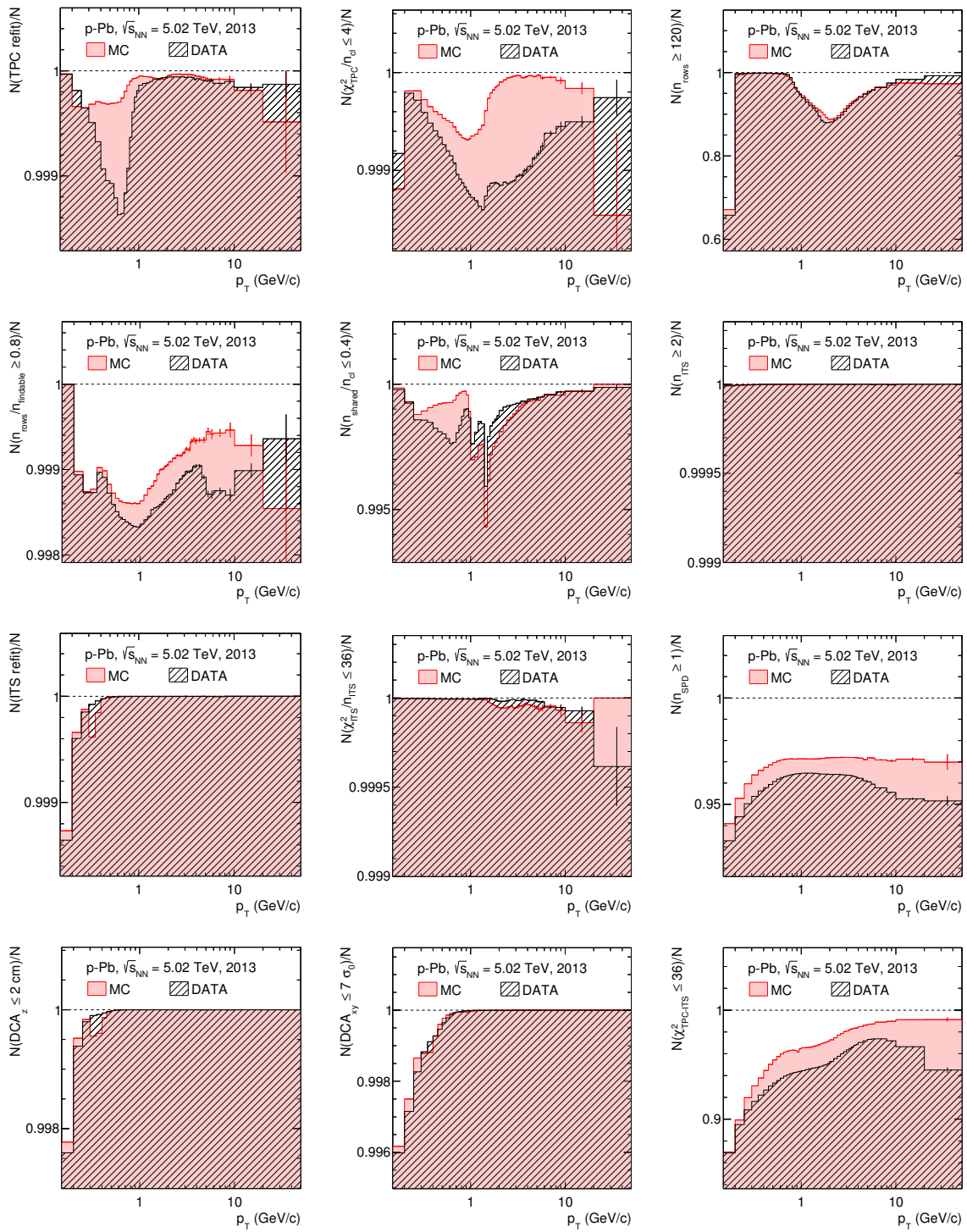


Figure D.11.: Track cut performance in p-Pb,  $\sqrt{s_{NN}} = 5.02$  TeV data and MC simulation for all track cuts applied in the analysis using the 2012 data and MC sets. The fraction of tracks accepted by a given track cut is shown as a function of  $p_T$ , integrated over the pseudorapidity acceptance  $|\eta_{\text{lab}}| < 0.8$ . For each track cut only tracks that pass all other selection criteria are considered. Note that the event numbers in MC and data are comparable in magnitude (MC:  $\approx 70 \cdot 10^6$  events, data:  $\approx 100 \cdot 10^6$  events).

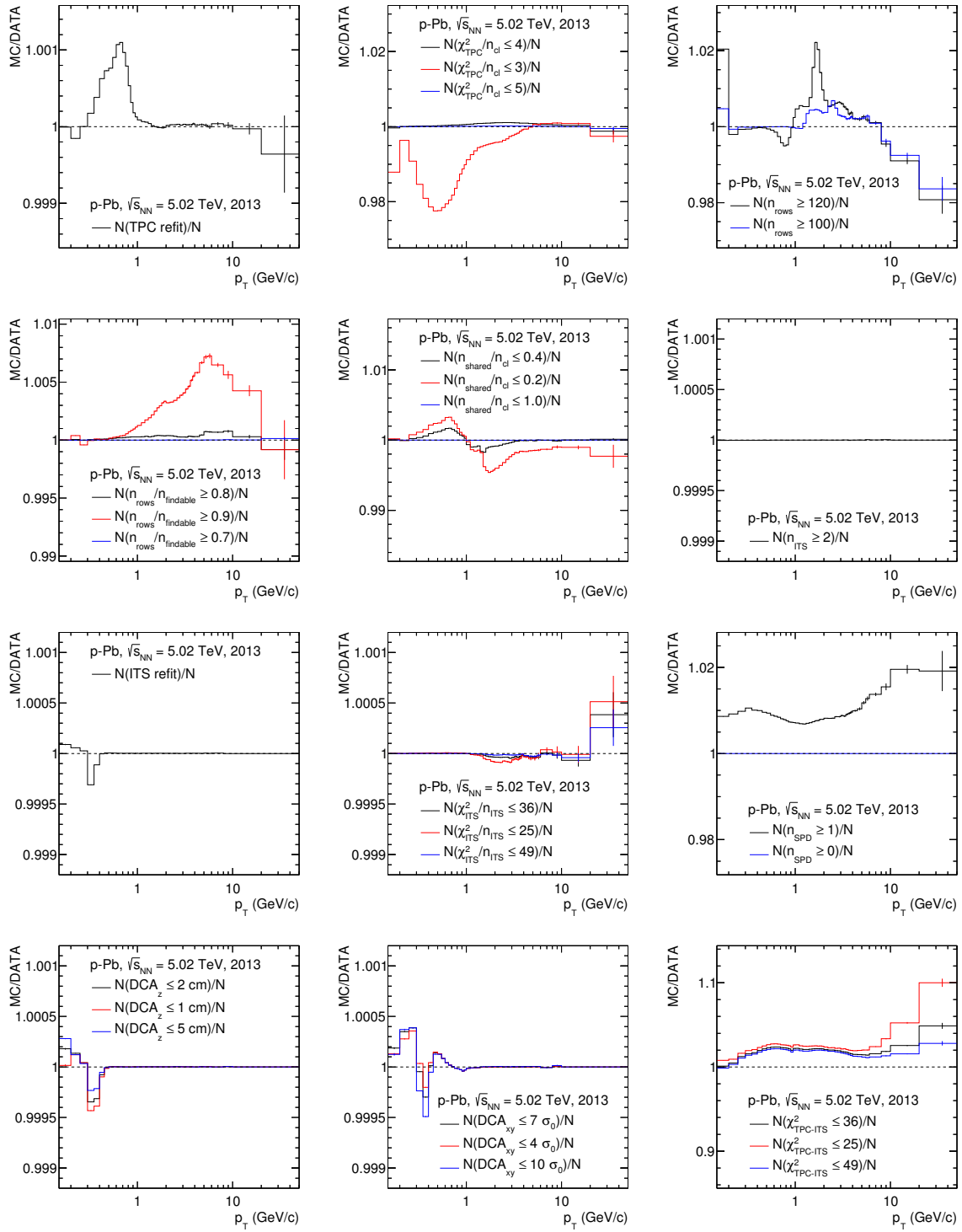


Figure D.12.: Comparison of the fraction of tracks accepted by a given track cut in the 2012 sets of p-Pb,  $\sqrt{s_{NN}} = 5.02$  TeV MC simulation and data in terms of the double ratio  $(N_{\text{accepted}}/N_{\text{all}})_{\text{MC}}/(N_{\text{accepted}}/N_{\text{all}})_{\text{DATA}}$ . The black line corresponds to the nominal cut values, it is the ratio of the two histograms in Figure D.8. In addition, alternative cuts shown as red line (more restrictive cut) and blue line (looser cut) display the sensitivity of the cut against variations. The alternative cut values are the ones used for the evaluation of systematic uncertainties.

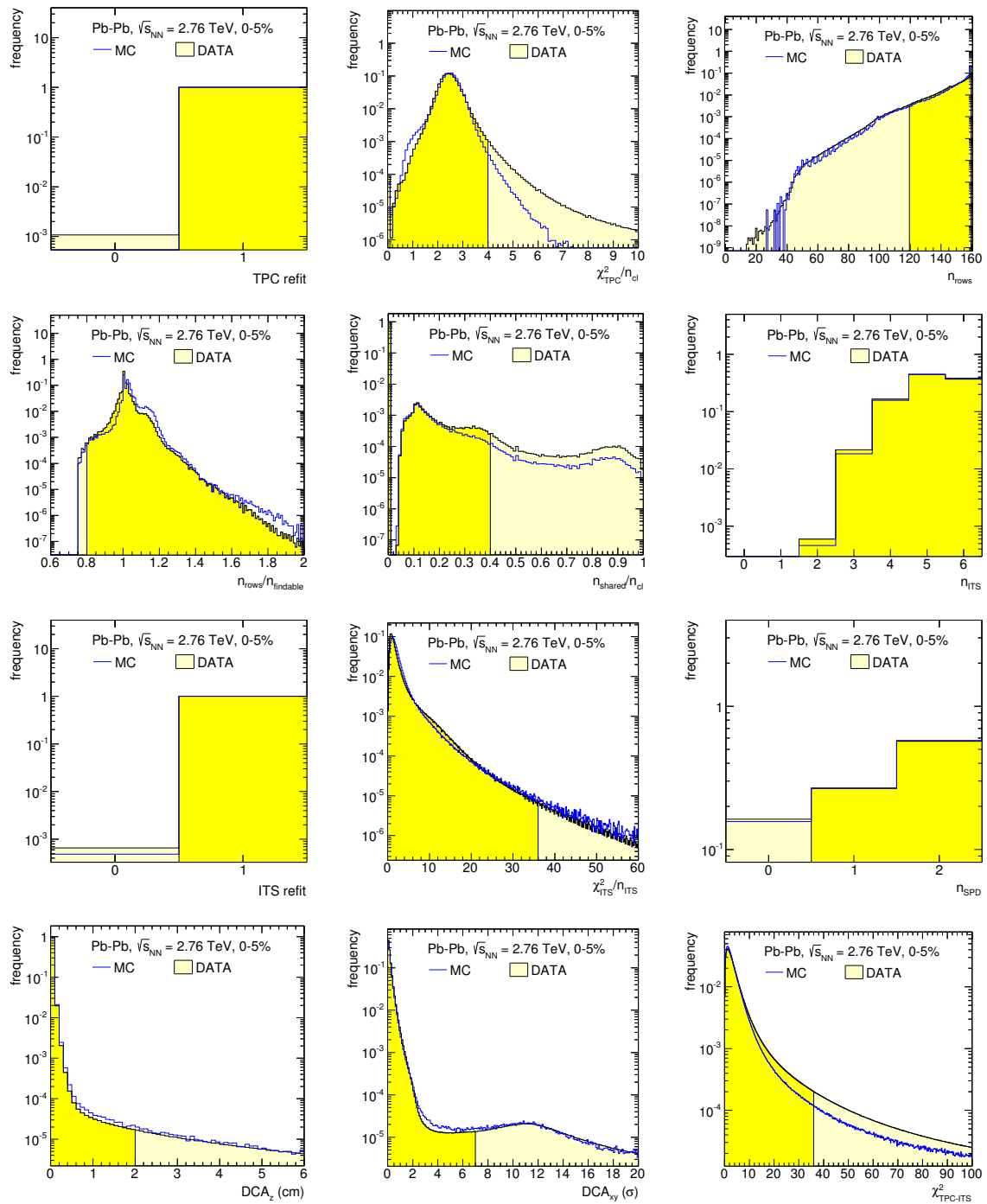


Figure D.13.: Distributions of all track cut variables in MC simulation and data Pb-Pb,  $\sqrt{s_{NN}} = 2.76$  TeV for the centrality interval 0-5%. The distributions are normalized to an integral equal to unity and integrated over the kinematic range  $0.15 < p_T < 50$  GeV/c and  $|\eta| < 0.8$ . As a consequence the distributions are dominated by tracks with low  $p_T$ . Note that the event numbers in MC are about a factor 80 lower compared to data (MC:  $\approx 11 \cdot 10^3$  events, data:  $\approx 860 \cdot 10^3$  events). For a given cut variable the distribution includes all tracks that fulfil the remaining track selection criteria. Ranges selected by the cuts are indicated in yellow.

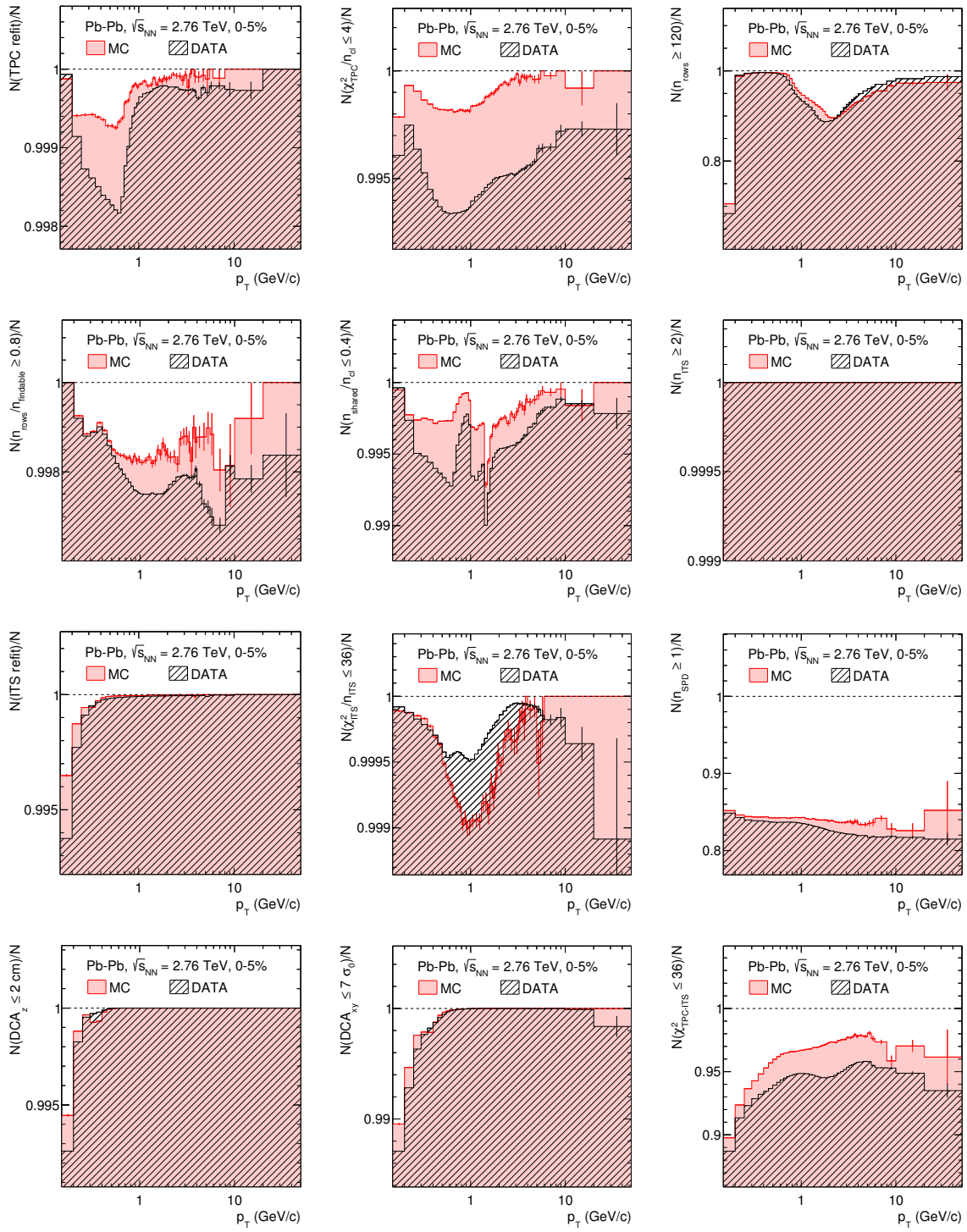


Figure D.14.: Track cut performance in the centrality interval 0-5% of Pb-Pb,  $\sqrt{s} = 2.76$  TeV data and MC simulation for all track cuts applied in the analysis. The fraction of tracks accepted by a given track cut is shown as a function of  $p_T$ , integrated over the pseudorapidity acceptance  $|\eta| < 0.8$ . For each track cut only tracks that pass all other selection criteria are considered. Note that the event numbers in MC are about a factor 80 lower compared to data (MC:  $\approx 11 \cdot 10^3$  events, data:  $\approx 860 \cdot 10^3$  events).

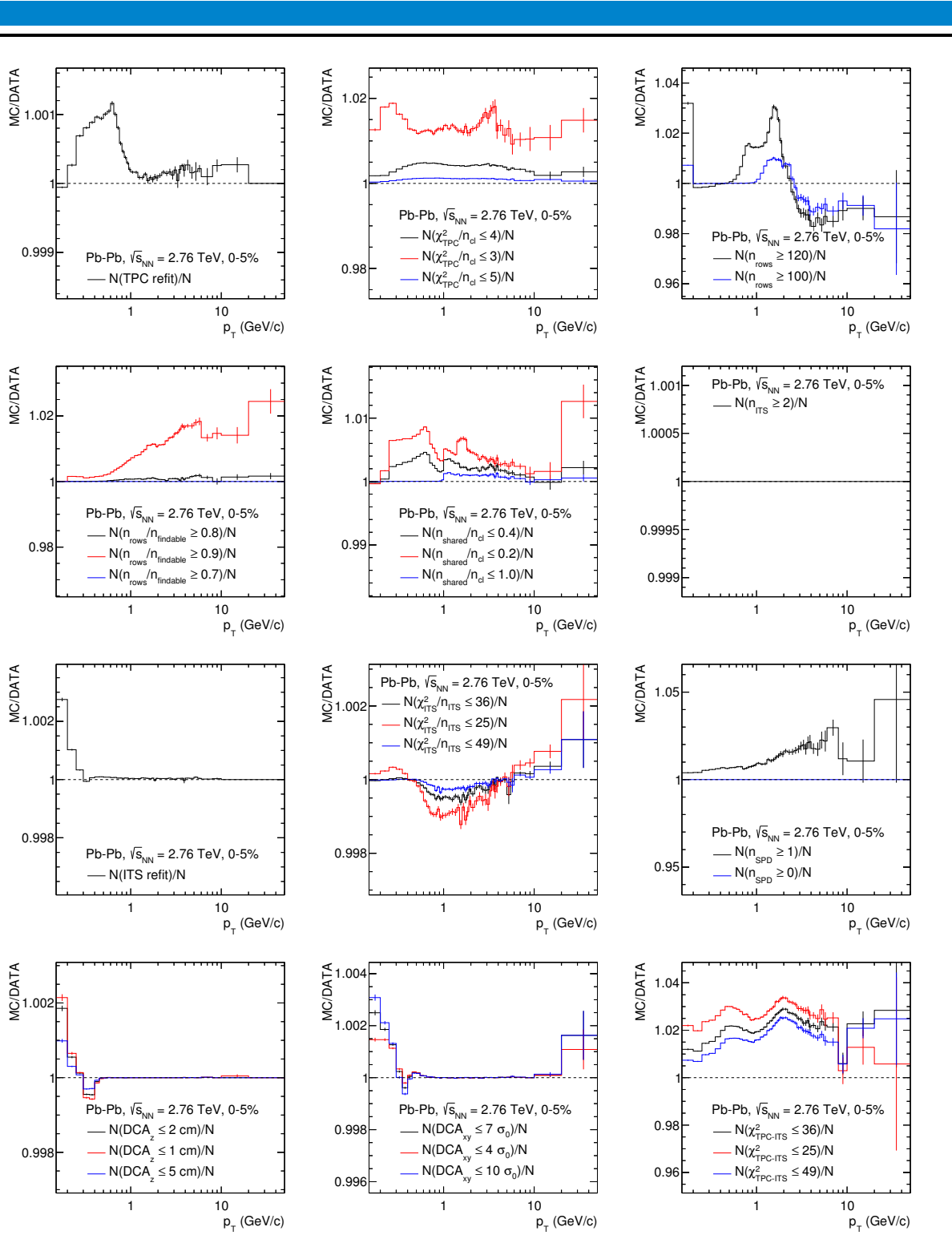


Figure D.15.: Comparison of the fraction of tracks accepted by a given track cut in data and MC simulation in terms of the double ratio  $(N_{\text{accepted}}/N_{\text{all}})_{\text{MC}}/(N_{\text{accepted}}/N_{\text{all}})_{\text{DATA}}$  for the centrality interval 0-5% in Pb-Pb,  $\sqrt{s_{\text{NN}}} = 2.76$  TeV. The black line corresponds to the nominal cut values, it is the ratio of the two histograms in Figure D.14. In addition, alternative cuts shown as red line (more restrictive cut) and blue line (looser cut) display the sensitivity of the cut against variations. The alternative cut values are the ones used for the evaluation of systematic uncertainties.

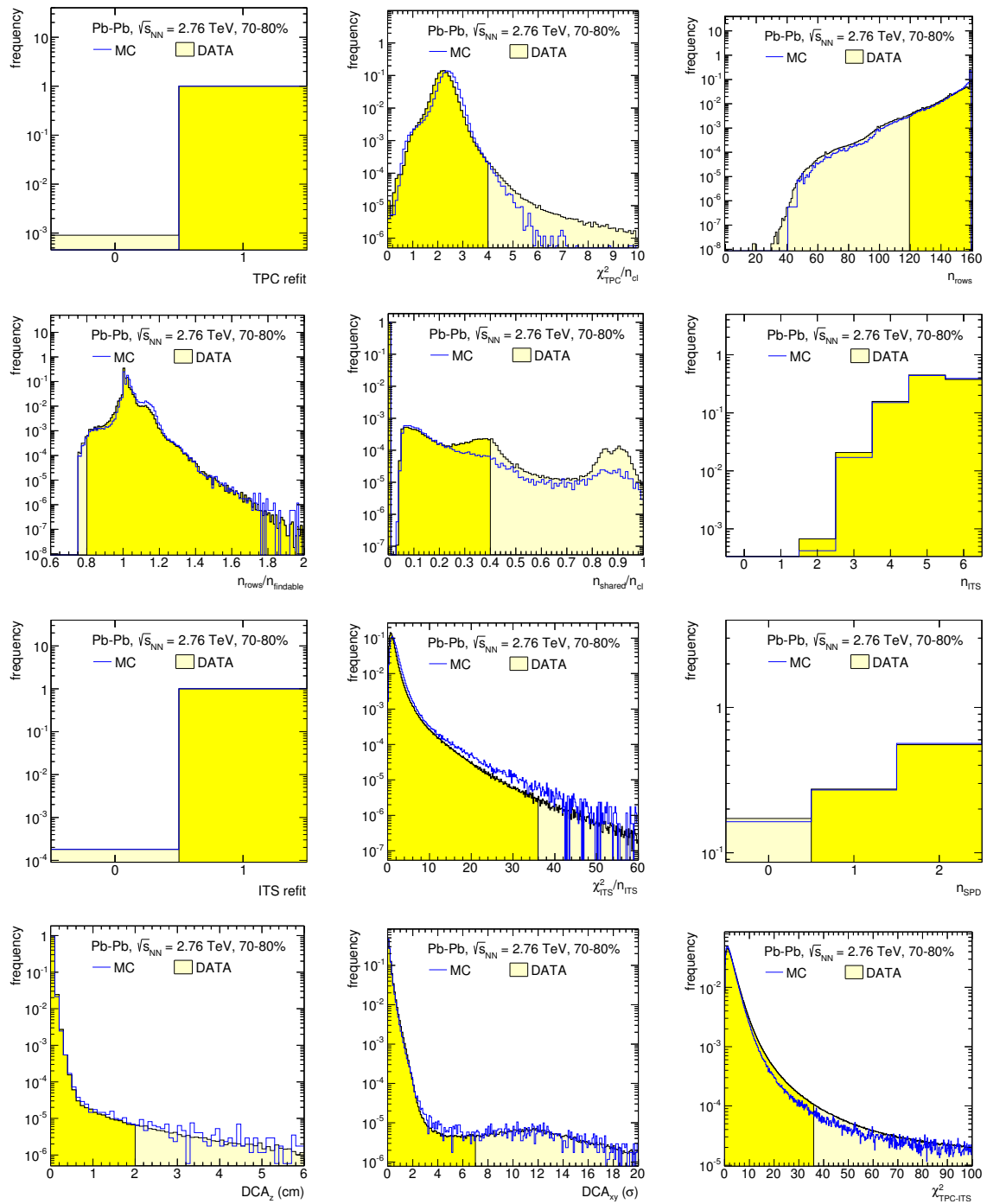


Figure D.16.: Distributions of all track cut variables in MC simulation and data Pb-Pb,  $\sqrt{s_{NN}} = 2.76$  TeV for the centrality interval 70-80%. The distributions are normalized to an integral equal to unity and integrated over the kinematic range  $0.15 < p_T < 50$  GeV/c and  $|\eta| < 0.8$ . As a consequence the distributions are dominated by tracks with low  $p_T$ . Note that the event numbers in MC are about a factor 40 lower compared to data (MC:  $\approx 44 \cdot 10^3$  events, data:  $\approx 1.7 \cdot 10^6$  events). For a given cut variable the distribution includes all tracks that fulfil the remaining track selection criteria. Ranges selected by the cuts are indicated in yellow.

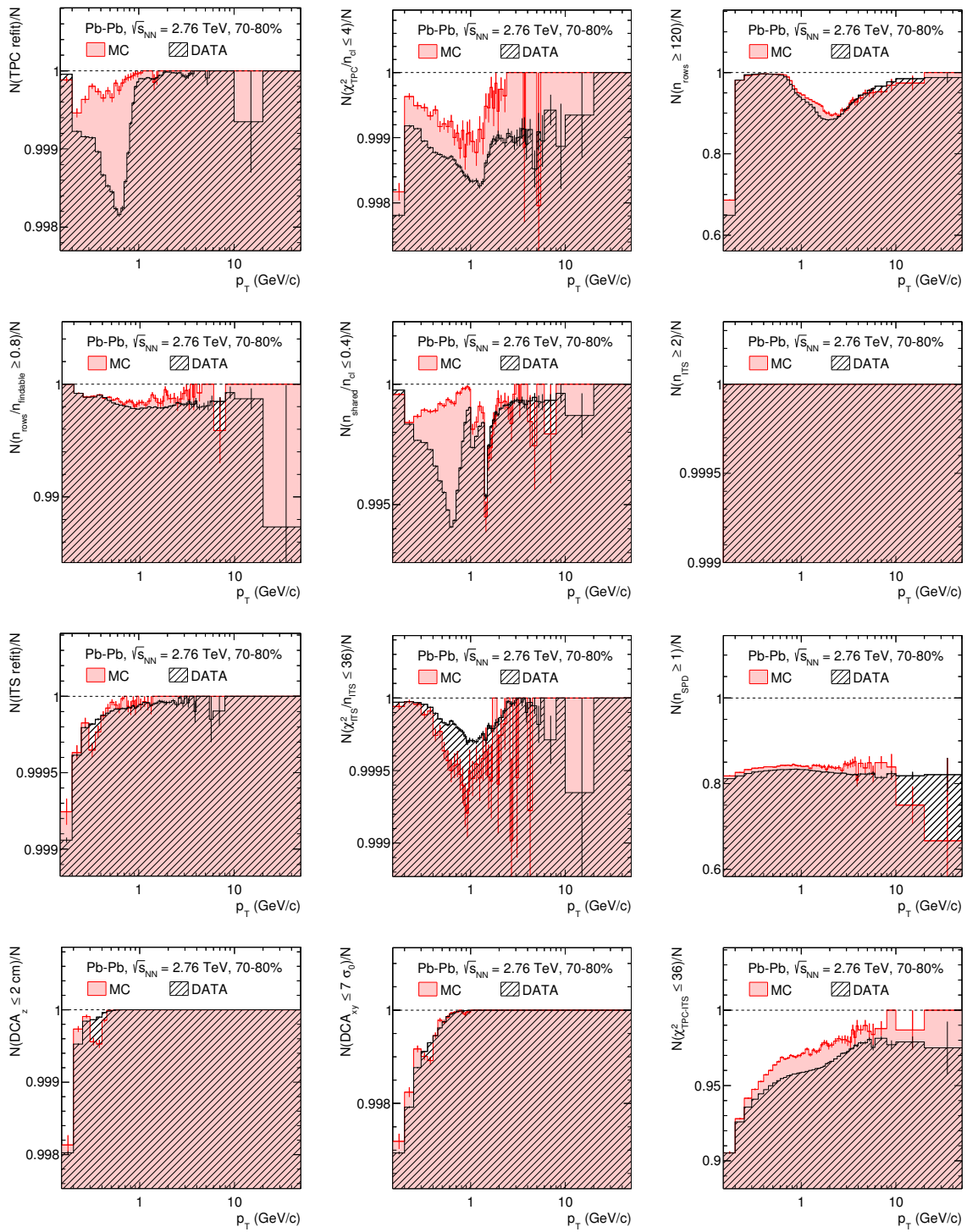


Figure D.17.: Track cut performance in the centrality interval 70-80% of Pb-Pb,  $\sqrt{s} = 2.76$  TeV data and MC simulation for all track cuts applied in the analysis. The fraction of tracks accepted by a given track cut is shown as a function of  $p_T$ , integrated over the pseudorapidity acceptance  $|\eta| < 0.8$ . For each track cut only tracks that pass all other selection criteria are considered. Note that the event numbers in MC are about a factor 40 lower compared to data (MC:  $\approx 44 \cdot 10^3$  events, data:  $\approx 1.7 \cdot 10^6$  events).

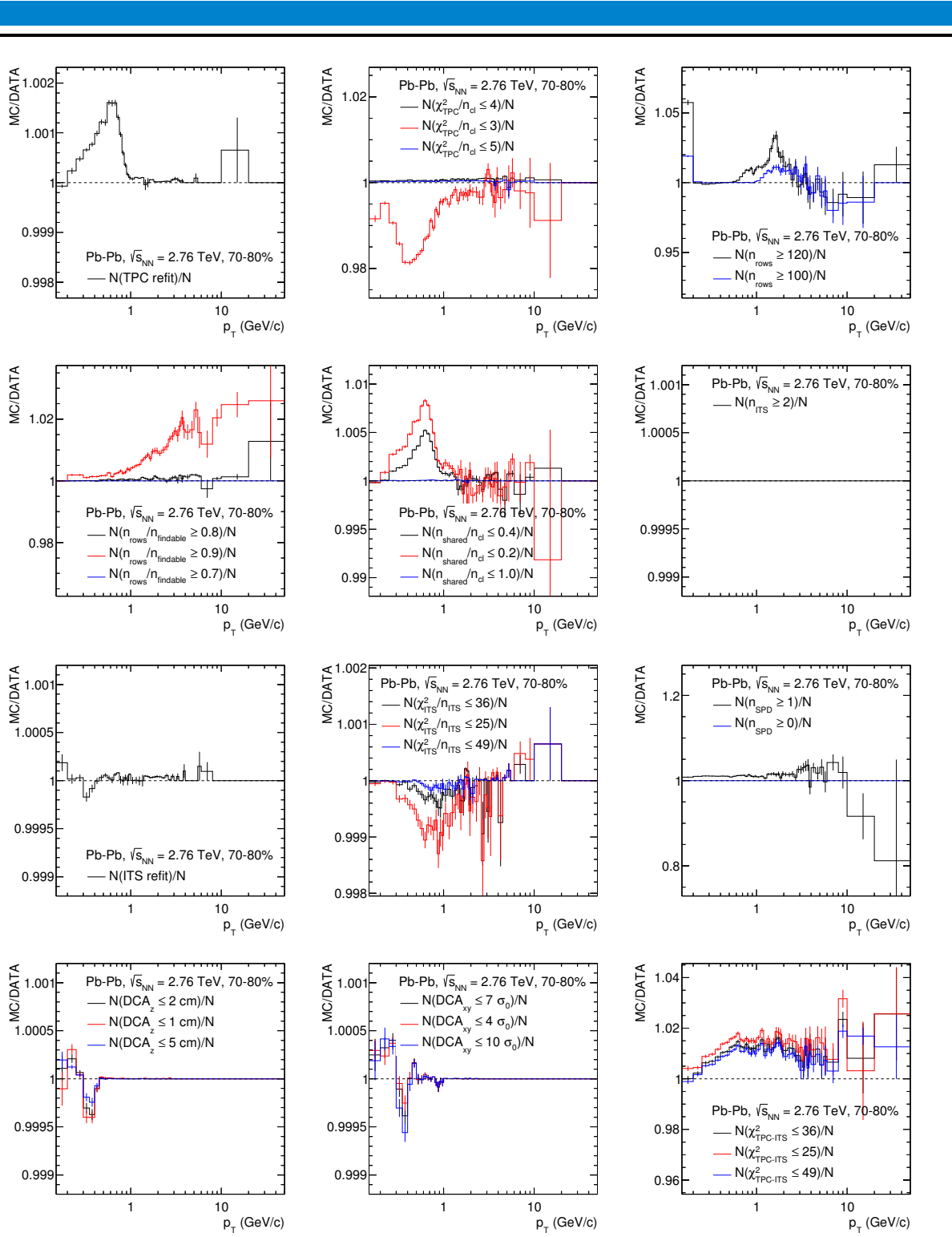
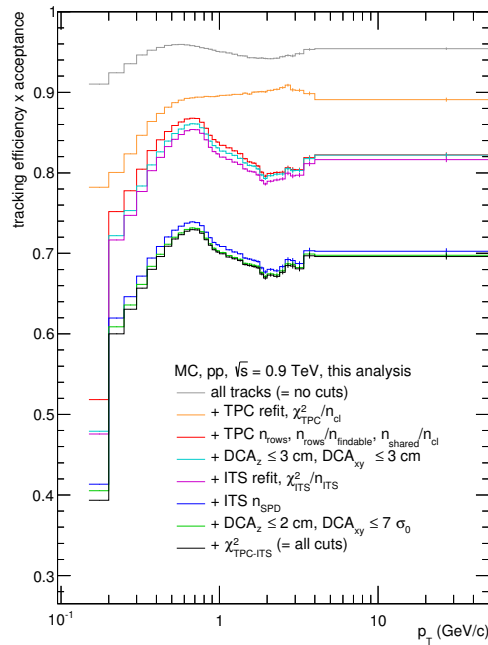


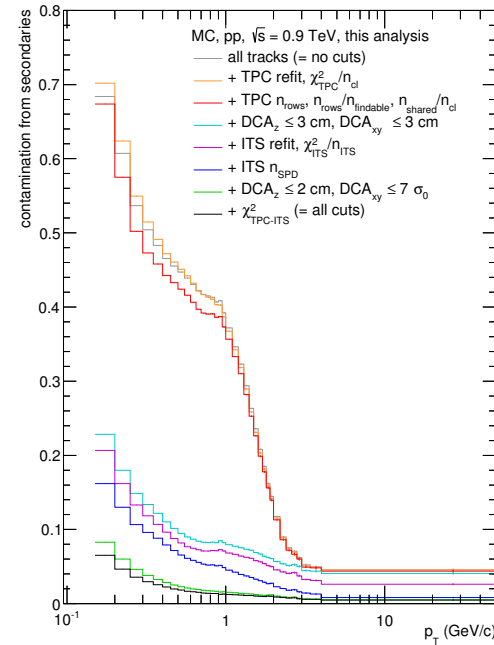
Figure D.18.: Comparison of the fraction of tracks accepted by a given track cut in data and MC simulation in terms of the double ratio  $(N_{\text{accepted}}/N_{\text{all}})_{\text{MC}}/(N_{\text{accepted}}/N_{\text{all}})_{\text{DATA}}$  for the centrality interval 70-80% in Pb-Pb,  $\sqrt{s_{\text{NN}}} = 2.76 \text{ TeV}$ . The black line corresponds to the nominal cut values, it is the ratio of the two histograms in Figure D.17. In addition, alternative cuts shown as red line (more restrictive cut) and blue line (looser cut) display the sensitivity of the cut against variations. The alternative cut values are the ones used for the evaluation of systematic uncertainties.



## E Cut Performance

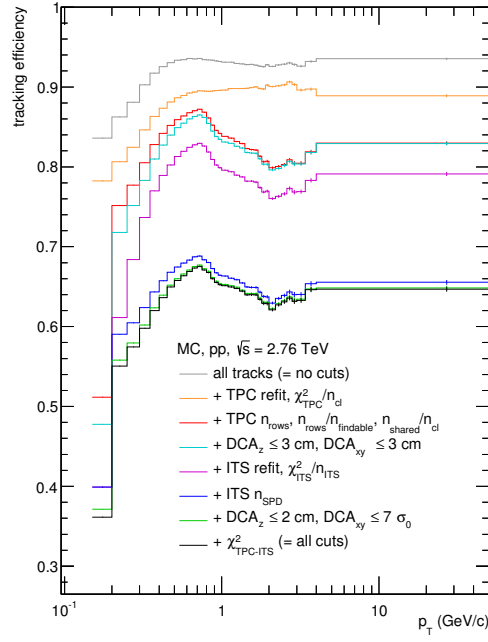


(a) Tracking efficiency

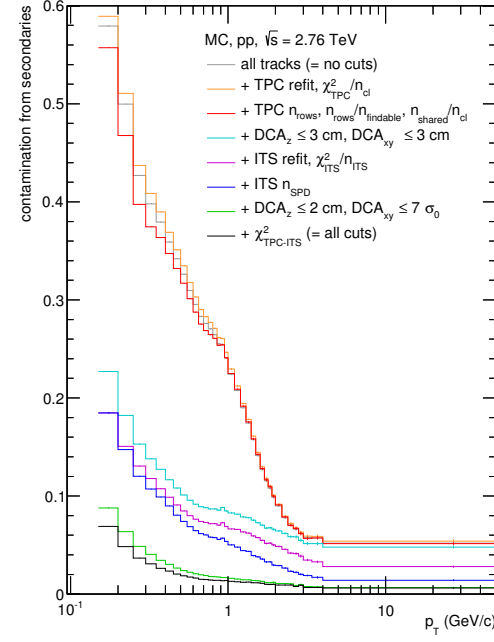


(b) Contamination

Figure E.1.: Evolution of the tracking efficiency (a) and contamination (b) in pp collisions at  $\sqrt{s} = 0.9$  TeV simulated with PYTHIA and GEANT under the successive inclusion of the track selection criteria.

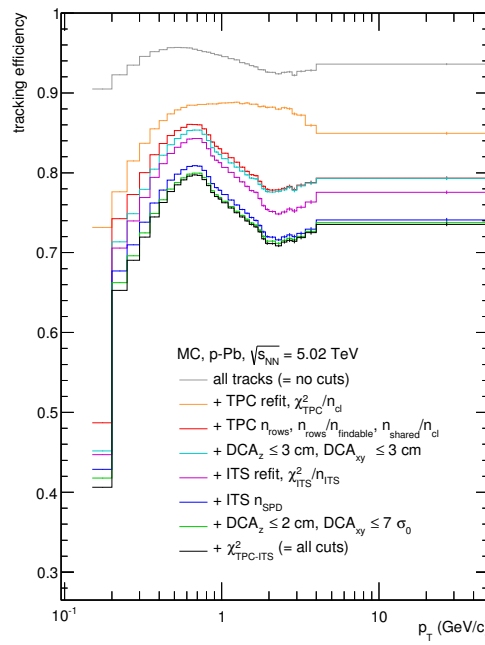


(a) Tracking efficiency

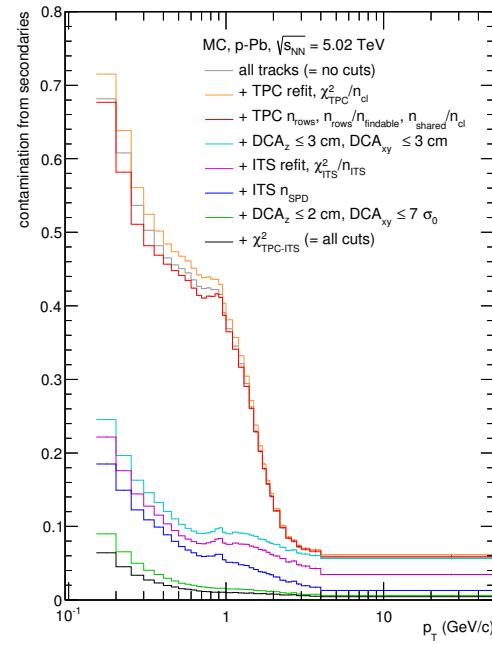


(b) Contamination

Figure E.2.: Evolution of the tracking efficiency (a) and contamination (b) in pp collisions at  $\sqrt{s} = 2.76$  TeV simulated with PYTHIA and GEANT under the successive inclusion of the track selection criteria.

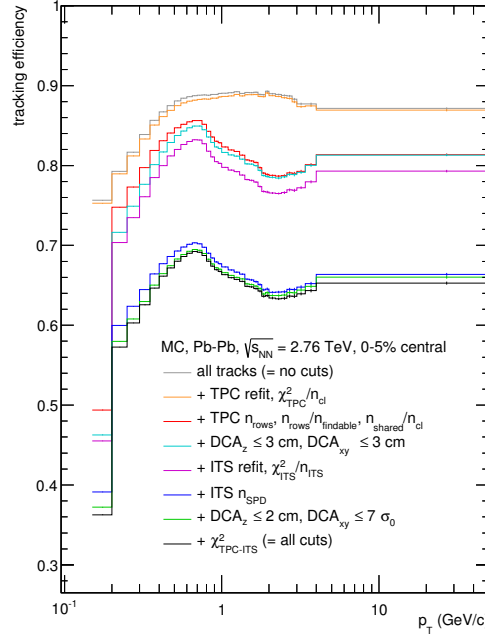


(a) Tracking efficiency

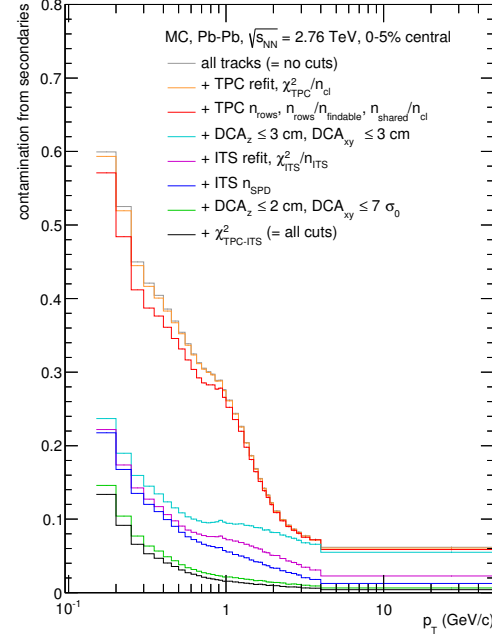


(b) Contamination

Figure E.3.: Evolution of the tracking efficiency (a) and contamination (b) simulated with DP-MJET and GEANT under the successive inclusion of the track selection criteria for 2012 p-Pb collisions at  $\sqrt{s} = 5.02$  TeV.

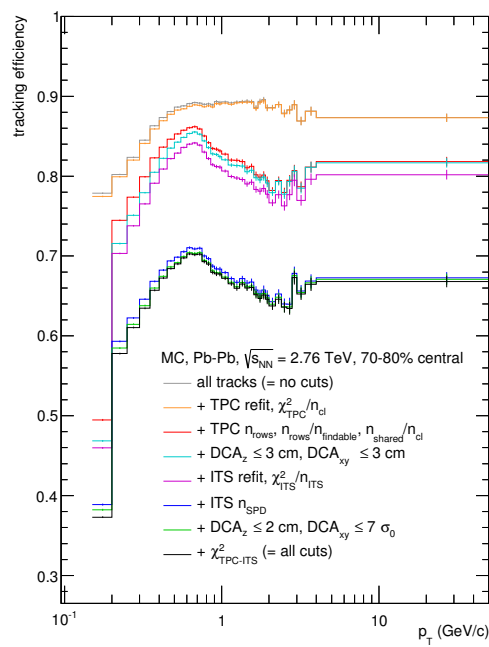


(a) Tracking efficiency

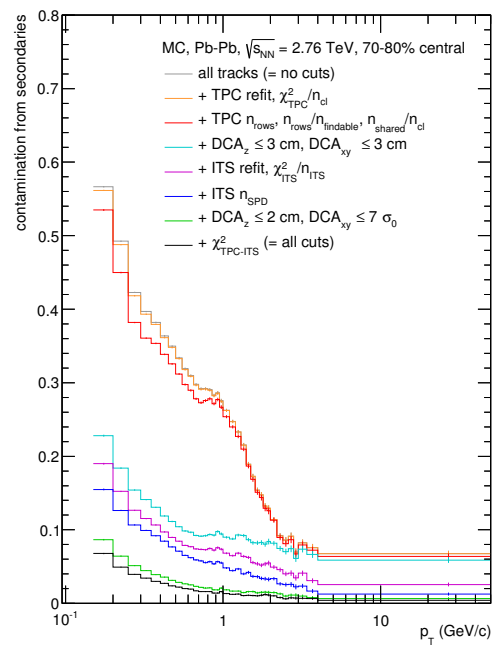


(b) Contamination

Figure E.4.: Evolution of the tracking efficiency (a) and contamination (b) in 0-5% central Pb-Pb collisions at  $\sqrt{s} = 2.76$  TeV simulated with HIJING and GEANT under the successive inclusion of the track selection criteria.



(a) Tracking efficiency



(b) Contamination

Figure E.5.: Evolution of the tracking efficiency (a) and contamination (b) in 70-80% central Pb-Pb collisions at  $\sqrt{s} = 2.76$  TeV simulated with HIJING and GEANT under the successive inclusion of the track selection criteria.

## References

- [1] K. Tamvakis, *An introduction to the physics of the Early Universe*, Lect.Notes Phys. **653**, 3 (2004).
- [2] HST Collaboration, W. Freedman *et al.*, *Final results from the Hubble Space Telescope key project to measure the Hubble constant*, Astrophys.J. **553**, 47 (2001), arXiv:astro-ph/0012376, doi:10.1086/320638.
- [3] WMAP Collaboration, C. Bennett *et al.*, *Nine-Year Wilkinson Microwave Anisotropy Probe (WMAP) Observations: Final Maps and Results*, Astrophys.J.Suppl. **208**, 20 (2013), arXiv:1212.5225, doi:10.1088/0067-0049/208/2/20.
- [4] Planck Collaboration, P. Ade *et al.*, *Planck 2013 results. I. Overview of products and scientific results*, 1303.5062, arXiv:1303.5062, doi:10.1051/0004-6361/201321529.
- [5] D. Boyanovsky, H. de Vega and D. Schwarz, *Phase transitions in the early and the present universe*, Ann.Rev.Nucl.Part.Sci. **56**, 441 (2006), arXiv:hep-ph/0602002, doi:10.1146/annurev.nucl.56.080805.140539.
- [6] D. G. d'Enterria and D. Peressounko, *Probing the QCD equation of state with thermal photons in nucleus-nucleus collisions at RHIC*, Eur.Phys.J. **C46**, 451 (2006), arXiv:nucl-th/0503054, doi:10.1140/epjc/s2006-02504-0.
- [7] M. Klasen, C. Klein-Bösing, F. König and J. Wessels, *How robust is a thermal photon interpretation of the ALICE low- $p_T$  data?*, JHEP **1310**, 119 (2013), arXiv:1307.7034, doi:10.1007/JHEP10(2013)119.
- [8] ALICE Collaboration, K. Aamodt *et al.*, *Two-pion Bose-Einstein correlations in central Pb-Pb collisions at  $\sqrt{s_{NN}} = 2.76$  TeV*, Phys.Lett. **B696**, 328 (2011), arXiv:1012.4035, doi:10.1016/j.physletb.2010.12.053.
- [9] PHENIX Collaboration, K. Adcox *et al.*, *Suppression of hadrons with large transverse momentum in central Au+Au collisions at  $\sqrt{s_{NN}} = 130$  GeV*, Phys.Rev.Lett. **88**, 022301 (2002), arXiv:nucl-ex/0109003, doi:10.1103/PhysRevLett.88.022301.
- [10] PHENIX Collaboration, S. Adler *et al.*, *Suppressed  $\pi^0$  production at large transverse momentum in central Au+Au collisions at  $\sqrt{s_{NN}} = 200$  GeV*, Phys.Rev.Lett. **91**, 072301 (2003), arXiv:nucl-ex/0304022, doi:10.1103/PhysRevLett.91.072301.
- [11] STAR Collaboration, C. Adler *et al.*, *Centrality dependence of high  $p_T$  hadron suppression in Au+Au collisions at  $\sqrt{s_{NN}} = 130$  GeV*, Phys.Rev.Lett. **89**, 202301 (2002), arXiv:nucl-ex/0206011, doi:10.1103/PhysRevLett.89.202301.
- [12] STAR Collaboration, J. Adams *et al.*, *Transverse momentum and collision energy dependence of high  $p_T$  hadron suppression in Au+Au collisions at ultrarelativistic energies*, Phys.Rev.Lett. **91**, 172302 (2003), arXiv:nucl-ex/0305015, doi:10.1103/PhysRevLett.91.172302.

[13] BRAHMS Collaboration, I. Arsene *et al.*, *Transverse momentum spectra in Au+Au and d+Au collisions at  $\sqrt{s_{NN}} = 200$  GeV and the pseudorapidity dependence of high  $p_T$  suppression*, Phys.Rev.Lett. **91**, 072305 (2003), arXiv:nucl-ex/0307003, doi:10.1103/PhysRevLett.91.072305.

[14] PHOBOS Collaboration, B. Back *et al.*, *Charged hadron transverse momentum distributions in Au + Au collisions at  $\sqrt{s_{NN}} = 200$  GeV*, Phys.Lett. **B578**, 297 (2004), arXiv:nucl-ex/0302015, doi:10.1016/j.physletb.2003.10.101.

[15] ATLAS Collaboration, G. Aad *et al.*, *Observation of a new particle in the search for the Standard Model Higgs boson with the ATLAS detector at the LHC*, Phys.Lett. **B716**, 1 (2012), arXiv:1207.7214, doi:10.1016/j.physletb.2012.08.020.

[16] CMS Collaboration, S. Chatrchyan *et al.*, *Observation of a new boson at a mass of 125 GeV with the CMS experiment at the LHC*, Phys.Lett. **B716**, 30 (2012), arXiv:1207.7235, doi:10.1016/j.physletb.2012.08.021.

[17] Particle Data Group, J. Beringer *et al.*, *Review of Particle Physics (RPP)*, Phys.Rev. **D86**, 010001 (2012), doi:10.1103/PhysRevD.86.010001.

[18] WMAP Collaboration, D. Spergel *et al.*, *First year Wilkinson Microwave Anisotropy Probe (WMAP) observations: Determination of cosmological parameters*, Astrophys.J.Suppl. **148**, 175 (2003), arXiv:astro-ph/0302209, doi:10.1086/377226.

[19] C. Rovelli, *Notes for a brief history of quantum gravity*, gr-qc/0006061, arXiv:gr-qc/0006061.

[20] S. Carlip, *Quantum gravity: A Progress report*, Rept.Prog.Phys. **64**, 885 (2001), arXiv:gr-qc/0108040, doi:10.1088/0034-4885/64/8/301.

[21] ALEPH Collaboration, DELPHI Collaboration, L3 Collaboration, OPAL Collaboration, SLD Collaboration, LEP Electroweak Working Group, SLD Electroweak Group, SLD Heavy Flavour Group, S. Schael *et al.*, *Precision electroweak measurements on the Z resonance*, Phys.Rept. **427**, 257 (2006), arXiv:hep-ex/0509008, doi:10.1016/j.physrep.2005.12.006.

[22] T. van Ritbergen, J. Vermaseren and S. Larin, *The Four loop beta function in quantum chromodynamics*, Phys.Lett. **B400**, 379 (1997), arXiv:hep-ph/9701390, doi:10.1016/S0370-2693(97)00370-5.

[23] S. Bethke, *Experimental tests of asymptotic freedom*, Prog.Part.Nucl.Phys. **58**, 351 (2007), arXiv:hep-ex/0606035, doi:10.1016/j.ppnp.2006.06.001.

[24] S. Bethke, *World Summary of  $\alpha_s$*  (2012), Nucl.Phys.Proc.Suppl. **234**, 229 (2013), arXiv:1210.0325, doi:10.1016/j.nuclphysbps.2012.12.020.

[25] D. J. Gross and F. Wilczek, *Ultraviolet Behavior of Nonabelian Gauge Theories*, Phys.Rev.Lett. **30**, 1343 (1973), doi:10.1103/PhysRevLett.30.1343.

[26] H. D. Politzer, *Reliable Perturbative Results for Strong Interactions?*, Phys.Rev.Lett. **30**, 1346 (1973), doi:10.1103/PhysRevLett.30.1346.

[27] G. Parisi, R. Petronzio and F. Rapuano, *A Measurement of the String Tension Near the Continuum Limit*, Phys.Lett. **B128**, 418 (1983), doi:10.1016/0370-2693(83)90930-9.

[28] A. Bazavov *et al.*, *Nonperturbative QCD simulations with 2+1 flavors of improved staggered quarks*, Rev.Mod.Phys. **82**, 1349 (2010), arXiv:0903.3598, doi:10.1103/RevModPhys.82.1349.

[29] F. Bissey *et al.*, *Gluon flux-tube distribution and linear confinement in baryons*, Phys.Rev. D**76**, 114512 (2007), arXiv:hep-lat/0606016, doi:10.1103/PhysRevD.76.114512.

[30] D. Leinweber, <http://www.physics.adelaide.edu.au/theory/staff/leinweber/VisualQCD/Nobel/>.

[31] B. Andersson, G. Gustafson, G. Ingelman and T. Sjostrand, *Parton Fragmentation and String Dynamics*, Phys.Rept. **97**, 31 (1983), doi:10.1016/0370-1573(83)90080-7.

[32] T. Sjostrand, S. Mrenna and P. Z. Skands, *PYTHIA 6.4 Physics and Manual*, JHEP **0605**, 026 (2006), arXiv:hep-ph/0603175, doi:10.1088/1126-6708/2006/05/026.

[33] J. C. Collins, D. E. Soper and G. F. Sterman, *Factorization of Hard Processes in QCD*, Adv.Ser.Direct.High Energy Phys. **5**, 1 (1988), arXiv:hep-ph/0409313.

[34] CTEQ Collaboration, R. Brock *et al.*, *Handbook of perturbative QCD: Version 1.0*, Rev.Mod.Phys. **67**, 157 (1995), doi:10.1103/RevModPhys.67.157.

[35] V. Gribov and L. Lipatov, *Deep inelastic e p scattering in perturbation theory*, Sov.J.Nucl.Phys. **15**, 438 (1972).

[36] Y. L. Dokshitzer, *Calculation of the Structure Functions for Deep Inelastic Scattering and e+ e- Annihilation by Perturbation Theory in Quantum Chromodynamics.*, Sov.Phys.JETP **46**, 641 (1977).

[37] G. Altarelli and G. Parisi, *Asymptotic Freedom in Parton Language*, Nucl.Phys. **B126**, 298 (1977), doi:10.1016/0550-3213(77)90384-4.

[38] L. Lipatov, *Reggeization of the Vector Meson and the Vacuum Singularity in Nonabelian Gauge Theories*, Sov.J.Nucl.Phys. **23**, 338 (1976).

[39] E. Kuraev, L. Lipatov and V. S. Fadin, *The Pomeranchuk Singularity in Nonabelian Gauge Theories*, Sov.Phys.JETP **45**, 199 (1977).

[40] I. Balitsky and L. Lipatov, *The Pomeranchuk Singularity in Quantum Chromodynamics*, Sov.J.Nucl.Phys. **28**, 822 (1978).

[41] G. P. Salam, *An Introduction to leading and next-to-leading BFKL*, Acta Phys.Polon. **B30**, 3679 (1999), arXiv:hep-ph/9910492.

[42] R. D. Ball *et al.*, *Parton distributions with LHC data*, Nucl.Phys. **B867**, 244 (2013), arXiv:1207.1303, doi:10.1016/j.nuclphysb.2012.10.003.

[43] L. Gribov, E. Levin and M. Ryskin, *Semihard Processes in QCD*, Phys.Rept. **100**, 1 (1983), doi:10.1016/0370-1573(83)90022-4.

[44] A. H. Mueller and J.-w. Qiu, *Gluon Recombination and Shadowing at Small Values of x*, Nucl.Phys. **B268**, 427 (1986), doi:10.1016/0550-3213(86)90164-1.

[45] A. Martin, W. Stirling, R. Thorne and G. Watt, *Parton distributions for the LHC*, Eur.Phys.J. **C63**, 189 (2009), arXiv:0901.0002, doi:10.1140/epjc/s10052-009-1072-5.

[46] Particle Data Group, K. A. Olive *et al.*, *Review of Particle Physics (RPP)*, Chin.Phys. **C38**, 090001 (2014), doi:[10.1088/1674-1137/38/9/090001](https://doi.org/10.1088/1674-1137/38/9/090001).

[47] F. Gelis, *Color Glass Condensate and Glasma*, Int.J.Mod.Phys. **A28**, 1330001 (2013), arXiv:[1211.3327](https://arxiv.org/abs/1211.3327), doi:[10.1142/S0217751X13300019](https://doi.org/10.1142/S0217751X13300019).

[48] K. Eskola, H. Paukkunen and C. Salgado, *EPS09: A New Generation of NLO and LO Nuclear Parton Distribution Functions*, JHEP **0904**, 065 (2009), arXiv:[0902.4154](https://arxiv.org/abs/0902.4154), doi:[10.1088/1126-6708/2009/04/065](https://doi.org/10.1088/1126-6708/2009/04/065).

[49] K. Rith, *Present Status of the EMC effect*, 1402.5000, arXiv:[1402.5000](https://arxiv.org/abs/1402.5000).

[50] I. Helenius, K. J. Eskola, H. Honkanen and C. A. Salgado, *Impact-Parameter Dependent Nuclear Parton Distribution Functions: EPS09s and EKS98s and Their Applications in Nuclear Hard Processes*, JHEP **1207**, 073 (2012), arXiv:[1205.5359](https://arxiv.org/abs/1205.5359), doi:[10.1007/JHEP07\(2012\)073](https://doi.org/10.1007/JHEP07(2012)073).

[51] G. Marchesini *et al.*, *HERWIG: A Monte Carlo event generator for simulating hadron emission reactions with interfering gluons. Version 5.1 - April 1991*, Comput.Phys.Commun. **67**, 465 (1992), doi:[10.1016/0010-4655\(92\)90055-4](https://doi.org/10.1016/0010-4655(92)90055-4).

[52] V. Koch, *Introduction to chiral symmetry*, nucl-th/9512029, arXiv:[nucl-th/9512029](https://arxiv.org/abs/nucl-th/9512029).

[53] H. G. Dosch and S. Narison, *Direct extraction of the chiral quark condensate and bounds on the light quark masses*, Phys.Lett. **B417**, 173 (1998), arXiv:[hep-ph/9709215](https://arxiv.org/abs/hep-ph/9709215), doi:[10.1016/S0370-2693\(97\)01370-1](https://doi.org/10.1016/S0370-2693(97)01370-1).

[54] J. C. Collins and M. Perry, *Superdense Matter: Neutrons Or Asymptotically Free Quarks?*, Phys.Rev.Lett. **34**, 1353 (1975), doi:[10.1103/PhysRevLett.34.1353](https://doi.org/10.1103/PhysRevLett.34.1353).

[55] N. Cabibbo and G. Parisi, *Exponential Hadronic Spectrum and Quark Liberation*, Phys.Lett. **B59**, 67 (1975), doi:[10.1016/0370-2693\(75\)90158-6](https://doi.org/10.1016/0370-2693(75)90158-6).

[56] A. M. Polyakov, *Thermal Properties of Gauge Fields and Quark Liberation*, Phys.Lett. **B72**, 477 (1978), doi:[10.1016/0370-2693\(78\)90737-2](https://doi.org/10.1016/0370-2693(78)90737-2).

[57] L. Susskind, *Lattice Models of Quark Confinement at High Temperature*, Phys.Rev. **D20**, 2610 (1979), doi:[10.1103/PhysRevD.20.2610](https://doi.org/10.1103/PhysRevD.20.2610).

[58] HotQCD Collaboration, A. Bazavov *et al.*, *Equation of state in (2+1)-flavor QCD*, Phys.Rev. **D90**, 094503 (2014), arXiv:[1407.6387](https://arxiv.org/abs/1407.6387), doi:[10.1103/PhysRevD.90.094503](https://doi.org/10.1103/PhysRevD.90.094503).

[59] F. Karsch and E. Laermann, *Thermodynamics and in medium hadron properties from lattice QCD*, hep-lat/0305025, arXiv:[hep-lat/0305025](https://arxiv.org/abs/hep-lat/0305025).

[60] A. Bazavov *et al.*, *The chiral and deconfinement aspects of the QCD transition*, Phys.Rev. **D85**, 054503 (2012), arXiv:[1111.1710](https://arxiv.org/abs/1111.1710), doi:[10.1103/PhysRevD.85.054503](https://doi.org/10.1103/PhysRevD.85.054503).

[61] T. Bhattacharya *et al.*, *The QCD phase transition with physical-mass, chiral quarks*, Phys.Rev.Lett. **113**, 082001 (2014), arXiv:[1402.5175](https://arxiv.org/abs/1402.5175), doi:[10.1103/PhysRevLett.113.082001](https://doi.org/10.1103/PhysRevLett.113.082001).

[62] Z. Fodor and S. Katz, *Lattice determination of the critical point of QCD at finite  $T$  and  $\mu$* , JHEP **0203**, 014 (2002), arXiv:[hep-lat/0106002](https://arxiv.org/abs/hep-lat/0106002), doi:[10.1088/1126-6708/2002/03/014](https://doi.org/10.1088/1126-6708/2002/03/014).

[63] B. Friman *et al.*, *The CBM physics book: Compressed baryonic matter in laboratory experiments*, Lect.Notes Phys. **814**, 1 (2011), doi:[10.1007/978-3-642-13293-3](https://doi.org/10.1007/978-3-642-13293-3).

[64] A. Andronic, P. Braun-Munzinger and J. Stachel, *Thermal hadron production in relativistic nuclear collisions: The Hadron mass spectrum, the horn, and the QCD phase transition*, Phys.Lett. **B673**, 142 (2009), arXiv:[0812.1186](https://arxiv.org/abs/0812.1186), doi:[10.1016/j.physletb.2009.06.021](https://doi.org/10.1016/j.physletb.2009.02.014).

[65] T. Schäfer, *Phases of QCD*, hep-ph/0509068, arXiv:[hep-ph/0509068](https://arxiv.org/abs/hep-ph/0509068).

[66] K. Fukushima and C. Sasaki, *The phase diagram of nuclear and quark matter at high baryon density*, Prog.Part.Nucl.Phys. **72**, 99 (2013), arXiv:[1301.6377](https://arxiv.org/abs/1301.6377), doi:[10.1016/j.ppnp.2013.05.003](https://doi.org/10.1016/j.ppnp.2013.05.003).

[67] F. Karsch, *Lattice QCD at high temperature and density*, Lect.Notes Phys. **583**, 209 (2002), arXiv:[hep-lat/0106019](https://arxiv.org/abs/hep-lat/0106019).

[68] P. Braun-Munzinger, K. Redlich and J. Stachel, *Particle production in heavy ion collisions*, nucl-th/0304013, arXiv:[nucl-th/0304013](https://arxiv.org/abs/nucl-th/0304013).

[69] A. Andronic *et al.*, *Hadron Production in Ultra-relativistic Nuclear Collisions: Quarkyonic Matter and a Triple Point in the Phase Diagram of QCD*, Nucl.Phys. **A837**, 65 (2010), arXiv:[0911.4806](https://arxiv.org/abs/0911.4806), doi:[10.1016/j.nuclphysa.2010.02.005](https://doi.org/10.1016/j.nuclphysa.2010.02.005).

[70] P. Braun-Munzinger and J. Wambach, *The Phase Diagram of Strongly-Interacting Matter*, Rev.Mod.Phys. **81**, 1031 (2009), arXiv:[0801.4256](https://arxiv.org/abs/0801.4256), doi:[10.1103/RevModPhys.81.1031](https://doi.org/10.1103/RevModPhys.81.1031).

[71] E. Iancu, *Theory summary for ISMD2000*, 1105.0751, arXiv:[1105.0751](https://arxiv.org/abs/1105.0751), doi:[10.5689/UA-PROC-2010-09/58](https://doi.org/10.5689/UA-PROC-2010-09/58).

[72] E. Iancu and R. Venugopalan, *The Color glass condensate and high-energy scattering in QCD*, hep-ph/0303204, arXiv:[hep-ph/0303204](https://arxiv.org/abs/hep-ph/0303204).

[73] J. Berges, J.-P. Blaizot and F. Gelis, *EMMI Rapid Reaction Task Force on 'Thermalization in Non-abelian Plasmas'*, J.Phys. **G39**, 085115 (2012), arXiv:[1203.2042](https://arxiv.org/abs/1203.2042), doi:[10.1088/0954-3899/39/8/085115](https://doi.org/10.1088/0954-3899/39/8/085115).

[74] T. Lappi and L. McLerran, *Some features of the glasma*, Nucl.Phys. **A772**, 200 (2006), arXiv:[hep-ph/0602189](https://arxiv.org/abs/hep-ph/0602189), doi:[10.1016/j.nuclphysa.2006.04.001](https://doi.org/10.1016/j.nuclphysa.2006.04.001).

[75] E. Schnedermann, J. Sollfrank and U. W. Heinz, *Thermal phenomenology of hadrons from 200 A GeV S+S collisions*, Phys.Rev. **C48**, 2462 (1993), arXiv:[nucl-th/9307020](https://arxiv.org/abs/nucl-th/9307020), doi:[10.1103/PhysRevC.48.2462](https://doi.org/10.1103/PhysRevC.48.2462).

[76] U. W. Heinz and M. Jacob, *Evidence for a new state of matter: An Assessment of the results from the CERN lead beam program*, nucl-th/0002042, arXiv:[nucl-th/0002042](https://arxiv.org/abs/nucl-th/0002042).

[77] STAR Collaboration, J. Adams *et al.*, *Experimental and theoretical challenges in the search for the quark gluon plasma: The STAR Collaboration's critical assessment of the evidence from RHIC collisions*, Nucl.Phys. **A757**, 102 (2005), arXiv:[nucl-ex/0501009](https://arxiv.org/abs/nucl-ex/0501009), doi:[10.1016/j.nuclphysa.2005.03.085](https://doi.org/10.1016/j.nuclphysa.2005.03.085).

[78] J. Rafelski and B. Muller, *Strangeness Production in the Quark-Gluon Plasma*, Phys.Rev.Lett. **48**, 1066 (1982), doi:[10.1103/PhysRevLett.48.1066](https://doi.org/10.1103/PhysRevLett.48.1066).

[79] S. Hamieh, K. Redlich and A. Tounsi, *Canonical description of strangeness enhancement from  $p$ - $A$  to  $Pb$ - $Pb$  collisions*, Phys.Lett. **B486**, 61 (2000), arXiv:hep-ph/0006024, doi:10.1016/S0370-2693(00)00762-0.

[80] T. Matsui and H. Satz,  *$J/\psi$  Suppression by Quark-Gluon Plasma Formation*, Phys.Lett. **B178**, 416 (1986), doi:10.1016/0370-2693(86)91404-8.

[81] H. Satz, *Quarkonium Binding and Dissociation: The Spectral Analysis of the QGP*, Nucl.Phys. **A783**, 249 (2007), arXiv:hep-ph/0609197, doi:10.1016/j.nuclphysa.2006.11.026.

[82] R. Rapp and J. Wambach, *Chiral symmetry restoration and dileptons in relativistic heavy ion collisions*, Adv.Nucl.Phys. **25**, 1 (2000), arXiv:hep-ph/9909229, doi:10.1007/0-306-47101-9\_1.

[83] S. Ellis, J. Huston, K. Hatakeyama, P. Loch and M. Tonnesmann, *Jets in hadron-hadron collisions*, Prog.Part.Nucl.Phys. **60**, 484 (2008), arXiv:0712.2447, doi:10.1016/j.ppnp.2007.12.002.

[84] G. P. Salam, *Towards Jetography*, Eur.Phys.J. **C67**, 637 (2010), arXiv:0906.1833, doi:10.1140/epjc/s10052-010-1314-6.

[85] S. Catani, Y. L. Dokshitzer, M. Olsson, G. Turnock and B. Webber, *New clustering algorithm for multi-jet cross-sections in  $e^+ e^-$  annihilation*, Phys.Lett. **B269**, 432 (1991), doi:10.1016/0370-2693(91)90196-W.

[86] S. D. Ellis and D. E. Soper, *Successive combination jet algorithm for hadron collisions*, Phys.Rev. **D48**, 3160 (1993), arXiv:hep-ph/9305266, doi:10.1103/PhysRevD.48.3160.

[87] M. Cacciari, G. P. Salam and G. Soyez, *The Anti- $k_t$  jet clustering algorithm*, JHEP **0804**, 063 (2008), arXiv:0802.1189, doi:10.1088/1126-6708/2008/04/063.

[88] TASSO Collaboration, R. Brandelik *et al.*, *Evidence for Planar Events in  $e^+ e^-$  Annihilation at High-Energies*, Phys.Lett. **B86**, 243 (1979), doi:10.1016/0370-2693(79)90830-X.

[89] ALICE Collaboration, B. Abelev *et al.*, *Measurement of charged jet suppression in  $Pb$ - $Pb$  collisions at  $\sqrt{s_{NN}} = 2.76$  TeV*, JHEP **1403**, 013 (2014), arXiv:1311.0633, doi:10.1007/JHEP03(2014)013.

[90] J. Bjorken, *Energy Loss of Energetic Partons in Quark-Gluon Plasma: Possible Extinction of High  $p_T$  Jets in Hadron-Hadron Collisions* (Fermilab, 1982), FERMILAB-PUB-82-059-THY, FERMILAB-PUB-82-059-T.

[91] U. A. Wiedemann, *Jet Quenching in Heavy Ion Collisions*, Landolt-Bornstein **23**, 521 (2010), arXiv:0908.2306, doi:10.1007/978-3-642-01539-7\_17.

[92] D. d'Enterria, *Jet quenching*, Landolt-Bornstein **23**, 471 (2010), arXiv:0902.2011, doi:10.1007/978-3-642-01539-7\_16.

[93] D. d'Enterria and B. Betz, *High- $p_T$  hadron suppression and jet quenching*, Lect.Notes Phys. **785**, 285 (2010), doi:10.1007/978-3-642-02286-9\_9.

[94] T. Renk, *The Phenomenology of Elastic Energy Loss*, Phys.Rev. **C76**, 064905 (2007), arXiv:0708.4319, doi:10.1103/PhysRevC.76.064905.

[95] N. Armesto *et al.*, *Comparison of Jet Quenching Formalisms for a Quark-Gluon Plasma 'Brick'*, Phys.Rev. **C86**, 064904 (2012), arXiv:1106.1106, doi:10.1103/PhysRevC.86.064904.

[96] S. Bass and A. Dumitru, *Dynamics of hot bulk QCD matter: From the quark gluon plasma to hadronic freezeout*, Phys.Rev. **C61**, 064909 (2000), arXiv:nucl-th/0001033, doi:10.1103/PhysRevC.61.064909.

[97] M. L. Miller, K. Reygers, S. J. Sanders and P. Steinberg, *Glauber modeling in high energy nuclear collisions*, Ann.Rev.Nucl.Part.Sci. **57**, 205 (2007), arXiv:nucl-ex/0701025, doi:10.1146/annurev.nucl.57.090506.123020.

[98] S. Navin, *Diffraction in Pythia*, 1005.3894, arXiv:1005.3894.

[99] L. Evans and P. Bryant, *LHC Machine*, JINST **3**, S08001 (2008), doi:10.1088/1748-0221/3/08/S08001.

[100] O. S. Bruning *et al.*, *LHC Design Report. 1. The LHC Main Ring* (CERN, 2004), CERN-2004-003-V-1, CERN-2004-003.

[101] O. Buning *et al.*, *LHC Design Report. 2. The LHC infrastructure and general services* (CERN, 2004), CERN-2004-003-V-2, CERN-2004-003.

[102] M. Benedikt, P. Collier, V. Mertens, J. Poole and K. Schindl, *LHC Design Report. 3. The LHC injector chain* (CERN, 2004), CERN-2004-003-V-3, CERN-2004-003.

[103] C. Lefèvre, *The CERN accelerator complex. Complexe des accélérateurs du CERN*, CERN CDS, 2008.

[104] ATLAS Collaboration, G. Aad *et al.*, *The ATLAS Experiment at the CERN Large Hadron Collider*, JINST **3**, S08003 (2008), doi:10.1088/1748-0221/3/08/S08003.

[105] CMS Collaboration, S. Chatrchyan *et al.*, *The CMS experiment at the CERN LHC*, JINST **3**, S08004 (2008), doi:10.1088/1748-0221/3/08/S08004.

[106] LHCb Collaboration, J. Alves, A. Augusto *et al.*, *The LHCb Detector at the LHC*, JINST **3**, S08005 (2008), doi:10.1088/1748-0221/3/08/S08005.

[107] LHCf Collaboration, O. Adriani *et al.*, *The LHCf detector at the CERN Large Hadron Collider*, JINST **3**, S08006 (2008), doi:10.1088/1748-0221/3/08/S08006.

[108] G. Antchev *et al.*, *The TOTEM detector at LHC*, Nucl.Instrum.Meth. **A617**, 62 (2010), doi:10.1016/j.nima.2009.08.083.

[109] MoEDAL Collaboration, J. Pinfold *et al.*, *Technical Design Report of the MoEDAL Experiment* (CERN, 2009), CERN-LHCC-2009-006. MoEDAL-TDR-001.

[110] ALICE Collaboration, *Technical proposal for a Large Ion collider Experiment at the CERN LHC* (CERN, 1995), CERN/LHCC/95-71, LHCC/P3.

[111] ALICE Collaboration, K. Aamodt *et al.*, *The ALICE experiment at the CERN LHC*, JINST **3**, S08002 (2008), doi:10.1088/1748-0221/3/08/S08002.

[112] ALICE Collaboration, F. Carminati *et al.*, *ALICE: Physics performance report, volume I*, J.Phys. **G30**, 1517 (2004), doi:10.1088/0954-3899/30/11/001.

[113] ALICE Collaboration, B. Alessandro *et al.*, *ALICE: Physics performance report, volume II*, J.Phys. **G32**, 1295 (2006), doi:10.1088/0954-3899/32/10/001.

[114] ALICE Collaboration, K. Aamodt *et al.*, *Charged-particle multiplicity density at mid-rapidity in central Pb–Pb collisions at  $\sqrt{s_{NN}} = 2.76$  TeV*, Phys.Rev.Lett. **105**, 252301 (2010), arXiv:1011.3916, doi:10.1103/PhysRevLett.105.252301.

[115] ALICE Collaboration, K. Aamodt *et al.*, *Centrality dependence of the charged-particle multiplicity density at mid-rapidity in Pb–Pb collisions at  $\sqrt{s_{NN}} = 2.76$  TeV*, Phys.Rev.Lett. **106**, 032301 (2011), arXiv:1012.1657, doi:10.1103/PhysRevLett.106.032301.

[116] ALICE Collaboration, E. Abbas *et al.*, *Centrality dependence of the pseudorapidity density distribution for charged particles in Pb–Pb collisions at  $\sqrt{s_{NN}} = 2.76$  TeV*, Phys.Lett. **B726**, 610 (2013), arXiv:1304.0347, doi:10.1016/j.physletb.2013.09.022.

[117] J. Alme *et al.*, *The ALICE TPC, a large 3-dimensional tracking device with fast readout for ultra-high multiplicity events*, Nuclear Instruments and Methods in Physics Research Section A: Accelerators, Spectrometers, Detectors and Associated Equipment **622**, 316 (2010), doi:10.1016/j.nima.2010.04.042.

[118] ALICE Collaboration, <http://aliceinfo.cern.ch>.

[119] ALICE Collaboration, B. Abelev *et al.*, *Performance of the ALICE Experiment at the CERN LHC*, 1402.4476, arXiv:1402.4476.

[120] ALICE Collaboration, *Definition of the ALICE Coordinate System and Basic Rules for Sub-detector Components Numbering* (CERN, 2003), ALICE-INT-2003-038.

[121] C. Lippmann and D. Vranic, *Alice TPC Numbering Conventions* (CERN, 2007).

[122] ALICE Collaboration, *Technical Design Report of the Inner Tracking System (ITS)* (CERN, 1999), CERN /LHCC 99-12, ALICE TDR 4.

[123] ALICE Collaboration, *ALICE time projection chamber: Technical Design Report* (CERN, 2000), ALICE TDR 7.

[124] ALICE Collaboration, *ALICE transition-radiation detector: Technical Design Report* Technical Design Report ALICE (CERN, 2001), ALICE-TDR-9, CERN-LHCC-2001-021, LYCEN-2001-97.

[125] ALICE Collaboration, *ALICE Time-Of-Flight system (TOF): Technical Design Report* Technical Design Report ALICE (CERN, 2000), ALICE-TDR-8, CERN-LHCC-2000-012.

[126] ALICE Collaboration, *ALICE Time-Of Flight system (TOF): addendum to the Technical Design Report* (CERN, 2002), ALICE-TDR-8-add-1, CERN-LHCC-2002-016.

[127] ALICE Collaboration, *The Electromagnetic Calorimeter - Addendum to the Technical Proposal* (CERN, 2006), CERN-LHCC-2006-014, CERN/LHCC 96-32-Add3.

[128] ALICE Collaboration, *Electromagnetic Calorimeter - Technical Design Report* (CERN, 2008), CERN-LHCC-2008-014, ALICE-TDR-014.

[129] ALICE EMCal Collaboration, U. Abeysekara *et al.*, *ALICE EMCal Physics Performance Report*, 1008.0413, arXiv:1008.0413.

---

[130] ALICE Collaboration, *Technical Design Report of the Photon Spectrometer (PHOS)* (CERN, 1999), CERN/LHCC 99-4, ALICE TDR 2.

[131] ALICE PHOS calorimeter Collaboration, D. Aleksandrov *et al.*, *A high resolution electromagnetic calorimeter based on lead-tungstate crystals*, Nucl.Instrum.Meth. **A550**, 169 (2005), doi:10.1016/j.nima.2005.03.174.

[132] ALICE Collaboration, *Technical Design Report of the High Momentum Particle Identification Detector* (CERN, 1998), CERN / LHCC 98-19, ALICE TDR 1.

[133] ALICE Collaboration, *Technical Design Report on Forward Detectors: FMD, T0 and V0* (CERN, 2004), CERN-LHCC-2004-025, ALICE-TDR-011.

[134] ALICE Collaboration, E. Abbas *et al.*, *Performance of the ALICE VZERO system*, JINST **8**, P10016 (2013), arXiv:1306.3130, doi:10.1088/1748-0221/8/10/P10016.

[135] ALICE Collaboration, *Technical Design Report of the Photon Multiplicity Detector (PMD)* (CERN, 1999), CERN / LHCC 99-32, ALICE TDR 6.

[136] ALICE Collaboration, *Addendum to the Technical Design Report of the Photon Multiplicity Detector (PMD)* (CERN, 2003), CERN / LHCC 2003-038, Addendum 1 to ALICE TDR 6.

[137] ALICE Collaboration, *Technical Design Report of the Zero Degree Calorimeter (ZDC)* (CERN, 1999), CERN/LHCC 99-5, ALICE TDR 3.

[138] ALICE Collaboration, *The forward muon spectrometer - Addendum to the ALICE Technical Proposal* (CERN, 1996), CERN/LHCC 96-53, LHCC/P3-Addendum 1.

[139] ALICE Collaboration, *Technical Design Report of the Dimuon Forward Spectrometer* (CERN, 1999), CERN/LHCC 99-22, ALICE TDR 5.

[140] ALICE Collaboration, *Addendum to the Technical Design Report of the Dimuon Forward Spectrometer* (CERN, 2000), CERN/LHCC 2000-046, Addendum 1 to ALICE TDR 5.

[141] Y. Belikov, M. Ivanov, K. Safarik and J. Bracinik, *TPC tracking and particle identification in high density environment*, eConf **C0303241**, TULT011 (2003), arXiv:physics/0306108.

[142] M. Ivanov, I. Belikov, P. Hristov and K. Safarik, *Track reconstruction in high density environment*, Nucl.Instrum.Meth. **A566**, 70 (2006), doi:10.1016/j.nima.2006.05.029.

[143] E. Bruna, A. Dainese, M. Masera and F. Prino, *Vertex reconstruction for proton-proton collisions in ALICE* (CERN, 2009), ALICE-INT-2009-018.

[144] ALICE Collaboration, B. Abelev *et al.*, *Centrality determination of Pb–Pb collisions at  $\sqrt{s_{NN}} = 2.76$  TeV with ALICE*, Phys.Rev. **C88**, 044909 (2013), arXiv:1301.4361, doi:10.1103/PhysRevC.88.044909.

[145] H. Buesching, M. Knichel, P. Luettig and J. Otwinowski, *Analysis Note for the pp Reference Paper*, ALICE internal note ANA-868, 2013.

[146] A. Andronic, M. Knichel, P. Luettig and J. Otwinowski, *Analysis Note for the  $R_{pPb}$  Paper*, ALICE internal note ANA-509, 2012.

[147] J. Otwinowski and M. Knichel,  *$R_{CP}$  of charged particles*, ALICE internal note ANA-1104, 2013.

[148] A. Andronic *et al.*, *Analysis Note: Multiplicity Dependence of the Average Transvers Momentum in  $p$ - $Pb$  and  $Pb$ - $Pb$  Collisions*, ALICE internal note ANA-777, 2013.

[149] R. Brun and F. Rademakers, *ROOT: An object oriented data analysis framework*, Nucl.Instrum.Meth. **A389**, 81 (1997), doi:10.1016/S0168-9002(97)00048-X.

[150] ALICE Collaboration, *AliRoot, ALICE Offline simulation, reconstruction and analysis framework*, <http://aliweb.cern.ch/Offline/>.

[151] ALICE Collaboration, K. Aamodt *et al.*, *First proton-proton collisions at the LHC as observed with the ALICE detector: Measurement of the charged particle pseudorapidity density at  $\sqrt{s} = 900$  GeV*, Eur.Phys.J. **C65**, 111 (2010), arXiv:0911.5430, doi:10.1140/epjc/s10052-009-1227-4.

[152] R. Brun *et al.*, *GEANT: Detector Description and Simulation Tool, CERN Program Library Long Writeup W5013* (CERN, Geneva, 1994).

[153] T. Sjostrand, *High-energy physics event generation with PYTHIA 5.7 and JETSET 7.4*, Comput.Phys.Commun. **82**, 74 (1994), doi:10.1016/0010-4655(94)90132-5.

[154] T. Sjostrand, S. Mrenna and P. Z. Skands, *PYTHIA 6.4 Physics and Manual*, JHEP **0605**, 026 (2006), arXiv:hep-ph/0603175, doi:10.1088/1126-6708/2006/05/026.

[155] P. Z. Skands, *The Perugia Tunes*, in *Proceedings, 1st International Workshop on Multiple Partonic Interactions at the LHC (MPI08)*, pp. 284–297, 2009, arXiv:0905.3418.

[156] R. Engel, J. Ranft and S. Roesler, *Hard diffraction in hadron hadron interactions and in photoproduction*, Phys.Rev. **D52**, 1459 (1995), arXiv:hep-ph/9502319, doi:10.1103/PhysRevD.52.1459.

[157] X.-N. Wang and M. Gyulassy, *HIJING: A Monte Carlo model for multiple jet production in  $pp$ ,  $pA$  and  $AA$  collisions*, Phys.Rev. **D44**, 3501 (1991), doi:10.1103/PhysRevD.44.3501.

[158] S. Roesler, R. Engel and J. Ranft, *The Monte Carlo event generator DPMJET-III*, in *Advanced Monte Carlo for radiation physics, particle transport simulation and applications. Proceedings, Conference, MC2000, Lisbon, Portugal, October 23-26, 2000*, pp. 1033–1038, 2000, arXiv:hep-ph/0012252, doi:10.1007/978-3-642-18211-2\_166.

[159] ALICE TPC Collaboration, *Definitions of TPC related track properties*, ALICE internal note, 2011.

[160] I. Narsky and F. C. Porter, *Statistical analysis techniques in particle physics* (Wiley-VCH, Weinheim, Germany, 2013).

[161] ALICE Collaboration, B. B. Abelev *et al.*, *Multiplicity Dependence of Pion, Kaon, Proton and Lambda Production in  $p$ - $Pb$  Collisions at  $\sqrt{s_{NN}} = 5.02$  TeV*, Phys.Lett. **B728**, 25 (2014), arXiv:1307.6796, doi:10.1016/j.physletb.2013.11.020.

[162] A. Andronic, J. Gronefeld, M. Knichel, P. Luettig and J. Otwinowski, *Nuclear Modification Factor of Charged Particles in  $p$ - $Pb$  2013 Data*, ALICE internal note ANA-1343, 2013.

[163] ALICE Collaboration, B. Abelev *et al.*, *Pseudorapidity density of charged particles  $p$ - $Pb$  collisions at  $\sqrt{s_{NN}} = 5.02$  TeV*, Phys.Rev.Lett. **110**, 032301 (2013), arXiv:1210.3615, doi:10.1103/PhysRevLett.110.032301.

[164] ALICE Collaboration, B. Abelev *et al.*, *Transverse Momentum Distribution and Nuclear Modification Factor of Charged Particles in  $p$ - $Pb$  Collisions at  $\sqrt{s_{NN}} = 5.02$  TeV*, Phys.Rev.Lett. **110**, 082302 (2013), arXiv:1210.4520, doi:10.1103/PhysRevLett.110.082302.

[165] ALICE Collaboration, B. Abelev *et al.*, *Measurement of inelastic, single- and double-diffraction cross sections in proton–proton collisions at the LHC with ALICE*, Eur.Phys.J. **C73**, 2456 (2013), arXiv:1208.4968, doi:10.1140/epjc/s10052-013-2456-0.

[166] S. van der Meer, *Calibration of the effective beam height in the ISR* (CERN, Geneva, 1968), CERN-ISR-PO-68-31. ISR-PO-68-31.

[167] UA5 Collaboration, R. Ansorge *et al.*, *Diffraction Dissociation at the CERN Pulsed Collider at CM Energies of 900 GeV and 200 GeV*, Z.Phys. **C33**, 175 (1986), doi:10.1007/BF01411134.

[168] M. Poghosyan, *Two remarks about UA5 published data on general characteristics of  $p\bar{p}$  collisions at  $\sqrt{s} = 900$  GeV*, 1005.1806, arXiv:1005.1806.

[169] G. Lafferty and T. Wyatt, *Where to stick your data points: The treatment of measurements within wide bins*, Nuclear Instruments and Methods in Physics Research Section A: Accelerators, Spectrometers, Detectors and Associated Equipment **355**, 541 (1995), doi:[http://dx.doi.org/10.1016/0168-9002\(94\)01112-5](http://dx.doi.org/10.1016/0168-9002(94)01112-5).

[170] R. Barlow, *Systematic errors: Facts and fictions*, hep-ex/0207026, arXiv:hep-ex/0207026.

[171] R. Barlow, *Asymmetric systematic errors*, physics/0306138, arXiv:physics/0306138.

[172] ALICE Collaboration, K. Aamodt *et al.*, *Suppression of Charged Particle Production at Large Transverse Momentum in Central  $Pb$ – $Pb$  Collisions at  $\sqrt{s_{NN}} = 2.76$  TeV*, Phys.Lett. **B696**, 30 (2011), arXiv:1012.1004, doi:10.1016/j.physletb.2010.12.020.

[173] ALICE Collaboration, B. B. Abelev *et al.*, *Transverse momentum dependence of inclusive primary charged-particle production in  $p$ – $Pb$  collisions at  $\sqrt{s_{NN}} = 5.02$  TeV*, Eur.Phys.J. **C74**, 3054 (2014), arXiv:1405.2737, doi:10.1140/epjc/s10052-014-3054-5.

[174] Segrè, E., *Nuclei and particles: an introduction to nuclear and subnuclear physics* (W.A. Benjamin, New York, 1964).

[175] ALICE Collaboration, K. Koch,  $\pi^0$  and  $\eta$  measurement with photon conversions in ALICE in proton-proton collisions at  $\sqrt{s} = 7$  TeV, Nucl.Phys. **A855**, 281 (2011), arXiv:1103.2217, doi:10.1016/j.nuclphysa.2011.02.059.

[176] ALICE Collaboration, K. Aamodt *et al.*, *Transverse momentum spectra of charged particles in proton-proton collisions at  $\sqrt{s} = 900$  GeV with ALICE at the LHC*, Phys.Lett. **B693**, 53 (2010), arXiv:1007.0719, doi:10.1016/j.physletb.2010.08.026.

[177] ALICE Collaboration, B. Abelev *et al.*, *Centrality Dependence of Charged Particle Production at Large Transverse Momentum in  $Pb$ – $Pb$  Collisions at  $\sqrt{s_{NN}} = 2.76$  TeV*, Phys.Lett. **B720**, 52 (2013), arXiv:1208.2711, doi:10.1016/j.physletb.2013.01.051.

---

[178] ALICE Collaboration, B. B. Abelev *et al.*, *Energy Dependence of the Transverse Momentum Distributions of Charged Particles in  $pp$  Collisions Measured by ALICE*, Eur.Phys.J. **C73**, 2662 (2013), arXiv:1307.1093, doi:10.1140/epjc/s10052-013-2662-9.

[179] T. Sjostrand, S. Mrenna and P. Z. Skands, *A Brief Introduction to PYTHIA 8.1*, Comput.Phys.Commun. **178**, 852 (2008), arXiv:0710.3820, doi:10.1016/j.cpc.2008.01.036.

[180] TeV4LHC QCD Working Group, M. G. Albrow *et al.*, *Tevatron-for-LHC Report of the QCD Working Group*, hep-ph/0610012, arXiv:hep-ph/0610012.

[181] P. Z. Skands, *Tuning Monte Carlo Generators: The Perugia Tunes*, Phys.Rev. **D82**, 074018 (2010), arXiv:1005.3457, doi:10.1103/PhysRevD.82.074018.

[182] R. Sassot, P. Zurita and M. Stratmann, *Inclusive Hadron Production in the CERN-LHC Era*, Phys.Rev. **D82**, 074011 (2010), arXiv:1008.0540, doi:10.1103/PhysRevD.82.074011.

[183] S. J. Brodsky and G. R. Farrar, *Scaling Laws at Large Transverse Momentum*, Phys.Rev.Lett. **31**, 1153 (1973), doi:10.1103/PhysRevLett.31.1153.

[184] D. W. Sivers, S. J. Brodsky and R. Blankenbecler, *Large Transverse Momentum Processes*, Phys.Rept. **23**, 1 (1976), doi:10.1016/0370-1573(76)90015-6.

[185] R. Blankenbecler, S. J. Brodsky and J. Gunion, *The Magnitude of Large Transverse Momentum Cross-Sections*, Phys.Rev. **D18**, 900 (1978), doi:10.1103/PhysRevD.18.900.

[186] F. Arleo, S. J. Brodsky, D. S. Hwang and A. M. Sickles, *Higher-Twist Dynamics in Large Transverse Momentum Hadron Production*, Phys.Rev.Lett. **105**, 062002 (2010), arXiv:0911.4604, doi:10.1103/PhysRevLett.105.062002.

[187] F. Arleo, D. d'Enterria and A. S. Yoon, *Single-inclusive production of large- $p_T$  charged particles in hadronic collisions at TeV energies and perturbative QCD predictions*, JHEP **1006**, 035 (2010), arXiv:1003.2963, doi:10.1007/JHEP06(2010)035.

[188] M. Stratmann, *Private Communication*.

[189] C. Tsallis, *Possible Generalization of Boltzmann-Gibbs Statistics*, J.Statist.Phys. **52**, 479 (1988), doi:10.1007/BF01016429.

[190] R. Hagedorn, *Multiplicities,  $p_T$  distributions and the expected hadron  $\rightarrow$  quark-gluon phase transition*, La Rivista del Nuovo Cimento **6**, 1 (1983), doi:10.1007/BF02740917.

[191] P. M. Nadolsky *et al.*, *Implications of CTEQ global analysis for collider observables*, Phys.Rev. **D78**, 013004 (2008), arXiv:0802.0007, doi:10.1103/PhysRevD.78.013004.

[192] D. de Florian, R. Sassot and M. Stratmann, *Global analysis of fragmentation functions for pions and kaons and their uncertainties*, Phys.Rev. **D75**, 114010 (2007), arXiv:hep-ph/0703242, doi:10.1103/PhysRevD.75.114010.

[193] D. de Florian, R. Sassot and M. Stratmann, *Global analysis of fragmentation functions for protons and charged hadrons*, Phys.Rev. **D76**, 074033 (2007), arXiv:0707.1506, doi:10.1103/PhysRevD.76.074033.

[194] ALICE Collaboration, B. Abelev *et al.*, *Neutral pion and  $\eta$  meson production in proton-proton collisions at  $\sqrt{s} = 0.9$  TeV and  $\sqrt{s} = 7$  TeV*, Phys.Lett. **B717**, 162 (2012), arXiv: 1205.5724, doi:10.1016/j.physletb.2012.09.015.

[195] CMS Collaboration, S. Chatrchyan *et al.*, *Charged particle transverse momentum spectra in pp collisions at  $\sqrt{s} = 0.9$  and 7 TeV*, JHEP **1108**, 086 (2011), arXiv:1104.3547, doi:10.1007/JHEP08(2011)086.

[196] CMS Collaboration, S. Chatrchyan *et al.*, *Study of high- $p_T$  charged particle suppression in PbPb compared to pp collisions at  $\sqrt{s_{NN}} = 2.76$  TeV*, Eur.Phys.J. **C72**, 1945 (2012), arXiv:1202.2554, doi:10.1140/epjc/s10052-012-1945-x.

[197] R. Sassot, P. Zurita and M. Stratmann, *Inclusive Hadron Production in the CERN-LHC Era*, Phys.Rev. **D82**, 074011 (2010), arXiv:1008.0540, doi:10.1103/PhysRevD.82.074011.

[198] D. d'Enterria, K. J. Eskola, I. Helenius and H. Paukkunen, *Confronting current NLO parton fragmentation functions with inclusive charged-particle spectra at hadron colliders*, Nucl.Phys. **B883**, 615 (2014), arXiv:1311.1415, doi:10.1016/j.nuclphysb.2014.04.006.

[199] J. Cronin *et al.*, *Production of Hadrons with Large Transverse Momentum at 200 GeV, 300 GeV, and 400 GeV*, Phys.Rev. **D11**, 3105 (1975), doi:10.1103/PhysRevD.11.3105.

[200] D. Antreasyan *et al.*, *Production of Hadrons at Large Transverse Momentum in 200 GeV, 300 GeV and 400 GeV pp and pn Collisions*, Phys.Rev. **D19**, 764 (1979), doi:10.1103/PhysRevD.19.764.

[201] STAR Collaboration, J. Adams *et al.*, *Evidence from d+Au measurements for final state suppression of high  $p_T$  hadrons in Au+Au collisions at RHIC*, Phys.Rev.Lett. **91**, 072304 (2003), arXiv:nucl-ex/0306024, doi:10.1103/PhysRevLett.91.072304.

[202] PHENIX Collaboration, S. Adler *et al.*, *Absence of suppression in particle production at large transverse momentum in  $\sqrt{s_{NN}} = 200$  GeV d+Au collisions*, Phys.Rev.Lett. **91**, 072303 (2003), arXiv:nucl-ex/0306021, doi:10.1103/PhysRevLett.91.072303.

[203] BRAHMS Collaboration, I. Arsene *et al.*, *Transverse momentum spectra in Au+Au and d+Au collisions at  $\sqrt{s_{NN}} = 200$  GeV and the pseudorapidity dependence of high  $p_T$  suppression*, Phys.Rev.Lett. **91**, 072305 (2003), arXiv:nucl-ex/0307003, doi:10.1103/PhysRevLett.91.072305.

[204] PHOBOS Collaboration, B. Back *et al.*, *Pseudorapidity dependence of charged hadron transverse momentum spectra in d+Au collisions at  $\sqrt{s_{NN}} = 200$  GeV*, Phys.Rev. **C70**, 061901 (2004), arXiv:nucl-ex/0406017, doi:10.1103/PhysRevC.70.061901.

[205] P. Tribedy and R. Venugopalan, *QCD saturation at the LHC: comparisons of models to p+p and A+A data and predictions for p+Pb collisions*, Phys.Lett. **B710**, 125 (2012), arXiv:1112.2445, doi:10.1016/j.physletb.2012.02.047, 10.1016/j.physletb.2012.12.004.

[206] J. L. Albacete, A. Dumitru, H. Fujii and Y. Nara, *CGC predictions for p+Pb collisions at the LHC*, Nucl.Phys. **A897**, 1 (2013), arXiv:1209.2001, doi:10.1016/j.nuclphysa.2012.09.012.

[207] A. H. Rezaeian, *CGC predictions for  $p+A$  collisions at the LHC and signature of QCD saturation*, Phys.Lett. **B718**, 1058 (2013), arXiv:1210.2385, doi:10.1016/j.physletb.2012.11.066.

[208] ALICE Collaboration, M. L. Knichel, *Production of light flavour hadrons at intermediate and high  $p_T$  in  $pp$ ,  $p$ - $Pb$  and  $Pb$ - $Pb$  collisions measured with ALICE*, Nucl. Phys. **A931**, 309 (2014), arXiv:1408.0216, doi:10.1016/j.nuclphysa.2014.08.009.

[209] Z.-B. Kang, I. Vitev and H. Xing, *Nuclear modification of high transverse momentum particle production in  $p+A$  collisions at RHIC and LHC*, Phys.Lett. **B718**, 482 (2012), arXiv:1209.6030, doi:10.1016/j.physletb.2012.10.046.

[210] R. Xu, W.-T. Deng and X.-N. Wang, *Nuclear modification of high- $p_T$  hadron spectra in  $p+A$  collisions at LHC*, Phys.Rev. **C86**, 051901 (2012), arXiv:1204.1998, doi:10.1103/PhysRevC.86.051901.

[211] R. Xu, W.-T. Deng and X.-N. Wang, *Suppression of high  $p_T$  hadron spectra in  $p+A$  collisions*, Nucl.Phys. **A910-911**, 514 (2013), arXiv:1207.6836, doi:10.1016/j.nuclphysa.2012.12.025.

[212] CMS Collaboration, *Charged particle nuclear modification factor and pseudorapidity asymmetry in  $pPb$  collisions at  $\sqrt{s_{NN}}=5.02$  TeV with CMS* (CERN, Geneva, 2013), CMS-PAS-HIN-12-017.

[213] ATLAS collaboration, *Transverse Momentum Dependence of Charged Particle Production in  $p+Pb$   $\sqrt{s_{NN}}=5.02$  TeV collisions measured by ATLAS experiment at the LHC* (CERN, Geneva, 2013), ATLAS-CONF-2013-107, ATLAS-COM-CONF-2013-135.

[214] ATLAS Collaboration, *Charged hadron production in  $p+Pb$  collisions at  $\sqrt{s_{NN}}=5.02$  TeV measured at high transverse momentum by the ATLAS experiment* (CERN, Geneva, 2014), ATLAS-CONF-2014-029.

[215] ALICE Collaboration, B. Abelev *et al.*, *Centrality dependence of  $\pi$ ,  $K$ ,  $p$  production in  $Pb-Pb$  collisions at  $\sqrt{s_{NN}}=2.76$  TeV*, Phys.Rev. **C88**, 044910 (2013), arXiv:1303.0737, doi:10.1103/PhysRevC.88.044910.

[216] ALICE, B. B. Abelev *et al.*, *Production of charged pions, kaons and protons at large transverse momenta in  $pp$  and  $Pb-Pb$  collisions at  $\sqrt{s_{NN}}=2.76$  TeV*, Phys. Lett. **B736**, 196 (2014), arXiv:1401.1250, doi:10.1016/j.physletb.2014.07.011.

[217] PHENIX Collaboration, S. Adler *et al.*, *High  $p_T$  charged hadron suppression in  $Au+Au$  collisions at  $\sqrt{s_{NN}}=200$  GeV*, Phys.Rev. **C69**, 034910 (2004), arXiv:nucl-ex/0308006, doi:10.1103/PhysRevC.69.034910.

[218] T. Renk, *Pathlength dependence of energy loss within in-medium showers*, Phys.Rev. **C83**, 024908 (2011), arXiv:1010.4116, doi:10.1103/PhysRevC.83.024908.

[219] T. Renk, H. Holopainen, R. Paatelainen and K. J. Eskola, *Systematics of the charged-hadron  $p_T$  spectrum and the nuclear suppression factor in heavy-ion collisions from  $\sqrt{s}=200$  GeV to  $\sqrt{s}=2.76$  TeV*, Phys.Rev. **C84**, 014906 (2011), arXiv:1103.5308, doi:10.1103/PhysRevC.84.014906.

[220] X.-F. Chen, T. Hirano, E. Wang, X.-N. Wang and H. Zhang, *Suppression of high  $p_T$  hadrons in Pb+Pb Collisions at LHC*, Phys.Rev. **C84**, 034902 (2011), arXiv:1102.5614, doi:10.1103/PhysRevC.84.034902.

[221] W. Horowitz and M. Gyulassy, *The Surprising Transparency of the sQGP at LHC*, Nucl.Phys. **A872**, 265 (2011), arXiv:1104.4958, doi:10.1016/j.nuclphysa.2011.09.018.

[222] C. A. Salgado and U. A. Wiedemann, *Calculating quenching weights*, Phys.Rev. **D68**, 014008 (2003), arXiv:hep-ph/0302184, doi:10.1103/PhysRevD.68.014008.

[223] A. Majumder and C. Shen, *Suppression of the High  $p_T$  Charged Hadron  $R_{AA}$  at the LHC*, Phys.Rev.Lett. **109**, 202301 (2012), arXiv:1103.0809, doi:10.1103/PhysRevLett.109.202301.

[224] K. C. Zapp, F. Krauss and U. A. Wiedemann, *Explaining Jet Quenching with Perturbative QCD Alone*, 1111.6838, arXiv:1111.6838.

[225] K. C. Zapp, F. Krauss and U. A. Wiedemann, *A perturbative framework for jet quenching*, JHEP **1303**, 080 (2013), arXiv:1212.1599, doi:10.1007/JHEP03(2013)080.

[226] A. Bialas, M. Bleszynski and W. Czyz, *Multiplicity Distributions in Nucleus-Nucleus Collisions at High-Energies*, Nucl.Phys. **B111**, 461 (1976), doi:10.1016/0550-3213(76)90329-1.

[227] ALICE Collaboration, K. Aamodt *et al.*, *Charged-particle multiplicity measurement in proton-proton collisions at  $\sqrt{s} = 0.9$  and 2.36 TeV with ALICE at LHC*, Eur.Phys.J. **C68**, 89 (2010), arXiv:1004.3034, doi:10.1140/epjc/s10052-010-1339-x.

[228] ALICE Collaboration, K. Aamodt *et al.*, *Charged-particle multiplicity measurement in proton-proton collisions at  $\sqrt{s} = 7$  TeV with ALICE at LHC*, Eur.Phys.J. **C68**, 345 (2010), arXiv:1004.3514, doi:10.1140/epjc/s10052-010-1350-2.

[229] ALICE Collaboration, B. B. Abelev *et al.*, *Multiplicity dependence of the average transverse momentum in pp, p-Pb, and Pb-Pb collisions at the LHC*, Phys.Lett. **B727**, 371 (2013), arXiv:1307.1094, doi:10.1016/j.physletb.2013.10.054.

[230] A. Ortiz, P. Christiansen, E. Cuautle, I. Maldonado and G. Paic, *Color reconnection and flow-like patterns in pp collisions*, Phys.Rev.Lett. **111**, 042001 (2013), arXiv:1303.6326, doi:10.1103/PhysRevLett.111.042001.

[231] T. Pierog, I. Karpenko, J. Katzy, E. Yatsenko and K. Werner, *EPOS LHC : test of collective hadronization with LHC data*, 1306.0121, arXiv:1306.0121.

[232] Z.-W. Lin, C. M. Ko, B.-A. Li, B. Zhang and S. Pal, *A Multi-phase transport model for relativistic heavy ion collisions*, Phys.Rev. **C72**, 064901 (2005), arXiv:nucl-th/0411110, doi:10.1103/PhysRevC.72.064901.

[233] A. H. Rezaeian, *Comparison of the Color Glass Condensate to multiplicity dependence of the average transverse momentum in p+p, p+Pb and Pb+Pb collisions at the LHC*, Phys.Lett. **B727**, 218 (2013), arXiv:1308.4736, doi:10.1016/j.physletb.2013.10.038.

[234] ALICE Collaboration, B. Abelev *et al.*, *Measurement of the inclusive differential jet cross section in  $pp$  collisions at  $\sqrt{s} = 2.76$  TeV*, Phys.Lett. **B722**, 262 (2013), arXiv:1301.3475, doi:10.1016/j.physletb.2013.04.026.

[235] CMS Collaboration, V. Khachatryan *et al.*, *Observation of Long-Range Near-Side Angular Correlations in Proton-Proton Collisions at the LHC*, JHEP **1009**, 091 (2010), arXiv:1009.4122, doi:10.1007/JHEP09(2010)091.

[236] CMS Collaboration, S. Chatrchyan *et al.*, *Measurement of isolated photon production in  $pp$  and  $PbPb$  collisions at  $\sqrt{s_{NN}} = 2.76$  TeV*, Phys.Lett. **B710**, 256 (2012), arXiv:1201.3093, doi:10.1016/j.physletb.2012.02.077.

[237] CMS Collaboration, S. Chatrchyan *et al.*, *Study of  $W$  boson production in  $PbPb$  and  $pp$  collisions at  $\sqrt{s_{NN}} = 2.76$  TeV*, Phys.Lett. **B715**, 66 (2012), arXiv:1205.6334, doi:10.1016/j.physletb.2012.07.025.

[238] CMS Collaboration, S. Chatrchyan *et al.*, *Study of  $Z$  boson production in  $PbPb$  collisions at nucleon-nucleon centre of mass energy = 2.76 TeV*, Phys.Rev.Lett. **106**, 212301 (2011), arXiv:1102.5435, doi:10.1103/PhysRevLett.106.212301.

[239] ALICE Collaboration, R. Haake, *Charged Jets in Minimum Bias  $p$ - $Pb$  Collisions at  $\sqrt{s_{NN}} = 5.02$  TeV with ALICE*, PoS **EPS-HEP2013**, 176 (2013), arXiv:1310.3612.

[240] G. G. Barnafoldi, P. Levai, G. Fai, G. Papp and B. A. Cole, *Does the Cronin Peak Disappear at LHC Energies?*, Int.J.Mod.Phys. **E16**, 1923 (2007), arXiv:hep-ph/0703059, doi:10.1142/S0218301307007234.

[241] ALICE, A. Morsch,  *$p$ - $Pb$  Results from ALICE with an Emphasis on Centrality Determination*, J. Phys. Conf. Ser. **509**, 012021 (2014), arXiv:1309.5525, doi:10.1088/1742-6596/509/1/012021.

[242] B. Kopeliovich, J. Nemchik, I. Potashnikova and I. Schmidt, *Quenching of high- $p_T$  hadrons: Energy Loss vs Color Transparency*, Phys.Rev. **C86**, 054904 (2012), arXiv:1208.4951, doi:10.1103/PhysRevC.86.054904.

[243] P. Bozek, A. Bzdak and V. Skokov, *The rapidity dependence of the average transverse momentum in  $p$ + $Pb$  collisions at the LHC: the Color Glass Condensate versus hydrodynamics*, Phys.Lett. **B728**, 662 (2014), arXiv:1309.7358, doi:10.1016/j.physletb.2013.12.034.

[244] ALICE Collaboration, A. Toia, *ALICE Measurements in  $p$ - $Pb$  Collisions: Charged Particle Multiplicity, Centrality Determination and implications for Binary Scaling*, Nucl.Phys. **A926**, 78 (2014), arXiv:1403.5143, doi:10.1016/j.nuclphysa.2014.03.020.

[245] ALICE Collaboration, B. Abelev *et al.*, *Multi-strange baryon production in  $pp$  collisions at  $\sqrt{s} = 7$  TeV with ALICE*, Phys.Lett. **B712**, 309 (2012), arXiv:1204.0282, doi:10.1016/j.physletb.2012.05.011.

[246] ALICE Collaboration, B. B. Abelev *et al.*,  *$K_S^0$  and  $\Lambda$  production in  $Pb$ - $Pb$  collisions at  $\sqrt{s_{NN}} = 2.76$  TeV*, Phys.Rev.Lett. **111**, 222301 (2013), arXiv:1307.5530, doi:10.1103/PhysRevLett.111.222301.

---

---

- [247] ALICE Collaboration, B. B. Abelev *et al.*, *Multi-strange baryon production at mid-rapidity in Pb–Pb collisions at  $\sqrt{s_{NN}} = 2.76$  TeV*, Phys.Lett. **B728**, 216 (2014), arXiv:1307.5543, doi:10.1016/j.physletb.2013.11.048.
- [248] M. Ivanov, *Private Communication*.
- [249] ALICE, B. Abelev *et al.*, *Upgrade of the ALICE Experiment: Letter Of Intent*, J. Phys. **G41**, 087001 (2014), doi:10.1088/0954-3899/41/8/087001.
- [250] ALICE, B. Abelev *et al.*, *Technical Design Report for the Upgrade of the ALICE Inner Tracking System*, J. Phys. **G41**, 087002 (2014), doi:10.1088/0954-3899/41/8/087002.
- [251] ALICE Collaboration, *Upgrade of the ALICE Time Projection Chamber* (CERN, Geneva, 2013), CERN-LHCC-2013-020, ALICE-TDR-016.
- [252] ALICE Collaboration, P. Antonioli, A. Kluge and W. Riegler, *Upgrade of the ALICE Readout & Trigger System* (CERN, Geneva, 2013), CERN-LHCC-2013-019. ALICE-TDR-015.



# Acknowledgments

After having finished my thesis I would like to express my gratitude to all people who have helped and accompanied me in the past years.

First of all I would like to thank Prof. Dr. Peter Braun-Munzinger for giving me the opportunity and continuing support to do my dissertation in his research group and participate in the exciting LHC physics.

Many thanks to Dr. Jacek Otwinowski, for getting me involved in the analysis, his mentoring and the great collaboration. Many thanks also for proofreading my thesis.

I would like to express my gratitude to Dr. Anton Andronic, for many interesting discussions and his catching enthusiasm. Thanks also for valuable comments on my thesis.

Thanks to Philipp Lüttig for the enjoyable cooperation on the analysis, to Dr. Kai Schweda for many discussions and his precious comments on my thesis and to Dr. Marian Ivanov for all his ideas and fascinating competence.

For the fruitful collaboration on the publications I would like to thank Dr. Anton Andronic, Prof. Dr. Harald Appelshäuser, Prof. Dr. Henner Büsching, Julius Gronefeld, Marco Marquard, Dr. Jacek Otwinowski, Dr. Kai Schweda and Dr. Jochen Thäder.

Dr. Silvia Masciocchi, the team leader of the GSI group, I thank for her incredible support. Thanks also to my fellow PhD students and the whole ALICE group at GSI for the nice working environment, especially to my former office mate Markus Köhler. Thanks also to Prof. Dr. Johanna Stachel and the entire Heidelberg group.

Michael Winn and Daniel Beul I thank for their contribution to the proofreading. Thanks to Prof. Dr. Jochen Wambach for the second review of my thesis.

Taraneh, thank You for always encouraging and supporting me.



# Curriculum Vitae

---

## Michael Linus Knichel

---

### Personal data

- born 16 January 1981 in Mainz
- Nationality: German

### Education

since 01/2014	Research associate at Ruprecht-Karls-Universität Heidelberg
05/2013 – 11/2013	Fellowship of the ExtreMe Matter Institute EMMI
11/2009 – 04/2013	Fellowship of the Helmholtz Research School for Quark Matter Studies
since 10/2009	Doctoral research studies at Technische Universität Darmstadt and GSI, Darmstadt
08/2004 – 08/2005	Studies at University of Saskatchewan, Department of Physics and Engineering Physics, Saskatoon, Canada
10/2001 – 09/2009	Diplom in physics, Technische Universität Darmstadt, Germany Overall grade: very good Diploma thesis " <i>Characterization of a fully equipped ALICE TPC readout chamber</i> " at GSI, Germany, and CERN, Switzerland

### Publications with significant contribution

- Michael Linus Knichel for the ALICE Collaboration, *Production of light flavour hadrons at intermediate and high  $p_T$  in  $pp$ ,  $p$ – $Pb$  and  $Pb$ – $Pb$  collisions measured with ALICE*, Nucl. Phys. A 931, 309 (2014)
- ALICE Collaboration, *Transverse momentum dependence of inclusive primary charged-particle production in  $p$ – $Pb$  collisions at  $\sqrt{s_{NN}} = 5.02$  TeV*, Eur. Phys. J. C 74, 3054 (2014)
- ALICE Collaboration, *Multiplicity dependence of the average transverse momentum in  $pp$ ,  $p$ – $Pb$ , and  $Pb$ – $Pb$  collisions at the LHC*, Phys. Lett. B 727, 371 (2013)
- ALICE Collaboration, *Energy Dependence of the Transverse Momentum Distributions of Charged Particles in  $pp$  Collisions Measured by ALICE*, Eur. Phys. J. C 73, 2662 (2013)
- ALICE Collaboration, *Transverse Momentum Distribution and Nuclear Modification Factor of Charged Particles in  $p$ – $Pb$  Collisions at  $\sqrt{s_{NN}} = 5.02$  TeV*, Phys. Rev. Lett. 110, 082302 (2013)

- ALICE Collaboration, *Centrality Dependence of Charged Particle Production at Large Transverse Momentum in Pb–Pb Collisions at  $\sqrt{s_{\text{NN}}} = 2.76 \text{ TeV}$* , Phys. Lett. B 720 (2013) 52-62
- ALICE Collaboration, *Suppression of Charged Particle Production at Large Transverse Momentum in Central Pb–Pb Collisions at  $\sqrt{s_{\text{NN}}} = 2.76 \text{ TeV}$* , Phys. Lett. B 696 (2011) 30-39
- ALICE Collaboration, *Transverse momentum spectra of charged particles in proton-proton collisions at  $\sqrt{s} = 900 \text{ GeV}$  with ALICE at the LHC*, Phys. Lett. B 693 (2010) 53-68

### Talk and poster presentations

- *Production of light flavor hadrons at intermediate and high  $p_{\text{T}}$  measured with ALICE*, talk at Quark Matter, Darmstadt, Germany, May 19-24, 2014
- *Transverse Momentum Spectra of Charged Particles measured in pp, p–Pb and Pb–Pb Collisions with ALICE at the LHC*, talk at 77th Annual Meeting of the DPG and DPG Spring Meeting, Dresden, Germany, March 4-8, 2013
- *p–Pb collisions at the LHC: First results from ALICE*, talk at RNM Seminar, GSI, Darmstadt, Germany, January 17, 2013
- *Transverse Momentum Distribution and Nuclear Modification Factor of Charged Particles in p–Pb Collisions at  $\sqrt{s_{\text{NN}}} = 5.02 \text{ TeV}$* , poster at EMMI Physics Days, GSI, Darmstadt, Germany, November 13-14, 2012
- *Suppression of Charged Particle Production at Large Transverse Momentum in Pb–Pb Collisions at  $\sqrt{s_{\text{NN}}} = 2.76 \text{ TeV}$* , poster at LHCC poster session, CERN, Geneva, Switzerland, March 21, 2012
- *Charged particle production at large transverse momentum in Pb–Pb collisions at  $\sqrt{s_{\text{NN}}} = 2.76 \text{ TeV}$  measured with ALICE at the LHC*, talk at DPG Spring Meeting, Mainz, Germany, March 19-23, 2012
- *Hard probes at ALICE*, talk at Rencontres de Moriond – QCD and High Energy Interactions, La Thuile, Italy, March 10-17, 2012
- *Suppression of Charged Particle Production at Large Transverse Momentum in Pb–Pb Collisions at  $\sqrt{s_{\text{NN}}} = 2.76 \text{ TeV}$* , poster at EMMI Physics Days, GSI, Darmstadt, Germany, November 7-8, 2011
- *$R_{\text{AA}}$  in ALICE*, talk at High-pT Probes of High-Density QCD at the LHC, Ecole Polytechnique, Palaiseau, France, May 30 - June 01, 2011
- *Charged-particle transverse momentum spectra in proton-proton collisions at  $\sqrt{s} = 0.9 \text{ TeV}$ , 2.76 TeV and 7 TeV measured with ALICE at the LHC*, poster at Quark Matter, Annecy, France, May 23-28, 2011

---

# Eigenständigkeitserklärung

Hiermit versichere ich die vorliegende Dissertation ohne Hilfe Dritter nur mit den angegebenen Quellen und Hilfmitteln angefertigt zu haben. Alle Stellen, die aus Quellen entnommen wurden, sind als solche kenntlich gemacht. Diese Arbeit hat in gleicher oder ähnlicher Form noch keiner Prüfungsbehörde vorgelegen. Des weiteren versichere ich, dass ich bisher keinen Versuch einer Promotion unternommen habe.

Darmstadt, den 20. September 2014

---

Michael Linus Knichel

